

---


Electronic Theses and Dissertations, 2020-

---

2020

## Pathological Tremor as a Mechanical System: Modeling and Control of Artificial Muscle-Based Tremor Suppression

Christopher Kelley  
University of Central Florida

 Part of the [Mechanical Engineering Commons](#)  
Find similar works at: <https://stars.library.ucf.edu/etd2020>  
University of Central Florida Libraries <http://library.ucf.edu>

This Doctoral Dissertation (Open Access) is brought to you for free and open access by STARS. It has been accepted for inclusion in Electronic Theses and Dissertations, 2020- by an authorized administrator of STARS. For more information, please contact [STARS@ucf.edu](mailto:STARS@ucf.edu).

---

### STARS Citation

Kelley, Christopher, "Pathological Tremor as a Mechanical System: Modeling and Control of Artificial Muscle-Based Tremor Suppression" (2020). *Electronic Theses and Dissertations, 2020-*. 70.  
<https://stars.library.ucf.edu/etd2020/70>

PATHOLOGICAL TREMOR AS A MECHANICAL SYSTEM: MODELING AND  
CONTROL OF ARTIFICIAL MUSCLE-BASED TREMOR SUPPRESSION

by

CHRISTOPHER R. KELLEY  
B.S. University of Florida, 2013  
M.S. University of Central Florida, 2016

A dissertation submitted in partial fulfillment of the requirements  
for the degree of Doctor of Philosophy  
in the Department of Mechanical and Aerospace Engineering  
in the College of Engineering and Computer Science  
at the University of Central Florida  
Orlando, Florida

Spring Term  
2020

Major Professor: Jeffrey L. Kauffman



© 2020 Christopher R. Kelley

## **ABSTRACT**

Central nervous system disorders produce the undesired, approximately rhythmic movement of body parts known as pathological tremor. This undesired motion inhibits the patient's ability to perform tasks of daily living and participate in society. Typical treatments are medications and deep brain stimulation surgery, both of which include risks, side effects, and varying efficacy. Since the pathophysiology of tremor is not well understood, empirical investigation drives tremor treatment development. This dissertation explores tremor from a mechanical systems perspective to work towards theory-driven treatment design. The primary negative outcome of pathological tremor is the undesired movement of body parts: mechanically suppressing this motion provides effective tremor treatment by restoring limb function. Unlike typical treatments, the mechanisms for mechanical tremor suppression are well understood: applying joint torques that oppose tremor-producing muscular torques will reduce tremor irrespective of central nervous system pathophysiology. However, a tremor suppression system must also consider voluntary movements. For example, mechanically constraining the arm in a rigid cast eliminates tremor motion, but also eliminates the ability to produce voluntary motions. Indeed, passive mechanical systems typically reduce tremor and voluntary motions equally due to the close proximity of their frequency content. Thus, mechanical tremor suppression requires active actuation to reduce tremor with minimal influence

on voluntary motion. However, typical engineering actuators are rigid and bulky, preventing clinical implementations.

This dissertation explores dielectric elastomers as tremor suppression actuators to improve clinical implementation potential of mechanical tremor suppression. Dielectric elastomers are often called “artificial muscles” due to their similar mechanical properties as human muscle; these similarities may enable relatively soft, low-profile implementations. The primary drawback of dielectric elastomers is their relatively low actuation levels compared to typical actuators. This research develops a tremor-active approach to dielectric elastomer-based tremor suppression. In a tremor-active approach, the actuators only actuate to oppose tremor, while the human motor system must overcome the passive actuator dynamics. This approach leverages the low mechanical impedance of dielectric elastomers to overcome their low actuation levels. Simulations with recorded tremor datasets demonstrate excellent and robust tremor suppression performance. Benchtop experiments validate the control approach on a scaled system. Since dielectric elastomers are not yet commercially available, this research quantifies the necessary dielectric elastomer parameters to enable clinical implementations and evaluates the potential of manufacturing approaches in the literature to achieve these parameters. Overall, tremor-active control using dielectric elastomers represents a promising alternative to medications and surgery. Such a system may achieve comparable tremor reduction as medications and deep brain stimulation with minimal risks and greater efficacy, but at the cost of increased patient effort to produce voluntary motions. Parallel advances in scaled dielectric elastomer manufacturing processes and high-voltage power electronics will enable consumer implementations.

In addition to tremor suppression, this dissertation investigates the mechanisms of central nervous system tremor generation from a control systems perspective. This research investigates a delay-based model for parkinsonian tremor. Besides tremor, Parkinson's disease generally inhibits movement, with typical symptoms including rigidity, bradykinesia, and increased reaction times. This fact raises the question as to how the same disease produces excessive movement (tremor) despite characteristically inhibiting movement. One possible answer is that excessive central nervous system inhibition produces unaccounted feedback delays that cause instability. This dissertation develops an optimal control model of human motor control with an unaccounted delay between the state estimator and controller. This delay represents the increased inhibition projected from the basal ganglia to the thalamus, delaying signals traveling from the cerebellum (estimator) to the primary motor cortex (controller). Model simulations show increased delays decrease tremor frequency and increase tremor amplitude, consistent with the evolution of tremor as the disease progresses. Simulations that incorporate tremor resetting and random variation in control saturation produce simulated tremor with similar characteristics as recorded tremor. Delay-induced tremor explains the effectiveness of deep brain stimulation in both the thalamus and basal ganglia since both regions contribute to the presence of feedback delay. Clinical evaluation of mechanical tremor suppression may provide clinical evidence for delay-induced tremor: unlike state-independent tremor, suppression of delay-induced tremor increases tremor frequency. Altogether, establishing the mechanisms for tremor generation will facilitate pathways towards improved treatments and cure development.

*For Clare, whose delivery room was also the birthplace of the first draft of this dissertation.*

## ACKNOWLEDGMENTS

I begin by acknowledging Jeff Kauffman, without whom I would very likely be spending my days hollowly saying, “Working hard or hardly working?” to my fellow clock punchers as we anxiously await the weekend. Jeff gave me an opportunity at a time when I felt completely lost and somewhat worthless. He helped me discover research and somehow made me believe that I could do it. He gave me confidence, knowledge, and the freedom to use it. His guidance has been invaluable and it has shaped my goals. Jeff always said life is about the journey—this journey was a good one.

Thank you to Helen Huang, Tuhin Das, and Aman Behal for your insight and feedback as committee members. Our discussions improved my dissertation and produced new research ideas. I also appreciate the camaraderie of my fellow labmates: Dan Geiyer, Garrett Lopp, Taylor Hynds, Jim Little, Brandi McPherson, Andres Rodriguez, and Christian Vazquez. I enjoyed our research discussions, post-conference travels, and liberal use of bad puns (Piezochu and Kauffing stand out, inspired by those peak Pokémon GO days).

My family motivated and supported me during this journey. Mom, you always believed there were no limits to what I could accomplish and you were willing to do anything to help me succeed. Jake, you get me like no one else and I owe a great portion of my happiness to you. Ed, Lori, and Mike, you welcomed me into your family with unconditional support and admiration. Drew, you enriched my life through our numerous adventures. Phil, you helped me grow into who I am today.

My friends carried me through this journey in a manner not dissimilar to T-Mac carrying an undermanned team. So thank you to the friends with whom I spent the past few years living in the good old days (in random order via Name Selector Lite): Drew Fulcher, Keith Brinsko, Jake Kelley, Jim Little, Paul Heagney, Tarique Henriques, Brennen Crenshaw, Kent Bailey, Travis Henriques, Armando Perez, and Phil Lakin. We banished monsters, rolled sevens, and even played regular beer from time to time. We were the Cresto Crew and the Wessex Boys—names from ordinary places that became synonymous with the good times we shared. The hardest part about completing this dissertation is knowing the future likely leads me away from these places. However, our journey together is far from over and I am looking forward to our next adventures.

Finally, I must attempt to properly acknowledge my wife. Kate, you supported me in every way throughout this journey, but I appreciate your companionship most of all. It was a special time in our lives: we had our wedding during my first semester and our first child (Clare, see dedication) during my last (not counting Brody and Deacon, who, by law, are not human). In between, I researched and you worked; we traveled and stayed home; we went out and stayed home—regardless of what we did, the enjoyment of your company refreshed me so that I could enjoy my research. I am excited to write the next chapters of our lives together.

## TABLE OF CONTENTS

LIST OF FIGURES .....	xiv
LIST OF TABLES .....	xix
CHAPTER 1 : INTRODUCTION .....	1
1.1 Tremor as a Mechanical System .....	2
1.1.1 Tremor Dynamics .....	3
1.1.2 Mechanical Tremor Suppression .....	5
1.2 Artificial Muscles for Tremor Suppression .....	7
1.3 CNS Response to Tremor Suppression .....	9
1.3.1 Parkinsonian Tremor as an Increased CNS Delay .....	10
1.4 Dissertation Structure .....	12
CHAPTER 2 : BACKGROUND .....	14
2.1 Pathological Tremor.....	14
2.1.1 Subsets of Pathological Tremor .....	15



2.1.2	Pathophysiology of Tremor . . . . .	16
2.1.3	Tremor Treatments . . . . .	18
2.2	Mechanical Suppression of Tremor . . . . .	21
2.2.1	Subsets of Mechanical Treatments . . . . .	22
2.2.2	Control Strategies . . . . .	24
2.2.3	Actuator Selection . . . . .	27
2.3	Dielectric Elastomers . . . . .	28
2.3.1	Characteristics of DEAs . . . . .	30
2.3.2	Limitations . . . . .	36
2.4	Human Motor Control . . . . .	38
2.4.1	Internal Models . . . . .	39
2.4.2	Optimal Control . . . . .	41
2.4.3	Roles of CNS Regions . . . . .	43
CHAPTER 3 : DESA-BASED TREMOR SUPPRESSION . . . . .		46
3.1	Model Development . . . . .	46
3.1.1	DESA Model . . . . .	47
3.1.2	DESA-Joint Interaction . . . . .	51
3.1.3	Parameter Selection . . . . .	57

3.1.4	Muscular Torque .....	62
3.2	Fully Active Controller .....	67
3.2.1	Adaptive Notch Filter .....	67
3.2.2	Fully Active Simulations .....	72
3.3	Tremor-Active Controller .....	80
3.3.1	Impedance Controller with Adaptive Gain .....	81
3.3.2	Tremor-Active Simulations .....	85
CHAPTER 4 : DESA IMPLEMENTATION OUTLOOK .....		95
4.1	Experiments .....	95
4.1.1	DESA Manufacturing .....	96
4.1.2	Scaled Tremor Suppression .....	98
4.2	Necessary Parameters for Tremor Suppression .....	108
4.2.1	Performance Limits .....	109
4.2.2	Tremor-Active Parameters .....	112
4.2.3	Fully Active Parameters .....	119
4.2.4	Outlook .....	122
CHAPTER 5 : PARKINSON'S DISEASE TREMOR MODEL .....		126
5.1	Delay-Induced Tremor .....	126

5.1.1	Optimal Controller .....	129
5.1.2	Tremor Model Simulations .....	135
5.2	Implications .....	144
5.2.1	Physiological Models .....	145
5.2.2	Treatments .....	146
5.2.3	Mechanical Tremor Suppression .....	147
CHAPTER 6 : CONCLUSIONS & REMAINING QUESTIONS .....		149
6.1	Key Contributions .....	152
6.1.1	DESA-Based Tremor Suppression .....	152
6.1.2	Tremor Produced via CNS Delay .....	154
6.2	Remaining Questions .....	156
6.2.1	DESA Implementation .....	156
6.2.2	Clinical Evaluation of Delay-Induced Tremor .....	157
APPENDIX A : MATLAB CODE FOR TREMOR SUPPRESSION SIMULATIONS ....		159
A.1	Fully Active Simulation .....	160
A.1.1	Execution Script .....	160
A.1.2	Associated Functions .....	166
A.2	Tremor-Active Simulation .....	167

A.2.1	Execution Script .....	167
A.2.2	Associated Functions .....	172
APPENDIX B : MATLAB CODE FOR DELAY-INDUCED TREMOR SIMULATIONS .		174
B.1	SDOF Reach-Posture-Reach-Posture Task .....	175
B.1.1	Execution Script .....	175
B.1.2	Associated Scripts and Functions .....	176
B.2	3DOF Rest Tremor .....	186
B.2.1	Execution Script .....	186
B.2.2	Associated Scripts and Functions .....	189
LIST OF REFERENCES .....		197

## LIST OF FIGURES

Figure 1.1	Recorded time series examples of parkinsonian tremor and essential tremor . .	3
Figure 1.2	FFT of essential tremor and parkinsonian tremor data . . . . .	4
Figure 1.3	Tremor amplitudes and frequencies over time . . . . .	5
Figure 1.4	Active tremor suppression block diagram . . . . .	7
Figure 1.5	Dielectric elastomers as agonist-antagonist pairs . . . . .	8
Figure 1.6	The delay-based Parkinson’s disease model . . . . .	11
Figure 2.1	Theories for parkinsonian tremor pathophysiology . . . . .	17
Figure 2.2	Deep brain stimulation . . . . .	19
Figure 2.3	Functional electrical stimulation . . . . .	20
Figure 2.4	Subsets of mechanical tremor suppression . . . . .	23
Figure 2.5	Control strategies for active tremor suppression . . . . .	25
Figure 2.6	Previous ambulatory, active tremor suppression implementations . . . . .	28
Figure 2.7	Actuation of dielectric elastomer actuators . . . . .	29
Figure 2.8	Different configurations of dielectric elastomer actuators . . . . .	32

Figure 2.9	Existing DESAs from the literature	33
Figure 2.10	Spring-dashpot viscoelasticity models	35
Figure 2.11	Spring-dashpot viscoelasticity models	35
Figure 2.12	Voltage safety limit based on DESA capacitance	37
Figure 2.13	Internal models enable feedback and feedforward control	40
Figure 2.14	Optimal control theory captures human movement characteristics	42
Figure 2.15	Optimal control of reaching movements	42
Figure 2.16	Tradeoff between movement speed and endpoint variation	43
Figure 3.1	DESA model	48
Figure 3.2	Kinematic relationship between DESA and joint angle	52
Figure 3.3	FRF of open-loop system	59
Figure 3.4	Optimal stiffness for energy efficiency	61
Figure 3.5	Objective function for material selection	62
Figure 3.6	Recorded parkinsoninan tremor time series from online database	64
Figure 3.7	Recorded essential tremor time series from online database	65
Figure 3.8	Functional tasks used in simulations	66
Figure 3.9	Fully active control block diagram	68
Figure 3.10	Fully active control for the jar-opening task with ‘PD5’ tremor	74

Figure 3.11	Fully active control for the jar-opening task with ‘PD4’ tremor . . . . .	75
Figure 3.12	Fully active control for the jar-opening task for all parkinsonian tremor datasets	76
Figure 3.13	Fully active control for the jar-opening task for all essential tremor datasets . .	77
Figure 3.14	Fully active control for the carton-pouring task for parkinsonian tremor . . . . .	78
Figure 3.15	Fully active control for the carton-pouring task for essential tremor . . . . .	79
Figure 3.16	Comparing fully active and tremor-active control . . . . .	81
Figure 3.17	Block diagram for adaptive impedance control . . . . .	82
Figure 3.18	Tremor-active suppression for jar-opening task . . . . .	86
Figure 3.19	Tremor-active control for the jar-opening task for parkinsonian tremor . . . . .	87
Figure 3.20	Tremor-active control for the jar-opening task for essential tremor . . . . .	88
Figure 3.21	Tremor-active control for the carton-pouring task for parkinsonian tremor . . .	89
Figure 3.22	Tremor-active control for the carton-pouring task for essential tremor . . . . .	90
Figure 3.23	FRF for tremor-active controller . . . . .	93
Figure 3.24	Tracking error for tremor suppression simulations . . . . .	93
Figure 3.25	MDOF tremor suppression simulations . . . . .	94
Figure 4.1	Manufacturing DESAs by folding . . . . .	97
Figure 4.2	Experimental setup for scaled DESA-based tremor suppression . . . . .	99
Figure 4.3	Signal block diagram for scaled DESA-based tremor suppression . . . . .	100

Figure 4.4	Experimental time series for jar-opening task . . . . .	101
Figure 4.5	All PD experimental time series for jar-opening task . . . . .	102
Figure 4.6	All ET experimental time series for jar-opening task . . . . .	103
Figure 4.7	Experimental time series with sinusoidal voluntary motion . . . . .	105
Figure 4.8	Tracking error and voluntary motion resistance for PD . . . . .	106
Figure 4.9	Tracking error and voluntary motion resistance for ET . . . . .	107
Figure 4.10	Tradeoff between tremor suppression and voluntary motion resistance . . . . .	108
Figure 4.12	Viscoelastic parameter limits . . . . .	114
Figure 4.13	Effect of phase limits on viscoelastic parameter limits . . . . .	115
Figure 4.14	Effect of actuation ratio on voltage saturation for tremor-active control . . . . .	118
Figure 4.15	Effect of actuation rate ratio on current saturation for tremor-active control . . . . .	118
Figure 4.16	Tradeoff between voltage and current saturation . . . . .	119
Figure 4.17	Fully active actuation ratio effect on voltage saturation . . . . .	121
Figure 4.18	Fully active actuation rate ratio effect on current saturation . . . . .	121
Figure 4.19	Increased passive stiffness reduces fully active performance . . . . .	122
Figure 4.20	Literature DESA parameters . . . . .	123
Figure 4.21	Tremor-active simulation with UV-acrylic DESA . . . . .	125
Figure 5.1	Block diagram of delay-induced tremor . . . . .	128



Figure 5.2	Rest task simulation . . . . .	139
Figure 5.3	Reach-posture-reach-posture simulation . . . . .	139
Figure 5.4	Effect of delay on amplitude and frequency . . . . .	140
Figure 5.5	Rest tremor simulation for 3DOF wrist . . . . .	143
Figure 5.6	Comparison of simulated and recorded tremor . . . . .	144
Figure 5.7	Mechanical suppression of delay-induced tremor . . . . .	148

## LIST OF TABLES

Table 2.1	Comparison of different tremor treatments . . . . .	21
-----------	---	----

# **CHAPTER 1**

## **INTRODUCTION**

Certain nervous system disorders produce the involuntary, approximately rhythmic movement of body parts known as pathological tremor [1–3]. These involuntary motions can prevent individuals from accomplishing everyday tasks such as eating, writing, and grasping objects. Tremor also negatively impacts emotional health as the physical symptoms inhibit participation in society and cause social embarrassment [4,5]. Overall, tremor decreases quality of life by forcing dependence on others for daily living while simultaneously alienating the afflicted person from society. The prevalence of tremor further motivates the need for effective treatment options: tremor is the most common movement disorder, with approximately 7 million Americans afflicted by essential tremor alone [6,7]. Typical treatments are medications and surgery, both of which include inherent risks and provide varying effectiveness [1,8]. Therefore, recent research proposes mechanical suppression of tremor as an alternative treatment, whereby actuator torques counteract tremor-producing muscular torques to reduce tremor motion. This dissertation investigates mechanical tremor suppression using soft actuators to improve clinical implementation potential by increasing human body compatibility. Dielectric elastomers can easily conform to the human body since they have similar mechanical properties as human muscle, thereby reducing device profile and improving patient acceptance compared to rigid actuators. In addition, this research models parkinsonian

tremor using a control systems approach to investigate tremor generation and the central nervous system (CNS) response to tremor suppression. In particular, this study explores the evidence that pathological CNS delay causes feedback instability to produce tremor. Previous clinical evidence maps the delay to excessive basal ganglia inhibition of the thalamus, reflecting an unaccounted delay in signal transmission from the cerebellum (estimator) to primary motor cortex (controller).

### **1.1 Tremor as a Mechanical System**

Neural dysfunction produces tremor, but the primary negative result is involuntary movement of body parts: the mechanical motion is the variable of interest for tremor treatment. Therefore, one may view tremor as a purely mechanical system, where the CNS is a black box that specifies muscular torques that produce both voluntary and tremor motion. In theory, it is possible to eliminate tremor motion by applying mechanical torques that exactly cancel the motion. Only considering the mechanical domain of tremor removes the complex neurological and sensorimotor systems from the treatment design, greatly simplifying the fundamental problem structure. However, simplifying the fundamental problem complicates the applied problem: actually identifying the tremor motion and applying appropriate torques is a significant challenge. Understanding the dynamics and mechanical characteristics of tremor helps to achieve this difficult task.

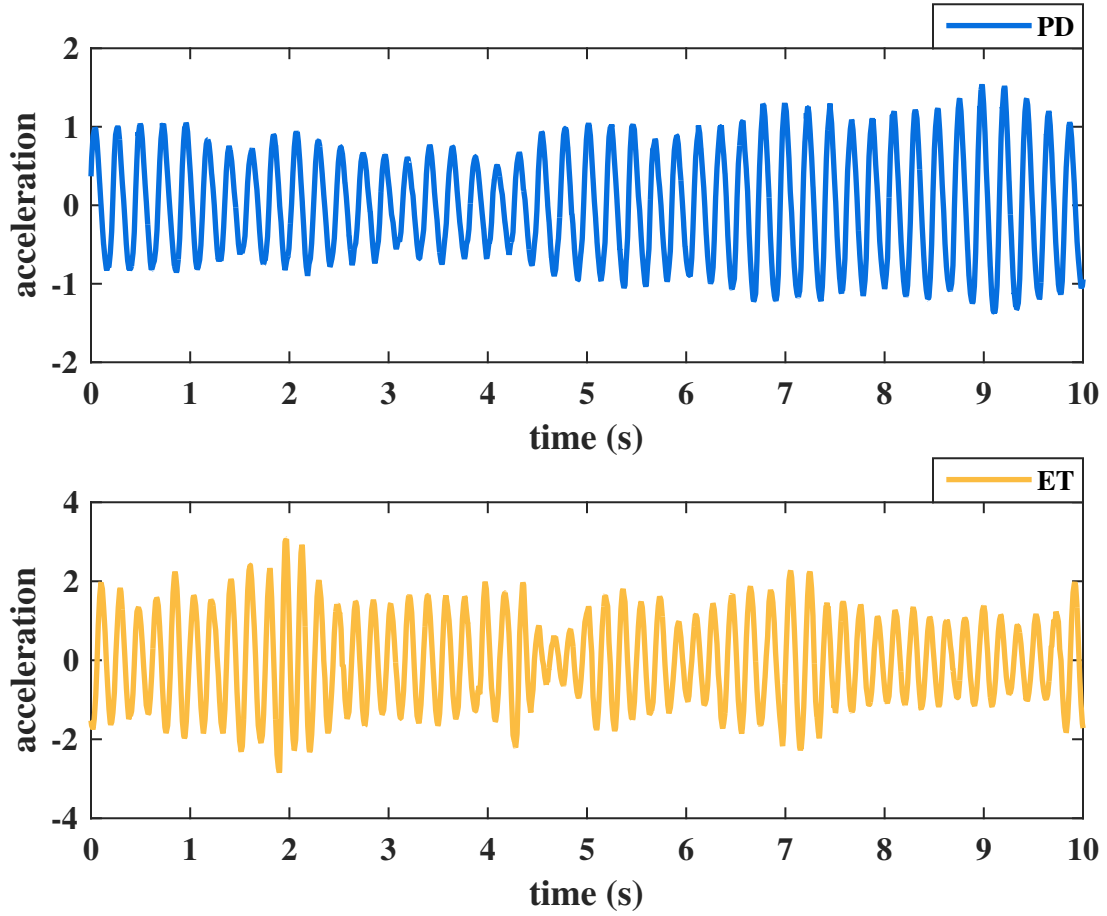


Figure 1.1: Recorded time series examples of parkinsonian tremor and essential tremor (data from [9])

### 1.1.1 Tremor Dynamics

Tremor data recordings provide insight into the dynamics of tremor. Previous research recorded the acceleration of the outstretched hand of several patients with Parkinson’s disease or essential tremor; this data is available online<sup>1</sup> [9]. Figure 1.1 illustrates the acceleration time series of one

---

<sup>1</sup>[http://jeti.uni-freiburg.de/path\\_tremor/](http://jeti.uni-freiburg.de/path_tremor/)

patient with essential tremor (ET) and one patient with parkinsonian tremor (PD). While both time series show approximately sinusoidal behavior, the signals clearly demonstrate amplitude and frequency variation. Figure 1.2 presents the Fast Fourier Transform (FFT) of the same tremor recordings: the dominant tremor frequency lies between 4 Hz and 6 Hz. Finally, Fig. 1.3 illustrates the amplitude and frequency variation over time. The amplitude variation is more pronounced than the frequency variation, a characteristic attributed to the variations being different types of noise [2]. In addition, previous research showed parkinsonian and essential tremor are better modeled by nonlinear stochastic second-order processes compared to deterministic chaotic processes [9]. The primary takeaway for tremor identification is that tremor has time-varying dominant frequency and time-varying amplitude.

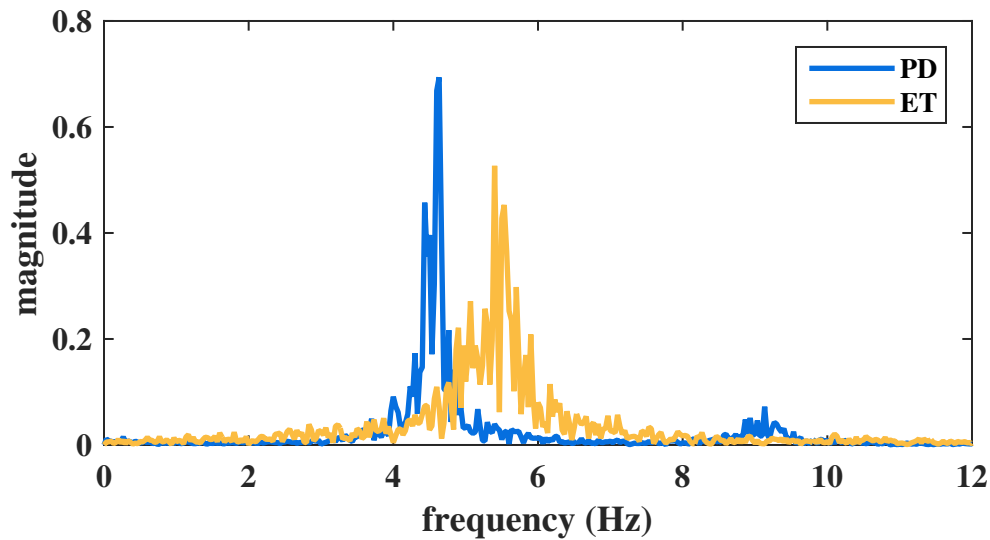


Figure 1.2: FFT of essential tremor and parkinsonian tremor data

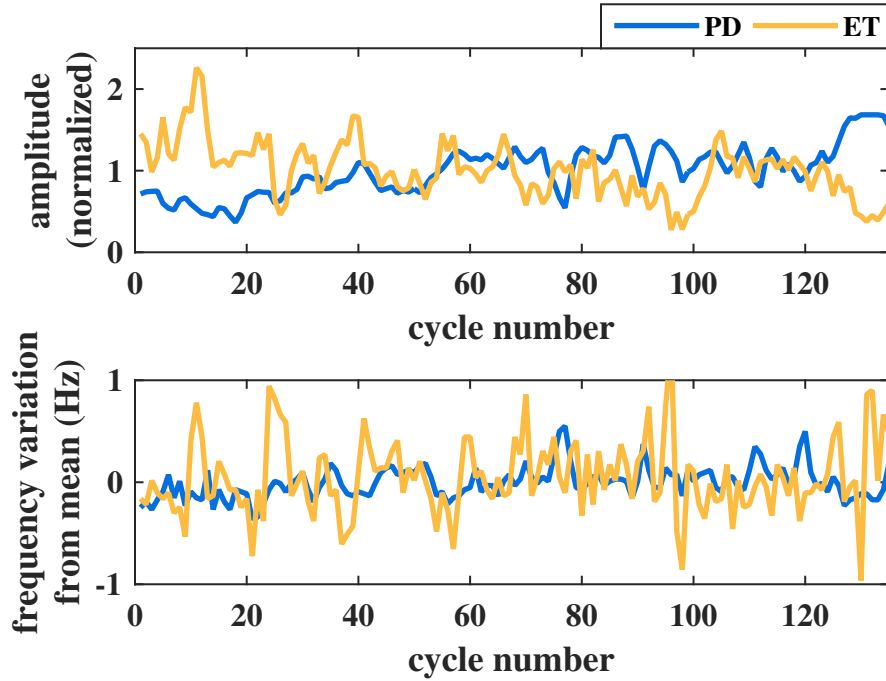


Figure 1.3: The amplitudes and dominant frequencies of pathological tremor change over time.

### 1.1.2 Mechanical Tremor Suppression

Mechanical methods of tremor suppression offer an interesting alternative to typical treatments [10–21]. A mechanical suppression system works at the joint level, producing a torque in the opposite direction of the tremor-producing muscle torque. A key advantage of mechanical methods is that the mechanism of tremor suppression is well understood: only considering mechanics reduces the complex human motor system to well-defined outputs. Application of the correct mechanical torques will reduce motion regardless of the source. However, identifying and applying the correct torques is no simple task. A mechanical suppression system must suppress tremor without significantly affecting any intended motion. Passive mechanical systems reduce all

motion regardless of whether the the motion was intentional or tremor [10, 11]. Therefore, recent research focuses on applying actuators to actively suppress tremor [14–21].

Figure 1.4 presents a block diagram of the general strategy for active tremor suppression. The suppression system acts in parallel to the human motor system control loop, providing a torque about a given joint to oppose the muscular torque that produces tremor. The CNS selects desired motions and plans muscular signals to produce those motions while considering sensory information. Thus, this voluntary component of the motion is some combination of feedforward and feedback control. When pathological tremor is present, the associated nervous system disorder also sends signals to the muscles that produce the tremor motion. The source of these tremor-causing signals depends on the disorder and remains an open research question in the medical community. Regardless of the pathophysiology, the tremor signals lead to muscular activation that produces undesired motion. The mechanical tremor suppression device must use a measurement to determine and apply the appropriate torque to reduce tremor with minimal influence on the desired motion. Thus, the controller must filter the signal to distinguish between tremor and voluntary components. Fortunately, tremor frequency content (greater than 3 Hz) differs from typical voluntary motion frequency content (0–2 Hz) [18, 22]. Filtering techniques may separate tremor and voluntary signals from the measurement. However, the close proximity of the frequency ranges prohibits the use of linear filters for real-time applications. The need of an accurate, real-time, and zero-phase tremor estimate is one significant challenge in active tremor suppression.



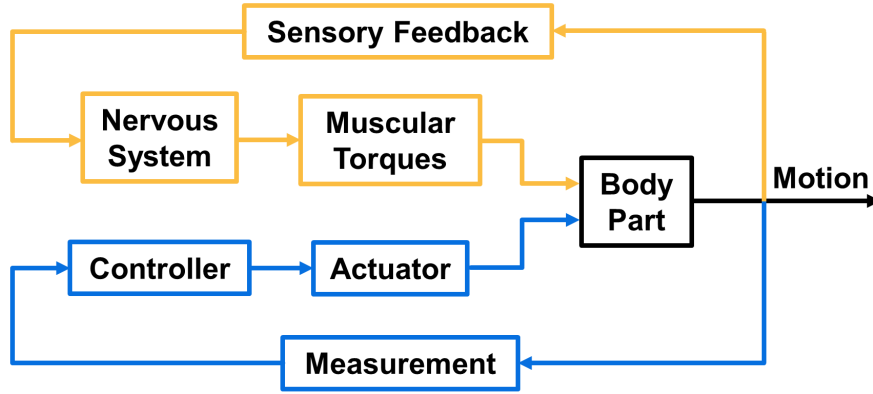


Figure 1.4: Active mechanical tremor suppression methods (blue) apply control in parallel to the human motor control loop (yellow).

Most previous mechanical tremor suppression implementations use DC motors to actuate against the tremor [16–21, 23]. Other implementations use magnetorheological (MR) dampers, pneumatic cylinders, or permanent magnet linear motors [11–15, 24]. All of these exoskeleton systems are rigid and bulky, limiting their use to laboratory settings. This fact highlights another major challenge for active tremor suppression: the lack of human body compatibility of traditional engineering actuators prevents clinical applications.

## 1.2 Artificial Muscles for Tremor Suppression

This dissertation proposes dielectric elastomers as the actuators for mechanical tremor suppression. Researcher often label dielectric elastomers as *artificial muscles* due to their many similarities with human muscles [25, 26]. Compared to human muscle, dielectric elastomers have similar stiffness and actuation speed while having greater maximum strain, pressure, and energy density [25]. Di-

electric elastomers even have the potential for self-sensing, drawing similarities to proprioceptive feedback in human muscle [26–29]. Furthermore, dielectric elastomer actuators are electrically activated and can be designed to operate as contractile actuators like human muscle.

The similarities of dielectric elastomers and natural muscle enable the design of a tremor suppression system that mimics human mechanics. The artificial muscles serve as external analogs to the internal muscles that produce motion about a joint. Figure 1.5 demonstrates a schematic example of such a system to reduce tremor in elbow flexion-extension. The biceps and triceps form a well known agonist-antagonist pair: activation of the biceps flexes the forearm about the joint while activation of the triceps extends the forearm about the joint. To produce motion, the active muscle group must overcome the passive impedance of the antagonist muscle group. Since dielectric elastomers have similar passive properties as natural muscle, they may also use an agonist-antagonist approach. This approach enables bi-directional actuation with contractile dielectric elastomer actuators without requiring an offset voltage.

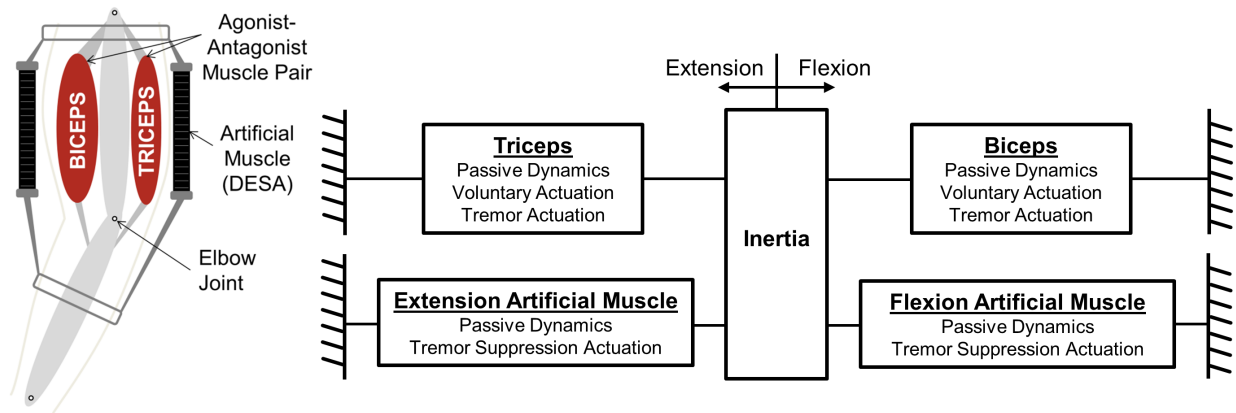


Figure 1.5: Dielectric elastomer actuators may act as agonist-antagonist pairs similar to human muscle: external artificial muscles counteract the tremor-producing torques from the underlying natural muscles.

Dielectric elastomers have relatively low actuation levels compared to typical engineering actuators. This drawback may limit applicability towards tremor suppression applications. Therefore, this dissertation develops a unique control approach tailored to dielectric elastomer-based tremor suppression. The approach reduces actuation requirements by shifting the burden of the passive actuator dynamics to the human motor system, which can overcome the increased passive influence since it is predictable and on the same order as (or potentially lower than) the passive impedance of muscle. In other words, the approach overcomes low actuation capabilities by exploiting the low mechanical impedance of dielectric elastomers. Thus, the system improves the potential for low-profile tremor suppression implementations at the cost of increased user effort.

### **1.3 CNS Response to Tremor Suppression**

The physiological response to tremor suppression depends on how the CNS produces tremor. In other words, will pathological CNS activity decrease, increase, or remain the same in the presence of mechanical tremor suppression? This research considers two general hypotheses for the CNS response to tremor suppression:

1. *State-independent neural oscillations produce tremor*: This hypothesis suggests CNS dysfunction produces neural signals that do not change due to external forces. Thus, tremor torque remains the same irrespective of tremor suppression.

2. *Motor control dysfunction produces tremor*: This hypothesis implies tremor depends on the joint state. Thus, tremor suppression alters neural signals that may change tremor characteristics.

If tremor is state-independent, muscles activate the same amount regardless of external forces. A tremor suppression device must continuously oppose the tremor torque, but it is possible to produce an equal and opposite torque to reduce tremor. In this case, the muscles still have tremorous actuation, but the joints do not include tremorous displacements. Most tremor suppression analyses in this dissertation assume this form for tremor since it is a relatively conservative approach and enables incorporation of real tremor data in simulations.

State-dependent tremor could increase, decrease, or have negligible effect on tremor torque amplitude. If tremor is a CNS-targeted movement, muscular activation may increase to overcome mechanical tremor suppression. However, this possibility is unlikely since previous implementations demonstrate effective mechanical tremor suppression [16]. Feedback instability is another potential state-dependent mechanism for tremor generation. This dissertation explores increased CNS delay as the instability that produces tremor and evaluates its effect on tremor suppression.

### **1.3.1 Parkinsonian Tremor as an Increased CNS Delay**

Apart from tremor, Parkinson's disease is associated with general movement inhibition, including slowness of movement and increased reaction times [30]. Due to this fact, previous researchers suggest tremor arises from increased feedback delays [31–33]. This dissertation investigates clini-

cal research to develop a delay-based model for parkinsonian tremor: the model includes increased CNS delay due to excessive inhibition projected from the basal ganglia to the thalamus. Figure 1.6 illustrates the block diagram for this model.

The tremor model adds the Parkinson’s disease pathology to a model for healthy motor control. In particular, optimal control theory produces an excellent approximation of human motion, producing task-specific and minimum-energy movements [34–39]. Even healthy motor control includes feedback delays since neural signals must travel between limbs and the CNS. Forward models in the CNS compensate for feedback delays to produce stable feedback control. Present-state predictions produced from delayed measurements compensate for healthy feedback delays [40,41]. Increased CNS delay in Parkinson’s disease represents an uncompensated delay in the feedback loop. This unaccounted delay produces instability leading to tremor. This model enables investigation of tremor suppression on state-dependent tremor and also provides new interpretations of physiologically based tremor models and treatment effectiveness.

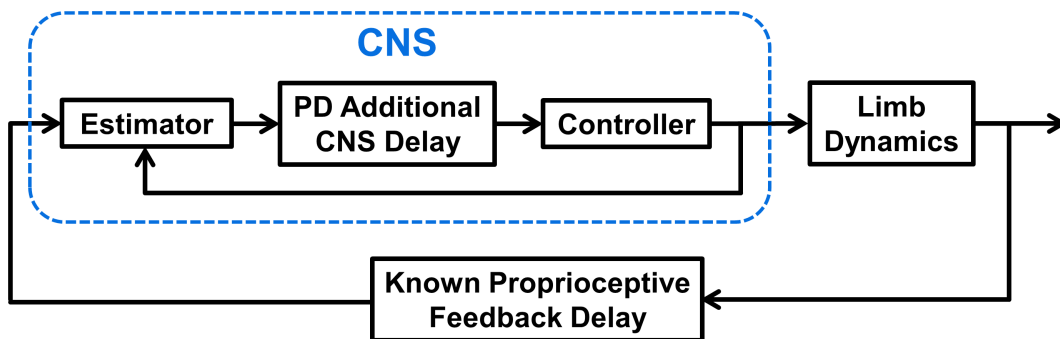


Figure 1.6: The delay-based Parkinson’s disease model proposes that increased CNS delays produce tremor.

## 1.4 Dissertation Structure

This dissertation works towards improved treatment and fundamental understanding of pathological tremor by approaching tremor from a mechanical systems perspective. This work includes two general topics: dielectric elastomer-based tremor suppression (Chapters 3 and 4) and parkinsonian tremor model development (Chapter 5).

Chapter 2 provides relevant background information related to pathological tremor, mechanical tremor suppression, dielectric elastomers, and human motor control modeling. It includes discussion of tremor treatments and prevailing theories of tremor pathophysiology. Mechanical tremor suppression background details typical control strategies and actuator implementations. Dielectric elastomer background characterizes actuator capabilities and limitations. Finally, the chapter discusses control systems approaches to modeling the human motor system to facilitate the development of a parkinsonian tremor model.

Chapter 3 develops a low-order model to simulate dielectric-elastomer based tremor suppression. It develops controllers for two different control approaches and demonstrates tremor suppression performance for each approach.

Chapter 4 evaluates the current outlook for dielectric elastomer-based tremor suppression. It provides experimental validation of tremor suppression simulations with a scaled benchtop system. It then quantifies the required actuator characteristics to enable clinical implementations of dielectric elastomer-based tremor suppression.

Chapter 5 develops a low-order model for parkinsonian tremor. It models healthy motor control using an optimal control approach and models Parkinson's disease pathology as an increased CNS delay. The model produces simulated tremor with similar characteristics as recorded tremor. In addition, the chapter discusses the implications of delay-based tremor on treatment effectiveness, existing tremor models, and mechanical tremor suppression.

Finally, Chapter 6 discusses the conclusions of this research, highlighting the novelty of the proposed tremor suppression system and its potential long-term impact. It also discusses the significance of the proposed parkinsonian tremor model, with improved disease pathophysiology knowledge providing pathways toward improved treatments and cure development. The chapter motivates future research directions to work towards realizing the high-impact potential of the early-stage research in this dissertation.

## **CHAPTER 2**

### **BACKGROUND**

This chapter describes relevant background and previous research related to pathological tremor, mechanical tremor suppression, dielectric elastomer actuators, and human motor control. Section 2.1 provides fundamental background and typical treatments for pathological tremor, along with theories on the pathophysiology of the two most common forms of tremor: essential tremor and Parkinson’s disease. Section 2.2 describes mechanical tremor suppression considerations and previous implementations. Section 2.3 describes relevant background for dielectric elastomer actuators and motivates their application to tremor suppression. Finally, Section 2.4 presents fundamentals and low-order modeling of human motor control.

#### **2.1 Pathological Tremor**

Tremor is an involuntary, approximately rhythmic movement of body parts. Physiological tremor occurs in all healthy people due to random firing of motoneurons [9]. This tremor type is only relevant for very precise tasks, such as high-precision surgery [42, 43]. In contrast, pathological tremor manifests from a CNS disorder and can affect day-to-day living significantly [2–4, 44]. This



section provides an overview of pathological tremor and typical treatments for reducing tremor to improve quality of life.

### **2.1.1 Subsets of Pathological Tremor**

Classifications of pathological tremor depend on the associated disease and the qualitative properties it exhibits. Tremor types based on etiology include essential tremor, parkinsonian tremor, cerebellar tremor, and Holmes' tremor [44]. Each of these classes has defining characteristics in terms of frequency content and the qualitative tremor subtypes they typically exhibit. Still, it is often difficult to distinguish between different tremor types; diagnosis methods are an active area of research [33, 45, 46]. The qualitative subtypes of tremor include rest tremor and action tremor; action tremor is further categorized into postural tremor and kinetic tremor. [44]. Rest tremor occurs when the muscles are not attempting to move or maintain any posture and is most common in Parkinson's disease. Postural tremor occurs when the muscles are attempting to maintain a position against gravity. Kinetic tremor occurs during a directed movement. One common type of kinetic tremor is intention tremor, where the tremor amplitude increases as the limb approaches the target.

Essential tremor and Parkinson's disease are the most common tremor-producing disorders. Therefore, previous research focuses on these tremor types for analysis of tremor [2, 9]. Rest tremor is a defining characteristic for Parkinson's disease, but postural and kinetic tremor may also be present [44, 47]. Postural and kinetic tremors are prominent for essential tremor, but again, rest tremors may occur [44, 47]. The reported frequency content of these tremors varies slightly, but

parkinsonian tremor typically ranges from approximately 3–6 Hz, while essential tremor ranges from 4–12 Hz [47].

### **2.1.2 Pathophysiology of Tremor**

The primary pathology in Parkinson’s disease is loss of dopaminergic cells in the basal ganglia [48]. How basal ganglia dopamine depletion translates to bradykinesia, rigidity, and tremor remains unclear. In addition, the varying effectiveness of dopaminergic medications implies the presence of other pathological mechanisms. Indeed, serotonergic pathology may affect tremor type and treatment effectiveness: recent research suggests dopaminergic and serotonergic pathology cause re-emergent and pure postural tremors, respectively [49]. Several theories exist for tremor generation, typically centered on propagation of oscillatory activity through neural circuits [50]. Pacemaker models hypothesize that abnormal oscillatory activity in the thalamus or basal ganglia drives abnormal activity in the remaining neural circuitry. Since hyperpolarization of thalamic cells produces oscillation at 6 Hz (approximately tremor frequency), the thalamic pacemaker hypothesis suggests thalamic nuclei hyperpolarization drives tremor. However, this model does not explain why basal ganglia deep brain stimulation (DBS) reduces tremor (see following subsection for more information on DBS). In contrast, the basal ganglia pacemaker hypothesis suggests pathological oscillations originate in the basal ganglia. This hypothesis links basal ganglia dopamine depletion to tremor generation, but does not explain tremor suppression for thalamic DBS. The dimmer-switch hypothesis combines supporting evidence for each of these models: the basal gan-

glia initiates tremor activity while the cerebello-thalamo-cortical (CTC) circuit drives tremor [51]. The finger-switch-dimmer model extends this theory by further breaking down the roles of CTC circuit elements: the thalamus creates tremor oscillations while the cerebellum treats these tremor oscillations as a voluntary movement [52]. Figure 2.1 illustrates these theories for parkinsonian tremor pathophysiology.

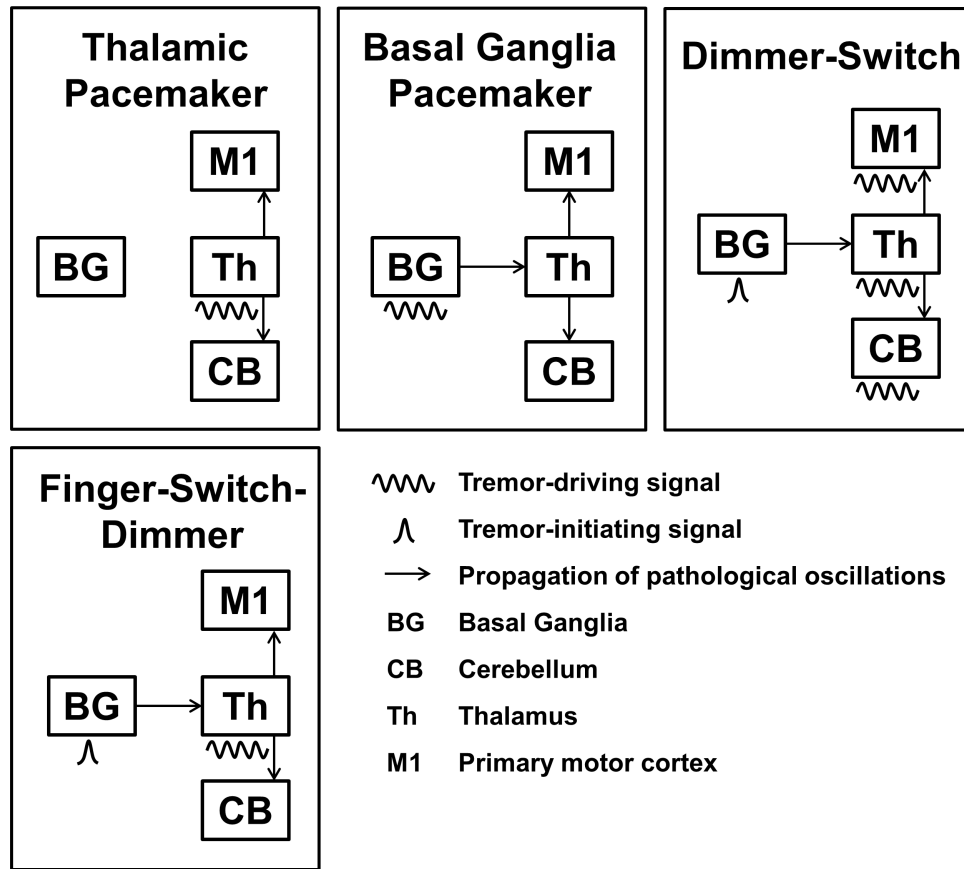


Figure 2.1: Theories for parkinsonian tremor pathophysiology attempt to explain the neural mechanisms that cause tremor.

Essential tremor exhibits diverse characteristics due to the potential for misdiagnosis and existence of different subtypes [50]. Theories for essential tremor pathophysiology include the neurodegeneration hypothesis, the GABA hypothesis, and the oscillating network hypothesis [50].

The neurodegeneration hypothesis argues essential tremor is a neurodegenerative disease and is supported by postmortem evidence of cerebellar and brain stem disease. The GABA hypothesis suggests dysfunction of the neurotransmitter GABA causes essential tremor, with evidence again pointing towards reduced cerebellar GABA activity. Finally, the oscillating network hypothesis suggests oscillators in the CTC circuit entrain each other to produce tremor.

### **2.1.3 Tremor Treatments**

Typical treatments for reducing tremor vary based on the tremor type, but include two main categories: medications and surgery. The most common medications for essential tremor are primidone and propranolol, both of which provide an average tremor reduction of about 50% [8]. The effectiveness of these drugs varies from person-to-person, with about half of patients having no long-term benefit [8]. Furthermore, these drugs have side effects that can cause patients to stop taking their doses and drug long-term effects are unknown [8]. Levodopa and dopamine agonists are typical pharmaceutical treatments for Parkinson's disease and can cause side effects that include motor complications, impulsive and compulsive behaviors, nausea, and hallucinations [53]. Altogether, pharmaceutical treatments are moderately successful in reducing tremor, but side effects and irregular efficacy motivate the need for alternative options.

Surgical intervention is a more extreme option for tremor treatment, but can offer substantial benefits. The two common surgical interventions for tremor are thalamotomy (lesion to thalamus) and deep brain stimulation, with DBS being the preferred option since it has fewer complica-

tions [8]. In DBS surgery, the surgeon implants an electrode into the brain that is connected with a wire to a stimulator implanted under the skin in the chest. The electrode is positioned to stimulate a targeted area of the brain, typically the ventrolateral thalamus, subthalamic nucleus, or the internal globus pallidus [54,55]. Figure 2.2 illustrates the positioning of the hardware and the surgical procedure for DBS. The stimulation produces excellent reduction of tremor, typically providing about 90% reduction [8]. However, DBS also has associated side effects that can cause patients to turn off their stimulators [8]. More importantly, DBS includes the risk of serious surgical complications, with rates of perioperative death as high as 4% [8,56]. Other negative factors for DBS include significant risk of hardware complications and hardware-related infection (about 25% of patients), the need for battery replacement (which is also associated with an increased risk of infection), and a loss of benefit over time and the need to reprogram the device [8,57,58].

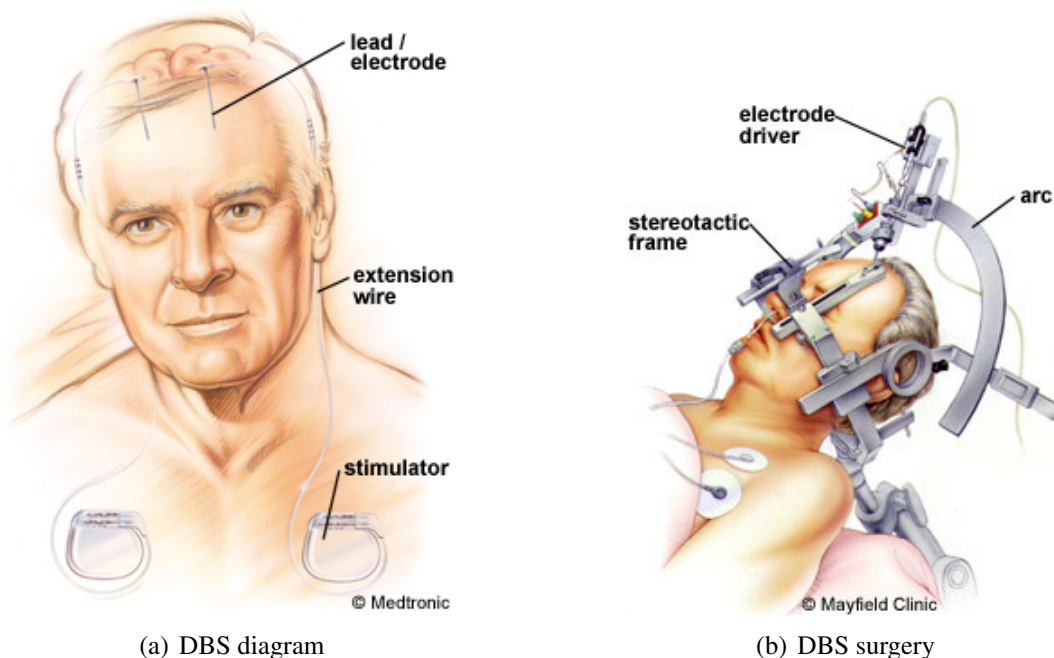


Figure 2.2: In DBS surgery, the surgeon implants an electrode in the brain that emits a tunable pulse to a targeted area (from [59]).

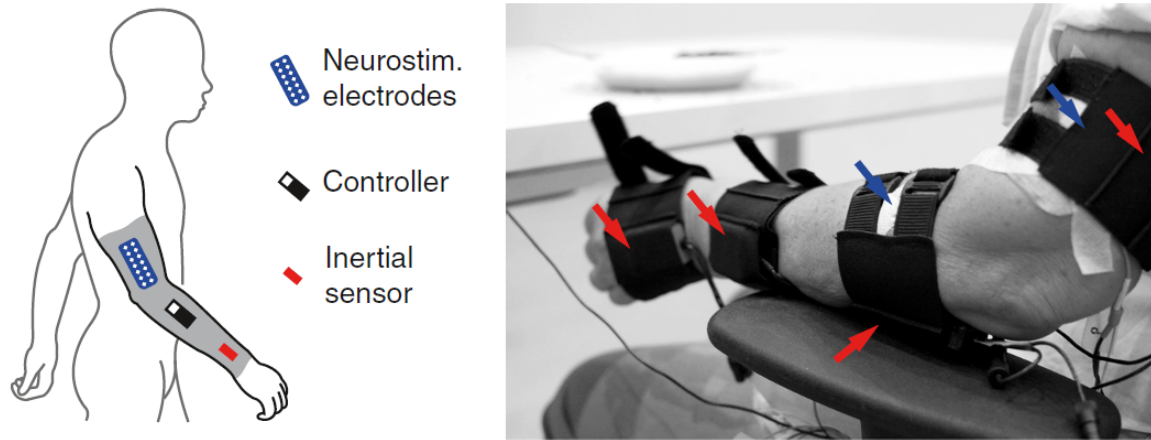


Figure 2.3: In FES, externally-placed electrodes stimulate the muscles to augment the dynamics in a way that reduces tremor (from [60]).

Recent research seeks to develop alternative tremor treatments due to the inherent drawbacks of pharmaceutical and surgical treatments. One alternative attempts to use the benefits of electrical stimulation while eliminating the risks associated with surgery. This approach, termed functional electrical stimulation (FES), applies electrical stimulation from outside the body to stimulate the underlying muscles in a way that reduces tremor [60,61]. This stimulation either activates muscles out-of-phase with tremor or activates antagonist pairs to produce co-contraction that augments the mechanics of the limb [60, 61]. Figure 2.3 illustrates an implementation of FES, which achieved tremor reduction up to 50% [60]. The only side effect of FES is the potential for muscle fatigue since the stimulation activates the muscles. However, stimulation below the motor threshold also shows promise for tremor reduction [62,63].

Finally, mechanical tremor suppression is an active field of research due to the potential for excellent tremor reduction with limited risks and side effects. A significant advantage of mechanical tremor suppression is that the mechanisms involved are well understood and quantifiable. Since the

disorders that cause tremor are not well understood, the development of drugs and the implementation of electrical stimulation involves guesswork and intuition. Furthermore, these treatments operate on the extremely complex human nervous system. The theory of FES is slightly more understood since it involves augmenting the mechanics of muscles, but the electrical interaction with the muscles is still difficult to quantify. Mechanical tremor suppression has the potential to eliminate tremor motion regardless of the source. Indeed, the potential effectiveness of mechanical tremor suppression is only matched by its difficulty in developing a feasible implementation. Such a device must mechanically suppress tremor without affecting the mechanics of voluntary motion, all while being comfortable and compact. Table 2.1 presents qualitative assessments of each of the presented treatment options.

Table 2.1: Comparison of different tremor treatments

<b>Treatment</b>	<b>Level of Understanding</b>	<b>Implementation Difficulty</b>	<b>Effectiveness</b>	<b>Robustness</b>	<b>Risk</b>
<i>Medication</i>	Low	Low	Medium	Low	Low
<i>DBS</i>	Low	Medium	High	Medium	Medium
<i>FES</i>	Medium	Medium	Medium	Medium	Low
<i>Mechanical</i>	High	High	High*	High*	Low*

\* Theoretical predictions

## 2.2 Mechanical Suppression of Tremor

Mechanical tremor suppression methods vary in approach and implementation. The approach (ambulatory, non-ambulatory, active, passive) has a significant impact on the potential benefits and

implementation difficulty. Even the same general approach (say, an ambulatory, active system) can have different strategies (impedance control, voluntary-motion tracking, tremor torque cancellation) that affect the overall performance. The implementation refers to the execution of the tremor reduction approach. The method of implementation has a significant influence on the effectiveness of the approach and the feasibility of reaching clinical applications. This section describes general approaches for mechanical tremor suppression, discusses the motivation for targeting ambulatory, active tremor suppression, and explains why current implementations are not suitable for clinical use.

### **2.2.1 Subsets of Mechanical Treatments**

Mechanical tremor treatments may be organized into several categories. Figure 2.4 illustrates the hierarchy of these classes. First, mechanical tremor suppression is either ambulatory or non-ambulatory [18]. Ambulatory devices are only mechanically connected to the user and produce moments about a joint to reduce tremor. In contrast, non-ambulatory devices are mounted to another object, such as a wheelchair. Examples of non-ambulatory tremor suppression devices include the wheelchair joystick and the Liftware spoon [64, 65]. These non-ambulatory devices are easier to implement and have already had commercial success. However, non-ambulatory devices are inherently limited to task-specific applications. Ambulatory devices have the potential to suppress tremor regardless of the task, marking a significant advantage over non-ambulatory devices.



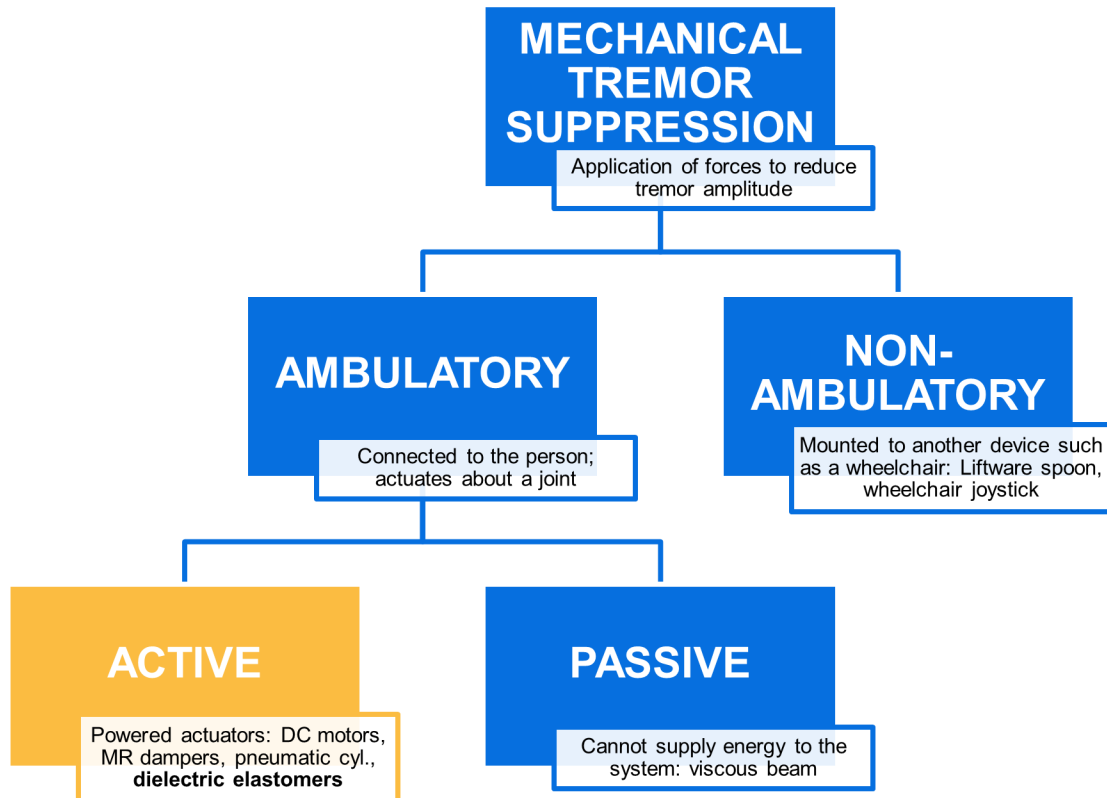


Figure 2.4: Mechanical tremor suppression contains several subsets, with active ambulatory suppression having the most potential benefits.

Similar to other vibration reduction designs, tremor suppression is also divided into active and passive subsets. Passive designs are non-powered and cannot supply energy to the system. Therefore, there is no risk of instability or the device causing harm to the user. However, passive systems suppress both tremor and voluntary motion. An example of a passive tremor suppression device is the viscous beam orthosis [10]. In contrast, active tremor suppression uses powered actuators to apply forces that oppose tremor. Active devices do add energy to the system; thus, they should be designed carefully to minimize risk of injury. The primary advantage of using active control is the ability to distinguish between tremor and voluntary motion to minimize the

effect on the desired motion. Overall, ambulatory, active devices offer the most potential benefits for treatment of pathological tremor. Thus, active tremor suppression has received a lot of attention in the literature and is also the focus of this research [14–21].

### **2.2.2 Control Strategies**

Previous designs for active tremor suppression include three general control strategies: impedance control, tremor torque cancellation, and voluntary motion tracking. Figure 2.5 presents the block diagrams for these three methods. In impedance control, the controller augments the effective inertia, damping, or stiffness of the system [16]. First, the controller filters the measurement to obtain an estimate of the tremor signal to add impedance only in the tremor frequency range. In the torque cancellation approach, the controller uses the measurement to generate an estimate of the tremor torque [14, 15]. Then the controller uses the dynamics of the actuator to determine the actuator input that produces the tremor torque. This method is often implemented with a notch filter centered about the dominant tremor frequency [15, 16, 18]. Finally, the voluntary motion tracking method employs a filter to estimate the desired motion of the joint [19, 20]. The controller then attempts to track this voluntary motion estimate while rejecting noise (in this case, the tremor). Thus, this method strongly depends on obtaining a good estimate of the voluntary motion; a poor estimate will lead to tracking an undesired trajectory.

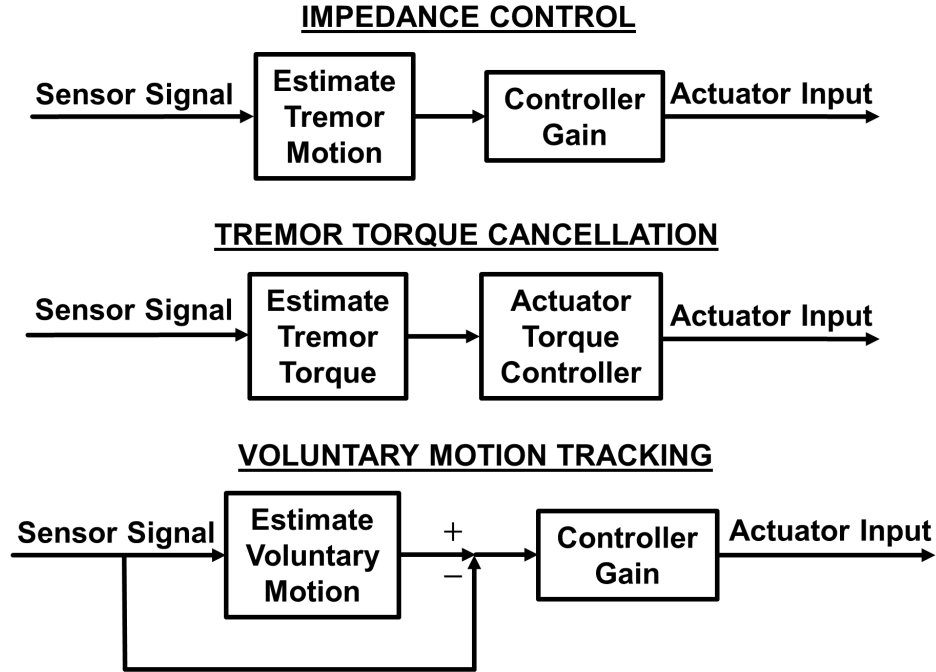


Figure 2.5: Control strategies for active tremor suppression include impedance control, tremor torque cancellation, and voluntary motion tracking.

Regardless of the control strategy, there is a need to filter the measurement to obtain an estimate of the tremor signal (or, conversely, the voluntary motion signal). This filter is what allows the system to reduce tremor while avoiding influence on voluntary motion. There are two approaches to estimating tremor: estimate the voluntary motion and subtract it from the measurement or directly estimate tremor. The close proximity of voluntary and tremor frequency ranges prohibits the use of traditional linear filters for real-time applications. Previous works use *gh*-filters and Kalman filters to estimate the voluntary motion [16, 18–20]. These filters produce a small phase lag that can reduce tremor suppression performance, so there is a trade-off between tracking error and phase lag.

Previous works use filters based on Fourier Linear Combiner (FLC) methods for direct estimation of the tremor signal. These filters have zero phase and approximate the signal as a summation of sinusoids. The two general algorithms used for real-time tremor identification are the Weighted Fourier Linear Combiner (WFLC) and the Band-Limited Multiple Fourier Linear Combiner (BMFLC). WFLC approximates the signal as sinusoid and a finite number of its harmonics [42, 43]. Recursive least squares updates the fundamental frequency and amplitudes to track the signal. However, WFLC requires pre-filtering to only include the tremor signal, defeating the purpose of using a zero-phase filter. However, this algorithm successfully tracks the tremor frequency and amplitude after pre-filtering, so it may estimate this information (with a slight delay) for use in other parts of the controller (like an adaptive notch filter) [15].

In contrast to WFLC, the BMFLC algorithm does not allow the frequency to adapt. This property prevents the estimate from converging to the low-frequency voluntary signal. BMFLC approximates the signal as a summation of many sinusoids with equally spaced frequencies between a lower- and upper-frequency limit [66]. The recursive least squares only updates the amplitudes of the sinusoids. This filter works in real-time without the need for pre-filtering. Previous works use BMFLC for tremor estimation for suppression of physiological tremor in surgical instruments [66, 67]. However, the frequency range of physiological tremor (8–12 Hz) is much higher than pathological tremor (as low as 3 Hz). For pathological tremor estimation, there may be spillover of the voluntary component via the adaptive amplitudes.

### 2.2.3 Actuator Selection

Active tremor suppression requires actuators to apply torques about joints to oppose tremor. The actuator must apply forces large enough to suppress tremor, operate in the tremor frequency range, and attach to the human body. Other desirable characteristics include being small, lightweight, and comfortable for the user; however, these characteristics are lacking in previous designs. Currently, the use of bulky and rigid actuators limits the application of active tremor suppression to laboratory settings. Most researchers use DC motors for tremor suppression since they are a well-established technology that provides easier, more reliable implementation [16–21, 68]. In fact, DC motors are the only actuators that have been tested on actual patients (other devices have performed benchtop tests) [16, 17, 68]. Other researchers have proposed MR dampers, pneumatic cylinders, and permanent magnet linear motors for tremor suppression, which still produce bulky systems [11–15, 24]. Figure 2.6 provides examples of tremor suppression exoskeletons that use DC motors, along with one design for MR dampers that also forms the basis for implementations with pneumatic cylinders and permanent magnet linear motors. Altogether, the actuators in mechanical tremor suppression devices need to become smaller and more compatible with the human body before mechanical tremor suppression becomes a viable clinical option for treatment. Recently, Zhou et al. developed a DC motor-based glove that achieves a relatively small form factor by using cable-actuated power transmission [23]. This approach may improve clinical implementation potential. This dissertation explores tremor suppression with soft actuators as another potential pathway towards clinical implementations.

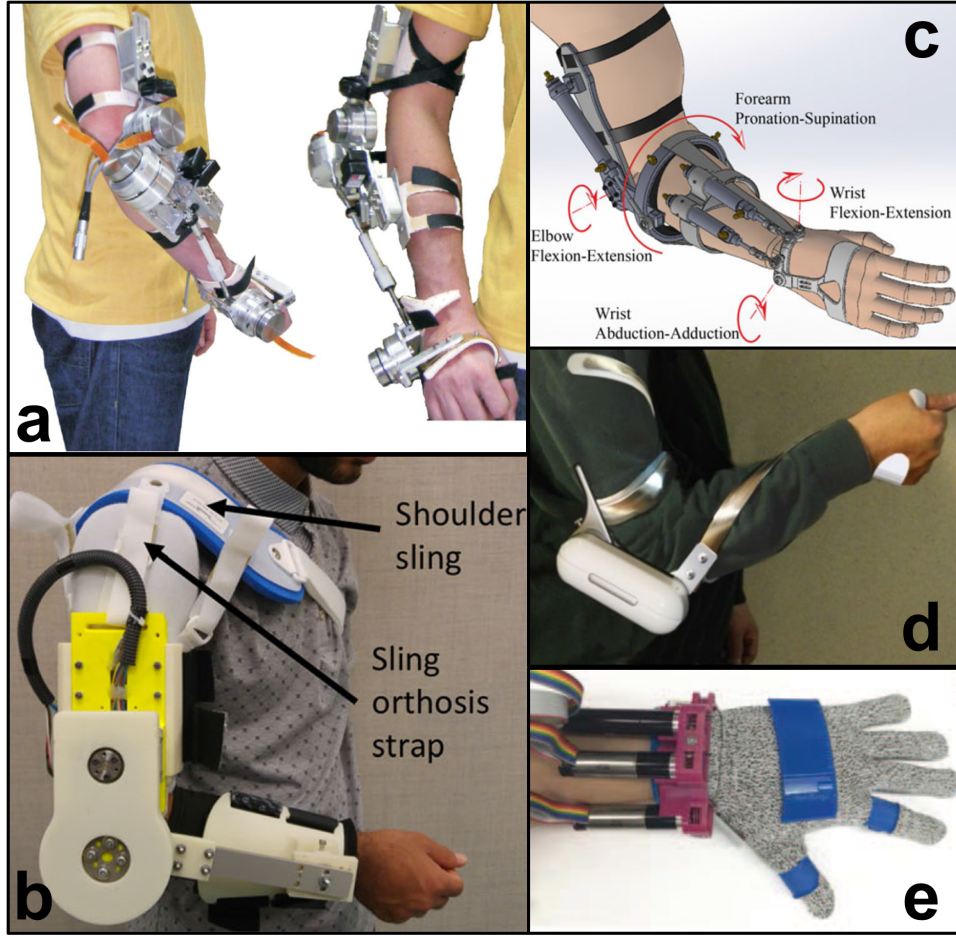


Figure 2.6: Previous ambulatory, active tremor suppression implementations produce bulky exoskeletons that prevent clinical applications: (a) from [16], (b) from [68], (c) from [13], (d) from [69], and (e) from [23].

### 2.3 Dielectric Elastomers

Dielectric elastomers belong to a class of soft actuators known as electroactive polymers (EAPs), which contains two sub-classes: electronic and ionic. Electronic EAPs exhibit electrical actuation via electrostrictive, electrostatic, piezoelectric, or ferroelectric forcing, while ionic EAPs actuate

via mobility or diffusion of ions [70]. Advantages of EAPs include their ability to achieve large strains and their similar mechanical properties as biological muscle. Thus, EAPs are an attractive option for interaction with the human body. This research targets dielectric elastomers for tremor suppression since they best address the critical needs of the system: fast response with the ability to produce relatively large forces.

Dielectric elastomers are a relatively new actuation technology: Pelrine, Kornbluh, and Joseph [71] first proposed dielectric elastomers as actuators in 1998. From a material perspective, dielectric elastomers are relatively soft (typical Young's Modulus between 0.01 MPa and 10 MPa), insulating (typical relative permittivity between 2 and 10), and nearly incompressible [25]. Applying conductive material (electrodes) to opposing surfaces of a dielectric elastomer creates a dielectric elastomer actuator (DEA), which is essentially a deformable capacitor. The electrode material must be very thin and compliant since the electrodes deform with the elastomer; researchers typically use carbon powder or grease [25, 71–74]. Applying a voltage across the electrodes produces electrostatic forcing as opposite charges attract and like charges repel [71, 72]. This electrostatic forcing tends to draw the electrodes closer together; since elastomers are nearly incompressible, the DEA also expands in-plane. Figure 2.7 illustrates this actuation process.

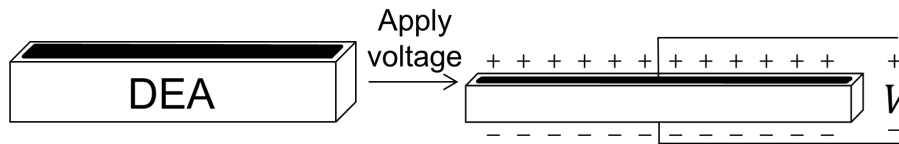


Figure 2.7: Electrostatic forces produce in-plane expansion and through-thickness contraction in dielectric elastomer actuators.

### **2.3.1 Characteristics of DEAs**

When proposing the DEA concept, Pelrine, Kornbluh, and Joseph showed the effective stress from the electrostatic forcing is proportional to the square of the electric field across the electrodes [71]. Since the electric field is equal to the voltage divided by DEA thickness, DEAs require very high voltages (typically greater than 1 kV) and very low thicknesses (typically 10–100  $\mu\text{m}$ ) to produce usable actuation [25]. These requirements are two of the greatest challenges in DEA applications. Fortunately, clever actuator design enables DEAs to meet force and displacement requirements in a variety of applications. Also, despite the need for high voltages, DEAs typically operate at relatively low currents, enabling implementation of relatively small power electronics. The capacitive nature of DEAs means they can remain in their actuated state without constant current flow and their electromechanical coupling can enable self-sensing transducers. Finally, DEA material selection and control design must consider the effect of viscoelastic properties on the system dynamics.

#### **2.3.1.1 Topology**

Dielectric elastomer actuators may exploit either the in-plane expansion or through-thickness contraction for actuation. Different geometries and designs produce significantly different characteristics and actuator capabilities. One important consideration for any design is the need to apply high electric fields to produce usable actuation. This requires the use of very thin elastomer films for



reasonable voltage levels. Thin DEAs are often prestretched and secured to rigid frames to further decrease the thickness of the actuator and improve the dielectric breakdown strength of the material [26]. Since DEA layers are necessarily very thin, single-layer actuators must utilize in-plane extension to achieve appreciable displacement. These types of DEAs typically require mechanical connections to stiff frames to transmit forces. Figure 2.8 demonstrates different DEA configurations that exploit planar actuation. First, Fig. 2.8(a) shows a planar DEA that exemplifies the large strains that are achievable with dielectric elastomers [75]. The diamond actuator in Fig. 2.8(b) pre-stretches the dielectric elastomer film in a diamond frame to improve the work output of planar actuation [76]. Spring roll actuators, illustrated in Fig. 2.8(c), wrap a thin dielectric membrane around a spring to produce linear extension upon actuation [77]. Including separate membrane sections enables multiple degree-of-freedom actuation with spring roll actuators, as demonstrated in Fig. 2.8(d) [78]. Frameless planar actuation suits low-actuation applications such as inflatable structures (Fig. 2.8(e)) and minimum energy grippers (Fig. 2.8(f)) [79,80]. Figure 2.8(g) illustrates a multilayer planar actuator to replicate human jaw movements [81]. Finally, Fig. 2.8(h) illustrates a cone membrane that exploits bistability to increase actuation stroke [82].

A single DEA film cannot produce forces great enough for tremor suppression. However, stacking many thin layers of dielectric elastomers results in a much larger actuator capable of macroscale actuation [73]. The literature often refers to these actuators as dielectric elastomer stack actuators (DESA), dielectric electroactive polymer stack transducers (DEAP), stacked dielectric elastomer actuators (SDEA), and dielectric elastomer stack transducers (DEST); this dissertation

uses DESA [83–85]. Similar to biological muscle, DESAs contract upon actuation. Thus, a tremor suppression system may employ DESAs as external analogs to human muscle.

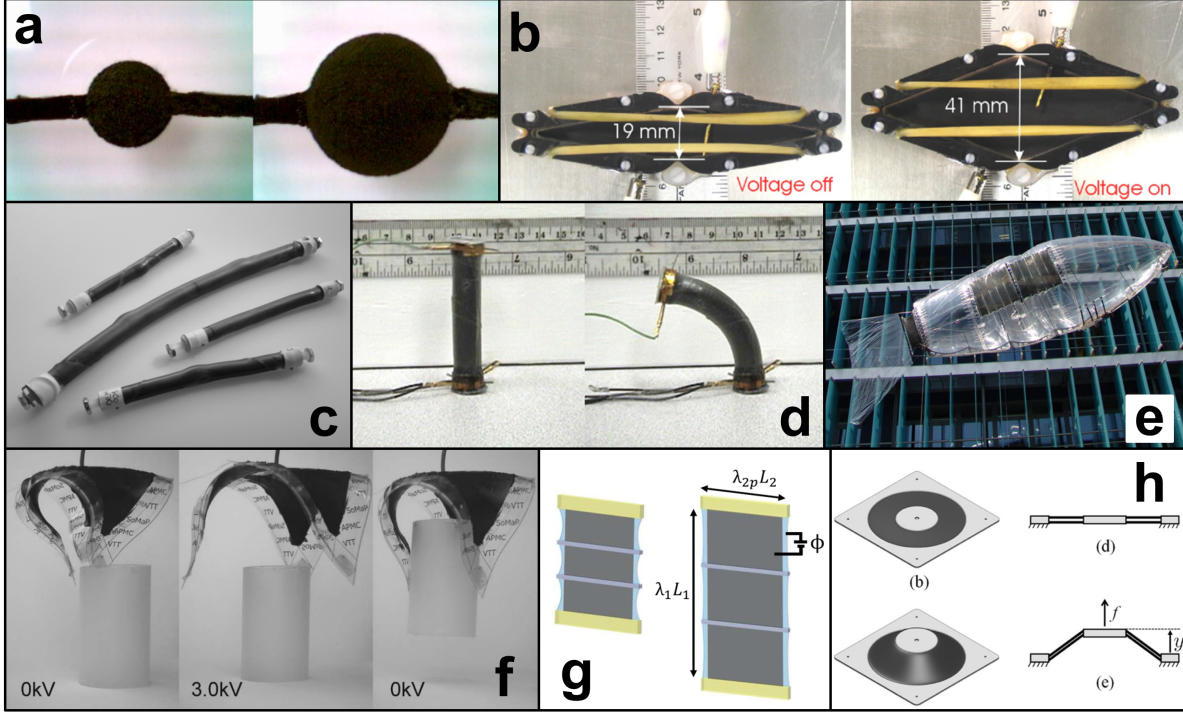


Figure 2.8: Different configurations of dielectric elastomers produce different functions and actuation capabilities: (a) from [75], (b) from [76], (c) from [77], (d) from [78], (e) from [79], (f) from [80], (g) from [81], and (h) from [82].

Dielectric elastomer stack actuators require tens to hundreds of very thin layers, complicating manufacturing. Most manufacturing approaches make smaller stacks, which are then piled up to reach the desired stack length. Manufacturing methods include folding [86, 87], spin coating [88, 89], automated thin film processing [73, 90, 91], spray deposition [92], liquid deposition [85, 93, 94], casting [95], and aerosol jet printing [96]. Figure 2.9 illustrates several DESAs from the literature. Figure 2.9(a) presents folded DESAs that simplify manufacturing: a single, continuous elastomer strip produces a large stack [86, 87]. Of particular note are the UV-cured acrylic DESAs

produced by spin coating in Fig. 2.9(g), (h), and (i): the manufacturing approach produces large stacks (greater than 10 cm) with very thin layers (approximately 30  $\mu\text{m}$ ), enabling relatively large actuation levels [97].

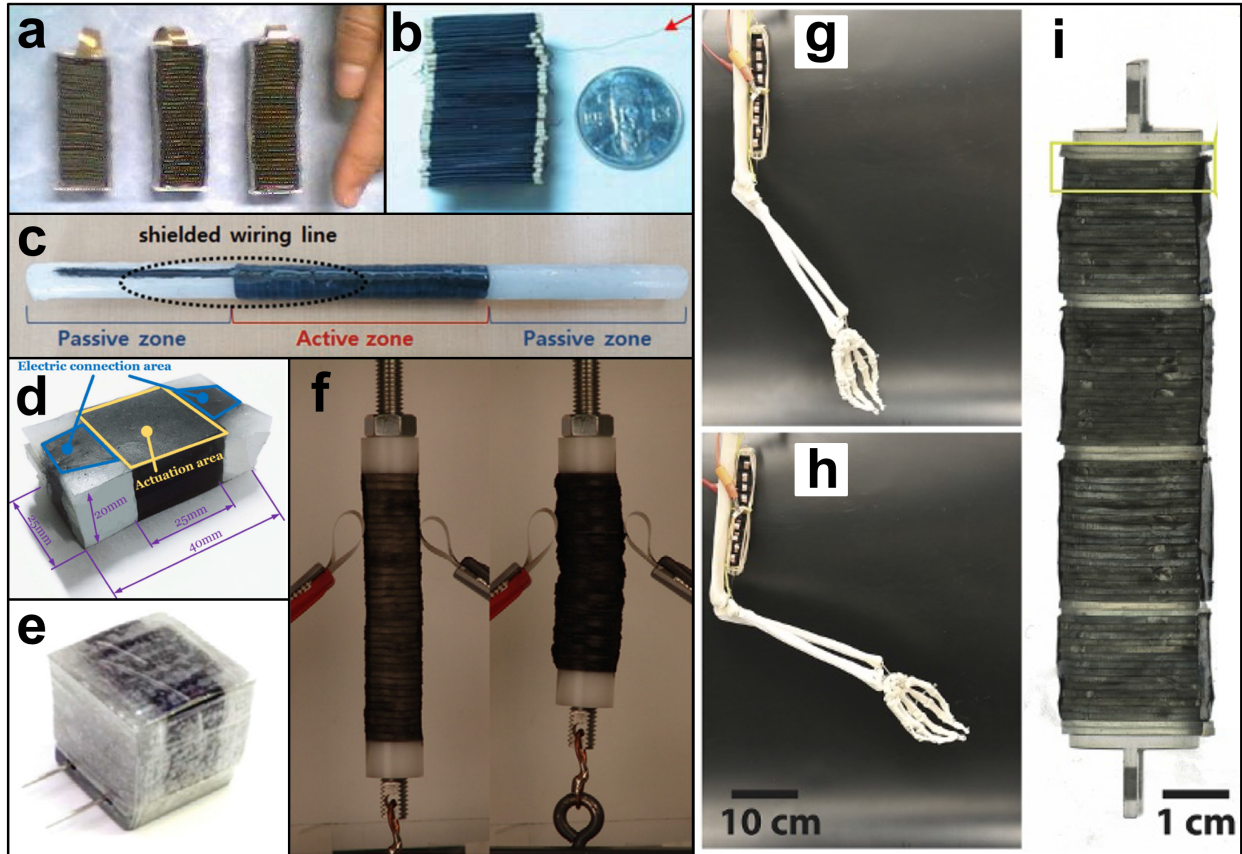


Figure 2.9: Several DESAs from the literature: (a) from [86], (b) from [93], (c) from [94], (d) from [95], (e) from [91], (f) from [73], and (g), (h), and (i) from [97]

### 2.3.1.2 Viscoelasticity

Dielectric elastomers exhibit viscoelastic material properties. Creep and stress relaxation capture the fundamental characteristics of viscoelastic material. When subject to a constant force, the ma-

material deforms over time rather than instantaneously—this property is known as creep. In addition, the material experiences decreased stress over time when fixed at a constant displacement—stress relaxation. Spring-dashpot models capture these properties. The Maxwell model (spring-dashpot in series) captures both effects, but does not converge to equilibrium values. The Kelvin-Voigt model (spring-dashpot in parallel) captures convergence to an equilibrium point during creep, but also produces instantaneous stress relaxation. The standard linear solid model (spring in parallel with Maxwell element) combines the benefits of these two models and captures both creep and stress relaxation. Figure 2.10 illustrates the stress relaxation and creep responses for these models. Higher-order combinations of linear mechanical elements allows a model to capture a wide range of viscoelastic behavior [98]. In addition, researchers have explored fractional-order elements to better capture the rate dependence of viscoelastic materials [99]. In the context of active tremor suppression, dielectric elastomer viscoelasticity represents another challenge in control design due to the rate and history dependence of actuator force and displacement [81].

### **2.3.1.3 Self-Sensing**

Just as electrostatic forcing produces DEA actuation, DEA deformation changes electrical properties. In particular, deformation changes the electrode area and layer thickness, producing a change in capacitance. As illustrated in Fig. 2.11, actuator deformation may be inferred by measuring the voltage across an external resistance connected to the DEA [100]. Superposition of a high-frequency signal onto the actuation voltage enables self-sensing actuators that detect deformation

via the high-frequency signal [28]. Existing self-sensing approaches exhibit decreased accuracy for higher speeds and controller gains, but higher-order approaches and improved electronics may enable higher-frequency applications [28, 82].

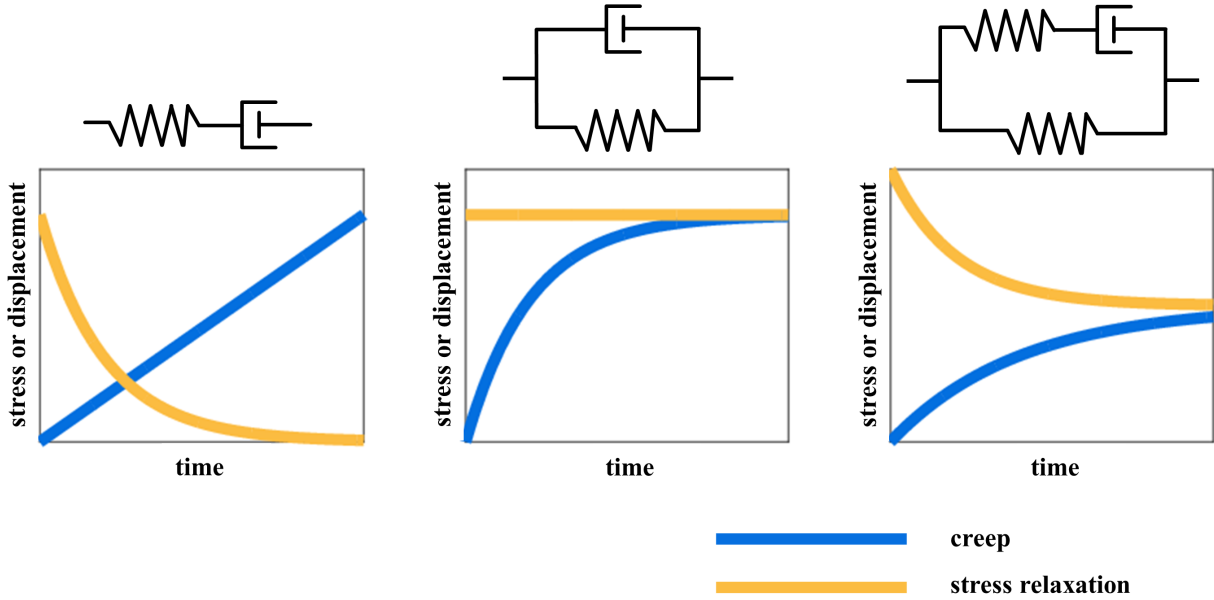


Figure 2.10: Spring-dashpot models capture fundamental viscoelastic characteristics like creep and stress relaxation.

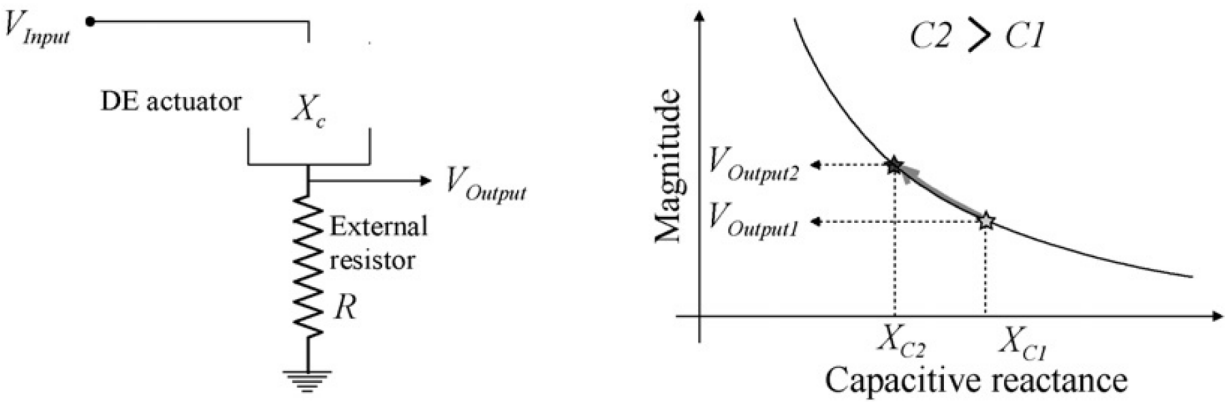


Figure 2.11: Measuring the voltage across an external resistor captures the change in DEA capacitance reactance, which relates to the DEA displacement (from [100]).

### 2.3.2 Limitations

The implementation of compact power electronics is one challenge for dielectric elastomer-based tremor suppression. Dielectric elastomers require high voltages at relatively low currents. The relatively low power and high efficiency of DEAs means compact implementations are possible. DC-DC converters enable high-voltage, low-current implementations in relatively compact form. Project Peta-pico-Voltron is an open-source power supply using DC-DC converters designed for DEA applications [101]. Recent research towards hydraulically amplified self-healing electrostatic (HASEL) actuators extended the concepts in Project Peta-pico-Voltron to produce a power supply that produces an 8 kV output at 0.3 mA while fitting in the palm of a hand with a mass of only 100 g [102]. Design optimization may further decrease the size of this prototype. In addition, flyback converters enable bidirectional energy flow, improving energy efficiency [103]. Overall, researchers continue to work towards compact power electronics for high-voltage, low-current applications. This dissertation focuses on the control and mechanical performance of dielectric elastomers for tremor suppression; physical implementations likely require parallel advances in power electronics to enable compact and lightweight systems.

Electrical safety is another challenge when dielectric elastomers interact with the human body. As discussed above, dielectric elastomers operate at very high voltages, but also at relatively low currents. The high voltage requirement initially seems troublesome for human body applications; however, careful design can ensure patient safety. Pourazadi et al. [104] quantified electrical safety for dielectric elastomers in close interaction with the human body based on guidelines from the

Underwriters Laboratories (UL) and the International Electrotechnical Commission (IEC). These guidelines specify the maximum current considered safe given the discharge duration. Since 20 mA is considered safe for any duration, human body DEA applications should limit the operating current to 20 mA. Higher currents may occur during discharge of DEA capacitance, but these higher currents may be acceptable due to the very small time period of discharge. This discharge duration depends on the capacitance, while the discharge current depends on the voltage. Thus, it is possible to define the maximum voltage in terms of the DEA capacitance, and vice versa; Fig. 2.12 presents the upper voltage limit given DEA capacitance. Enforcing these voltage and current limits nominally ensures electrical safety for the patient; however, real implementations require rigorous investigation of electrical safety before clinical use.

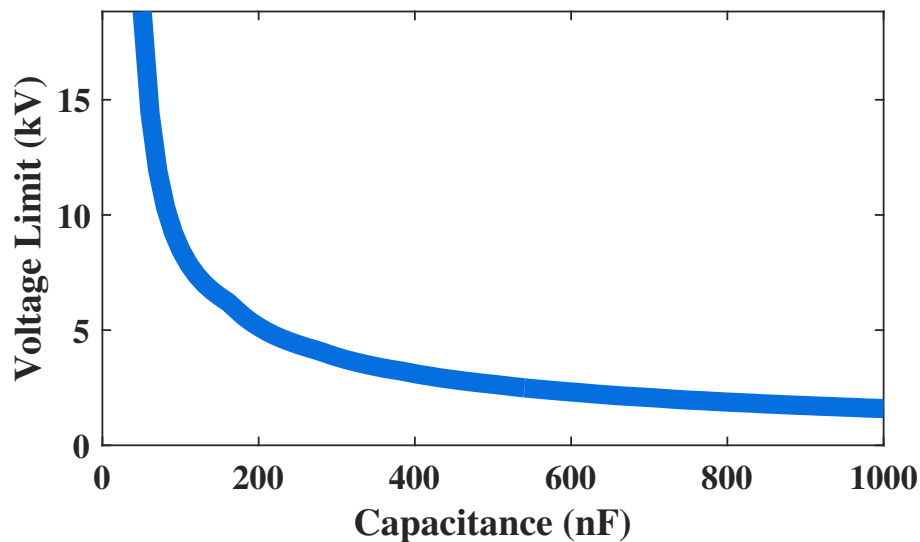


Figure 2.12: The maximum DESA voltage considered safe depends on the DESA capacitance.

## 2.4 Human Motor Control

Humans complete complex movements with seemingly little effort: catching a ball, playing an instrument, and timing a home run swing in Super Smash Brothers all appear relatively straightforward for the human motor system. However, robotics control challenges highlight the brilliance of human motor control. Humans can readily adapt to new environments and changes in task goals and constraints while demonstrating remarkable robustness to unexpected obstacles. In contrast, control algorithms for robots often focus on one predetermined task. How do humans produce robust movements that robots are, as of yet, incapable of achieving? Physically, neural structures plan and execute human movement. However, similar to robotic control systems, the human motor system includes sensory feedback, evidence of internal models of task dynamics, and error-based motor action. Regardless of the physical computation process, human motor control must include some fundamental elements of a control system: measurement and state estimation to plan movement and/or provide feedback along with feedback and/or feedforward control to execute the desired motion. Thus, modeling human motor control with a control system approach provides insight into how humans learn and execute tasks along with the roles of physiological structures. As this dissertation explores in Chapter 5, computational motor control models may also provide insight into disease pathophysiology.



### 2.4.1 Internal Models

The human motor system requires internal models of body and task dynamics to successfully complete motor tasks. Inverse models enable computation of motor commands to produce desired limb trajectories in an open-loop, or feedforward, approach. Forward models predict the sensory consequences of motor actions, enabling feedback control via state estimates even with sensory delay. Figure 2.13 illustrates a block diagram of a combination of feedforward and feedback control to represent human motor control. Early theories suggested movements include pre-programmed ballistic motion followed by terminal feedback to correct endpoint errors, but growing evidence supports the existence of continuous feedback accomplished via forward model predictions [105]. Kurtzer, Pruszynski, and Scott [106] showed long-latency reflexes (LLR) include internal models while short-latency reflexes (SLR) do not. For elbow motions, shoulder muscle SLR activated based on muscle stretch while shoulder muscle LLR activated even without shoulder stretch to compensate for interaction torques. This activation depended on limb geometry, implying the use of internal models that enable task-specific and multi-joint feedback. Crevecoeur and Scott [40] used known and unknown arm perturbations to show the LLR internal model includes a model of the expected perturbation. The LLR activated based on the expected perturbation profile, indicating a rapid update in the estimated current state based on delayed sensory feedback with forward model prediction. Finally, Maeda et al. [107] evaluated elbow movements with the shoulder in unlocked and locked positions to evaluate whether feedforward and feedback share an internal model. Feedforward control learned to decrease shoulder actuation when the shoulder was locked.

The addition of mechanical perturbations produced feedback that also showed decreased shoulder actuation in the locked position. Thus, feedback uses model information learned from feedforward control.

Internal models are adaptive and task-dependent. Motor learning enables task completion in new and changing environments by adapting internal models. Shadmehr and Mussa-Ivaldi [108] applied different force fields to reaching movements using a robotic manipulator. While force fields initially produced distorted movements, participants adapted to successfully complete the task. Participants also showed aftereffects of the learned dynamics when the force field was unexpectedly removed. Thus, motor learning updated the internal model, which takes time to adapt back to the no-field case. Immediately shifting force fields after learning showed that motor learning occurs on multiple timescales [109]. Altogether, humans develop internal models that adapt to the task and environment to enable feedback and feedforward control processes that complete desired tasks.

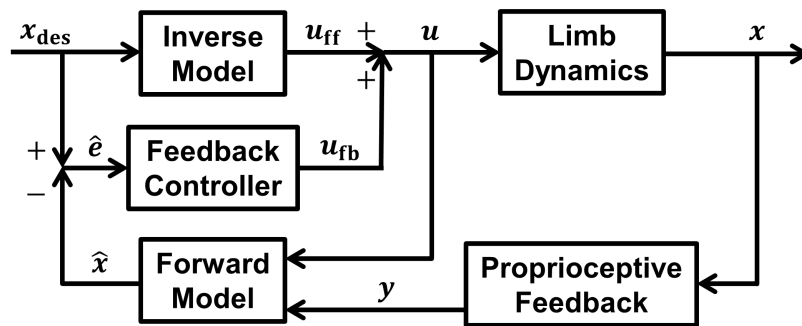


Figure 2.13: Internal models enable feedback and feedforward control in the human motor system.

## 2.4.2 Optimal Control

Optimal control theory captures many characteristics of human motor control [34,36,38,110,111]. Figure 2.14 illustrates the block diagram for optimal control as a representation of human motor control. An optimal controller implements estimator and controller gains based on a model of task dynamics—the shared internal model discussed above. An optimal controller effectively includes feedback and feedforward control since the state estimate depends on the relative confidence in the measurement and the model. Forward predictions enable feedback control despite large sensory delays [41]. The task-dependent cost function captures task-dependent motor behavior. For example, Nashed, Crevecoeur, and Scott [112] demonstrated the minimum intervention principle of optimal control on forward reaching movements. When the goal was to reach a forward position that spanned the width of the table, participants did not correct for horizontal perturbations because the horizontal direction was not relevant to the task goal. An optimal controller also captures the smooth movements that are characteristic of human motor control. The human motor system includes multiplicative noise that plays a critical role in how humans perform optimal movements; stochastic optimal control considers system noise in controller optimization [34]. This multiplicative noise explains the speed vs. accuracy tradeoff in human motor control. As illustrated in Fig. 2.15, an optimal controller with multiplicative noise considerations produces a smooth reaching motion with a bell-shaped velocity profile. Running many reaching simulations with varying movement durations demonstrates higher accuracy for slower movements: Fig. 2.16 illustrates higher endpoint variation for faster reaching durations.

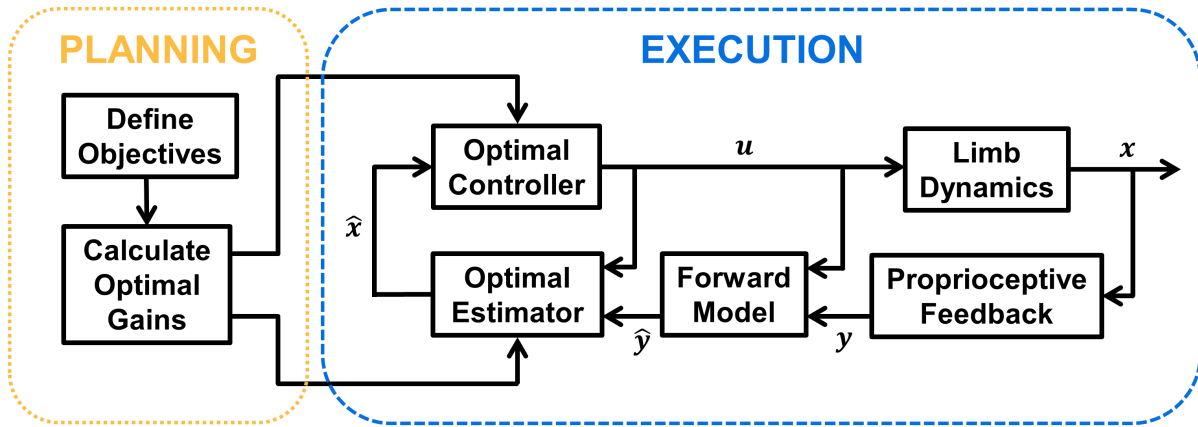


Figure 2.14: Optimal control theory captures human movement characteristics, while forward prediction enables compensation of feedback delays.

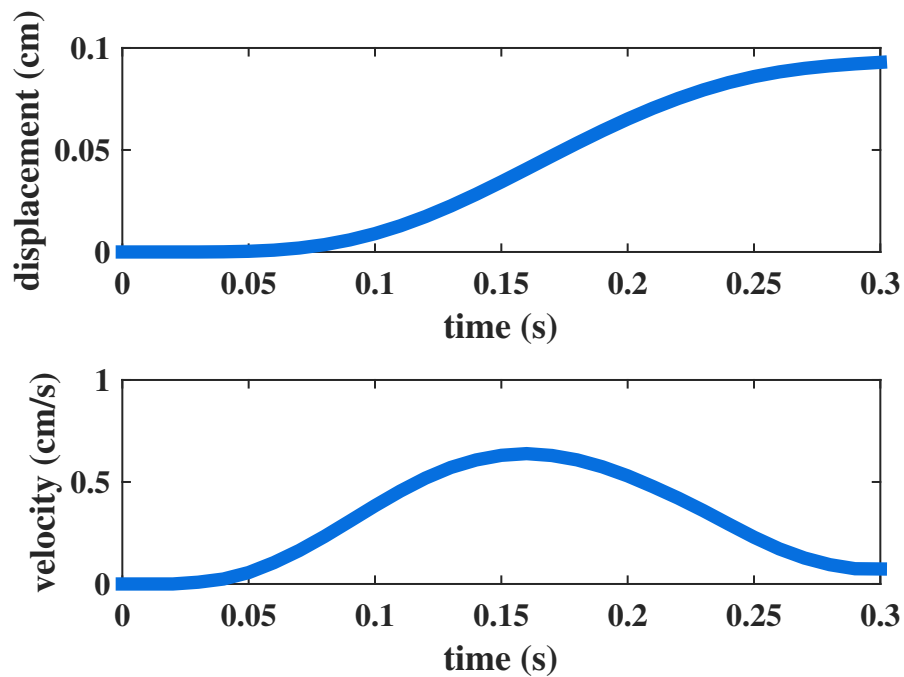


Figure 2.15: Optimal control of reaching movements produces smooth trajectories consistent with human motion.

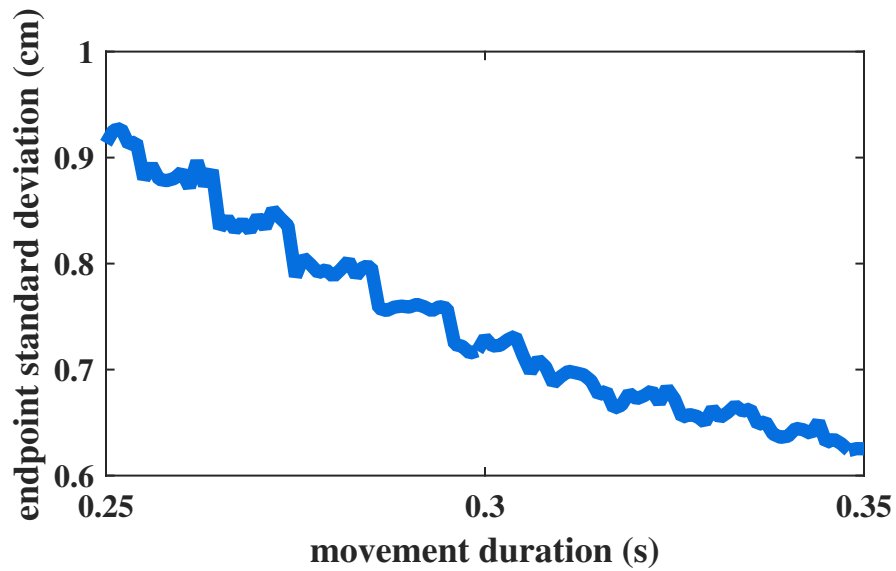


Figure 2.16: Inclusion of multiplicative noise produces a tradeoff between movement speed and endpoint variation.

### 2.4.3 Roles of CNS Regions

Movement studies involving patients with impaired CNS regions provide insight into the roles of different CNS regions in motor function. Three critical components of human motor control are the cerebellum, basal ganglia, and primary motor cortex. Patients with cerebellum dysfunction lack the ability to predict the sensory consequences of motor actions. Nowak, Timmann, and Hermsdörfer [113] demonstrated this fact through weight-catching tasks: participants used a basket to catch a weight dropped by either the participant or the practitioner. When personally dropping the weight, healthy participants increase grip force after releasing. These participants predict the sensory consequence (increased basket weight) from motor actions (dropping the weight). How-

ever, a patient with cerebellar agenesis did not adjust grip force upon releasing the weight, instead waiting until  $\sim 100$  ms after weight contact with the basket. Thus, the patient relies on delayed feedback rather than sensory prediction. Miall et al. [114] provide further support that the cerebellum includes internal models. Applying transcranial magnetic stimulation (TMS) to the cerebellum during initiation of reaching produced movements consistent with movements being planned  $\sim 140$  ms out-of-date. These studies, along with many others, suggest the cerebellum contains internal models that predict the sensory consequences of motor actions [115–117].

Basal ganglia dysfunction decreases motor vigor [115]. Mazzoni, Hristova, and Krakauer [118] compared healthy participants and Parkinson’s disease patients when reaching at a targeted speed. Parkinson’s disease patients required more trials to reach the targeted speed, showing decreased willingness to perform faster movements. Another study showed that inactivation of basal ganglia output in monkeys produces lower movement velocities and undershooting of target reaching [119]. Overall, clinical studies suggest the basal ganglia defines the cost and rewards for a task, effectively scaling movement speed based on the effort cost and the reward for task completion.

The primary motor cortex (M1) activates muscles, with different M1 regions corresponding to actuation of different muscle groups. However, M1 also performs intelligent processing to determine these muscular activation signals [120]. Pruszynski et al. [121] demonstrated the role of M1 in multi-joint feedback control. Mechanical elbow perturbation along with TMS stimulation of M1 shoulder-activating neurons produced supra-linear activation of shoulder muscles, indicating M1 includes fast feedback that considers interaction torques.

Finally, the thalamus relays signals among these regions [122]. The cerebellum projects to the motor cortex via the CTC circuit [123]. Based on the described optimal control model, the estimator represents the role of the cerebellum in predicting the sensory consequences of motor actions. The controller represents the role of the primary motor cortex in executing model-based feedback to control muscles. Thus, the CTC circuit contains the primary components of the feedback loop for human motor control. The planning stage of the optimal control model captures the role of the basal ganglia in determining the costs and rewards for a task. As discussed in Section 2.1.2, the CTC circuit and the basal ganglia exhibit abnormal activity in Parkinson's disease. Chapter 5 explores a potential parkinsonian tremor model by considering the roles of these structures in healthy motor control along with observed characteristics in Parkinson's disease.

## **CHAPTER 3**

### **DESA-BASED TREMOR SUPPRESSION**

Dielectric elastomers may improve the clinical implementation potential of mechanical tremor suppression by enabling soft, low-profile devices. This chapter presents a theoretical investigation of DESA-based tremor suppression to develop effective control strategies and motivate future work towards physical implementations. Section 3.1 develops a low-order model that enables numerical evaluation of DESA-based tremor suppression. Sections 3.2 and 3.3 present two different control approaches with simulations using the derived model. Research in this chapter is published in [124–126].

#### **3.1 Model Development**

This section develops a system model to investigate DESA-based tremor suppression. The DESA model includes geometric nonlinearities from large displacements as well as linear viscoelasticity. Low-order kinematics relate DESA states to human joint states. Finally, parameter optimization selects the DESA parameters for simulations in the remaining chapter sections.



### 3.1.1 DESA Model

Dielectric elastomers are essentially soft, deformable capacitors. Figure 2.7 illustrates the actuation of a DEA: applying a voltage across the compliant electrodes induces electrostatic forcing as opposite charges attract and like charges repel, causing through-thickness compression and in-plane expansion [71]. The effective pressure  $\sigma_{el}$  is proportional to the square of the electric field  $E$  by the permittivity of free space  $\epsilon_0$  and the relative permittivity of the elastomer  $\epsilon_r$  [71]. This electromechanical stress may be written in terms of the voltage across the electrodes  $V_p$  and the thickness of the actuator  $d$ :

$$\sigma_{el} = \epsilon_0 \epsilon_r E^2 = \epsilon_0 \epsilon_r \left( \frac{V_p}{d} \right)^2. \quad (3.1)$$

Since the electric field is inversely proportional to the thickness, reasonable voltage levels require very thin layers for usable actuation. Therefore, a single DEA does not have suitable geometry or actuation ability for macroscale applications. However, stacking many individual DEA layers results in actuation capabilities on the same scale as human motion [73, 83, 84, 124]. Figure 3.1 illustrates a DESA with  $n$  layers, undeformed layer thickness  $d_0$ , undeformed length  $l_0 = nd_0$ , undeformed cross-sectional area  $A_0$ , density  $\rho_0$ , and Young's modulus  $Y$ . The voltage supply connects to the electrodes in an alternating fashion such that a single voltage potential actuates all layers in parallel.

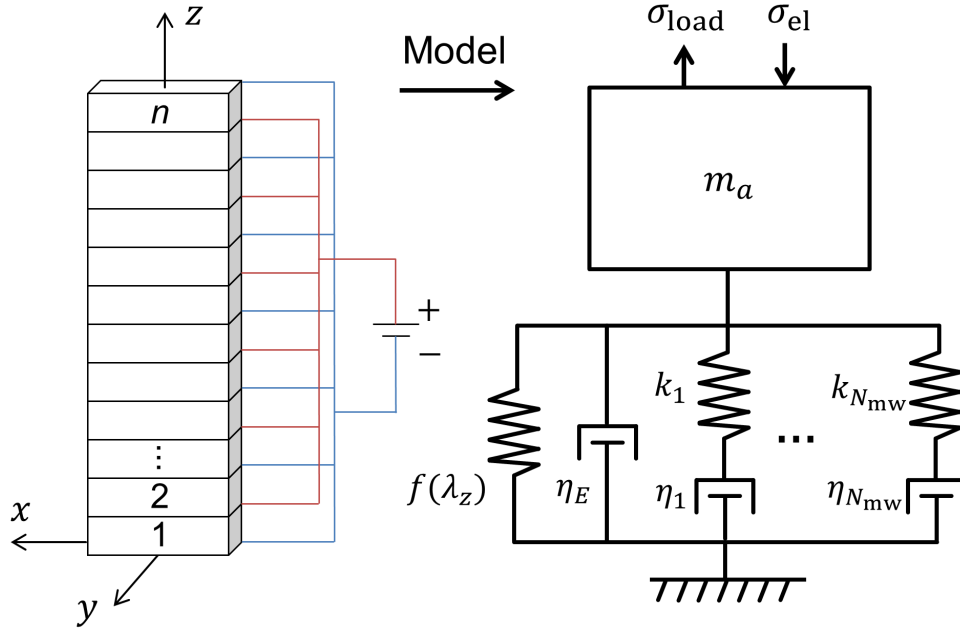


Figure 3.1: DESAs include many stacked DEA layers connected in parallel to scale-up actuation capabilities and can be modeled as a lumped-mass system.

The directional stretches  $\lambda_x$ ,  $\lambda_y$ , and  $\lambda_z$  typically represent the deformation of viscoelastic materials such as elastomers. The stretch is the ratio of the deformed length over the original length. Most researchers model dielectric elastomers as incompressible, producing a relation among the three stretches [25, 72, 127]:

$$\lambda_x \lambda_y \lambda_z = 1. \quad (3.2)$$

Using a square or circular cross section for the actuator produces equal stretches in the  $x$ - and  $y$ -directions for unidirectional loading in the  $z$ -direction ( $\lambda_x = \lambda_y$ ). Thus, a single stretch defines the full deformation state of the actuator. The state of interest for the model is  $\lambda_z$  since DESAs are designed for loading in the  $z$ -direction.

This study largely follows the lumped DESA model developed by Hoffstadt and Maas; Fig. 3.1 illustrates this lumped model [83]. The external load  $\sigma_{\text{load}}$  and the electrostatic pressure act on the lumped mass of the actuator  $m_a = \rho_0 A_0 l_0 / 3$ . This form of lumped mass assumes uniform deformation with the DESA fixed at one end and is analogous to a spring with non-negligible mass. A generalized Kelvin-Maxwell network models the viscoelastic nature of the material. This network includes a nonlinear spring in parallel with a viscous element and  $N_{\text{mw}}$  Maxwell elements. The nonlinear spring  $f(\lambda_z)$  is the derivative of the strain energy density with respect to  $\lambda_z$ . The viscous element  $\eta_E$  and the Maxwell elements model the dynamic behavior of the elastomer. A larger network (higher  $N_{\text{mw}}$ ) captures more complex viscoelastic behavior. Noting the deformed cross-sectional area  $A = A_0 / \lambda_z$ , a force balance produces the DESA equation of motion:

$$m_a l_0 \ddot{\lambda}_z = \frac{A_0}{\lambda_z} (\sigma_{\text{load}} - \sigma_{\text{elast}} - \sigma_{\text{visc}} - \sigma_{\text{mw}} - \sigma_{\text{el}}) \quad (3.3)$$

where  $\sigma_{\text{elast}}$ ,  $\sigma_{\text{visc}}$ , and  $\sigma_{\text{mw}}$  are the stresses from the nonlinear spring, viscous element, and Maxwell elements, respectively. Previous research shows good agreement with experiments for stretches between 0.8 and 1.25 when using the neo-Hookean model for strain energy, neglecting the viscous element ( $\sigma_{\text{visc}} = 0$ ), and using only one Maxwell element ( $N_{\text{mw}} = 1$ ) [83]. For this application, the model only needs to capture the viscoelastic effects for a small frequency range (approximately 0–8 Hz) and the actuator can be designed to only deform in the neo-Hookean region; these facts further justify the model assumptions. Thus, the material-dependent stresses

become

$$\sigma_{\text{elast}} = \frac{Y}{3}(\lambda_z^2 - \frac{1}{\lambda_z}) \quad (3.4)$$

$$\dot{\sigma}_{\text{mw}} = k_1 \dot{\lambda}_z - \frac{k_1}{\eta_1} \sigma_{\text{mw}}. \quad (3.5)$$

An external force  $F_{\text{load}}$  from the human joint produces the load stress:

$$\sigma_{\text{load}} = \frac{F_{\text{load}}}{A} = \frac{\lambda_z F_{\text{load}}}{A_0}. \quad (3.6)$$

Substituting into Eq. (3.3), the DESA equation of motion becomes

$$m_a l_0 \ddot{\lambda}_z + \frac{YA_0}{3} \left( \lambda_z - \frac{1}{\lambda_z^2} \right) + \frac{\varepsilon_0 \varepsilon_r A_0}{d_0^2} \frac{V_p^2}{\lambda_z^3} + \frac{A_0}{\lambda_z} \sigma_{\text{mw}} = F_{\text{load}}. \quad (3.7)$$

Thus, Eqs. (3.5) and (3.7) define the dynamics of a single DESA in terms of the states  $\lambda_z$ ,  $\dot{\lambda}_z$ , and  $\sigma_{\text{mw}}$  and the voltage input  $V_p$ . The dynamics also depend on the geometric parameters ( $l_0$ ,  $d_0$ ,  $A_0$ ) and the material parameters ( $\rho_0$ ,  $Y$ ,  $k_1$ ,  $\eta_1$ , and  $\varepsilon_r$ ).

This study assumes the controller directly controls the DESA voltage. In practice, a power source applies current to the DESA to achieve the desired voltage. The DESA is effectively an RC circuit, with the corresponding transfer function of input voltage  $V_s$  to DESA voltage  $V_p$  related to the capacitance  $C$  and resistance  $R$ :

$$\frac{\bar{V}_p}{\bar{V}_s} = \frac{1}{1 + sRC} \quad (3.8)$$

where an overbar represents the Laplace transform and  $s$  is the Laplace variable. The electrical current  $i_c$  is

$$\bar{i}_c = sC\bar{V}_c. \quad (3.9)$$

However, the transient dynamics of the RC circuit are much faster than the mechanical dynamics of the system. In fact, including these electrical dynamics is prohibitive for numerical integration due to the drastically different time scales. Simulations apply the 20 mA current limit by limiting the change in voltage between time steps.

### 3.1.2 DESA-Joint Interaction

The universal joint model often represents the mechanical behavior of human joints [15, 22, 124, 128]. When only considering a single rotational degree-of-freedom  $\theta$ , the system is a revolute joint with linear, second-order differential equation:

$$J\ddot{\theta} + B\dot{\theta} + K\theta = \tau \quad (3.10)$$

where the inertia  $J$ , damping  $B$ , and stiffness  $K$  depend on the passive mechanical properties of the joint. The torque about the joint  $\tau$  represents all active torques operating on the joint, including the nonlinear part of the stiffness and damping of the muscles [129, 130]. This model is valid for moderate rotations (at least up to  $\pm 15^\circ$ ) [129, 130]. This initial study only evaluates the system in this range since many functional tasks are completed near the neutral position. In the context

of tremor suppression, the torque about the joint includes the muscular torque  $\tau_m$  and the moment about the joint from any DESA loading  $M_{\text{DEA}}$ :

$$J\ddot{\theta} + B\dot{\theta} + K\theta = \tau_m + M_{\text{DEA}}. \quad (3.11)$$

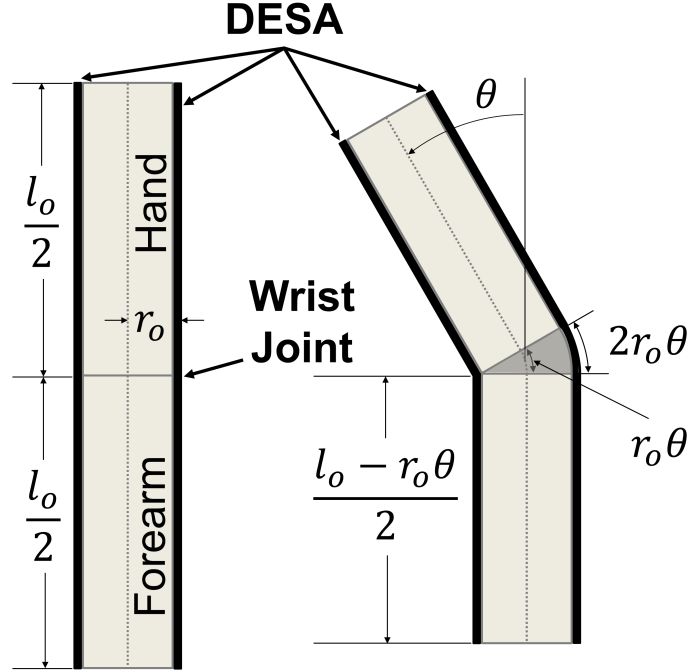


Figure 3.2: Two DESAs form an agonist-antagonist pair to enable bidirectional actuation. The kinematic relationships between DESA stretches and joint angle define the interaction between the DESAs and joint.

Defining kinematic relations between DESA stretches and joint angle reduces the system to a single displacement state. This study applies DESAs in an agonist-antagonist approach to enable bidirectional actuation without an offset voltage; Fig. 3.2 demonstrates this configuration. Assuming the centerline of the joint remains constant, the change in length of each actuator is equal to the change in length of the surface to which it is attached. Using the geometry in Fig. 3.2, the stretches

for the flexion (left) and extension (right) actuators are

$$\lambda_f = 1 - \frac{r_o}{l_o} \theta \quad (3.12)$$

$$\lambda_e = 1 + \frac{r_o}{l_o} \theta. \quad (3.13)$$

The DESA torque about the joint is the combination of the moment produced by the flexion actuator  $M_f$  and the moment produced by the extension actuator  $M_e$ :

$$M_{\text{DEA}} = M_f + M_e. \quad (3.14)$$

Consider the configuration in Fig. 3.2 to determine the correct signs for how  $M_f$  and  $M_e$  relate to the load force on each actuator. Applying a voltage to the flexion actuator produces a compressive force in the DESA, resulting in a positive moment:

$$M_f = r_0 F_{\text{load},f}. \quad (3.15)$$

However, a compressive force in the extension actuator produces a negative moment:

$$M_e = -r_0 F_{\text{load},e}. \quad (3.16)$$

Now substitution of Eqs. (3.12) and (3.13) into Eq. (3.7) provides the load forces for each actuator in terms of  $\theta$ . Algebra reveals the total DESA torque about the joint:

$$M_{\text{DEA}} = -2r_0^2 m_a \ddot{\theta} - \frac{2r_0^2 A_0 Y}{3l_0} \left( 1 + \frac{2}{(1 + \frac{r_0^2}{l_0^2} \theta^2)^2} \right) \theta + \frac{r_0 A_0 \epsilon_0 \epsilon_r}{d_0^2} \left( \frac{V_f^2}{(1 - \frac{r_0}{l_0} \theta)^3} - \frac{V_e^2}{(1 + \frac{r_0}{l_0} \theta)^3} \right) + r_0 A_0 \left( \frac{\sigma_{\text{mw},f}}{1 - \frac{r_0}{l_0} \theta} - \frac{\sigma_{\text{mw},e}}{1 + \frac{r_0}{l_0} \theta} \right). \quad (3.17)$$

Now define a controller voltage  $V$  that specifies the voltage on the flexion actuator  $V_f$  and extension actuator  $V_e$ :

$$\begin{aligned} \text{if } V \geq 0: V_f &= V \text{ and } V_e = 0 \\ \text{if } V < 0: V_f &= 0 \text{ and } V_e = V. \end{aligned} \quad (3.18)$$

This single control voltage fully defines the voltage state of both actuators. Rewrite the voltage-dependent terms using Eq. (3.18):

$$M_{\text{DEA}} = -2r_0^2 m_a \ddot{\theta} - \frac{2r_0^2 A_0 Y}{3l_0} \left( 1 + \frac{2}{(1 + \frac{r_0^2}{l_0^2} \theta^2)^2} \right) \theta + \frac{r_0 A_0 \epsilon_0 \epsilon_r}{d_0^2} \left( \frac{V^2 \text{sgn}(V)}{(1 - \frac{r_0}{l_0} \theta \text{sgn}(V))^3} \right) + r_0 A_0 \left( \frac{\sigma_{\text{mw},f}}{1 - \frac{r_0}{l_0} \theta} - \frac{\sigma_{\text{mw},e}}{1 + \frac{r_0}{l_0} \theta} \right). \quad (3.19)$$

Now the torque from the actuators only depends on the state of the joint, the controller voltage  $V$ , and the viscoelastic stresses from the two actuators. Rewrite the equations of motion for these



stresses in terms of the joint angle  $\theta$  rather than the stretch:

$$\dot{\sigma}_{\text{mw},f} = -\frac{r_0 k_1}{l_0} \dot{\theta} - \frac{k_1}{\eta_1} \sigma_{\text{mw},f} \quad (3.20)$$

$$\dot{\sigma}_{\text{mw},e} = \frac{r_0 k_1}{l_0} \dot{\theta} - \frac{k_1}{\eta_1} \sigma_{\text{mw},e}. \quad (3.21)$$

Inserting Eq. (3.19) into Eq. (3.11) produces the equation of motion of the DESA-joint system.

Finally, the controllers in the ensuing sections utilize the control input variable  $u$ , which inverts the voltage nonlinearity:

$$u \equiv V^2 \text{sgn}(V). \quad (3.22)$$

Thus,  $u$  fully defines  $V$  (and therefore the voltage applied to each actuator):

$$V = \sqrt{|u|} \text{sgn}(u). \quad (3.23)$$

Linearizing the equation of motion provides insight into the passive and active influence of the DESAs on the joint. The linearized DESA torque is

$$M_{\text{DEA}} = -2r_0^2 m_a \ddot{\theta} - \frac{2r_0^2 A_0 Y}{l_0} \theta + \frac{r_0 A_0 \epsilon_0 \epsilon_r}{d_0^2} u + r_0 A_0 (\sigma_{\text{mw},f} - \sigma_{\text{mw},e}). \quad (3.24)$$

Defining a new state  $\sigma_{\text{mw}}$  reduces the number of states for the Maxwell stresses by one:

$$\sigma_{\text{mw}} \equiv \sigma_{\text{mw,e}} - \sigma_{\text{mw,f}} \quad (3.25)$$

$$\dot{\sigma}_{\text{mw}} = \frac{2r_0k_1}{l_0}\dot{\theta} - \frac{k_1}{\eta_1}\sigma_{\text{mw}}. \quad (3.26)$$

Now the linearized equation of motion for the DESA-joint system becomes

$$(J + 2r_0^2m_a)\ddot{\theta} + B\dot{\theta} + r_0A_0\sigma_{\text{mw}} + \left(K + \frac{2r_0^2A_0Y}{l_0}\right)\theta = \tau_m + \frac{r_0A_0\varepsilon_0\varepsilon_r}{d_0^2}u. \quad (3.27)$$

Thus, applying DESAs to the joint increases system inertia and stiffness. The control input  $u$  provides a means to actuate against the tremor-producing muscular torque included in  $\tau_m$ . Define the effective inertia  $m_{\text{eff}}$ , effective stiffness  $k_{\text{eff}}$ , and electromechanical force factor  $\alpha$  to facilitate parameter selection analysis:

$$m_{\text{eff}} \equiv 2r_0^2m_a \quad (3.28)$$

$$k_{\text{eff}} \equiv \frac{2r_0^2A_0Y}{l_0} \quad (3.29)$$

$$\alpha \equiv \frac{r_0A_0\varepsilon_0\varepsilon_r}{d_0^2}. \quad (3.30)$$

Finally, the linear equations of motion enable analytical calculation of the system frequency response. The Laplace transform of the Maxwell stress is

$$\bar{\sigma}_{\text{mw}} = \frac{\frac{2r_0k_1}{l_0}s}{s + \frac{k_1}{\eta_1}}\bar{\theta}. \quad (3.31)$$

Therefore, the equation of motion in the frequency domain becomes

$$\left[ (J + 2r_0^2 m_a) s^2 + Bs + \left( K + \frac{2r_0^2 A_0 Y}{l_0} \right) + \frac{\frac{2r_0^2 k_1 A_0}{l_0} s}{s + \frac{k_1}{\eta_1}} \right] \bar{\theta} = \bar{\tau}_m + \frac{r_0 A_0 \epsilon_0 \epsilon_r}{d_0^2} \bar{u}. \quad (3.32)$$

This equation enables analysis of the passive effect of the material on the joint via  $\bar{\theta}/\bar{\tau}_m$  and the actuation capabilities of the DESAs via  $\bar{\theta}/\bar{u}$ . Furthermore, assumptions about the form of control and the measured quantity can produce a closed-loop transfer function. For instance, if a filter perfectly separates the voluntary and tremor motion, the two components may be represented by two separate loops with control only applied to the tremor loop. Defining the controller as a feedback of the tremor state (say,  $u = -\kappa s \bar{\theta}$ ) results in a transfer function from the tremor torque to the resulting undesired motion.

### 3.1.3 Parameter Selection

Optimal selection of DESA material and geometry produces better energy efficiency and user comfort. The optimal geometry largely depends on the targeted joint. From Eq. (3.27), it is clear that greater area  $A_0$  and smaller layer thickness  $d_0$  produce greater actuation force. Greater length  $l_0$  (or greater number of layers  $n$ ) produces greater displacements for a given force. The size of the joint limits the area and length of the actuators, while manufacturing capabilities limit the layer thickness. The ensuing simulations fix the geometry of the actuators to target suppression of wrist flexion-extension ( $A_0 = 1 \text{ cm}^2$ ,  $d_0 = 50 \text{ }\mu\text{m}$ , and  $n = 2000$  layers). Unless otherwise stated, the

simulations also use the mean male parameters for wrist flexion-extension ( $J = 0.00276 \text{ kg/m}^2$ ,  $B = 0.03 \text{ Nms/rad}$ , and  $K = 0.992 \text{ Nm/rad}$ ) [130]. The remaining DESA parameters depend on the elastomer material and include the relative permittivity  $\epsilon_r$ , the Young's modulus  $Y$ , and the viscoelastic parameters  $k_1$  and  $\eta_1$ . Since viscoelastic parameters are not readily available in the literature, this study assumes these parameters are proportional to the Young's modulus by constants  $p_1$  and  $p_2$ :

$$k_1 = p_1 Y \quad (3.33)$$

$$\eta_1 = p_2 Y. \quad (3.34)$$

This study selects constants that correspond to the experimentally-fitted values for the viscoelastic parameters of polyurethane ( $p_1 = 1.5$  and  $p_2 = 0.03$ ) [83].

Optimal selection of the Young's modulus depends on two factors: resistance to voluntary motion and energy efficiency. As will be discussed in Section 3.3, the tremor-active control approach requires the human motor system to overcome the DESA passive dynamics. Figure 3.3 illustrates the open-loop (zero voltage) frequency response function for wrist flexion-extension for several values of  $Y$ , where  $Y = 0$  is equivalent to removing the actuators. The angular displacement output decreases for higher values of  $Y$ . In other words, the patient must exert additional muscular torque to overcome the DESA material stiffness in the tremor-active approach. The additional stiffness should be kept at a minimum to avoid muscle fatigue and increase user comfort.

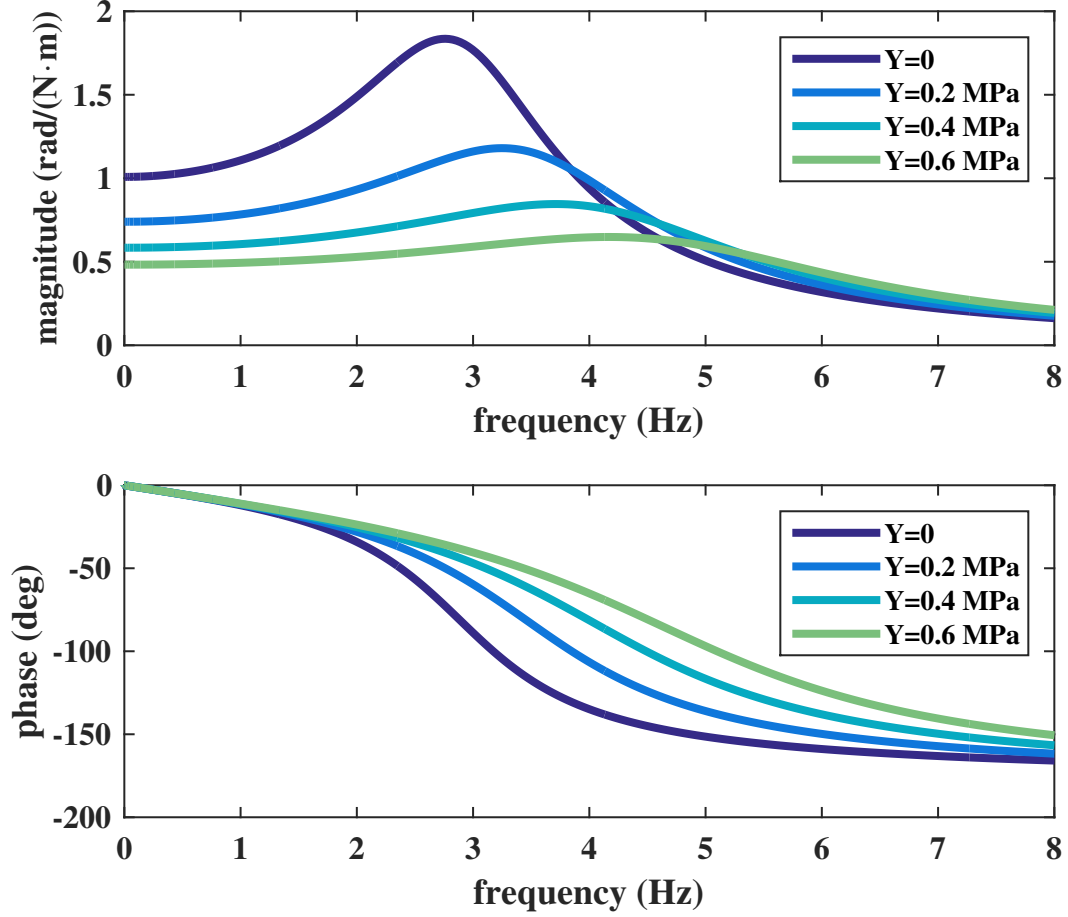


Figure 3.3: The FRF of the open-loop system demonstrates the passive effect of the DESA material on the joint: higher  $Y$  requires increased muscular effort.

The second aspect of stiffness selection is energy efficiency. This objective may be viewed as maximizing the electromechanical coupling of the DESA-joint system. This study defines a coupling parameter  $Q_c$  that is the ratio of the maximum mechanical potential energy during steady-state excitation at a given frequency to the maximum electrical potential energy that would exactly cancel that motion. The frequency response in Eq. (3.32) enables calculation of this parameter. First, the magnitude of the transfer function  $\bar{\theta}/\bar{\tau}_m$  produces the maximum value of the mechanical

potential energy  $U_{\text{mech}}$  based on the forcing frequency  $\omega$  and amplitude  $A$ :

$$U_{\text{mech}}(\omega) = \frac{1}{2}k_{\text{eff}} \left[ A \left| \frac{\bar{\theta}}{\bar{\tau}_m} \right|(\omega) \right]^2. \quad (3.35)$$

The amplitude of the control input that exactly cancels this motion is  $u_{\text{canc}} = A/\alpha$ . Therefore, the maximum electrical energy  $U_{\text{elec}}$  depends on the undeformed capacitance  $C_0 = n\epsilon_0\epsilon_r A_0/d_0$  and the DESA voltage:

$$U_{\text{elec}} = \frac{1}{2}C_0 V^2 = \frac{1}{2}C_0 u_{\text{canc}}^2 = \frac{1}{2}C_0 \frac{A^2}{\alpha^2}. \quad (3.36)$$

Thus, the frequency-dependent coupling parameter becomes

$$Q_c(\omega) = \frac{U_{\text{mech}}(\omega)}{U_{\text{elec}}} = \frac{r_0 k_{\text{eff}} A}{l_0} \left[ \left| \frac{\bar{\theta}}{\bar{\tau}_m} \right|(\omega) \right]^2. \quad (3.37)$$

Note that this parameter depends on the amplitude of the muscular torque  $A$ . Since the actuation targets tremor, the average coupling over the tremor frequency range  $\bar{Q}_c$  provides a general measure of energy efficiency for this application. Figure 3.4 illustrates the optimal stiffness for energy efficiency for the selected geometry and wrist parameters.

Finally, maximizing the relative permittivity  $\epsilon_r$  of the material provides greater actuation with lower voltages. Thus, material selection needs to balance energy efficiency (optimal  $Y$  for given amplitude), user comfort (minimize  $Y$ ), and actuation ability (maximize  $\epsilon_r$ ). This study defines the objective function  $L$  to optimize material selection: maximizing  $L$  produces the best performance from available materials. The weights  $w_1$ ,  $w_2$ , and  $w_3$  enable tailoring of the relative importance

of each performance metric:

$$L = e^{w_1 \varepsilon_r} - e^{w_2 Y} + e^{w_3 \tilde{Q}_c}. \quad (3.38)$$

Figure 3.5 presents some of the elastomers used as DEAs in the literature [25]. The curve represents a level set of the objective function with  $w_1 = 0.1$ ,  $w_2 = 1$ , and  $w_3 = 10$  (note  $Y$  is in MPa). Fluorosilicone is the optimal available material for this set of weights, with  $\varepsilon_r = 6.9$  and  $Y = 0.5$  MPa. The following simulations use these parameters for the DEA material.

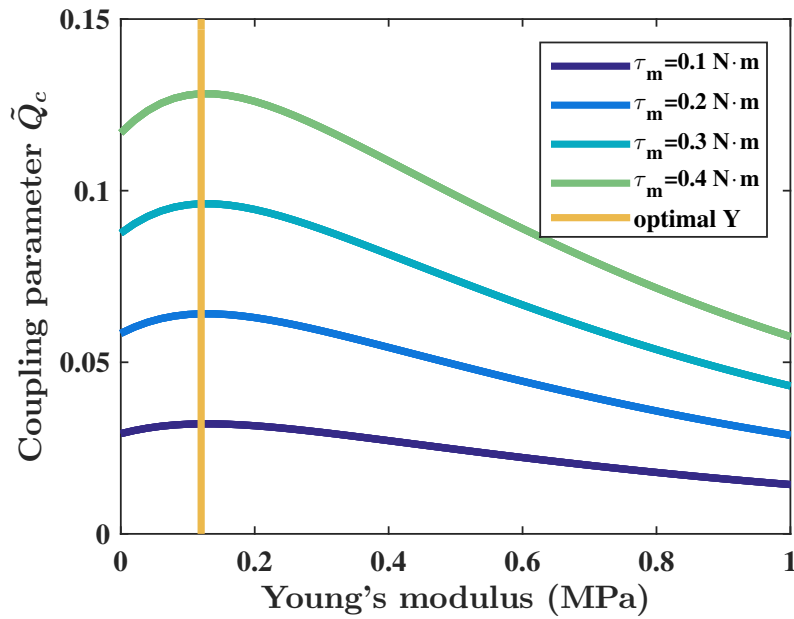


Figure 3.4: The optimal Young's modulus for energy efficiency maximizes the electromechanical coupling parameter.

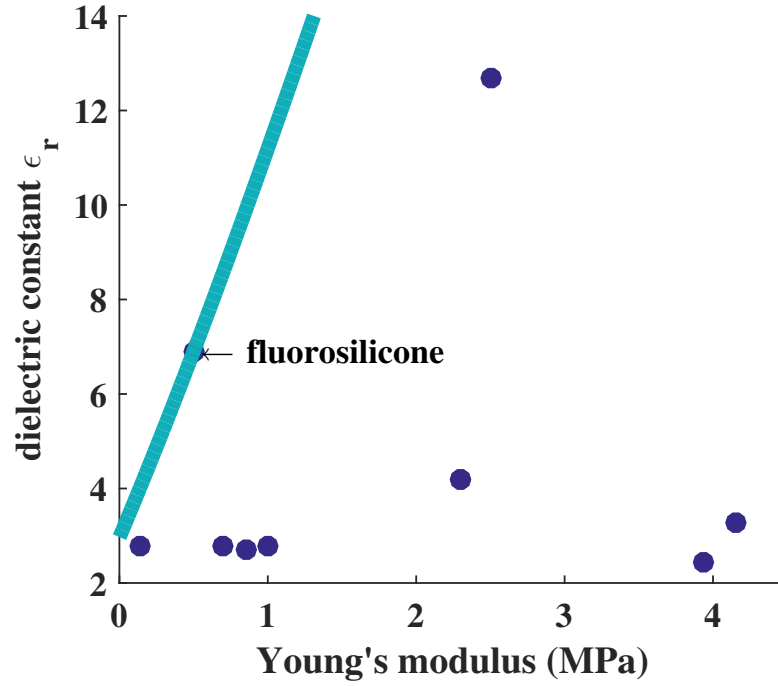


Figure 3.5: The curve shows a level set for the objective function, indicating that fluorosilicone is the optimal available material for this design.

### 3.1.4 Muscular Torque

Numerical investigations in this chapter simulate Eq. (3.11) via Eqs. (3.19), (3.20), (3.21), and (3.23) with states  $\theta$ ,  $\dot{\theta}$ ,  $\sigma_{mw,f}$ , and  $\sigma_{mw,e}$ . The controller determines  $u$ , leaving the muscular torque  $\tau_m$  as the only remaining undefined quantity. This study assumes the muscular torque includes a tremor-producing torque  $\tau_T$  and an independent torque  $\tau_V$  that produces the desired, or voluntary, motion:

$$\tau_m = \tau_T + \tau_V \quad (3.39)$$



As discussed in Section 1.3, simulations assume the tremor torque does not depend on the state; in other words, the signal that represents the tremor torque does not change due to the voluntary motion or tremor suppression.

This study uses recorded tremor data from an online database to implement tremor signals with realistic characteristics, including time-varying amplitude and frequency. This tremor data is associated with [9] and may be found online<sup>1</sup>. The database includes ten normalized acceleration time series recordings of the dorsum of the outstretched hand while the patient attempts to keep their hand at rest: five datasets measure Parkinson’s disease patients (referred to as ‘PD1’ through ‘PD5’) and five datasets measure essential tremor patients (‘ET1’ through ‘ET5’). One dataset (‘ET1’) is sampled at 300 Hz while the remaining datasets are sampled at 1000 Hz; all datasets are recorded for 30 seconds. Figures 3.6 and 3.7 illustrate the first ten seconds of the parkinsonian tremor datasets and the essential tremor datasets, respectively. Unless otherwise stated, simulations in this chapter set the tremor torque equal to a scaled version of a single tremor dataset: the data is scaled to achieve a targeted tremor displacement amplitude. Simulations implement this tremor torque in a point-by-point manner with linear interpolation between samples. Thus,  $\tau_T$  is a fixed function of time.

---

<sup>1</sup>[http://jeti.uni-freiburg.de/path\\_tremor/](http://jeti.uni-freiburg.de/path_tremor/)

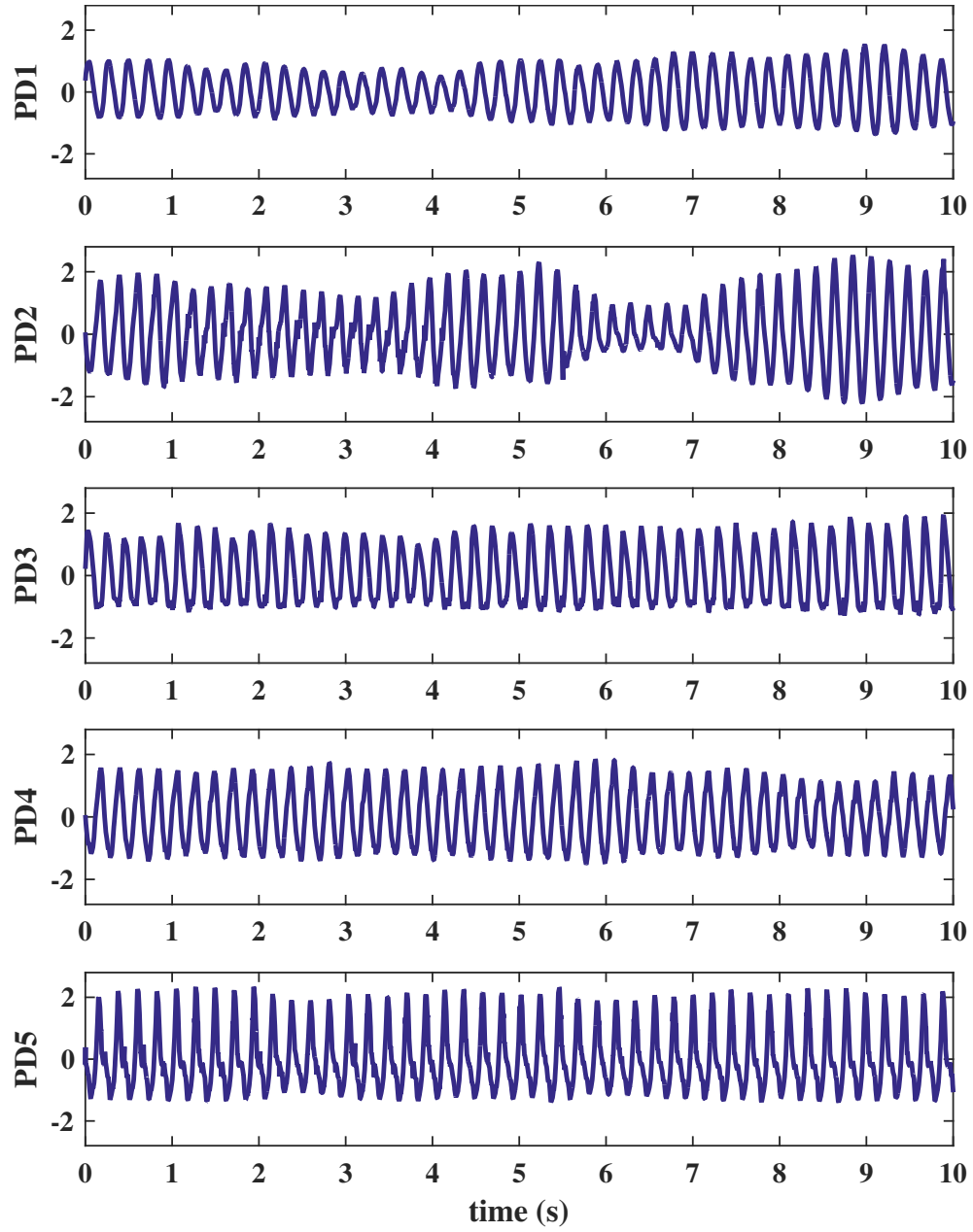


Figure 3.6: The online database from [9] includes five parkinsonian tremor datasets.

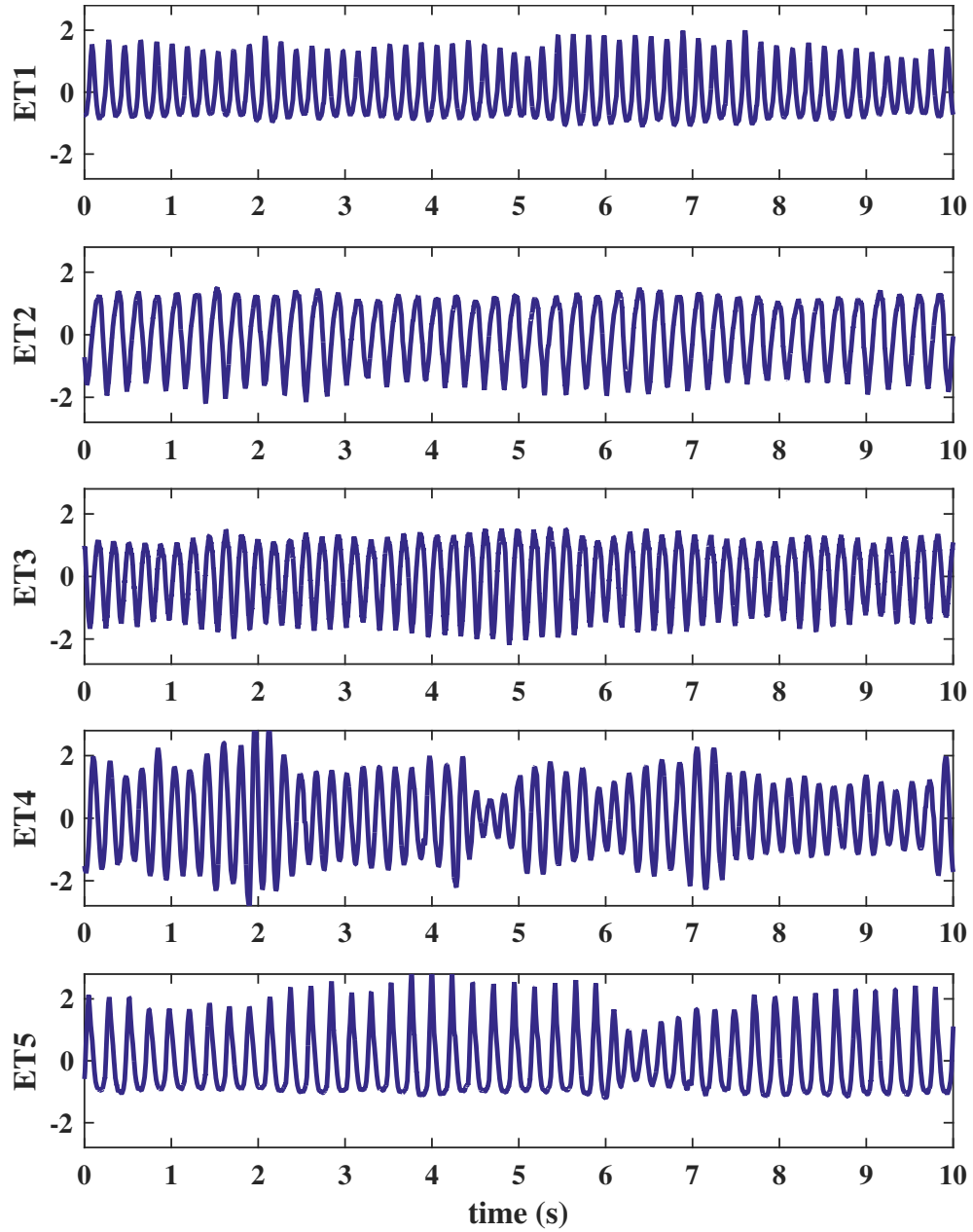


Figure 3.7: The online database from [9] includes five essential tremor datasets.

This chapter treats the voluntary torque as independent of the tremor torque. In general, the voluntary torque may be any signal with frequency content exclusively in the 0–2 Hz range. Some simulations in this chapter apply purely sinusoidal voluntary torque to capture fundamental system

characteristics. However, most simulations apply voluntary torque signals associated with functional tasks to provide examples of controller performance with realistic voluntary motion. The joint displacement time series for these functional tasks were extracted from trials in [131] using image processing software; Fig. 3.8 illustrates the joint angles for each task, including flexion-extension (FE) and radial-ulnar deviation (RUD). The first task, labeled “Jar Task”, involves reaching, opening, and replacing a jam jar. The second task, labeled “Pour Task”, involves picking up and pouring water from a carton into a jug before returning the carton to the table. The voluntary torque associated with each trial was calculated via Eq. (3.11) with zero tremor torque. Thus, similar to  $\tau_T$ ,  $\tau_V$  is a known, fixed function of time.

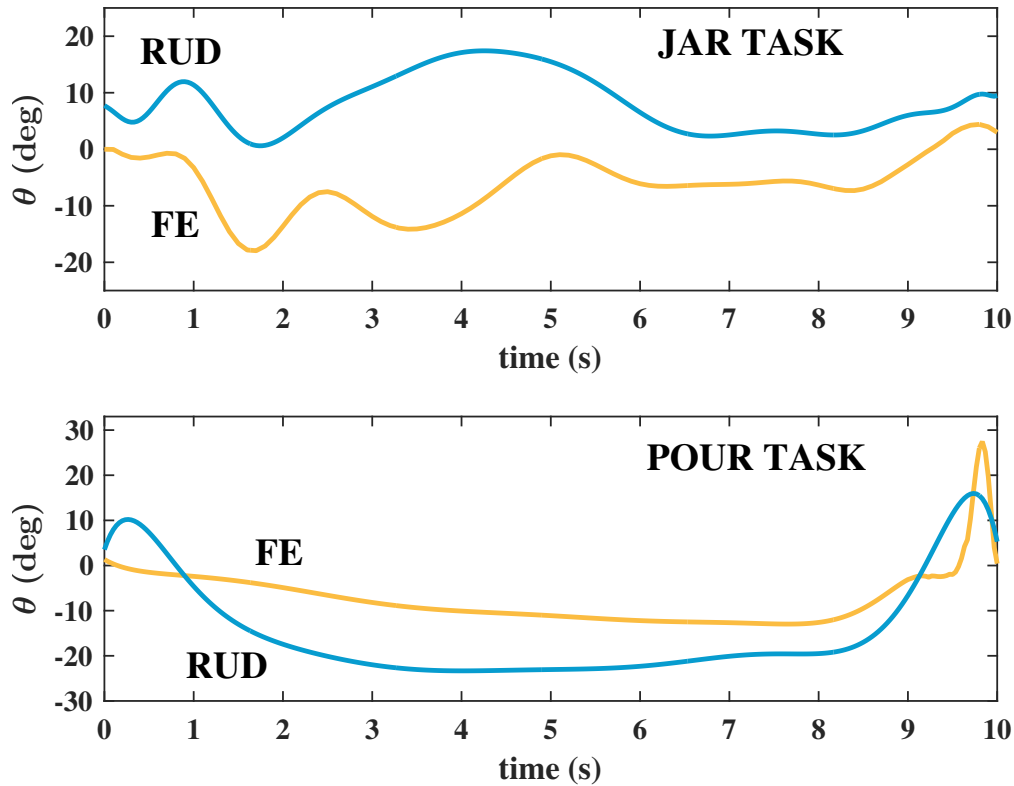


Figure 3.8: Recorded wrist angles from [131] include a jar-opening task and a carton-pouring task.

## 3.2 Fully Active Controller

Previous mechanical tremor suppression implementations use actuators that are rigid in their passive state. Therefore, the actuators must actuate to suppress tremor and to follow the desired voluntary motion. This study labels such an approach as *fully active* since the actuator is active for tremor suppression and voluntary motion tracking. In contrast, a *tremor-active* approach only actuates to suppress tremor; Section 3.3 discusses the motivation and application of tremor-active control. This section designs and simulates a fully active controller for DESA-based tremor suppression based on an adaptive notch filter approach previously implemented for pneumatic cylinder-based tremor suppression [15].

### 3.2.1 Adaptive Notch Filter

The fully active controller uses an adaptive notch filter to attenuate motion near the estimated dominant tremor frequency and its first harmonic. The adaptive notch filter takes the joint velocity as an input and outputs the estimated torque that would exactly cancel the tremor torque. The DESA controller attempts to track this desired actuator torque output  $\tau_d$  through force feedback. A dominant frequency estimator produces the estimate  $\omega_T$ , which adapts the center frequency of the adaptive notch filter. Figure 3.9 illustrates the block diagram for the fully active tremor suppression controller.

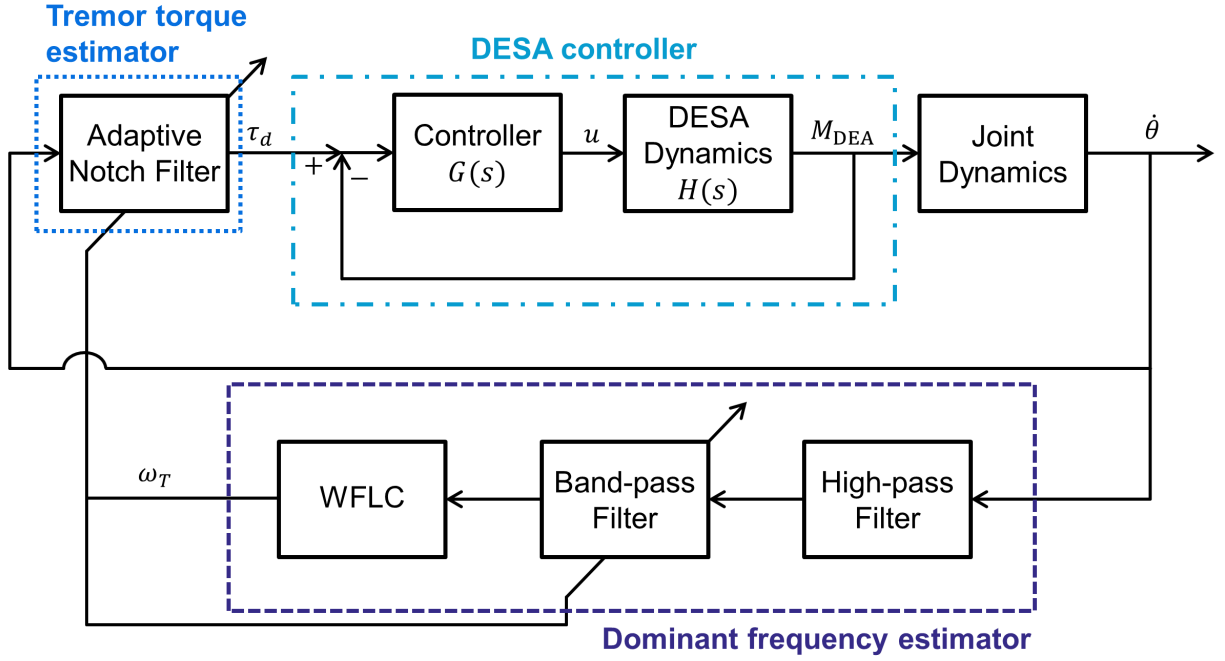


Figure 3.9: The DESA controller tracks the estimated tremor torque from the adaptive notch filter, which adapts to the estimated dominant tremor frequency.

The adaptive notch filter effectively acts as a tremor torque estimator since the output is the estimated tremor torque with opposite sign. Using superscript  $k$  to refer to the  $k^{\text{th}}$  iteration with sample time  $T_s$ , the adaptive notch filter output is the summation of contributions from the first ( $i = 1$ ) and second ( $i = 2$ ) harmonics of  $\omega_T$ :

$$\tau_d^k = \tau_{d1}^k + \tau_{d2}^k \quad (3.40)$$

$$\tau_{di}^k = \frac{1}{\frac{4}{T_s^2} + \frac{4i\zeta_i\omega_T}{T_s} + i^2\omega_T^2} \left[ \frac{2b_i}{T_s}\dot{\theta}^k - \frac{2b_i}{T_s}\dot{\theta}^{k-2} + \left(\frac{8}{T_s^2} - 2i^2\omega_T^2\right)\tau_d^{k-1} + \left(-\frac{4}{T_s^2} + \frac{4i\zeta_i\omega_T}{T_s} - i^2\omega_T^2\right)\tau_d^{k-2} \right] \quad (3.41)$$

where the parameters  $b_i$  determine the level of suppression and  $\zeta_i$  determine the width of the attenuation band [15].

The dominant frequency estimator outputs the estimate of the dominant tremor frequency given the measured velocity input. The dominant frequency estimator includes three parts: high-pass filter, band-pass filter, and WFLC filter. The high-pass filter outputs the tremor component of the measurement by attenuating frequency content in the voluntary range. The high-pass filter output  $\dot{\theta}_{hp}^k$  is

$$\begin{aligned} \dot{\theta}_{hp}^k = & \frac{1}{\frac{8}{T_s^3}\alpha_3 + \frac{4}{T_s^2}\alpha_2 + \frac{2}{T_s}\alpha_1 + \alpha_0} \left[ \left( \frac{8}{T_s^3}\beta_3 + \frac{4}{T_s^2}\beta_2 + \frac{2}{T_s}\beta_1 + \beta_0 \right) \dot{\theta}^k \right. \\ & + \left( -\frac{24}{T_s^3}\beta_3 - \frac{4}{T_s^2}\beta_2 + \frac{2}{T_s}\beta_1 + 3\beta_0 \right) \dot{\theta}^{k-1} + \left( \frac{24}{T_s^3}\beta_3 - \frac{4}{T_s^2}\beta_2 - \frac{2}{T_s}\beta_1 + 3\beta_0 \right) \dot{\theta}^{k-2} \\ & + \left( -\frac{8}{T_s^3}\beta_3 + \frac{4}{T_s^2}\beta_2 - \frac{2}{T_s}\beta_1 + \beta_0 \right) \dot{\theta}^{k-3} + \left( \frac{24}{T_s^3}\alpha_3 + \frac{4}{T_s^2}\alpha_2 - \frac{2}{T_s}\alpha_1 - 3\alpha_0 \right) \dot{\theta}_{hp}^{k-1} \\ & \left. + \left( -\frac{24}{T_s^3}\alpha_3 + \frac{4}{T_s^2}\alpha_2 + \frac{2}{T_s}\alpha_1 - 3\alpha_0 \right) \dot{\theta}_{hp}^{k-2} + \left( \frac{8}{T_s^3}\alpha_3 - \frac{4}{T_s^2}\alpha_2 + \frac{2}{T_s}\alpha_1 - \alpha_0 \right) \dot{\theta}_{hp}^{k-3} \right] \end{aligned} \quad (3.42)$$

where parameters  $\alpha_0$ ,  $\alpha_1$ ,  $\alpha_2$ ,  $\alpha_3$ ,  $\beta_0$ ,  $\beta_1$ ,  $\beta_2$ , and  $\beta_3$  shape the filter characteristics. Since the controller suppresses motion near the dominant tremor frequency, the band-pass filter amplifies the signal near  $\omega_T$  to compensate for tremor suppression [15]. The band-pass filter output  $\dot{\theta}_{bp}^k$  is

$$\begin{aligned} \dot{\theta}_{bp}^k = & \frac{1}{\frac{4}{T_s^2} + \frac{4\zeta_{bp}\omega_T}{T_s} + \omega_T^2} \left[ \frac{4\zeta_{bp}\omega_T}{T_s} \dot{\theta}_{hp}^k - \frac{4\zeta_{bp}\omega_T}{T_s} \dot{\theta}_{hp}^{k-2} + \left( \frac{8}{T_s^2} - 2\omega_T^2 \right) \dot{\theta}_{bp}^{k-1} \right. \\ & \left. + \left( -\frac{4}{T_s^2} + \frac{4\zeta_{bp}\omega_T}{T_s} + \omega_T^2 \right) \dot{\theta}_{bp}^{k-2} \right] \end{aligned} \quad (3.43)$$

where  $\zeta_{bp}$  determines filter bandwidth. The WFLC filter estimates a signal as the summation of a sinusoid with discrete frequency  $\omega_0^k$  and  $M$  harmonics of that frequency [42, 43]. The estimate  $\hat{y}^k$  of input  $y^k$  depends on the  $2M \times 1$  weight vector  $\mathbf{w}_k$  and the  $2M \times 1$  sinusoid vector  $\mathbf{x}_k$ :

$$\hat{y}^k = \mathbf{w}_k^T \mathbf{x}_k \quad (3.44)$$

where the iteration  $k$  is written as a subscript for vectors. The  $r^{\text{th}}$  element of  $\mathbf{x}_k$  is

$$\begin{aligned} x_r^k &= \sin \left( r \sum_{i=1}^k w_0^i \right) \quad \text{for } 1 \leq r \leq M \\ x_r^k &= \cos \left( (r-M) \sum_{i=1}^k w_0^i \right) \quad \text{for } M+1 \leq r \leq 2M. \end{aligned} \quad (3.45)$$

The estimate error  $e^k$  updates the dominant frequency estimate  $\omega_0^k$  and the weight vector via least squares algorithms:

$$e^k = y^k - \hat{y}^k \quad (3.46)$$

$$\omega_0^{k+1} = \omega_0^k + 2\mu_0 e^k \sum_{r=1}^M r(\omega_r^k x_{M+r}^k - \omega_{M+r}^k x_r^k) \quad (3.47)$$

$$\mathbf{w}_{k+1} = \mathbf{w}_k + 2\mu_1 \mathbf{x}_k e^k \quad (3.48)$$

where adaptation gains  $\mu_0$  and  $\mu_1$  affect the tracking ability and stability of the estimation. In the dominant frequency estimator, the WFLC filter receives input from the band-pass filter ( $y^k \equiv \hat{\theta}_{bp}^k$ )



and outputs the estimate for the dominant tremor frequency

$$\omega_T^{k+1} = \frac{\omega_0^{k+1}}{T_s} \quad (3.49)$$

that forms the adaptive element of the adaptive notch filter.

Finally, the DESA controller calculates  $u$  such that  $M_{\text{DEA}}$  tracks  $\tau_d$ . From the linearized version of  $M_{\text{DEA}}$  in Eq. (3.24), the transfer function  $H(s)$  from  $u$  to  $M_{\text{DEA}}$  is

$$H(s) \equiv \frac{M_{\text{DEA}}(s)}{u(s)} = \frac{r_o A_o \epsilon_o \epsilon_r}{d_o^2}. \quad (3.50)$$

Output torque is calculated from the measured force of the flexion ( $F_f$ ) and extension ( $F_e$ ) actuators:

$$M_{\text{DEA}} = r_0(F_e - F_f). \quad (3.51)$$

The controller  $G(s)$  produces the desired closed-loop transfer function given feedback of  $M_{\text{DEA}}$ :

$$\frac{M_{\text{DEA}}(s)}{\tau_d(s)} = \frac{G(s)H(s)}{1 + G(s)H(s)} = \frac{\omega_d^2}{s^2 + 2\zeta_d \omega_d s + \omega_d^2} \quad (3.52)$$

where  $\zeta_d$  and  $\omega_d$  define the desired controller closed-loop characteristics. Solving for  $G(s)$  produces

$$G(s) = \frac{\omega_d^2 d_o^2}{r_o A_o \epsilon_o \epsilon_r} \frac{1}{s^2 + 2\zeta_d \omega_d s}. \quad (3.53)$$

Discretization produces the control input  $u^k$  given the torque output error  $e_\tau^k$ :

$$e_\tau^k \equiv \tau_d^k - r_0(F_r^k - F_l^k) \quad (3.54)$$

$$u^k = \frac{1}{\frac{4}{T_s^2} + \frac{4\zeta_d\omega_d}{T_s}} \left[ \frac{\omega_d^2 d_o^2}{r_o A_o \epsilon_o \epsilon_r} e_\tau^k + \frac{2\omega_d^2 d_o^2}{r_o A_o \epsilon_o \epsilon_r} e_\tau^{k-1} + \frac{\omega_d^2 d_o^2}{r_o A_o \epsilon_o \epsilon_r} e_\tau^{k-2} + \frac{8\zeta_d \omega_d}{T_s^2} u^{k-1} + \left( -\frac{4}{T_s^2} + \frac{4\zeta_d \omega_d}{T_s} \right) u^{k-2} \right]. \quad (3.55)$$

Altogether, the dominant frequency estimator produces the center frequency  $\omega_T$  of the adaptive notch filter, the adaptive notch filter produces desired actuator output  $\tau_d$ , and the DESA controller produces DESA control voltage  $u$  such that the DESA torque tracks  $\tau_d$ .

### 3.2.2 Fully Active Simulations

Simulations use the same adaptive notch filter, high-pass filter, and band-pass filter parameters as [15]:  $b_1 = 3$ ,  $\zeta_1 = 0.01$ ,  $b_2 = 8$ ,  $\zeta_2 = 0.1$ ,  $\alpha_0 = 27970$ ,  $\alpha_1 = 631.5$ ,  $\alpha_2 = 68.69$ ,  $\alpha_3 = 1$ ,  $\beta_0 = 279.3$ ,  $\beta_1 = 65.18$ ,  $\beta_2 = 9.03$ ,  $\beta_3 = 1$ , and  $\zeta_{bp} = 0.025$ . The WFLC gains are  $\mu_0 = 5 \times 10^{-5}$  and  $\mu_1 = 5 \times 10^3$ . The parameters for the desired DESA controller closed-loop transfer function are  $\omega_d = 600$  and  $\zeta_d = 1$ . The controller sampling rate is  $f_s = 1000$  Hz. Appendix A.1 presents the MATLAB code for the fully active simulations.

First, Fig. 3.10 presents the simulated jar-opening task with ‘PD5’ tremor. The fully active controller produces excellent tracking of the desired motion. However, the electrical current safety limit causes current saturation ( $\Delta V$  saturation in simulations). The adaptive notch filter design does

not consider this nonlinearity, which could lead to instability. Indeed, Fig. 3.11 illustrates the same task with ‘PD4’ tremor: current saturation produces a drastic decrease in tracking performance. Figures 3.12 and 3.13 present jar-opening task simulations for all parkinsonian tremor and essential tremor datasets, respectively. Current saturation causes poor performance for ‘PD4’, ‘ET1’, and ‘ET4’ datasets. The carton-pouring task produces similar performance variation: Figures 3.14 and 3.15 demonstrate particularly poor performance for ‘PD2’, ‘PD5’, and ‘ET4’ datasets. Altogether, electrical safety limits the application of fully active control for DESA-based tremor suppression. As discussed further in Chapter 4, achievable DESA actuation levels also limit the applicability of fully active control. These limitations motivate the tremor-active approach described in the following section.

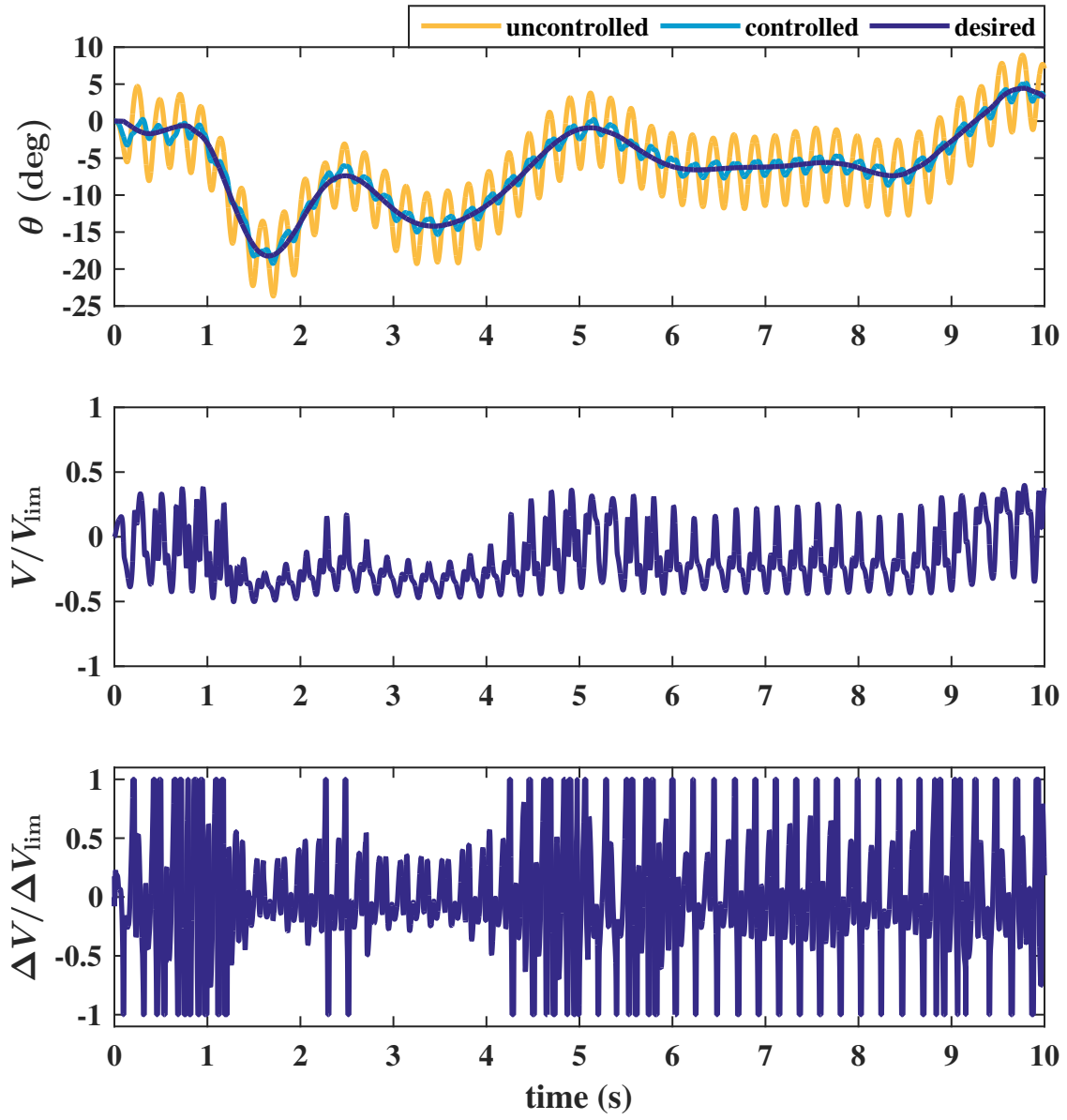


Figure 3.10: Fully active control for the jar-opening task with ‘PD5’ tremor

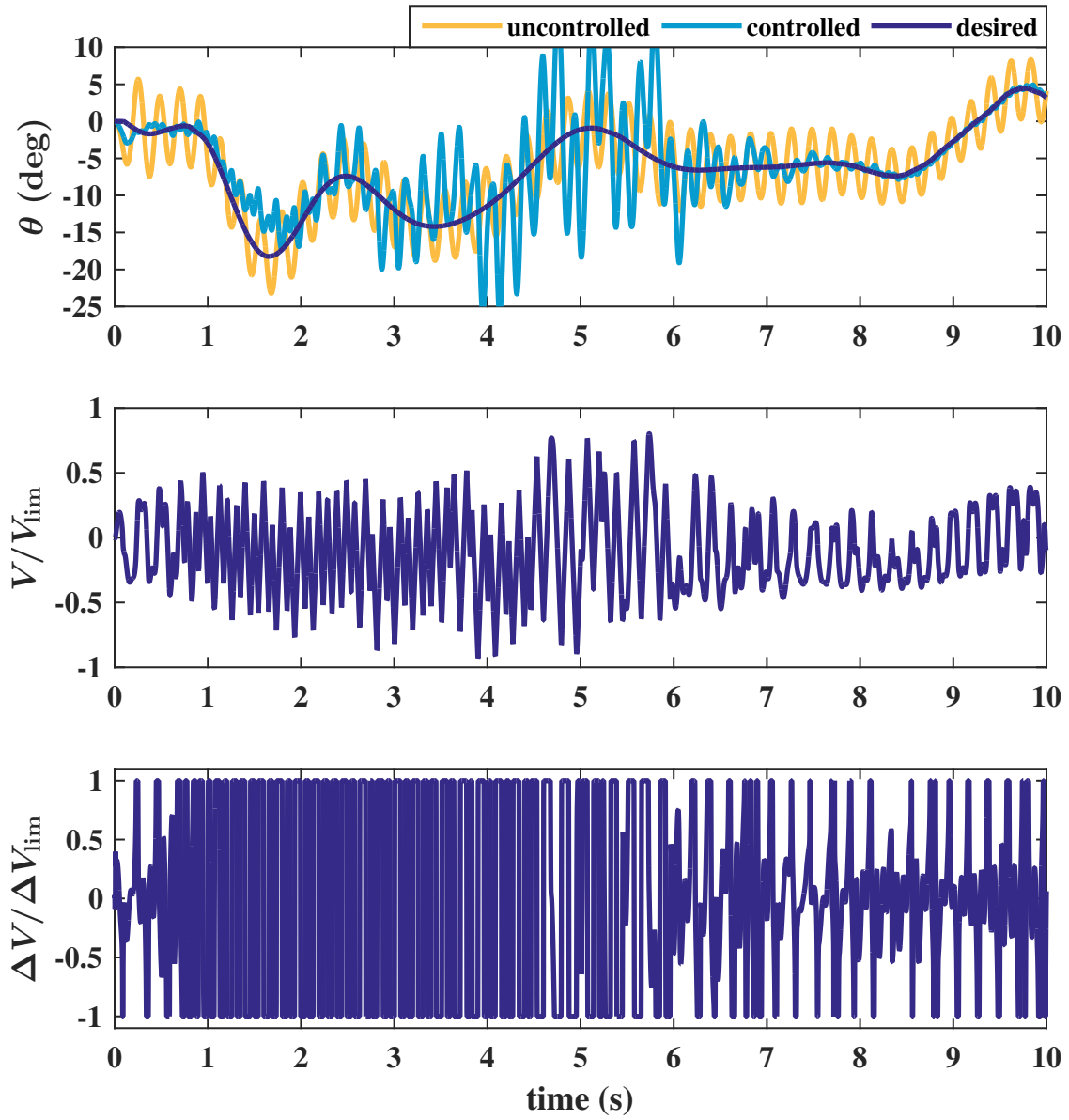


Figure 3.11: Fully active control for the jar-opening task with ‘PD4’ tremor

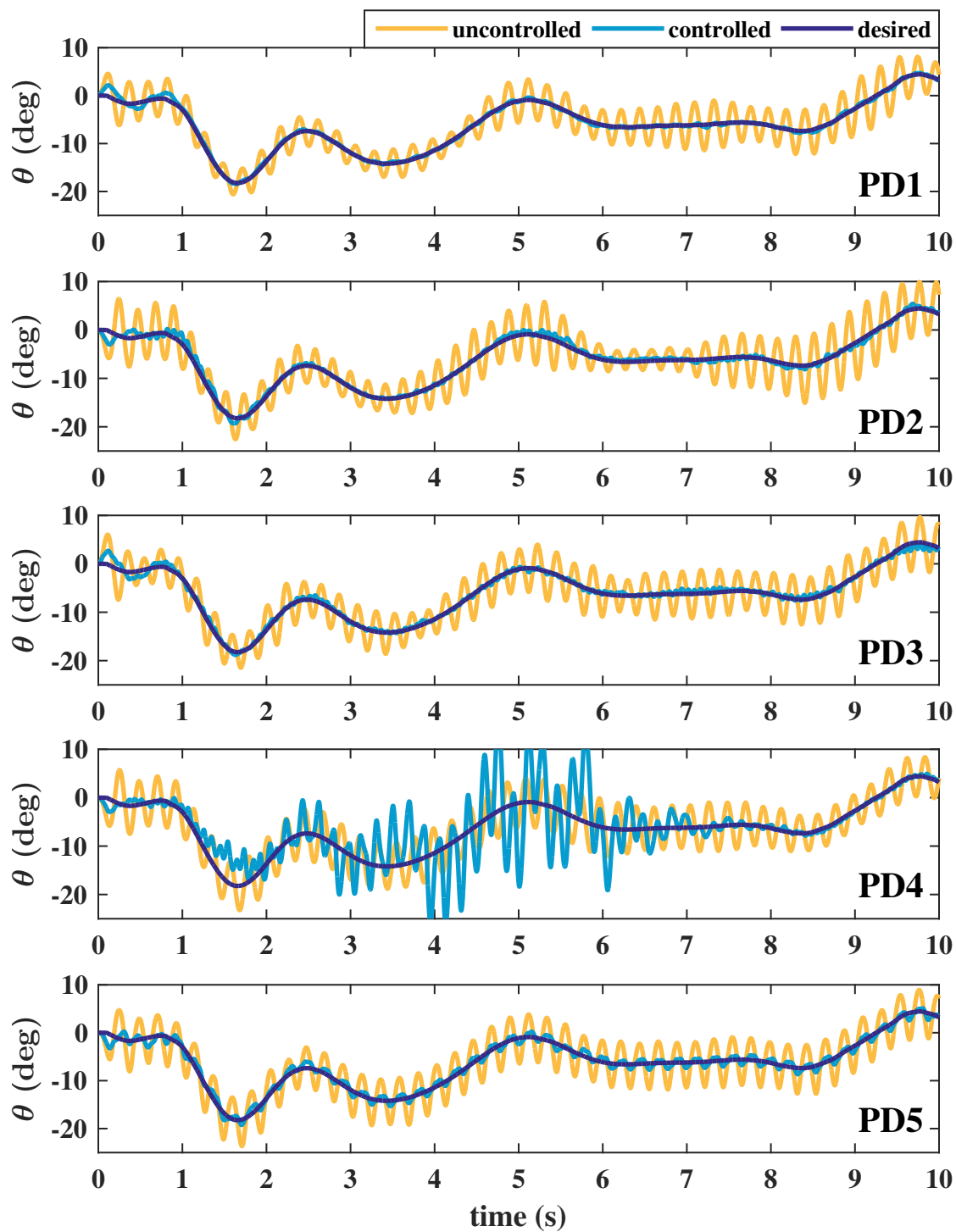


Figure 3.12: Fully active control for the jar-opening task for all parkinsonian tremor datasets

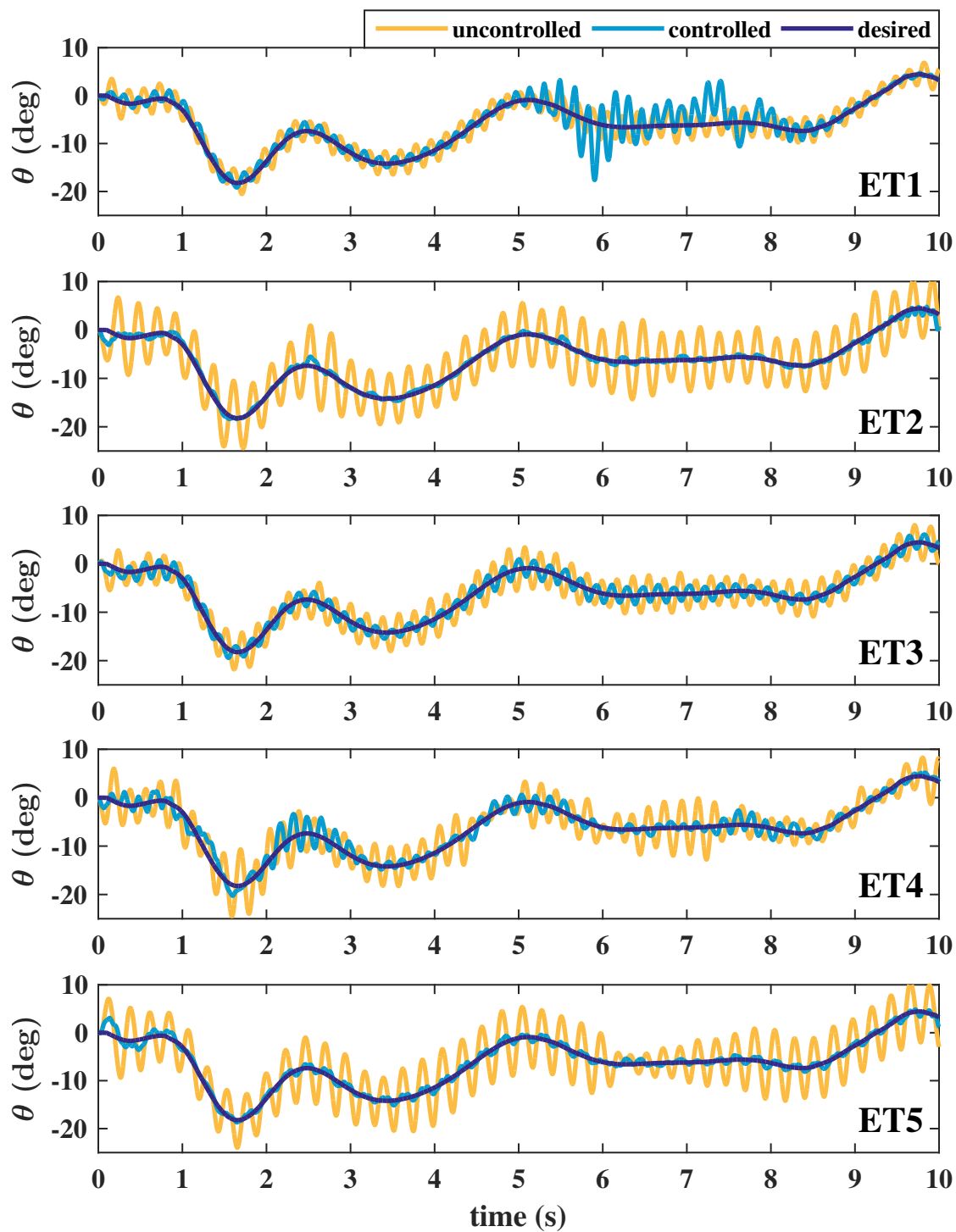


Figure 3.13: Fully active control for the jar-opening task for all essential tremor datasets

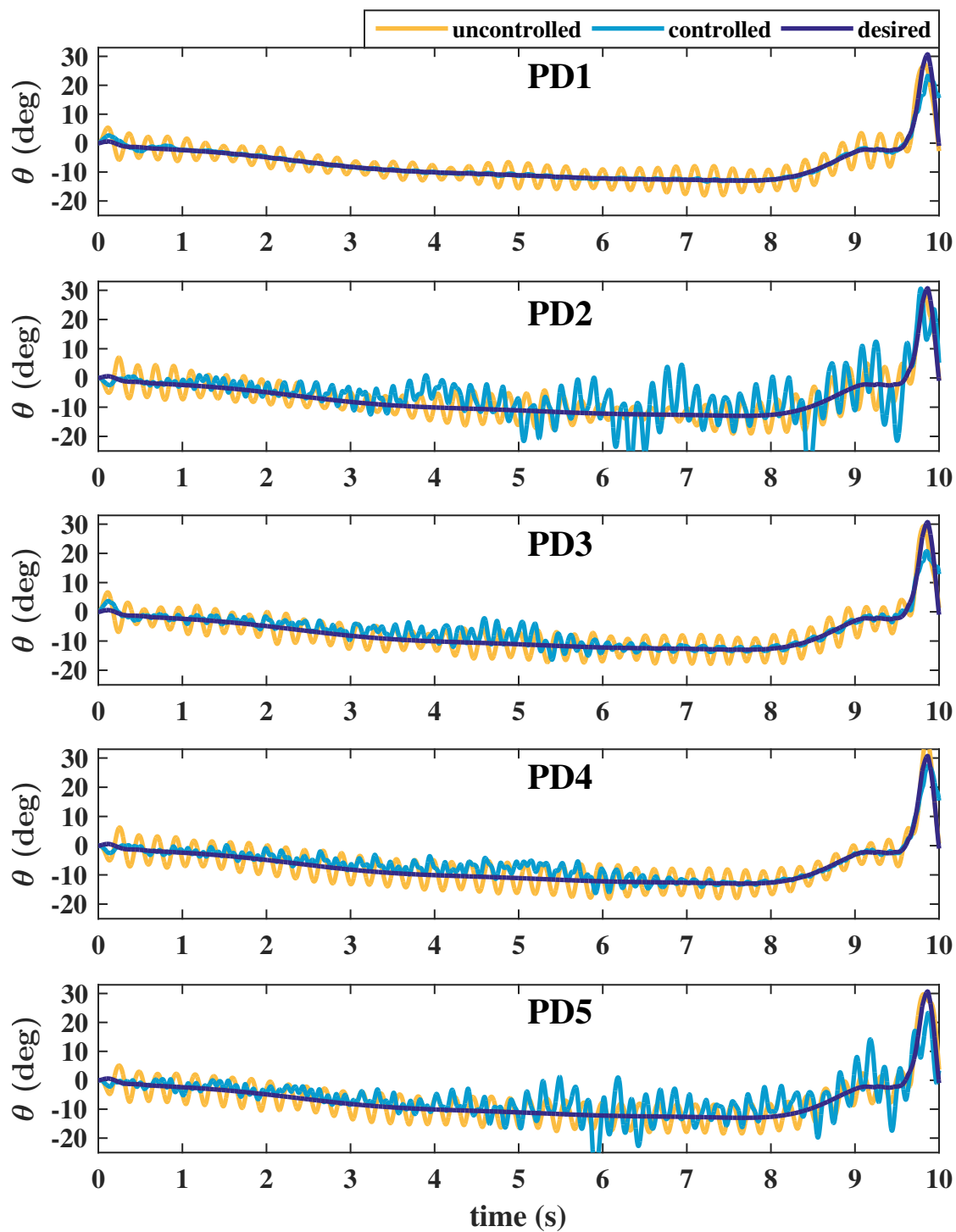


Figure 3.14: Fully active control for the carton-pouring task for all parkinsonian tremor datasets



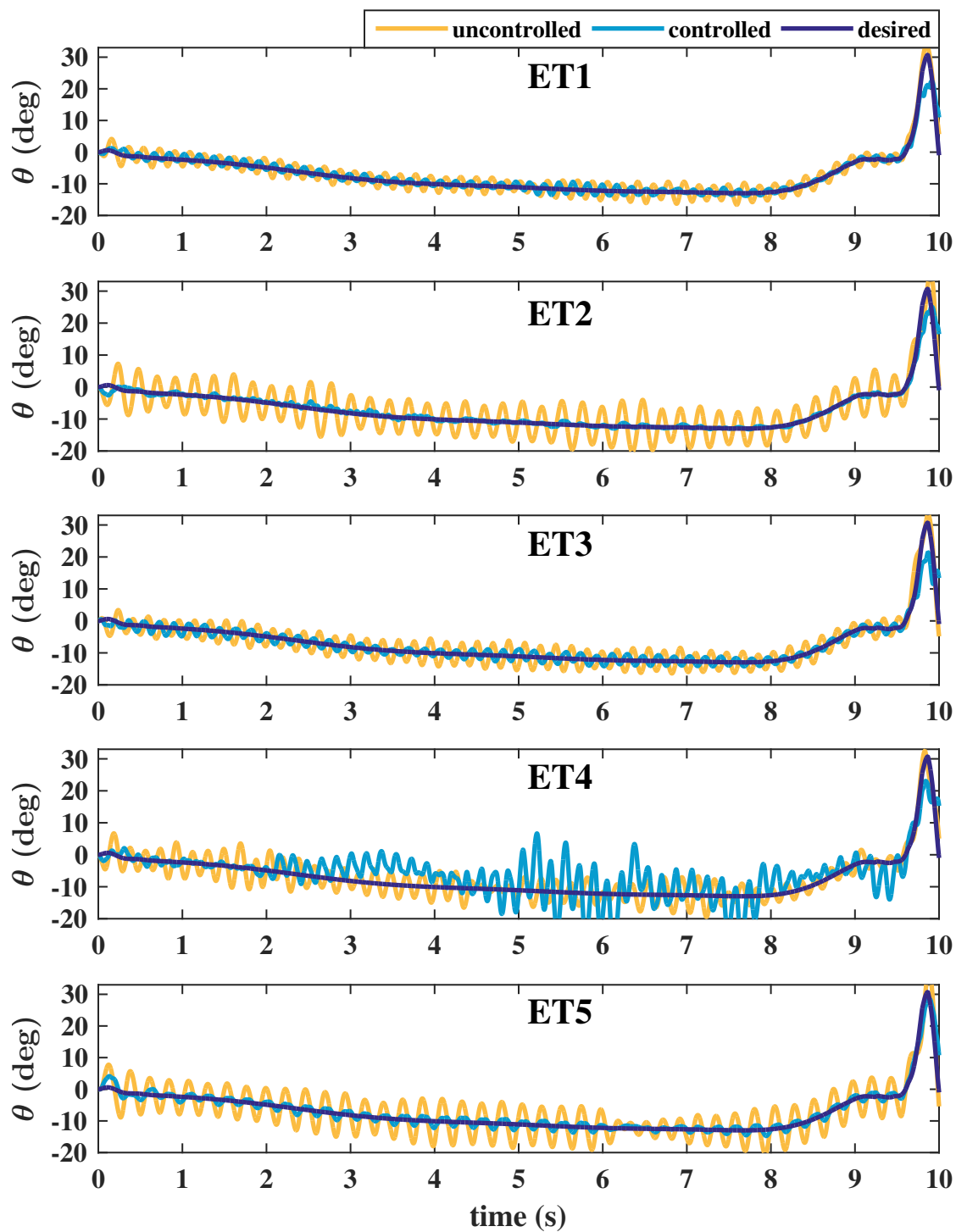


Figure 3.15: Fully active control for the carton-pouring task for all essential tremor datasets

### 3.3 Tremor-Active Controller

One of the major drawbacks of dielectric elastomers is their relatively low actuation levels compared with traditional actuators like DC motors. These low actuation levels coupled with electrical safety limits place fully active control at the extreme limits of potentially achievable DESA performance. This research proposes a *tremor-active* approach to overcome low actuation levels by exploiting the low mechanical impedance of dielectric elastomers. A tremor-active approach only actuates to suppress tremor while passively following voluntary motion. Thus, the DESA voltage need only apply a force that opposes tremor without needing to overcome the passive DESA dynamics to track voluntary motion. Figure 3.16 illustrates how tremor-active control shifts the burden of the DESA passive dynamics from the DESA to the human motor system. Unlike potential influences from a fully active controller, the material acts on the voluntary motion in a predictable manner. The human motor system can overcome the passive DESA dynamics just as it adapts to other predictable environmental changes. The patient must exert additional effort to complete a desired motion since the passive DESA dynamics add stiffness and damping to the joint that is not compensated by the actuators. This additional effort is not ideal, but may be an acceptable tradeoff to enable clinical implementations of low-profile tremor suppression. In summary, a DESA-based system will improve patient acceptance of mechanical tremor suppression by decreasing device profile and weight. Tremor-active control improves the likelihood of developing a DESA-based tremor suppression system, though at the cost of increased patient effort. The acceptable level of increased patient effort to enable tremor suppression implementation requires future research.

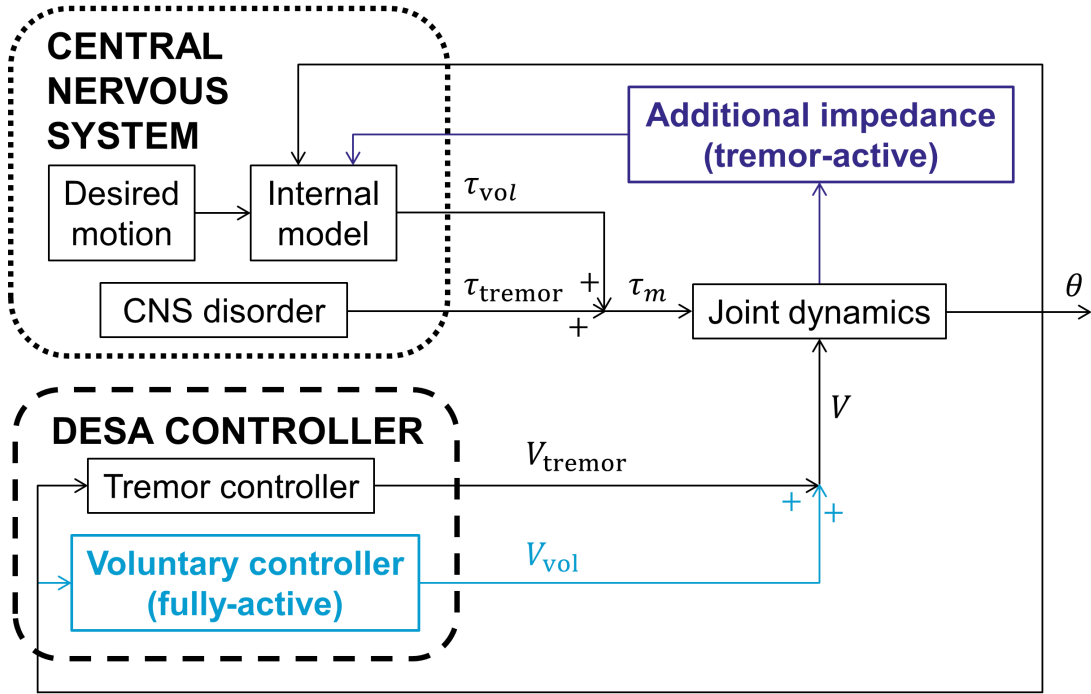


Figure 3.16: The tremor-active approach (purple, dark) shifts the burden of the passive DESA dynamics to the human motor system, significantly decreasing actuation requirements compared to the fully active approach (teal, light).

### 3.3.1 Impedance Controller with Adaptive Gain

The tremor-active approach employs impedance control for tremor suppression since it is robust, does not rely on an accurate model or system parameters, and is independent of the passive DESA dynamics. Figure 3.17 illustrates the block diagram for this control strategy. The controller only applies feedback on the tremor component of the measurement, ideally having no active effect on the voluntary motion. The controller includes an adaptive feedback gain to reduce feedback when the tremor estimate includes frequency content in the voluntary range. This adaptive gain ensures high tremor reduction given a high-quality tremor estimate and minimal controller influence when the tremor estimate is poor. In general, the impedance control method can apply feedback to any

measured state. This study assumes measurement of the velocity ( $y = \dot{\theta}$ ) to target an increase in the effective damping in the tremor frequency range. The controller may use sensors that measure other states (such as an accelerometer) by retuning the gains or estimating velocity with an observer. Self-sensing DESAs are another attractive option for physical implementation, eliminating the need for additional sensors [29].

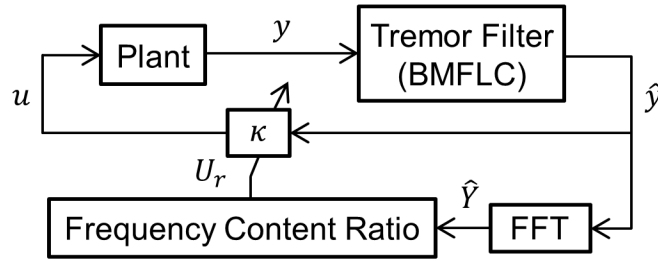


Figure 3.17: The feedback gain adapts to the quality of the tremor estimate to minimize the controller's influence on voluntary motion.

The controller uses the BMFLC filter for extracting tremor since it works without prefiltering and for multiple frequencies [66]. Also, since BMFLC is a zero-phase direct method of estimating tremor, it avoids the distortion associated with methods that subtract a voluntary estimate from the measured signal. Instead of assuming one dominant frequency like WFLC, BMFLC includes  $\beta$  equally spaced frequencies in the fixed range  $\omega_a$  to  $\omega_b$ . Having a high frequency resolution (high  $\beta$ ) allows the filter to capture all of the frequency content in that range. Since the frequency range is fixed, the dominant frequency cannot converge towards the low-frequency voluntary motion.

The  $r^{\text{th}}$  element of the sinusoid vector  $\varphi(t)$  at time  $t$  is

$$\begin{aligned}\varphi_r(t) &= \sin\left(\omega_a t + \frac{(r-1)(\omega_b - \omega_a)}{\beta}t\right) \\ &\quad \text{for } 1 \leq r \leq \beta + 1 \\ \varphi_r(t) &= \cos\left(\omega_a t + \frac{(r - \beta - 2)(\omega_b - \omega_a)}{\beta}t\right) \\ &\quad \text{for } \beta + 2 \leq r \leq 2\beta + 2.\end{aligned}\tag{3.56}$$

Given the weight vector  $\mathbf{w}$ , the estimate  $\hat{y}(t)$  of the measurement  $y(t)$  is

$$\hat{y}(t) = \mathbf{w}^T \boldsymbol{\varphi}.\tag{3.57}$$

A least mean squares algorithm updates the weights based on the error  $e(t)$  and gain  $\mu$ . A forgetting factor  $\rho$  may also be included to provide more weight to newer data [132]:

$$e(t) = y(t) - \hat{y}(t)\tag{3.58}$$

$$\mathbf{w}^T(n) = \rho \mathbf{w}^T(n-1) + 2\mu \boldsymbol{\varphi}(n)e(t).\tag{3.59}$$

Research on the BMFLC algorithm has mostly targeted suppression of physiological tremor for precision surgery [66, 67]. However, the frequency content for physiological tremor is 8–12 Hz, much higher than pathological tremor. The close proximity of the voluntary and pathological tremor frequency ranges can cause some of the voluntary frequency content to appear in the tremor estimate via the adaptive weights. The gain for the weight adaptation must be high enough to

track changes in tremor amplitude and phase. However, this fast adaptation can cause the weights to track voluntary motion, especially when voluntary and tremor frequencies are closer together. This spillover effect has limited the use of BMFLC in pathological tremor suppression systems. To compensate for the leakage of voluntary frequency content in the tremor estimate, this study develops an adaptive gain to reduce the prominence of the controller when the tremor estimate is poor.

The adaptive feedback gain depends on the quality of the tremor estimate. The power spectrum of the tremor estimate provides insight into the quality of the estimate. A sliding window FFT of the tremor estimate obtains this power spectrum information. The vector of coefficients from the FFT  $\hat{\mathbf{Y}}$  contains the power of the signal with frequency resolution  $df = f_s/N_w$ , where  $N_w$  is the length of the window. The ratio of the energy  $U_r$  in the voluntary frequency range  $U_v$  to the energy in the tremor frequency range  $U_t$  indicates the level of influence the voluntary motion has on the tremor estimate. These energies are calculated from the coefficients of the FFT, where  $\hat{Y}_n$  is the  $n^{\text{th}}$  element of  $\hat{\mathbf{Y}}$  and the dominant frequency range for the tremor is  $f_{t1}$  to  $f_{t2}$ :

$$U_r = \frac{U_v}{U_t} = \frac{\sum_{n=1}^{\lceil 1+2/df \rceil} \hat{Y}_n}{\sum_{n=\lceil 1+f_{t1}/df \rceil}^{\lceil 1+f_{t2}/df \rceil} \hat{Y}_n} \quad (3.60)$$

Thus, higher  $U_r$  corresponds with a lower-quality tremor estimate. The controller selects a feedback gain  $\kappa$  that suits the quality of the estimate to minimize influence on voluntary motion. The gain decreases exponentially with  $U_r$ :

$$\kappa = ae^{-bU_r}. \quad (3.61)$$

Proper tuning of gains  $a$  and  $b$  enables significant tremor suppression when the tremor dominates the estimate and minimal influence on voluntary motion regardless of the quality of the estimate. Finally, a moving average of the calculated gain from Eq. (3.61) smooths out the implemented gain.

### 3.3.2 Tremor-Active Simulations

Since the tremor datasets include dominant frequencies between 4 Hz and 7 Hz, the BMFLC filter applies these frequency limits for  $\omega_a$  and  $\omega_b$ , with ad hoc tuning of parameters to produce  $\mu = 1 \times 10^{-5}$  and  $\rho = 0.994$ . Similarly, tuning controller parameters produced  $a = 3 \times 10^7$  and  $b = 9$  for simulations. Appendix A.2 presents the MATLAB code for the tremor-active simulations. First, Fig. 3.18 illustrates tremor-active suppression for the jar-opening task with ‘PD4’ tremor. Unlike the fully active controller (see Fig. 3.11), the tremor-active controller produces good performance even with current saturation. Figures 3.19 and 3.20 illustrate the jar-opening task for all parkinsonian tremor and essential tremor datasets, respectively. Similarly, Figs. 3.21 and 3.22 present the carton-pouring task for all parkinsonian tremor and essential tremor datasets, respectively. The tremor-active controller provides excellent performance for all cases.

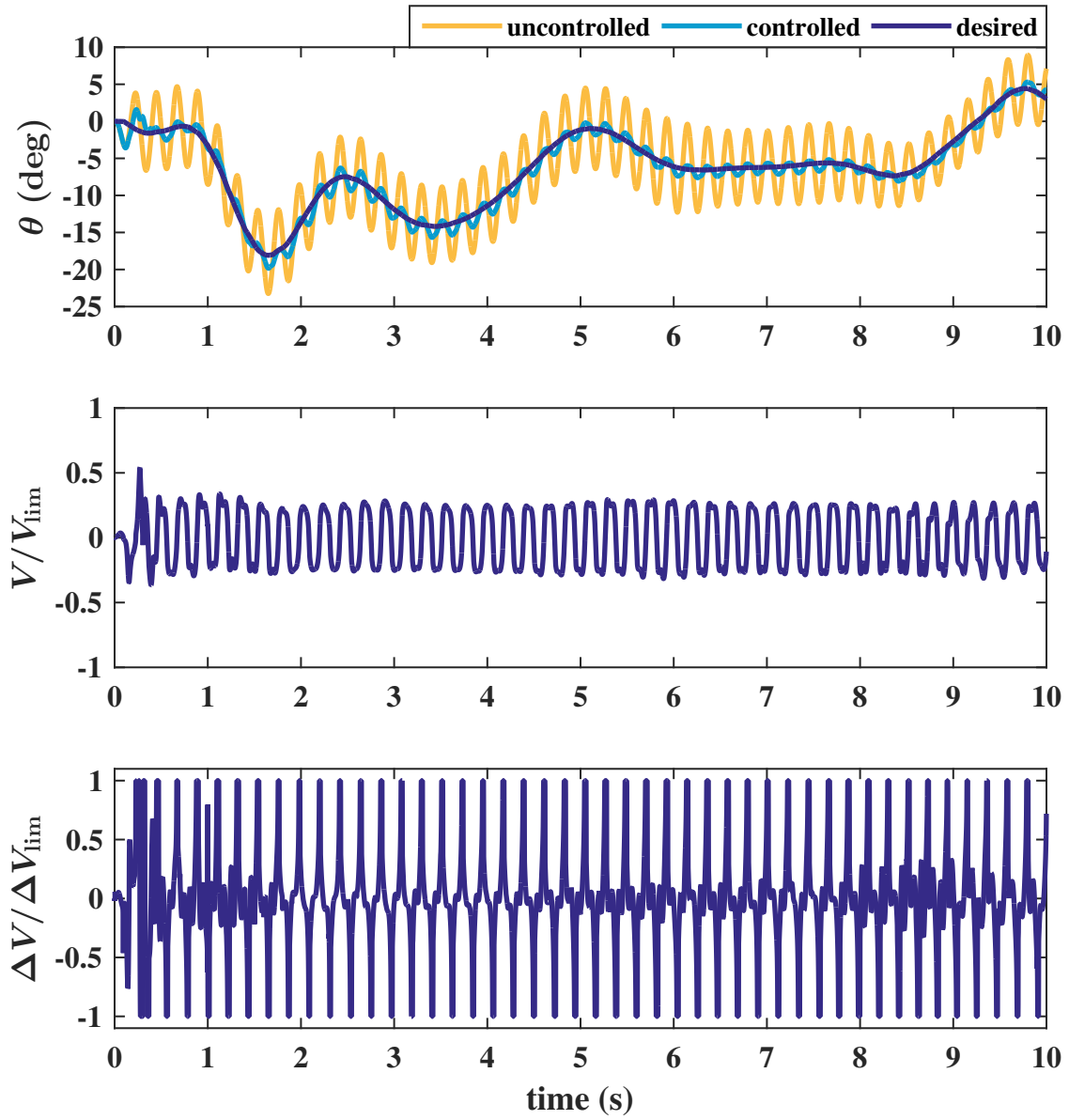


Figure 3.18: Tremor-active suppression produces effective tracking for the jar-opening task even with current saturation.



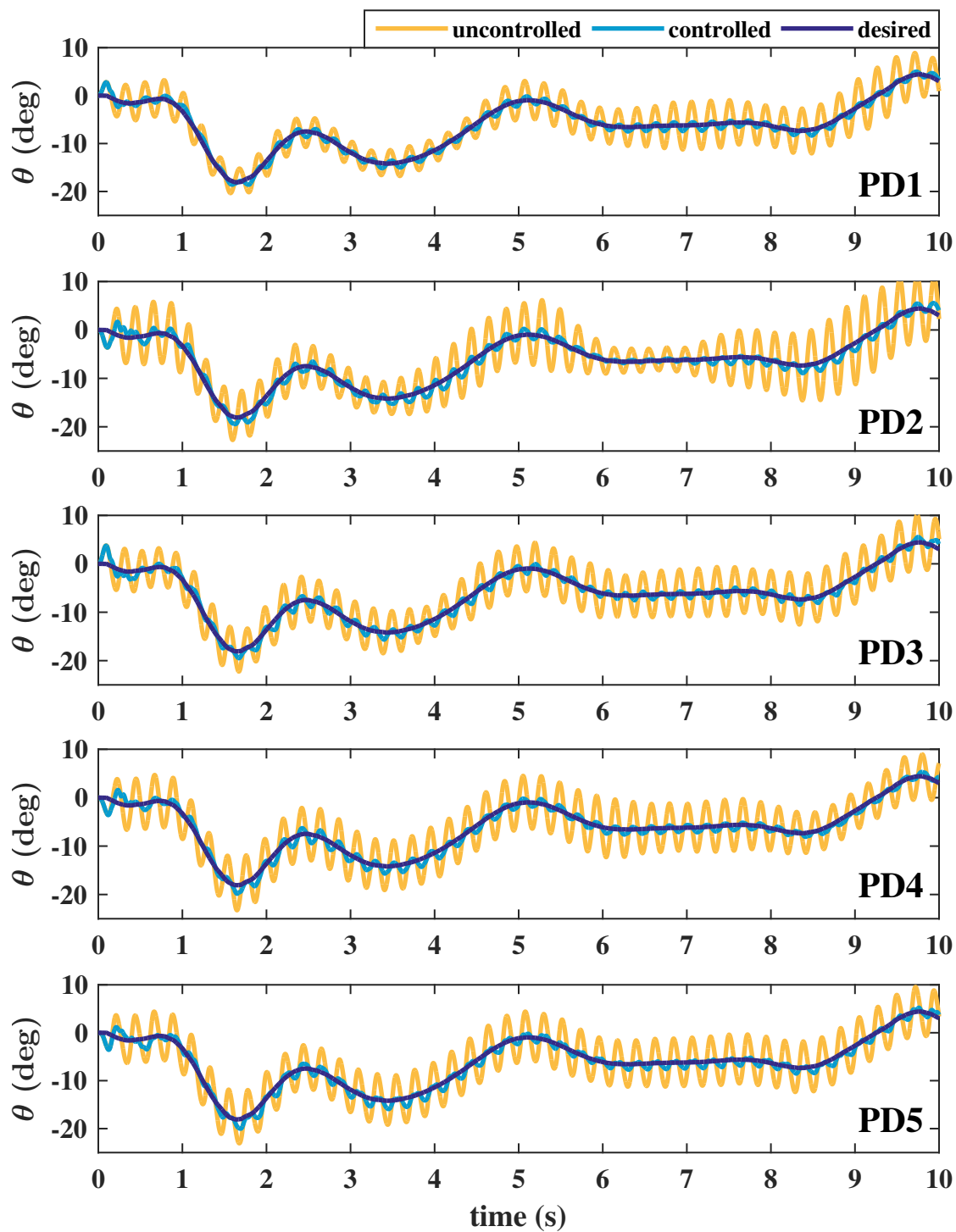


Figure 3.19: Tremor-active control for the jar-opening task for all parkinsonian tremor datasets

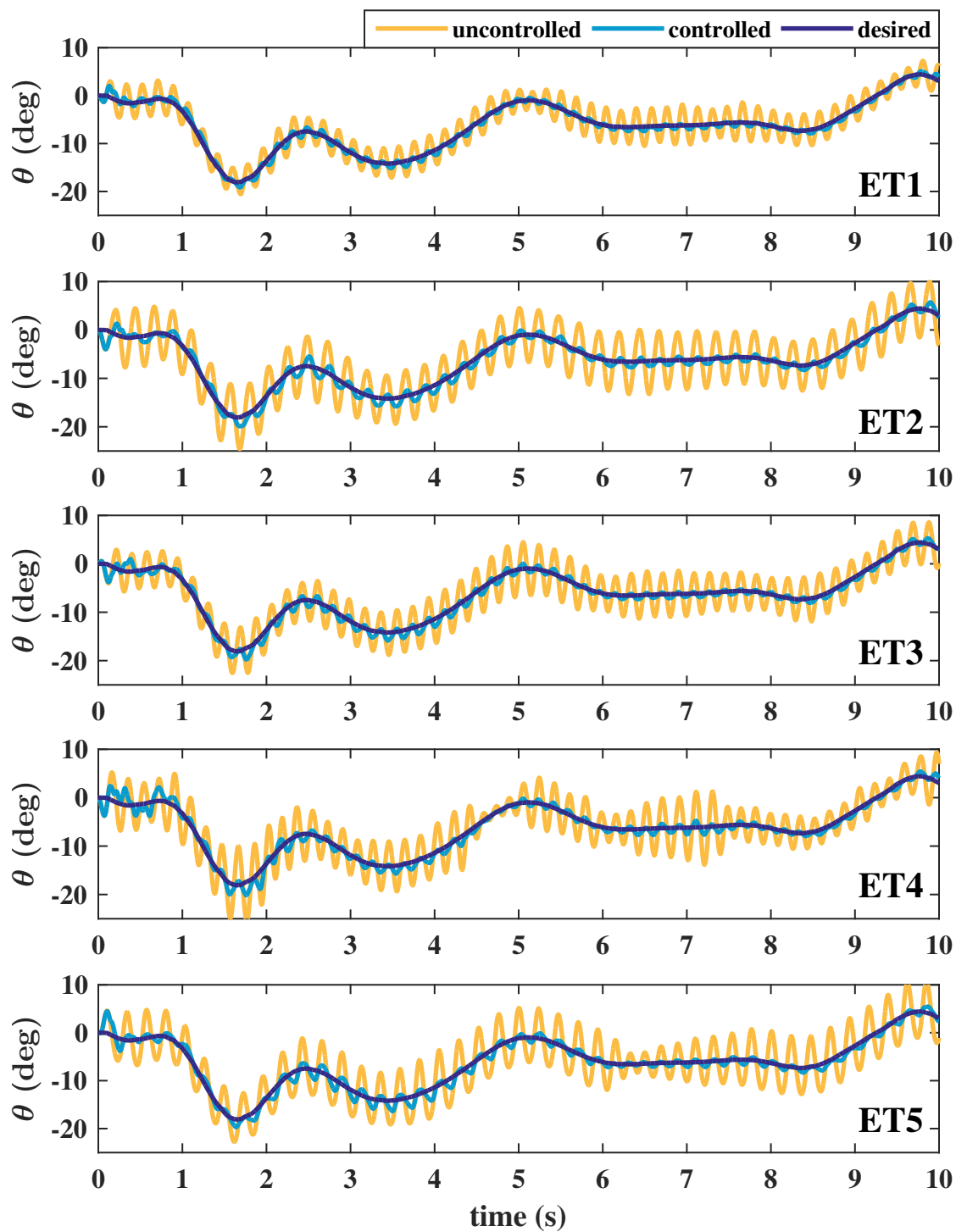


Figure 3.20: Tremor-active control for the jar-opening task for all essential tremor datasets

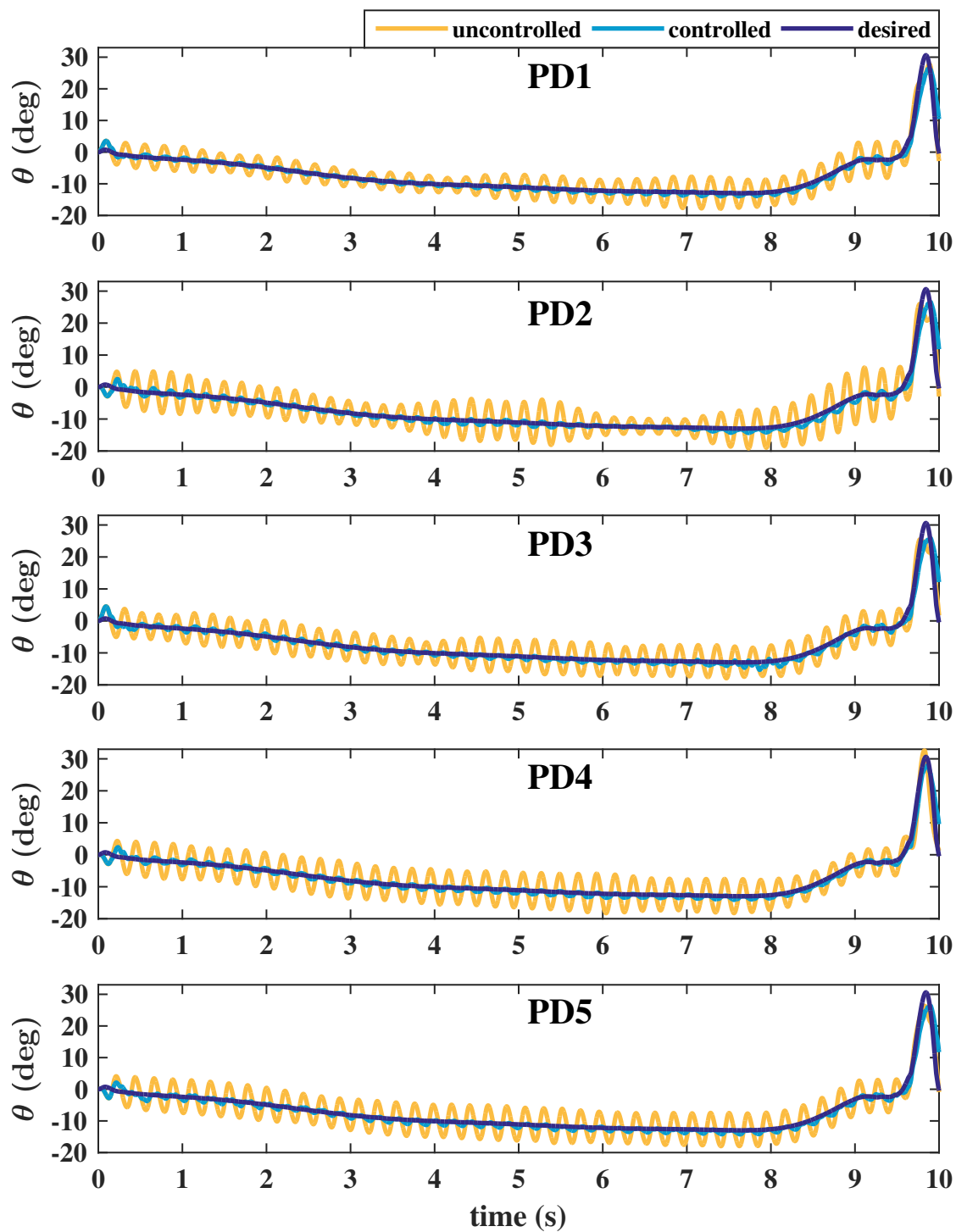


Figure 3.21: Tremor-active control for the carton-pouring task for all parkinsonian tremor datasets

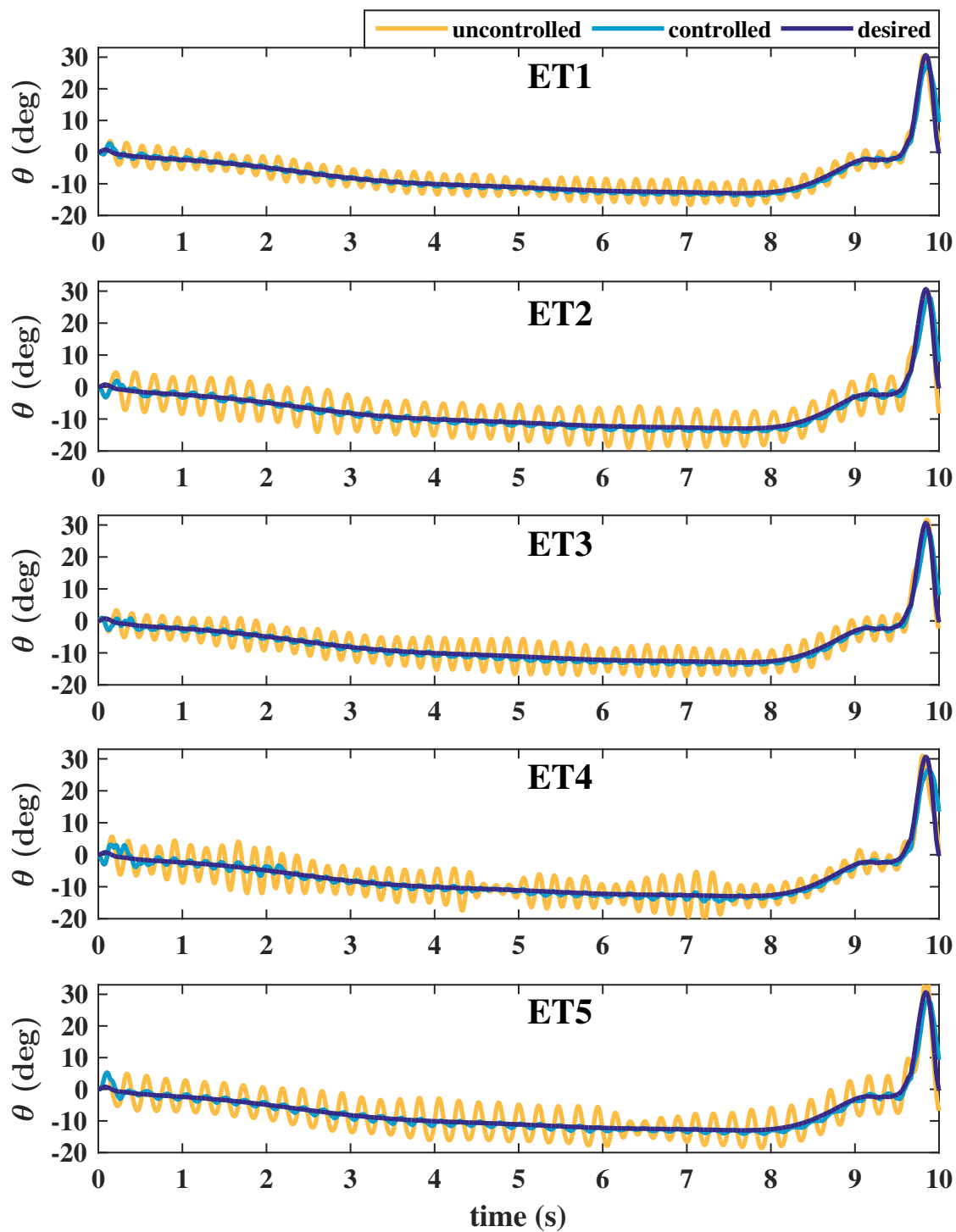


Figure 3.22: Tremor-active control for the carton-pouring task for all essential tremor datasets

Further analysis provides insight into the robustness and characteristics of the tremor-active controller. Figure 3.23 presents the closed-loop frequency response function (FRF) compared to the open-loop FRF. Each data point presents the steady-state amplitude obtained via simulation with a single sinusoidal muscular torque. The controller offers excellent amplitude reduction in the tremor frequency range with essentially no effect on the voluntary frequency range. Since joint parameters will not be exactly known in real implementations, Fig. 3.23 demonstrates the response for different joint parameters without changing controller parameters. For one case, the joint stiffness and damping are 50% higher than the average male values. For the second case, the joint stiffness and damping are 50% lower than the average female values [130]. These two variations cover the entire range of typical joint parameters for wrist flexion-extension. The controller provides nearly identical performance for all three cases.

Next, Fig. 3.24 provides insight into tremor-active controller performance based on the characteristics of the voluntary motion. Each data point represents the root-mean-square (RMS) tracking error for a simulation with sinusoidal voluntary motion and ‘ET2’ tremor, with tracking error normalized by the RMS error without control. Each simulation applies different voluntary frequency and amplitude; the figure presents voluntary amplitude normalized by the maximum value of the tremor torque. The controller produces better tracking for slower (lower frequency) and smaller amplitude movements since these motions do not spillover into the BMFLC estimation. Controller performance decreases for higher voluntary frequencies and amplitudes, but tracking error is always less than the uncontrolled system. Furthermore, the conditions of decreased performance are also the circumstances where tremor suppression is likely unnecessary—tremor is often less

prominent during large-scale motions and rapid motions approaching 2 Hz likely require far less precision than slower voluntary motions.

Finally, this research demonstrates extension of the proposed system to multiple degrees-of-freedom. Each additional degree-of-freedom may be treated separately by placing an additional agonist-antagonist actuator pair that only actuates the new degree-of-freedom. To demonstrate this concept, this study applies simultaneous tremor suppression of wrist FE and RUD. The linear, coupled equations of motion for wrist rotation are

$$J_1 \ddot{\theta}_1 + B_{11} \dot{\theta}_1 + B_{12} \dot{\theta}_2 + K_{11} \theta_1 + K_{12} \theta_2 = \tau_1 \quad (3.62)$$

$$J_2 \ddot{\theta}_2 + B_{12} \dot{\theta}_1 + B_{22} \dot{\theta}_2 + K_{12} \theta_1 + K_{22} \theta_2 = \tau_2 \quad (3.63)$$

where subscripts 1 and 2 refer to FE and RUD, respectively. Once again, this study applies average male parameters for the wrist [129, 130]. The simulations apply identical actuator pairs to both wrist angles, retuning the RUD gain to  $a_{\text{RUD}} = a_{\text{FE}}/2$ . Figure 3.25 presents simulations for the jar-opening task with ‘ET3’ and ‘ET4’ tremor in wrist FE and RUD, respectively, and the carton-pouring task with ‘PD3’ and ‘ET4’ tremor in wrist FE and RUD, respectively. These simulations demonstrate good performance even with joint coupling. Altogether, the tremor-active controller provides robust tremor suppression about a single joint and separate application to multiple joints enables scaling for global tremor suppression.

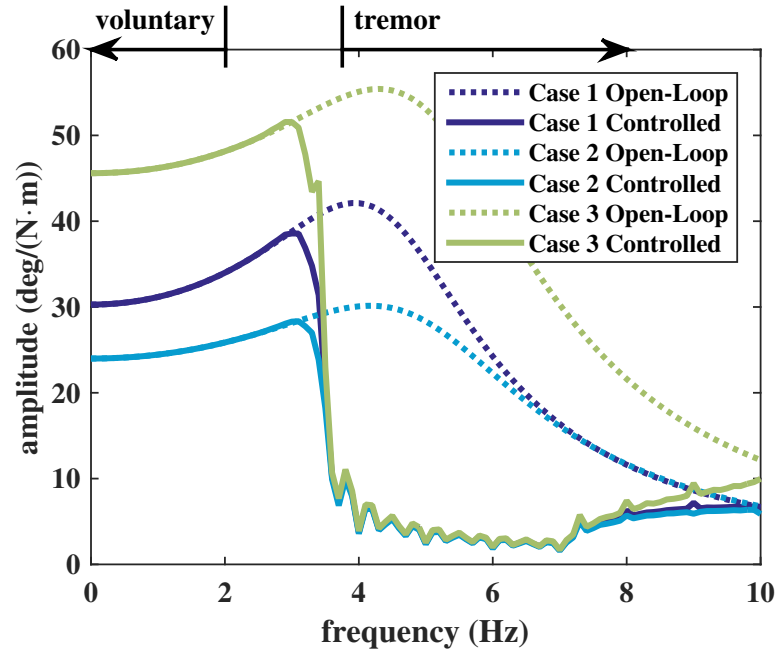


Figure 3.23: Frequency response function of the tremor-active controller (Case 1 = known parameters; Case 2 = high  $B$ ,  $K$ ; Case 3 = low  $B$ ,  $K$ )

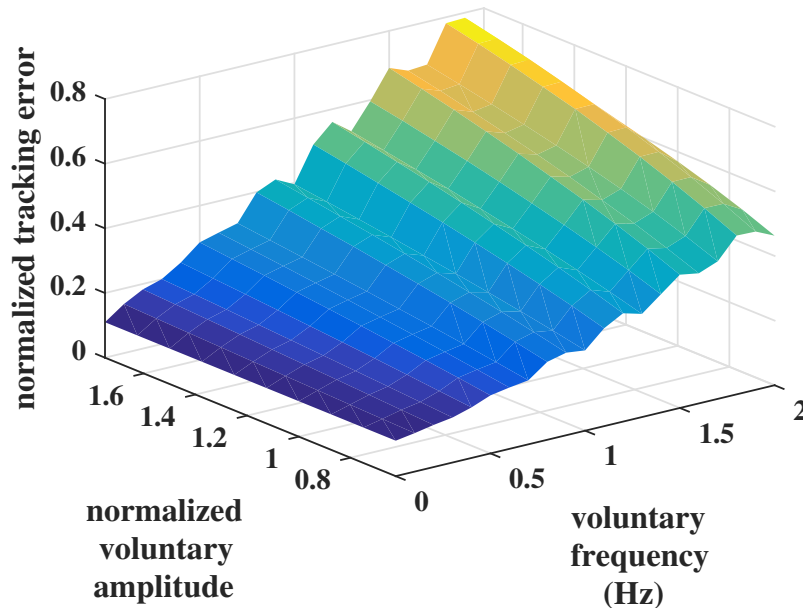


Figure 3.24: The tremor suppression system has diminishing effectiveness as the voluntary motion amplitude and frequency increase, but the controller never increases the tracking error above the open-loop case.

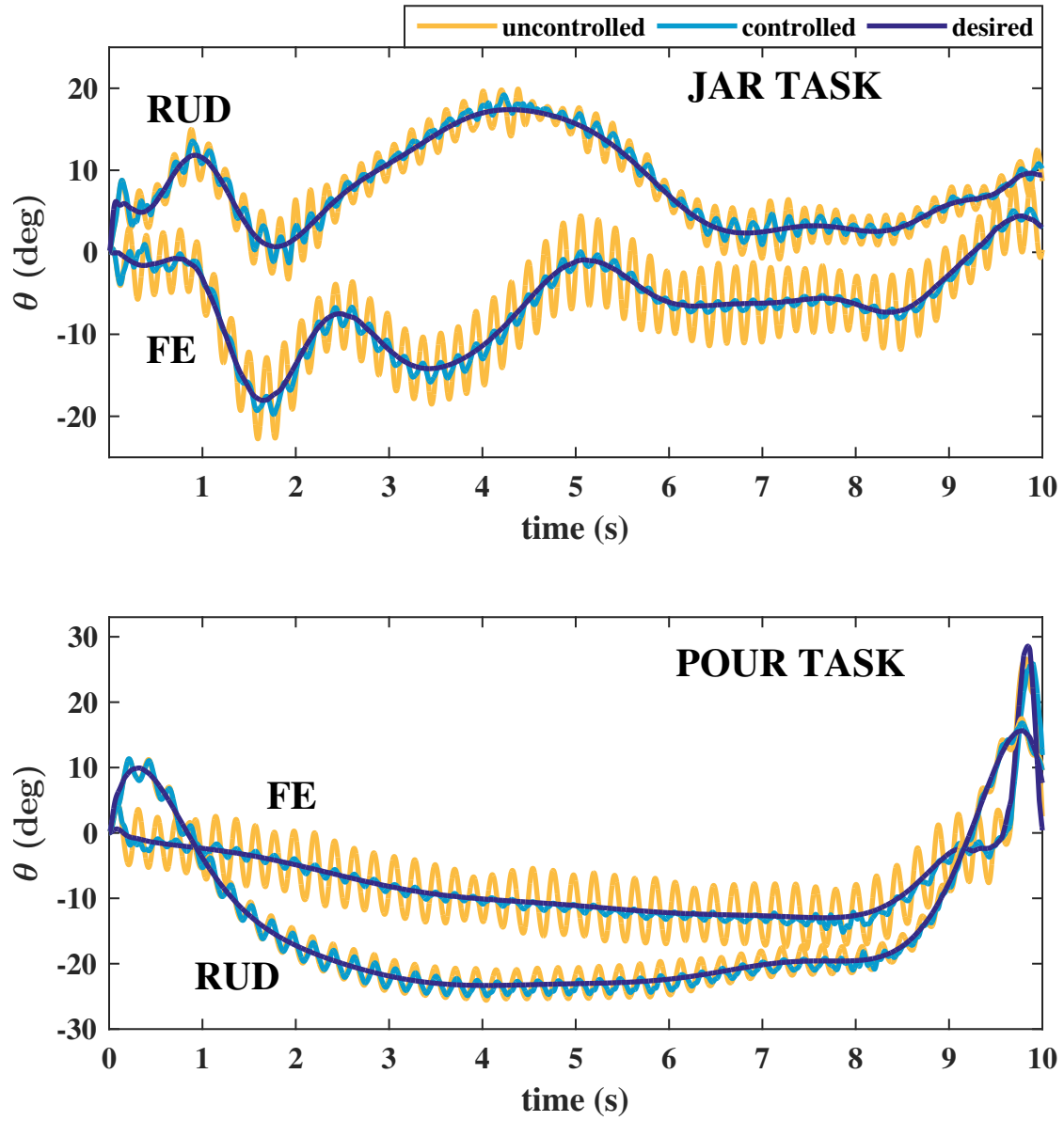


Figure 3.25: Application of the DESA system to each degree-of-freedom results in simultaneous suppression of tremor in FE and RUD.



## **CHAPTER 4**

### **DESA IMPLEMENTATION OUTLOOK**

Chapter 3 simulations provide numerical evidence of the potential effectiveness of DESA-based tremor suppression. These simulations use relatively optimistic DESA parameters: most DESA manufacturing approaches in the literature cannot produce stacks with hundreds of layers. Furthermore, approaches that can achieve hundreds of layers are not yet commercialized and require expensive equipment and specialized techniques [73,97]. To provide experimental validation of numerical tremor suppression results, this dissertation develops a scaled experimental system with folded DESAs manufactured by hand, presented in Section 4.1. Then, Section 4.2 quantifies the necessary DESA parameters to enable clinical implementations and evaluates the potential of existing manufacturing techniques to meet these parameter requirements. Research in this chapter is published in [133,134].

#### **4.1 Experiments**

Benchtop experiments physically validate tremor-active suppression using DESAs. The DESAs require layer thickness on the order of tens of microns to produce force levels required for wrist tremor suppression. Stiffness limitations require DESA length of at least a few centimeters, re-

quiring thousands of layers. Manufacturing methods that may achieve these requirements use expensive and specialized equipment; these resources were not available for this research. Since DESAs have not yet reached commercial availability, this study evaluates cost-efficient, easily-manufactured DESAs with lower actuation levels. These lower actuation levels require experimental evaluation of a scaled system: a cantilever beam represents the human joint, with muscular actuation implemented via piezoelectric material.

#### **4.1.1 DESA Manufacturing**

The folding manufacturing approach enables low-cost DESA manufacturing and does not require specialized techniques [86, 87]. Manufacturing by folding includes three general steps: mould-casting, electrode application, and folding. Figure 4.1 illustrates these manufacturing steps. Following [87], the elastomer is a three-part silicone (TC-5005 A/B-C) that cures for 24 hours at room temperature. Mixing Part A and Part B starts the curing process. Part C is a plasticizer that reduces the elastomer stiffness and may compose up to 50% of the mixture weight. High Part C concentration can produce sticky elastomers, which complicates folding; this study uses approximately 40% Part C concentration to achieve slightly sticky elastomers that help electrode application without prohibiting manual folding. After mixing, a syringe pulls air from the flask to remove air bubbles before pouring into a rectangular mould with length 89 cm, width 1.5 cm, and depth 1 mm—the mould also includes a 0.5 mm-depth channel as an attempt to achieve greater actuation, but the re-

sulting elastomers were too fragile to fold. The required high layer thickness is one of the primary drawbacks to manufacturing by folding.

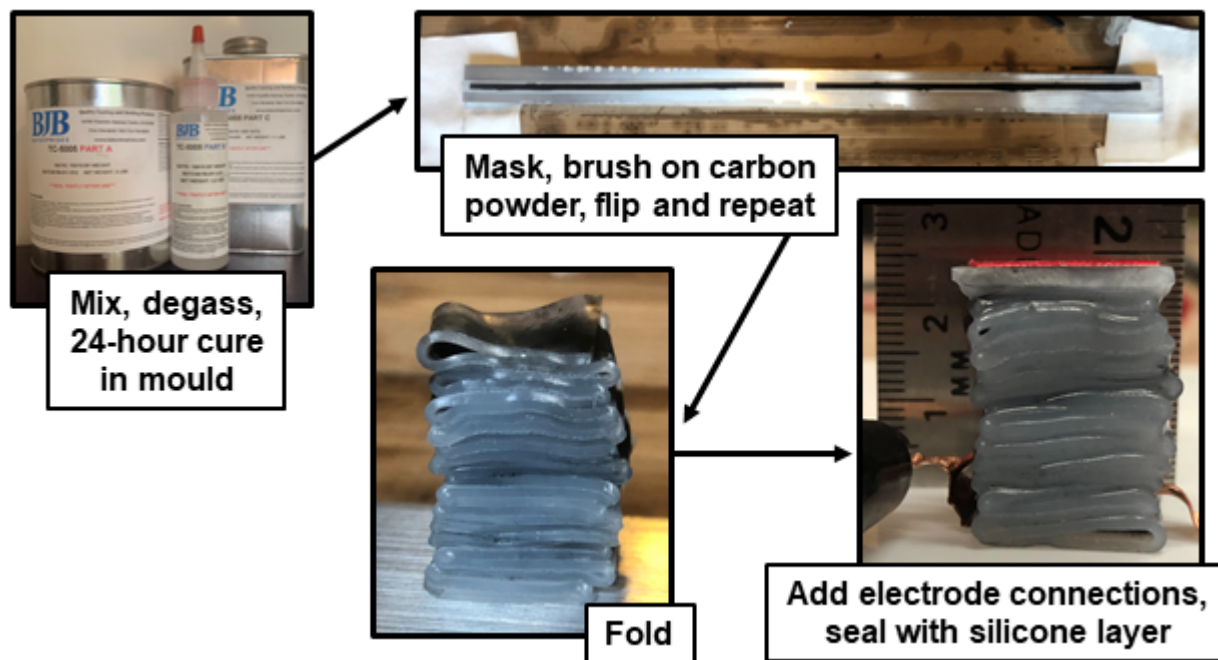


Figure 4.1: Manufacturing DESAs by folding includes mixing, degassing, curing in a mould, masking strip and brushing on carbon powder electrodes, folding, and sealing.

The elastomer is ready for electrode application after curing at room temperature for 24 hours. The cured elastomer is removed from the mould and placed on a flat surface (in this case, the backside of the mould). The DESAs require passive regions (no electrodes) along the edges to prevent dielectric breakdown: masking tape applied to each edge prevents electrode application in these regions. Previous folded DESAs use carbon black powder mixed in a one-part silicone paste (CAF 4) [87]. This approach included several drawbacks in preliminary manufacturing: the paste is very difficult to spread, cures too quickly, and produces very thick electrode layers. These drawbacks motivate the advantage of using a slightly sticky elastomer: the stickiness enables

application of loose carbon powder as the electrode material. Carbon powder was brushed onto the masked elastomer and loose powder that did not stick was removed via suction. After application to one side, the elastomer is flipped and the process repeated, producing a long, rectangular elastomer with compliant electrodes on both sides.

Finally, folding the DEA produces a DESA with continuous electrodes that enable straightforward electrical connections. The rectangular strip is folded by hand to produce a square cross section with width of approximately 1.5 cm. Another drawback for manufacturing by folding is the lack of precision in folding by hand. Folding the entire length to produce a single actuator proved difficult. Realized DESAs used half the strip length; thus, each manufactured strip produced two DESAs. Small copper tape inserted between the final layers provide electrical leads for the DESA. Finally, a thin layer of the TC-5005 mixture is poured over the folded elastomer to seal the DESA, providing electrical insulation and containment of the carbon powder while preventing unfolding of the actuator.

#### **4.1.2 Scaled Tremor Suppression**

This study evaluates tremor suppression on a scaled system due to the low actuation capabilities of the folded DESAs. Figure 4.2 illustrates the experimental setup, which includes a cantilever beam clamped at the base in a repurposed frame. The frame enables adjusting of the two DESAs to align with the beam tip. Two surface-mounted piezoelectric patches on the beam represent the

muscular torque, providing actuation to simulate tremor and voluntary actuation via a Trek Model 2205 High-Voltage Power Amplifier. A laser vibrometer measures the beam tip displacement.

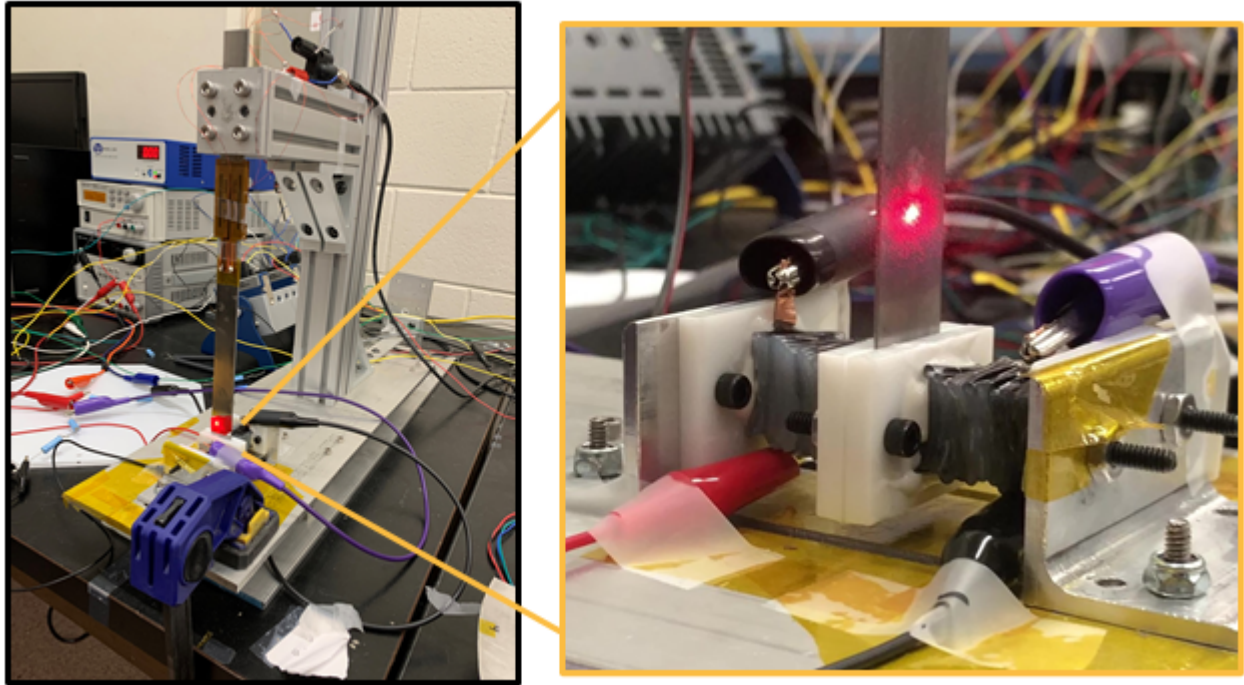


Figure 4.2: Experimental setup for scaled DESA-based tremor suppression

The controller is implemented on a National Instruments cRIO-9035 using the Real-Time Module in scan engine mode. The controller receives the displacement measurement from the vibrometer and outputs the control voltages for each DESA. Pico HVP5P DC/DC high-voltage converters proportionally scale the control voltages, producing DESA voltages up to 5 kV with maximum current of 1 mA. All non-controller data input and output was executed using MATLAB's Data Acquisition Toolbox with a National Instruments cDAQ-9188 chassis. This MATLAB script includes the voltage output for piezoelectric actuation and measurements of beam displacement and DESA voltages. Figure 4.3 illustrates a block diagram of the signals in the experimental setup.

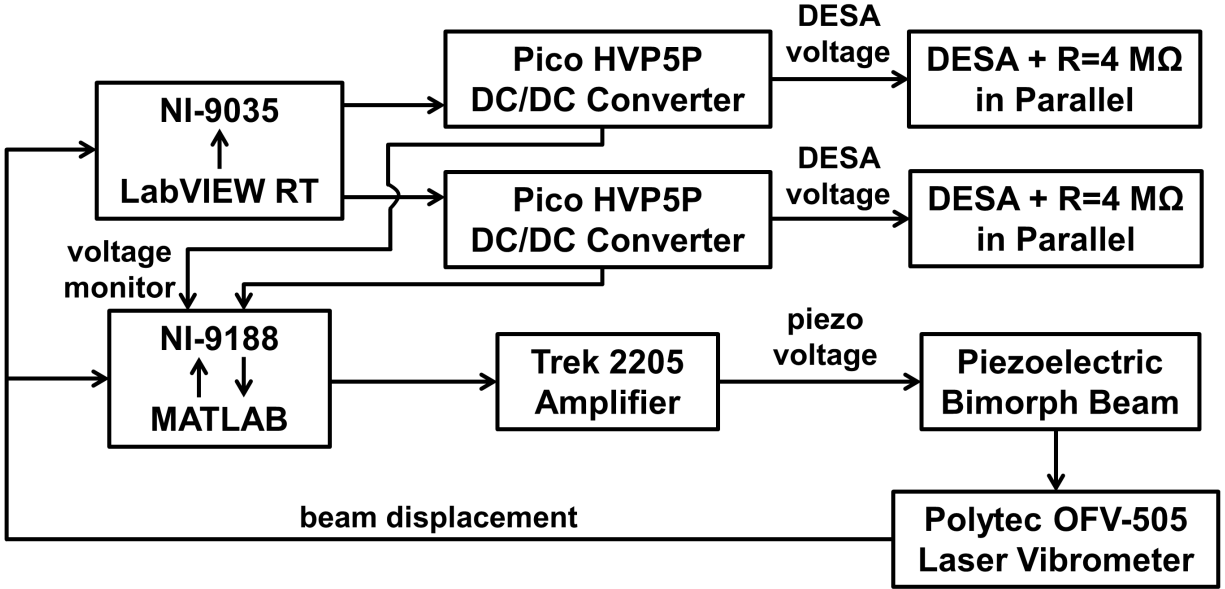


Figure 4.3: Signal block diagram for scaled DESA-based tremor suppression

Experiments implement tremor data from [9] and voluntary motion from [131] as described in Chapter 3. Each test implements a superposed piezoelectric voltage that includes voluntary and tremor components. The controller implements tremor-active control described in Section 3.3. However, the experimental controller provides displacement feedback rather than velocity feedback due to the difficulty of reliably measuring the relatively low velocities in this system. Experiments implement three different feedback gains to demonstrate the effect of the gain on performance.

First, Fig. 4.4 presents the experimental time series for the jar-opening task with ‘PD1’ tremor. The displacement time series includes two tests: one test without tremor suppression (uncontrolled) and one test with tremor suppression (controlled). Post-processing of the time series extracts the voluntary motion (low-pass filtering with MATLAB’s *filtfilt*). As demonstrated in the figure, the

controller reduces the amplitude of voluntary motion. This amplitude reduction reflects the higher power of voluntary motion content in the displacement measurement compared to measuring velocity in previous simulations. The BMFLC filter cannot completely remove the voluntary content; thus, the controller effectively increases stiffness in the voluntary range. However, the active approach still offers improvement over passive approaches since tremor suppression is greater than voluntary motion suppression. Figures 4.5 and 4.6 present experimental results for the jar-opening task for all parinsonian tremor and essential tremor datasets, respectively. The controller reduces tremor for all cases, but with varying effectiveness.

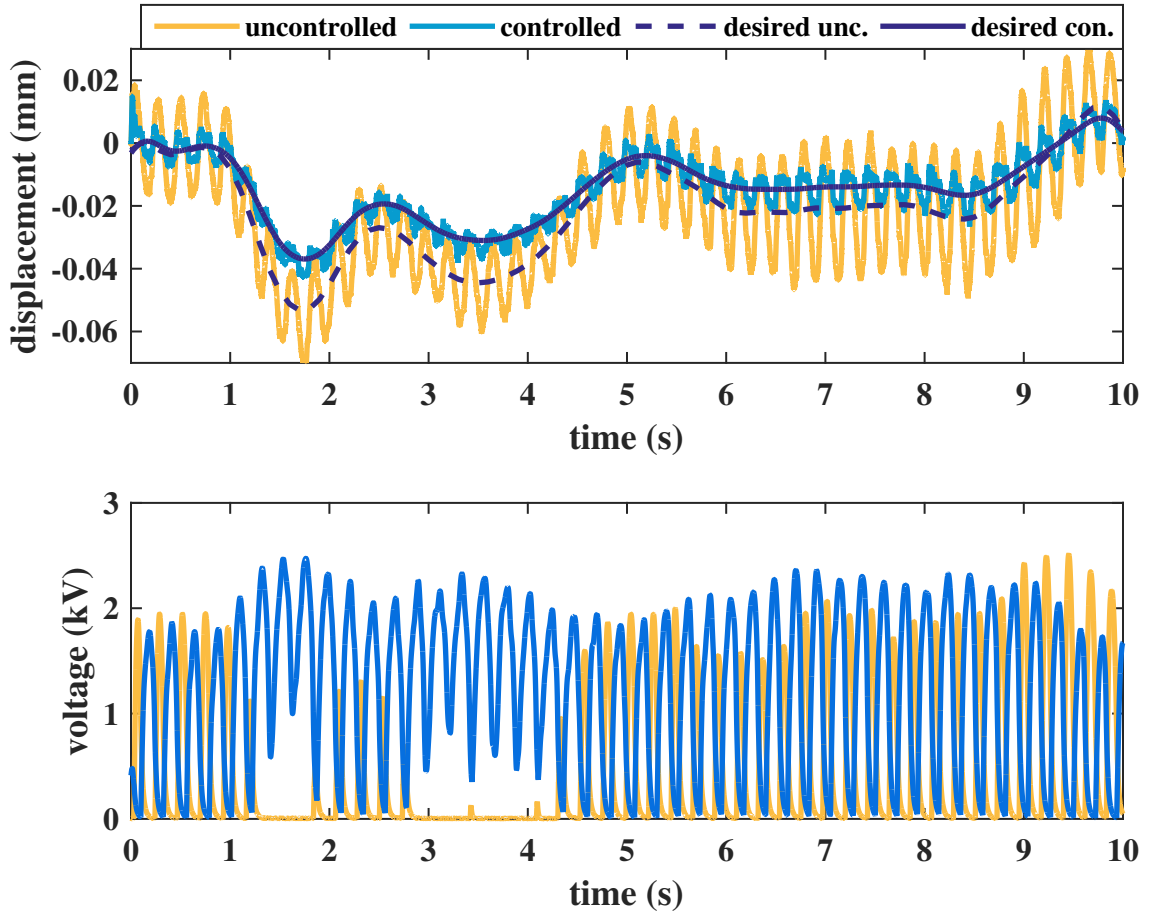


Figure 4.4: Experimental time series for jar-opening task with PD1 tremor.

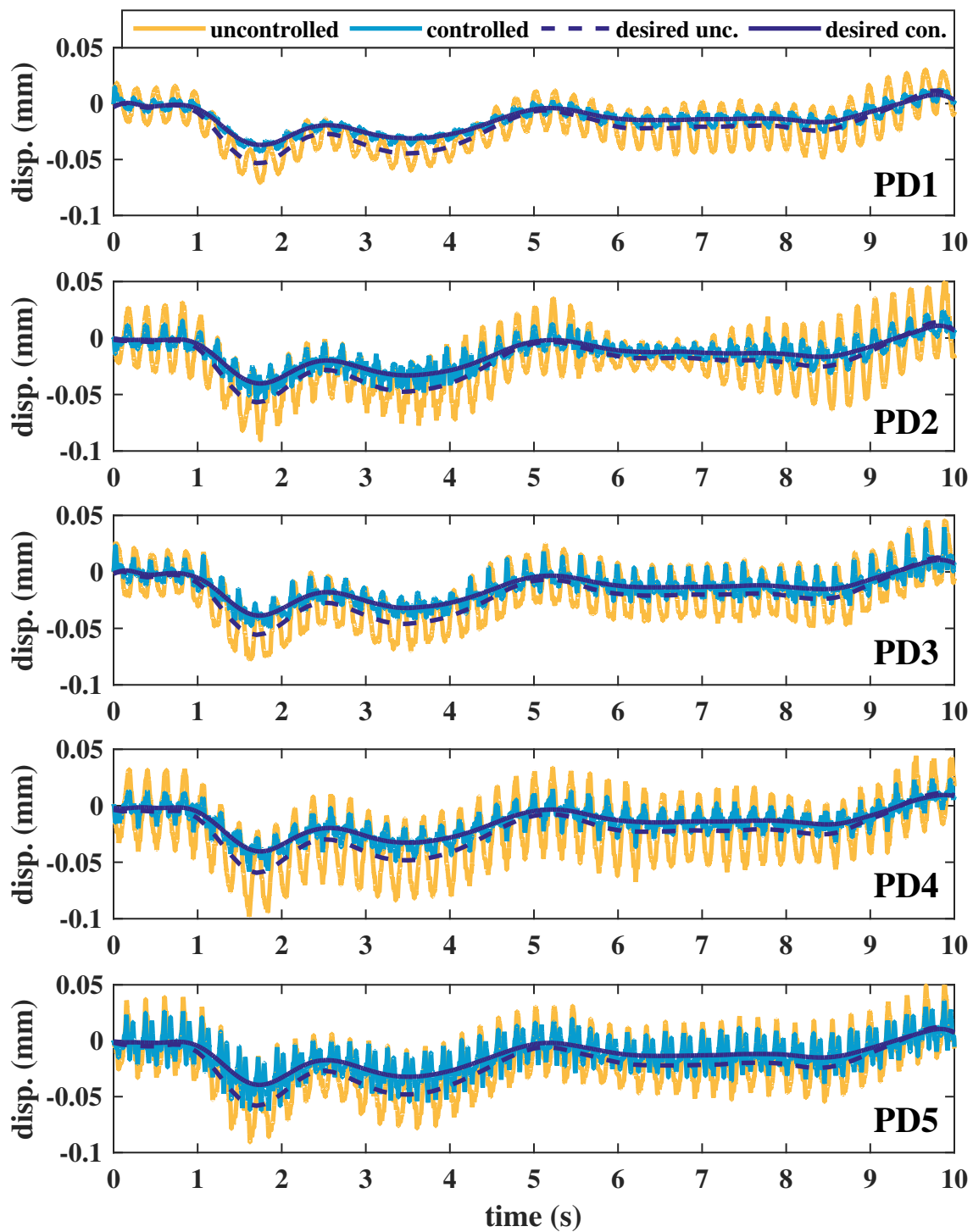


Figure 4.5: All PD experimental time series for jar-opening task.



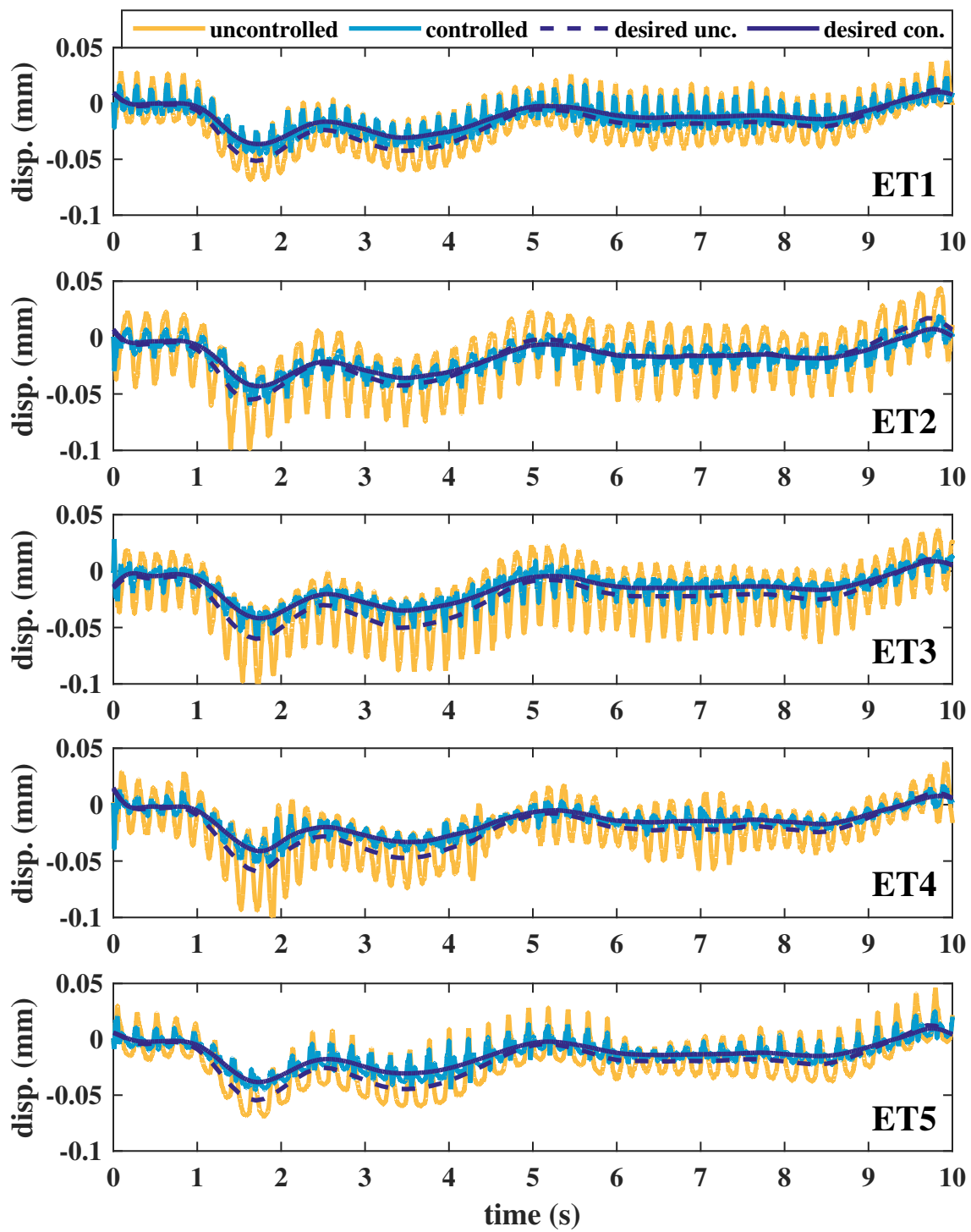


Figure 4.6: All ET experimental time series for jar-opening task.

Next, Fig. 4.7 illustrates the experimental time series for a sinusoidal voluntary motion. Once again, the controller reduces tremor and also reduces voluntary motion, but to a lesser extent. Exploring controller performance with sinusoidal voluntary motion provides insight into frequency-dependent performance. Figures 4.8 and 4.9 present the normalized tracking errors and voluntary amplitude ratios with varying parameters for the parkinsonian tremor and essential tremor datasets, respectively. The normalized tracking error is the RMS error between the desired position and the actual position, normalized by the RMS error in the uncontrolled case. The voluntary amplitude ratio is the ratio of the voluntary amplitude in the controlled case to the uncontrolled case. Thus, the normalized tracking error quantifies tremor suppression performance (lower error means better performance) while the voluntary amplitude ratio quantifies the increased active stiffness in the voluntary range (ideally, the voluntary amplitude ratio equals one). These figures indicate the experimental system exhibits low dependence on tremor amplitude and voluntary frequency. The controller gain has the largest effect on system performance: higher gains produce greater tremor suppression but also increase voluntary motion reduction. Figure 4.10 illustrates this trade-off between tremor suppression performance and voluntary motion resistance by comparing the two parameters for all experimental cases in Figs. 4.8 and 4.9. The highest controller gain reduces tremor by up to 80%, but can also reduce voluntary motion by  $\sim 50\%$ . The highest gain reduces tremor by  $\sim 50\%$  and only reduces voluntary motion by  $\sim 15\%$ . Altogether, the displacement-based feedback controller offers moderate tremor reduction at the expense of low-to-moderate increased stiffness for voluntary motions. These experiments demonstrate the ability of DESAs to reduce tremor via tremor-active control. Future improvements to actuator performance and controller de-

sign can lead to physical systems that achieve similar performance as simulations in Chapter 3. In particular, these DESAs require much thinner layers to increase actuation capabilities; other existing DESAs may lack other necessary properties for tremor-active control. The following section investigates the necessary parameters to achieve satisfactory performance.

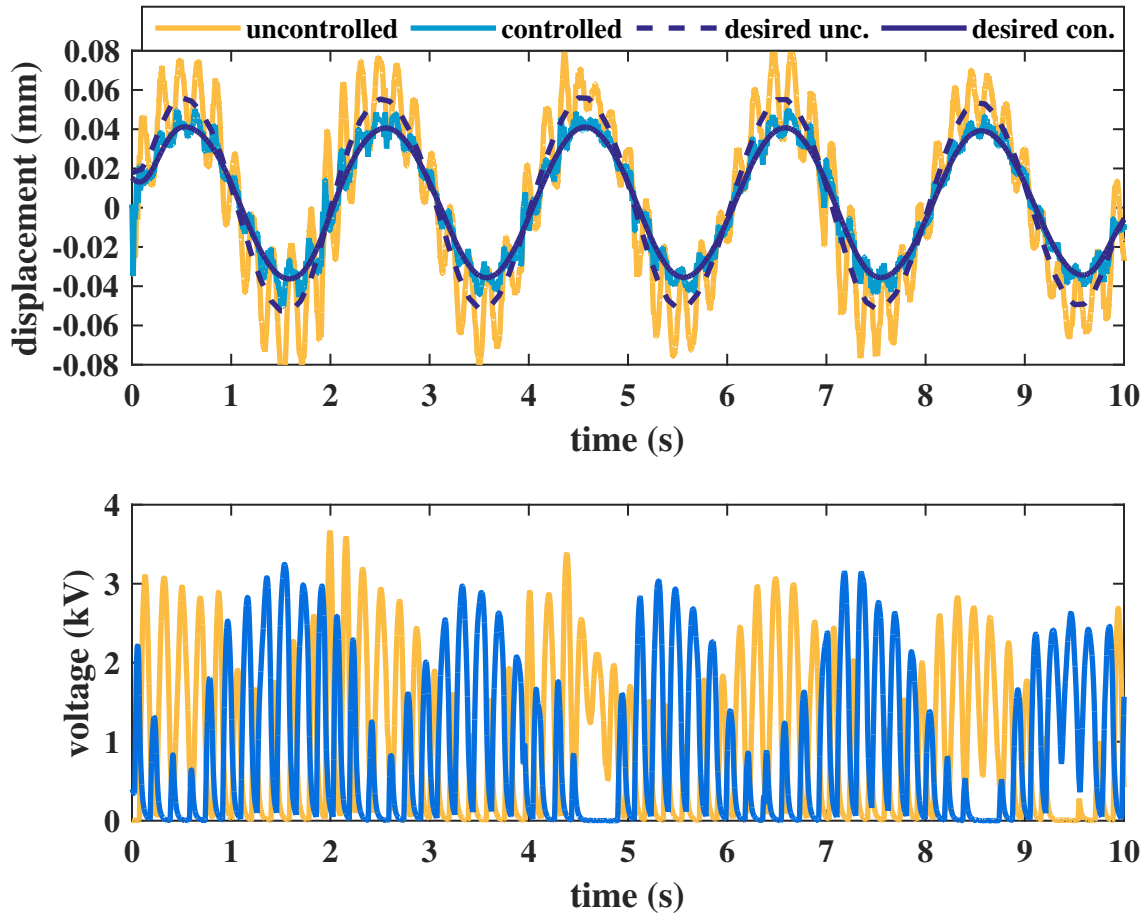


Figure 4.7: Experimental time series with sinusoidal voluntary motion (0.5 Hz) and ‘ET4’ tremor

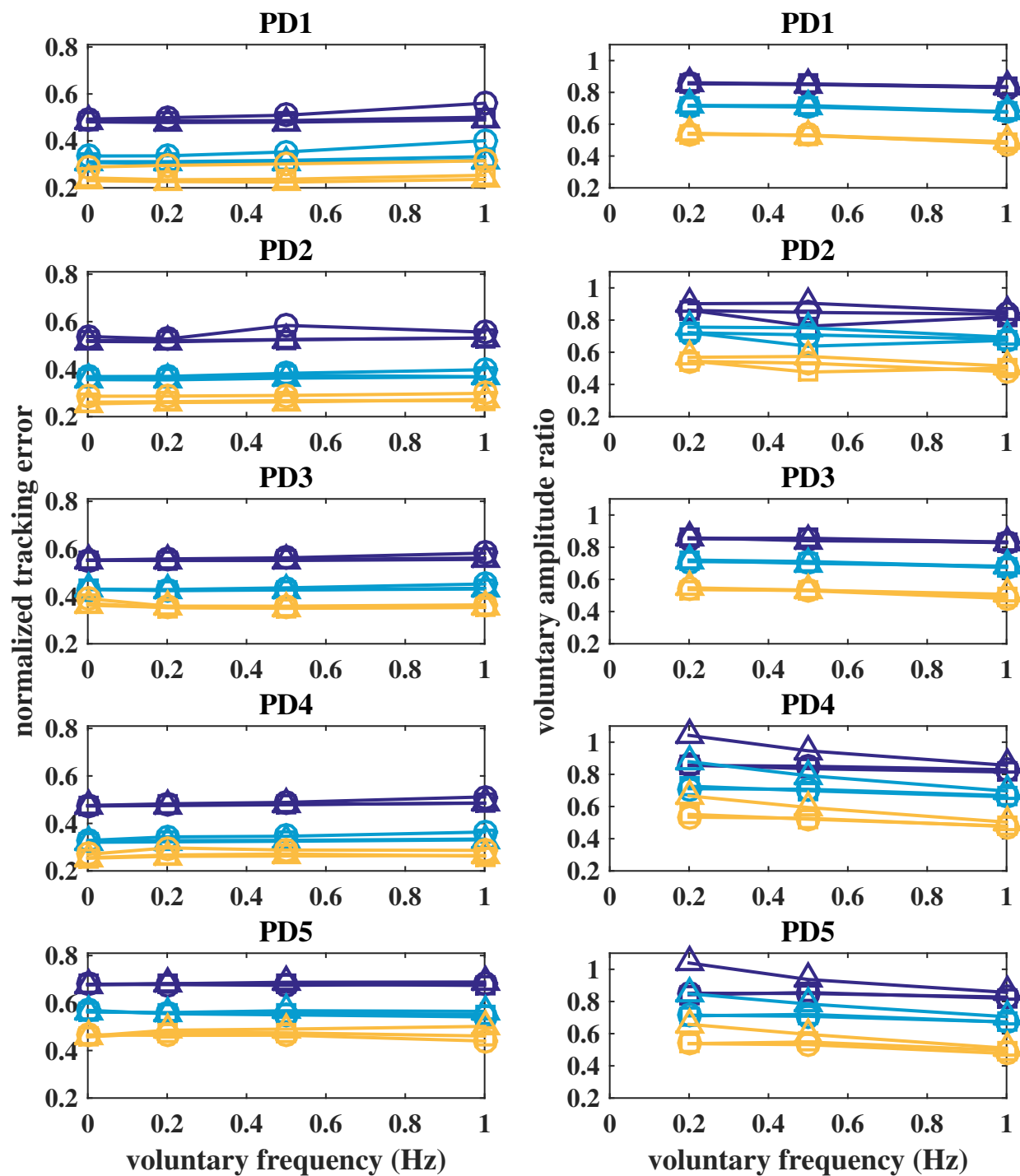


Figure 4.8: Tracking error and voluntary motion resistance for all PD experiments with sinusoidal voluntary motion (lighter color = higher gain)

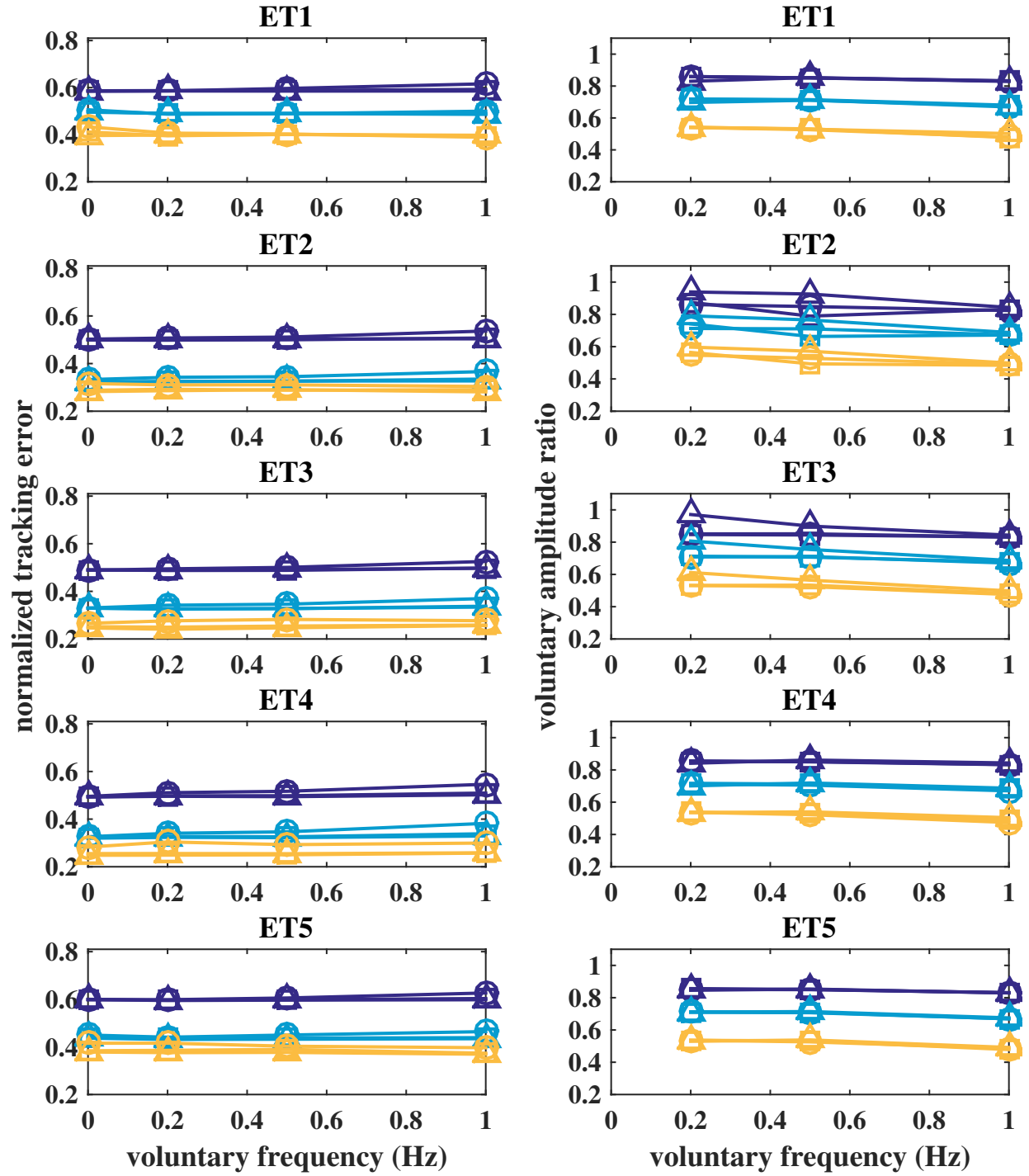


Figure 4.9: Tracking error and voluntary motion resistance for all ET experiments with sinusoidal voluntary motion (lighter color = higher gain)

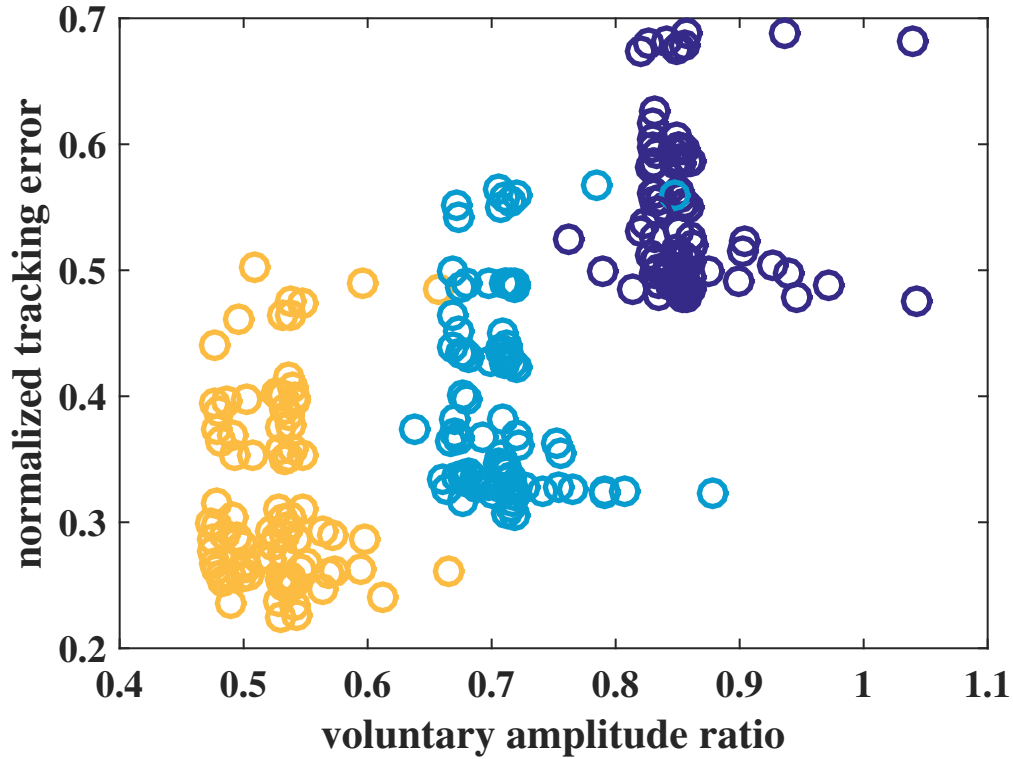


Figure 4.10: The controller offers a tradeoff between tremor suppression and voluntary motion resistance (lighter color = higher gain).

## 4.2 Necessary Parameters for Tremor Suppression

The previous section demonstrates the ability of DESAs to suppress tremor in a physical, but scaled system. This section quantifies the necessary DESA parameters to achieve clinical implementations of DESA-based tremor suppression. Given these necessary DESA characteristics, this section discusses the outlook for DESA-based tremor suppression and necessary advances to reach clinical implementations.

### **4.2.1 Performance Limits**

Performance limits quantify the required actuator characteristics that the DESA parameters must achieve. The limits include the passive effect of the DESAs on voluntary motion, tremor suppression performance, device size, and electrical safety. Some of these limits are qualitative in nature: different patients may accept different device sizes, levels of increased stiffness, or levels of tremor suppression. However, this study develops quantitative limits to characterize necessary DESA parameters by estimating performance limit values. Future implementations require clinical evaluation of these performance limits; this study provides a first-order approximation of DESA parameters that may enable clinical tremor suppression about a given joint.

#### **4.2.1.1 Passive effect of DESAs**

Applying only to the tremor-active approach, the passive effect of the DESAs increases patient effort and discomfort. This approach assumes patients will accept this increased effort to gain low-profile tremor suppression. The acceptable level of increased stiffness requires clinical evaluation; this study quantifies the increased stiffness as a ratio of the joint stiffness, then provides numeric values for an estimate of the acceptable stiffness increase. In addition to stiffness, DESAs exhibit viscoelasticity that affects the dynamic joint characteristics. The human motor system is capable of adapting to predictable changes in environment, but it is not clear to what extent viscoelasticity may be tolerated in a tremor suppression device. This study estimates the allowable passive DESA

dynamics by limiting the change in joint magnitude and phase. Without DESAs, the joint transfer function from muscular torque to joint angle is

$$\frac{\bar{\theta}}{\bar{\tau}_m} = \frac{1}{Js^2 + Bs + K}. \quad (4.1)$$

The transfer function produces the magnitude and phase at frequency  $\omega$  by inserting  $s = i\omega$ . From Eq. (3.32), the transfer function with DESAs is

$$\frac{\bar{\theta}}{\bar{\tau}_m} = \frac{1}{(J + 2r_0^2 m_a)s^2 + Bs + K + \frac{2r_0^2 A_0 Y}{l_0} + \frac{2r_0^2 A_0 k_1}{l_0} \frac{s}{s + \frac{k_1}{\eta_1}}}. \quad (4.2)$$

Comparing these transfer functions enables quantification of the passive effect of the DESAs on the joint. This passive effect only matters for the frequency content of voluntary motion (0–2 Hz). Furthermore, performance at higher frequencies is less important since faster motions are inherently less precise. Thus, this study defines a frequency-dependent performance limit:

$$L(f) = \frac{L_2 - L_0}{4} f^2 + L_0 \quad (4.3)$$

where  $L$  is the performance upper limit at frequency  $f$  given the 0 Hz and 2 Hz limits  $L_0$  and  $L_2$ , respectively. This study applies this limit function to the magnitude ratio (without-DESA over with-DESA) and the phase difference (with-DESA minus without-DESA). The magnitude ratio reflects increased patient effort while the phase difference represents greater motor system adaptation due to changes in muscular actuation timing. Unless otherwise stated, this study applies



limits  $L_0 = 2.5$  and  $L_2 = 4$  for the magnitude ratio and  $L_0 = 5^\circ$  and  $L_2 = 30^\circ$  for the phase difference as a first approximation of acceptable passive DESA performance.

#### **4.2.1.2 Tracking error**

The tracking error (difference between actual and desired joint angle) reflects the tremor suppression performance of the system. While perfect tremor cancellation is ideal, patients will likely be satisfied with moderate tremor reduction. Again, the level of tremor reduction that patients deem worthy of wearing a tremor suppression device requires clinical investigation. This study quantifies the tracking performance as the RMS error with control normalized by the RMS error without control.

#### **4.2.1.3 Size**

Device size is a limiting factor for existing mechanical tremor suppression systems. Patient acceptance and limb and joint size affect the maximum allowable actuator size. This study applies upper limits for DESA length and area that depend on the targeted joint. In addition, this study applies a lower limit on DESA length to maintain stretches near the linear range: the stretch change for a  $30^\circ$  degree joint rotation is limited to 0.3.

#### 4.2.1.4 Electrical safety

Finally, as discussed in Section 2.3.2, the current must be restricted to less than 20 mA and the voltage must be less than a value that depends on the DESA capacitance [104]. Simulations enforce the current limit by restricting the maximum change in voltage between fixed integration steps sampled at frequency  $f_s$ :

$$\Delta V_{\max} = \frac{i_{\max}}{f_s C_0} \quad (4.4)$$

$$C_0 = \frac{n\epsilon_0\epsilon_r A_{0a}}{d_0} \quad (4.5)$$

where  $C_0$  is the DESA capacitance calculated with the electrode-covered cross-sectional area  $A_{0a}$ . This study applies the electrical limits as the last step before simulations, thereby presenting the best-achievable performance when actuation and electrical limits do not allow perfect tremor cancellation.

#### 4.2.2 Tremor-Active Parameters

The tremor-active approach requires DESAs to suppress tremor sufficiently with passive influence on voluntary motion below the specified performance limits. Thus, the necessary DESA parameters may be categorized into those that affect the passive dynamics and those that affect actuation performance.

#### 4.2.2.1 Passive effect

First, the static stiffness of the DESAs reflects the additional effort the patient must exert to hold a desired position. Define the static response ratio limit  $X_{\text{stiffness}} \equiv L_0$  and set  $s = 0$  in Eqs. (4.1) and (4.2) to obtain the upper limit for DESA stiffness:

$$\frac{YA_0}{l_0} \leq \frac{K}{2r_0^2}(X_{\text{stiffness}} - 1). \quad (4.6)$$

Viscoelastic parameters  $k_1$  and  $\eta_1$  affect the ability of the DESAs to meet the phase difference limits. This study quantifies the viscoelastic parameter limits given the effective joint stiffness to generalize the results for any joint. These generalized viscoelastic parameters include the critical relaxation time  $T_{\text{cr}} \equiv \eta_{1,\text{cr}}/k_1$  (the maximum allowable relaxation time) and the effective Maxwell stiffness ratio  $\hat{k}_1$ :

$$\hat{k}_1 \equiv \frac{k_{1,\text{eff}}}{K_{\text{eff}}}. \quad (4.7)$$

Here, the effective joint stiffness is

$$K_{\text{eff}} \equiv K + \frac{2r_0^2 A_0 Y}{l_0} \quad (4.8)$$

and the Maxwell spring effective stiffness about the joint scales in a similar way as the Young's modulus:

$$k_{1,\text{eff}} \equiv \frac{2r_0^2 A_0 k_1}{l_0}. \quad (4.9)$$

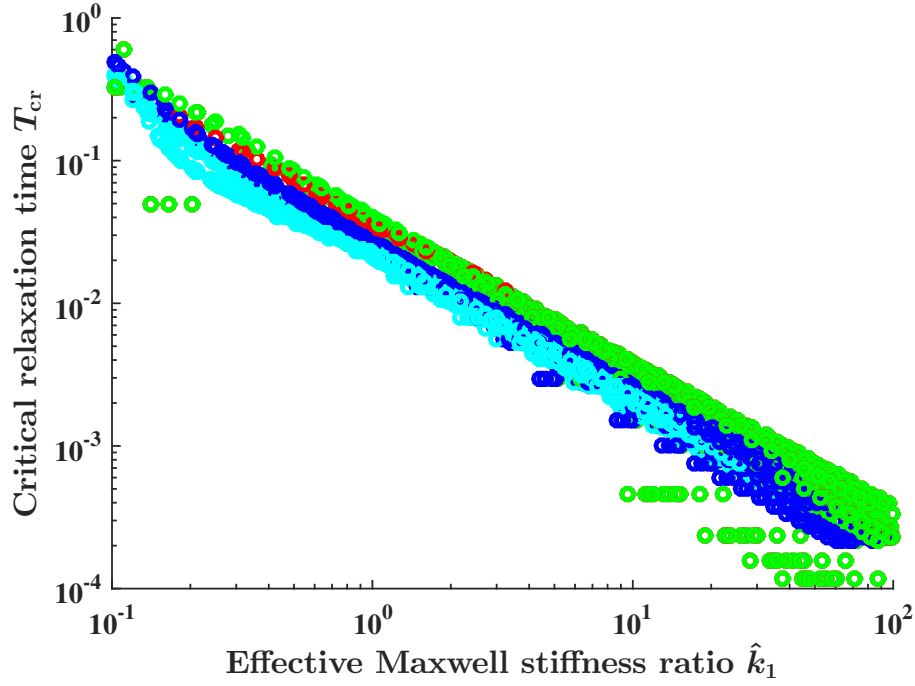


Figure 4.12: Varying joint parameters (different colors) produces similar normalized viscoelastic parameter limits.

Figure 4.12 illustrates the critical relaxation time with fixed performance limits but varying DESA stiffness and joint parameters. Many combinations of  $Y$ ,  $A_0$ , and  $l_0$  produce static stiffness ratios ranging from 1.2 to 2.4. Joint inertia and stiffness values range from one-third to six times average male flexion-extension values [130]. Even with these wide parameter ranges,  $T_{cr}$  forms a relatively consistent function of  $\hat{k}_1$ . Therefore, the joint stiffness approximately defines the viscoelastic parameter limits given phase difference performance limits. Figure 4.13 illustrates the effect the phase difference performance limit has on these parameters. More strict phase difference requirements produce more strict viscoelastic parameter requirements, though with a similar relation between  $T_{cr}$  and  $\hat{k}_1$ . Thus, as intuitively expected, the ability of the human motor system to adapt to viscoelastic behavior limits the allowable viscoelasticity of the DESAs. This analysis

provides a quantitative tool to characterize these viscoelastic parameter limits given an expected acceptable level of muscular phase adaptation.

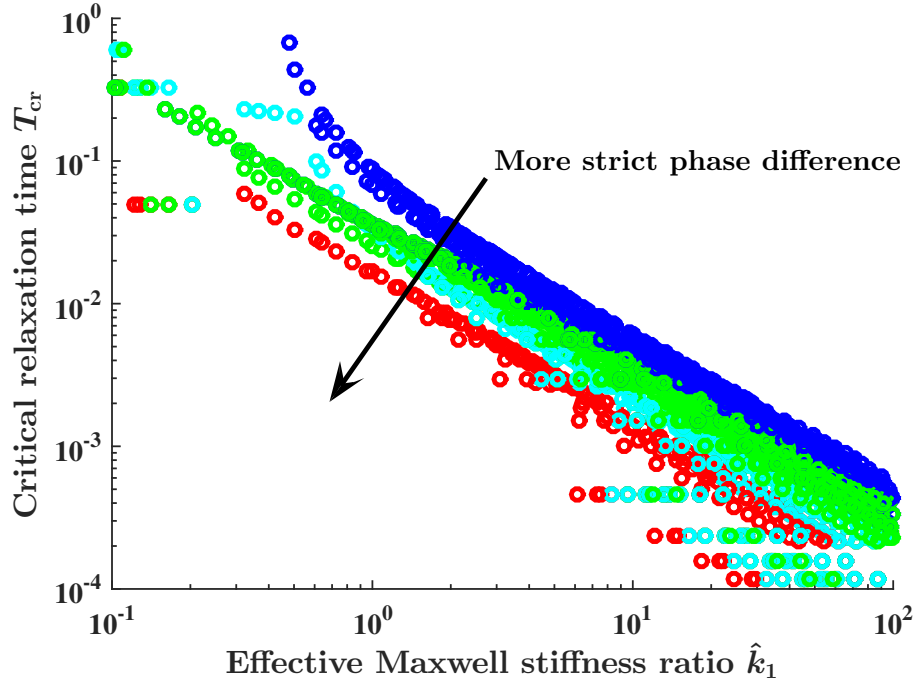


Figure 4.13: The allowable viscoelastic parameter range decreases for stricter phase limits (different colors).

#### 4.2.2.2 Actuation

In the tremor-active approach, actuation to suppress tremor depends only on the electrostatic force created by the DESA voltage. Electrical safety limits restrict the voltage and voltage rate (current). Furthermore, the electrical breakdown strength  $E_{br}$  of the material also affects the maximum voltage. Thus, these electrical limits affect the ability of the DESA to actuate to suppress tremor. This study defines the actuation ratio  $\tau_{ratio}$  and the actuation rate ratio  $\Delta V_{ratio}$  to characterize tremor sup-

pression performance in terms of electrical limits. Once again, this study uses tremor data from the online database as the tremor torque  $\tau_{\text{tremor}}$  [9]. Given the tremor torque time series, the controller time series that exactly cancels tremor is

$$u(t) = -\frac{d_0^2}{r_0 A_{0a} \epsilon_0 \epsilon_r} \tau_{\text{tremor}}(t). \quad (4.10)$$

Electrical limits may prohibit implementation of this controller time series. The actuation ratio quantifies the achievable actuation magnitude given the maximum allowable voltage  $V_{\text{max}}$ . This maximum allowable voltage may be imposed by the electrical breakdown limit of the material or by the electrical safety limit for the DESA capacitance. The actuation ratio is the maximum active DESA torque normalized by the maximum value of the tremor torque:

$$\tau_{\text{ratio}} \equiv \frac{r_0 A_{0a} \epsilon_0 \epsilon_r V_{\text{max}}^2}{d_0^2 |\tau_{\text{tremor}}|}. \quad (4.11)$$

The current limit restricts the rate of change of the DESA voltage. The actuation rate ratio quantifies this limit as the maximum allowable change in voltage normalized by the RMS voltage change required for perfect tremor cancellation  $\Delta V_{\text{canc}}$ :

$$\Delta V_{\text{ratio}} \equiv \frac{i_{\text{max}}}{f_s C_0 \Delta V_{\text{canc}}}. \quad (4.12)$$

The actuation ratio and actuation rate ratio limits determine the the necessary DESA layer thickness, relative permittivity, and electrical breakdown field. Simulations show how tremor am-

plitude and joint parameters affect the ratio limits given the limiting electrical parameter (electrical breakdown, voltage safety, or current safety). First, Fig. 4.14 presents the normalized tracking error when the electrical breakdown strength is the limiting electrical factor. The figure also shows the associated saturation fraction, or the fraction of time the voltage is saturated due to the electrical limit. More voltage saturation produces greater tracking error. Next, Fig. 4.15 presents similar results when the current is the limiting electrical factor (which is typically the case when electrical breakdown is not the limiting factor). In this case, current saturation fraction is analogous to voltage saturation in the previous case, and saturation produces increased tracking errors. Overall, DESA parameters must achieve high enough  $\tau_{\text{ratio}}$  and  $\Delta V_{\text{ratio}}$  to yield saturation fractions low enough to produce sufficient tracking performance. Figure 4.16 illustrates the tradeoff between actuation ratios when selecting DESA relative permittivity. Low relative permittivity produces a low actuation ratio, high voltage saturation fraction, and high tracking error. However, higher relative permittivity decreases actuation rate ratio, leading to increased current saturation fraction and tracking error. An optimal relative permittivity produces the greatest tremor suppression performance by finding the best balance between  $\tau_{\text{ratio}}$  and  $\Delta V_{\text{ratio}}$ . Significantly, there is a wide range of  $\epsilon_r$  values that achieve moderate to high levels of tremor suppression even in the presence of voltage and current saturation.

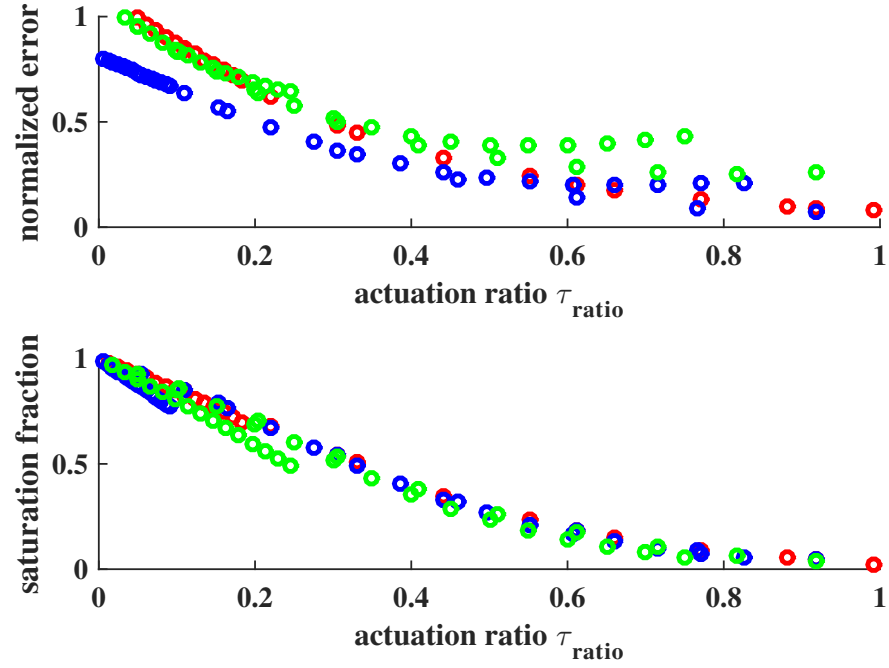


Figure 4.14: Effect of actuation ratio on voltage saturation for tremor-active control

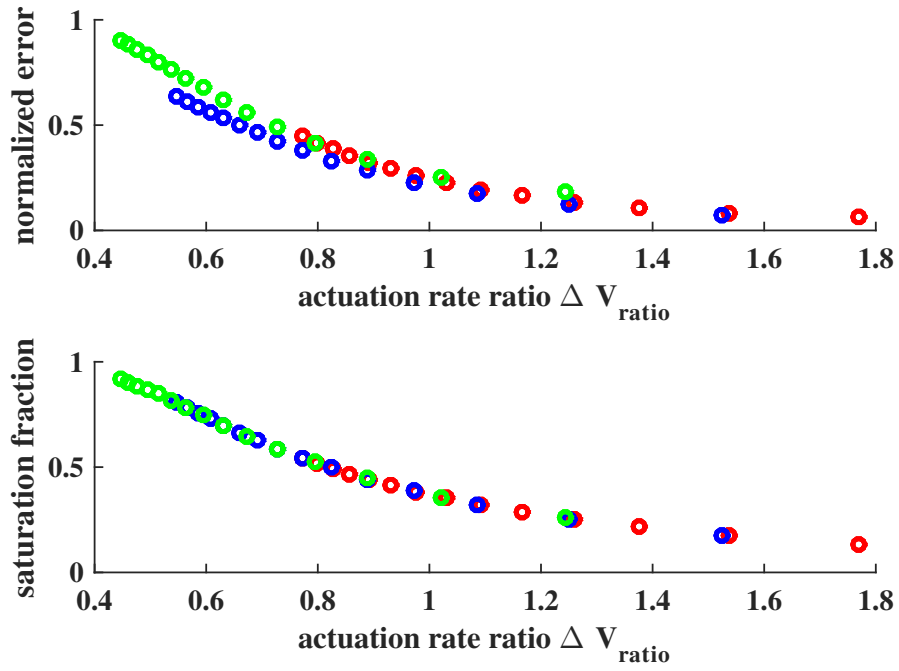


Figure 4.15: Effect of actuation rate ratio on current saturation for tremor-active control



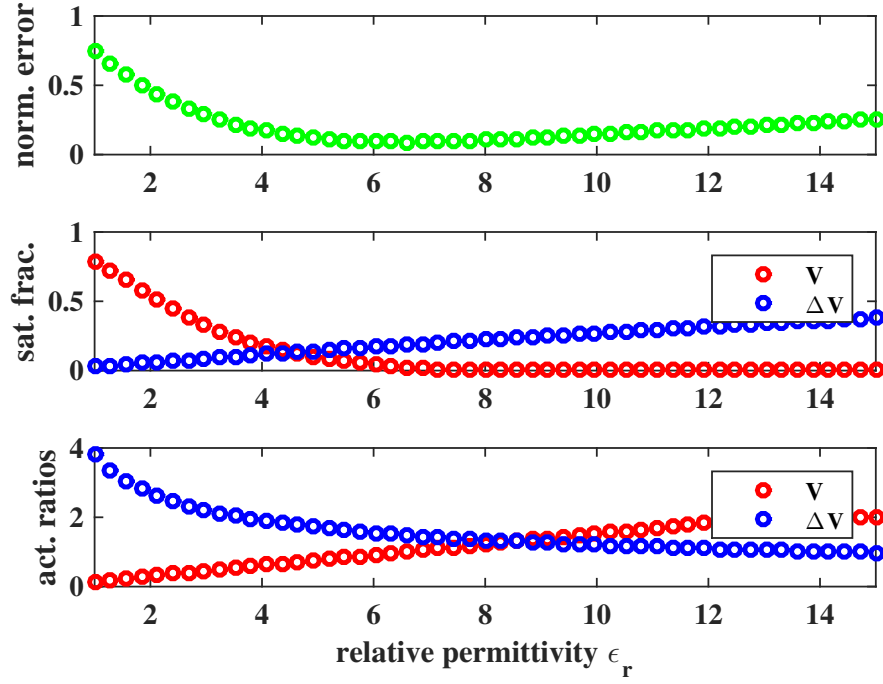


Figure 4.16: Optimal  $\epsilon_r$  selection finds tradeoff between voltage and current saturation.

### 4.2.3 Fully Active Parameters

The fully active approach requires DESAs to actuate to suppress tremor and follow voluntary motion. There are no limits on passive DESA characteristics, but the DESAs must be able to overcome their passive dynamics to track the voluntary motion. The actuation ratio and actuation rate ratios fully characterize the necessary parameters for the fully active approach. However, these parameters now include the additional torque  $\tau_{\text{passive}}$  and voltage rate  $\Delta V_{\text{passive}}$  required to

overcome the passive DESA dynamics:

$$\tau_{\text{ratio}} \equiv \frac{r_0 A_{0a} \epsilon_0 \epsilon_r V_{\text{max}}^2}{d_0^2 (|\tau_{\text{tremor}}| + |\tau_{\text{passive}}|)} \quad (4.13)$$

$$\Delta V_{\text{ratio}} \equiv \frac{i_{\text{max}}}{f_s C_0 (\Delta V_{\text{canc}} + \Delta V_{\text{passive}})}. \quad (4.14)$$

Figures 4.17 and 4.18 present fully active simulations analogous to those in Figs. 4.14 and 4.15, respectively. The tracking performances has a similar trend as with the tremor-active approach; however, actuation ratios in the fully active approach represent more strict DESA parameters compared to the tremor-active approach due to the additional actuation to track voluntary motion. The voltage-limited performance is slightly worse for fully active, indicating the DESAs struggle to track the magnitude of the voluntary motion. The current-limited performance is identical to the tremor-active approach since tremor dominates the actuation rate due to its higher frequency. Note that Fig. 4.17 uses the relatively low DESA stiffness values selected for tremor-active control; Fig. 4.19 demonstrates performance for higher stiffness values. DESAs with low actuation ratios cannot overcome the high stiffness values and produce tracking errors that are worse than those without control. Thus, the fully active approach requires actuation capabilities much greater than the passive DESA mechanical impedance. Unlike tremor-active control, fully active control offers little leeway for actuators with relatively low actuation levels. Overall, the tremor-active approach enables implementation with less strict DESA parameters, forming the most achievable option for clinical implementations.

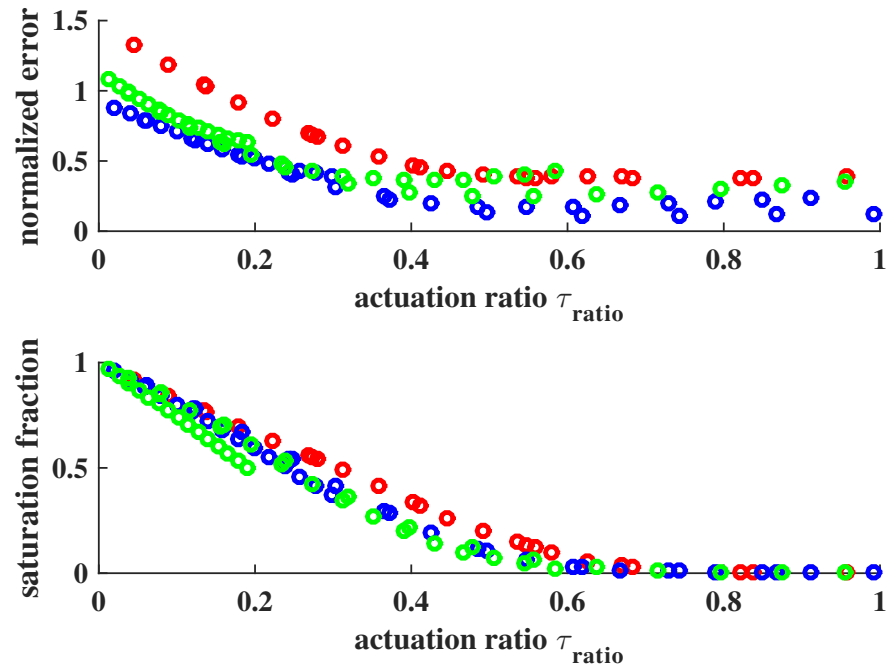


Figure 4.17: Effect of actuation ratio on voltage saturation for fully active control

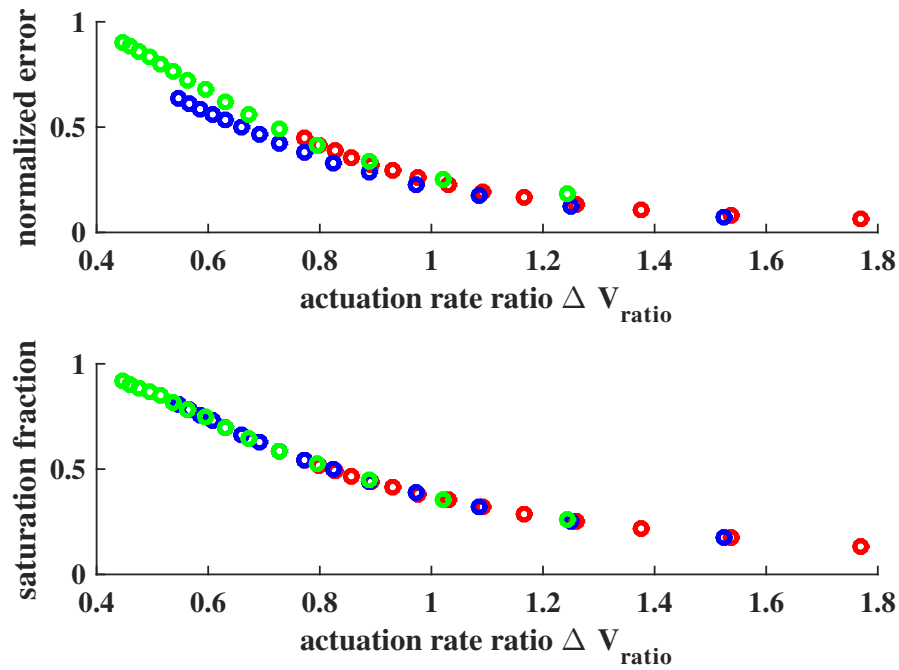


Figure 4.18: Effect of actuation rate ratio on current saturation for fully active control

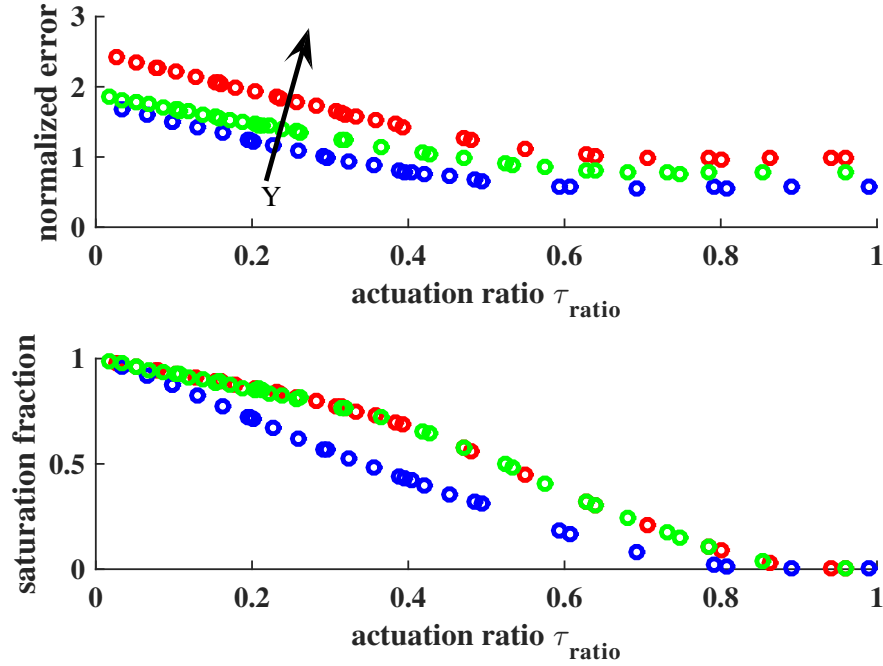


Figure 4.19: Increased passive stiffness can drastically reduce performance for fully active control.

#### 4.2.4 Outlook

Evaluation of DESAs available in the literature in context with the necessary parameters for clinical implementation provides insight into the outlook of DESA-based tremor suppression. This analysis targets suppression of wrist flexion-extension (an ideal first-step for mechanical tremor suppression) and fixes the DESA geometry ( $l_0 = 6.3$  cm and  $A_0 = 3.14$  cm<sup>2</sup>). Figure 4.20 illustrates the potential for DESAs to meet the performance requirements for tremor-active suppression of wrist flexion-extension, where the upper-left region above the actuation limit and below the stiffness limit contains suitable DESAs. This figure includes data points that correspond to specific DESAs in the literature as well as estimated regions of potential values for each material.

Literature DESA materials include silicone, IPN-acrylic, UV-cured acrylic, polyurethane, and rubber [73, 83, 86–91, 93–95, 97, 135, 136]. Among DESAs from the literature, only six meet the length requirement (star data points in Fig. 4.20) [73, 87, 93, 94, 97, 136]. The circle data points in Fig. 4.20 demonstrate the achieved parameters by scaling up the number of layers of literature DESAs to achieve the required length [83, 88]. Finally, the square data point indicates the effect of decreasing crosslinker or adding plasticizer to UV-cured acrylic [97, 137].

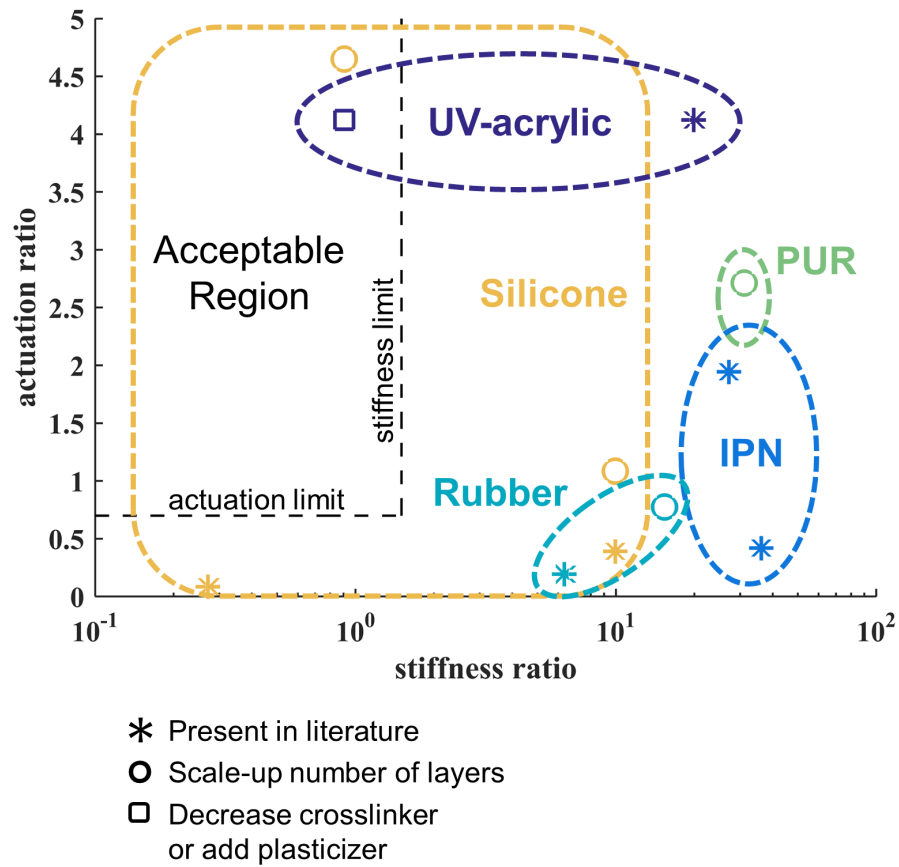


Figure 4.20: Slight modifications of literature DESAs produces DESAs that meet tremor suppression performance requirements (above actuation limit and below stiffness limit).

Interpreting Fig. 4.20 provides insight into the necessary modifications to literature DESAs to meet the requirements for tremor suppression. First, the low-actuation-ratio silicone DESAs have very thick layers ( $d_0 > 200 \mu\text{m}$ ) [87, 94]. One of the scaled-length silicone DESAs has thin layers ( $d_0 = 30 \mu\text{m}$ ) and is capable of meeting the performance requirements; however, the stacking process for this DESA can only achieve stacks of approximately 100 layers [88]. The capability of tuning the stiffness of silicone DESAs means they can meet the stiffness requirements for tremor suppression. Improving manufacturing methods to develop large stacks with greater than 1000 relatively thin layers ( $d_0 < 70 \mu\text{m}$ ) could enable tremor suppression with silicone-based DESAs.

UV-cured acrylic is another promising material for DESA-based tremor suppression. Recent research produces stacks of thousands of layers to achieve total lengths greater than 10 cm [97]. The achieved stiffness of this DESA is too high for tremor suppression, but the stiffness of UV-cured acrylic depends on the amount of added crosslinker [89, 137]. Furthermore, addition of plasticizer to UV-cured acrylic also decreases stiffness and can improve viscoelastic properties [137]. Thus, decreasing crosslinker concentration or adding plasticizer could produce UV-cured acrylic DESAs that are suitable for tremor suppression—these modifications are likely possible with an already-existing manufacturing process [97]. The square data point in Fig. 4.20 demonstrates the parameters produced by using one of these methods to reduce the Young’s modulus to 0.1 MPa: the DESA meets the performance requirements. Finally, Fig. 4.21 presents a simulation of tremor-active suppression using the DESA parameters of this square data point (assuming perfect knowledge of the tremor). This figure illustrates the ability of the DESAs to drastically reduce tremor at the cost of a moderate increase in muscular effort by the patient.

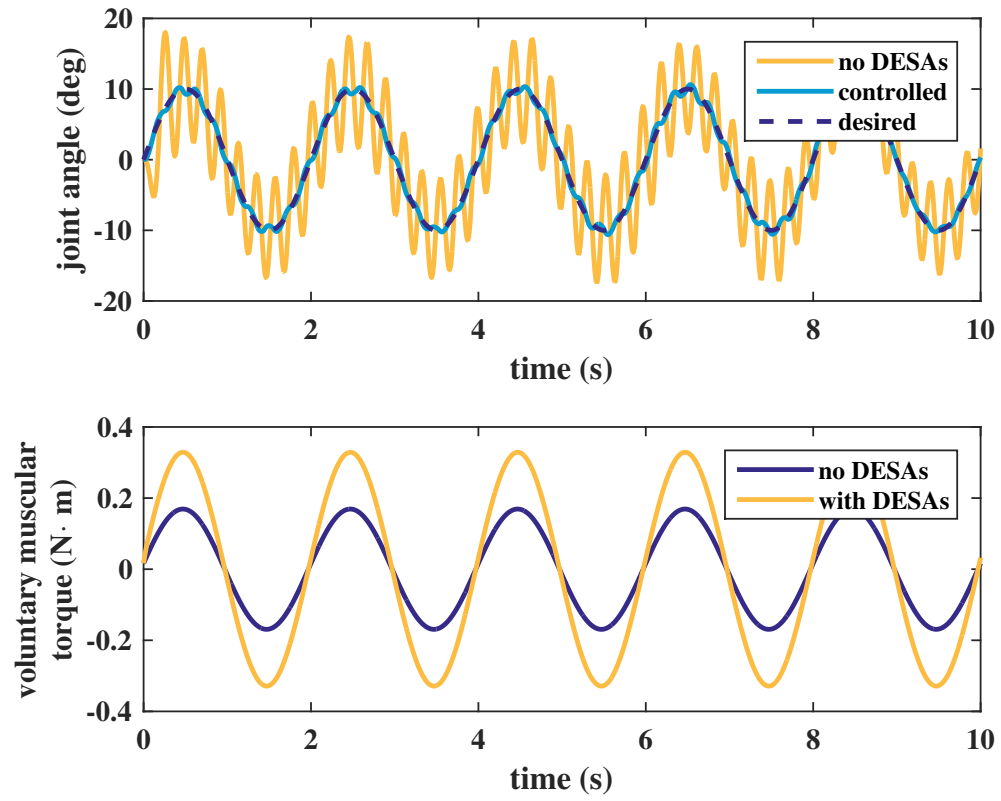


Figure 4.21: Tremor-active simulation of square data point in Fig. 4.20

## **CHAPTER 5**

### **PARKINSON’S DISEASE TREMOR MODEL**

Chapters 3 and 4 explore dielectric-based tremor suppression while assuming state-independent tremor generation. This chapter explores the evidence for delay-induced tremor in Parkinson’s disease. Section 5.1 describes the motivation for model structure and presents simulations of the tremor model. Section 5.2 discusses the implications of delay-induced tremor for interpretation of physiologically based models, treatment effectiveness, and the effect of mechanical tremor suppression. Research in this chapter is published in [138].

#### **5.1 Delay-Induced Tremor**

Parkinson’s disease generally inhibits movement: typical symptoms include rigidity, bradykinesia, and slowness of movement. Parkinsonian tremor represents a stark contrast to other Parkinson’s disease symptoms. Pathophysiology theories must explain why the same disease inhibits movement and also produces rapid, undesired motions. This symptom disparity has led researchers to suggest different pathophysiologies produce the different symptoms in Parkinson’s disease. However, increased feedback delay is one possible pathology that can explain the coexistence of movement inhibition and tremor. Previous works suggest feedback delay plays a role in parkinsonian



tremor: large enough delays produce unstable feedback loops [31–33, 41]. Increased CNS delays also explain increased reaction times and slowness of movement [30]. However, the human motor system already overcomes large sensory delays to successfully perform a wide range of tasks with feedback control. Forward models are the key to this successful feedback: these internal models predict the present state from delayed sensory information. Thus, the critical factor in delay-induced tremor is the increased delay is unaccounted by the CNS. This research develops an optimal control-based human motor system model with increased CNS delay. Clinical evidence motivates the model structure, enabling mapping of physiological substructures to model components. The proposed model provides insight into treatment effectiveness along with new interpretations of physiologically based models.

Human motor control includes a planning stage and an execution stage. In the planning stage, the basal ganglia and the motor cortex collaborate to identify the movement goal, quantify the costs and rewards for the task, and select the appropriate motor pathways for execution [115]. During execution, M1 sends control signals to the muscles via the spinal cord [39, 107, 121]. Proprioceptive feedback returns through the spinal cord to the cerebellum. The cerebellum integrates delayed sensory information using forward models of task dynamics and efferent copies of control inputs from M1 [37, 115, 139]. The thalamus relays this integrated signal from the cerebellum to M1 [50, 52]. Note the execution stage primarily involves the CTC circuit, which is associated with pathological activity in Parkinson’s disease [51]. Given these functions, Fig. 5.1 maps the execution stage of the proposed optimal control model to physiological substructures. Prior to execution, the optimal controller selects a task-based cost function and determines optimal feedback gains:

this initialization represents the planning stage of motor control and movement initiation by the basal ganglia. For healthy motor control, the optimal control model includes the limb dynamics, a known proprioceptive feedback delay, a state estimator (cerebellum), and a feedback controller (M1).

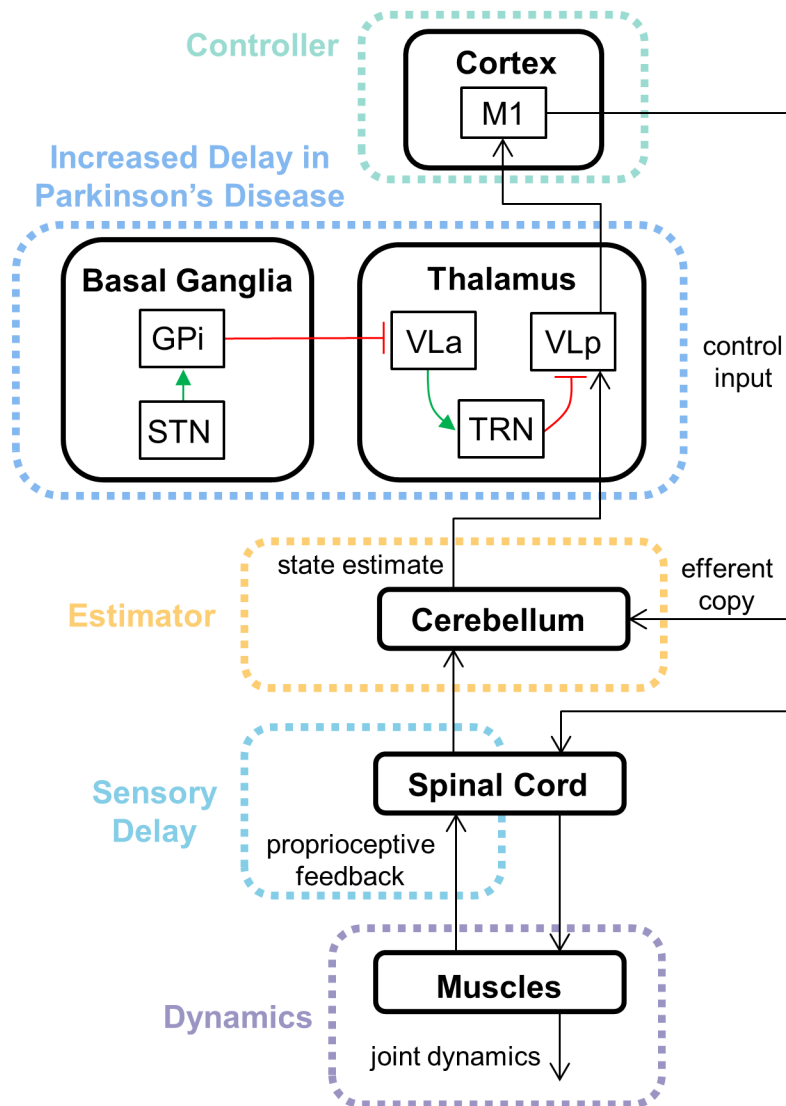


Figure 5.1: Increased inhibition in the thalamus delays the state estimate signal traveling from the cerebellum to the primary motor cortex via the thalamus.

As illustrated in Fig. 5.1, this research explores a potential increased CNS delay in Parkinson's disease by adding an unaccounted delay between the estimator and controller. Clinical evidence motivates this location: the basal ganglia internal globus pallidus (GPi) projects excessive inhibition to the anterior portion of the ventrolateral thalamus (VL<sub>a</sub>) [52]. The posterior portion of the ventrolateral thalamus (VL<sub>p</sub>) relays information from the cerebellum to M1. The excessive inhibition of VL<sub>a</sub> may spread to VL<sub>p</sub> via the thalamic reticular nucleus (TRN) [52]. This study hypothesizes that this excessive inhibition delays the signal traveling from the cerebellum to M1 via VL<sub>p</sub>. In optimal control terminology, the controller provides feedback using a delayed state estimate, producing an unstable feedback loop. Nonlinear elements in the human motor system convert instability to a stable limit cycle. As a first step towards modeling tremor as an increased feedback delay, this study applies control signal saturation to produce a limit cycle, as suggested in previous studies on delay-induced tremor [33, 140].

### 5.1.1 Optimal Controller

This section describes the optimal control algorithm for healthy motor control. The optimal controller largely follows previous works that derive optimal control for systems with multiplicative noise and state prediction for systems with feedback delays [36, 41]. The delay compensation extrapolates the delayed state to produce the *pseudomeasurement*, only extrapolating over the known proprioceptive feedback delay. This study refers to the extrapolated state as the pseudomeasurement since it replaces the role of the measurement in non-delayed optimal control. The model is

extended for simulating parkinsonian tremor by adding an unaccounted delay between the estimator and controller.

### 5.1.1.1 Problem Statement

The continuous dynamics of the human motor system are discretized over the small time interval  $\Delta t$  to facilitate discrete control design. The discrete system includes

$$\begin{aligned}
\textbf{Dynamics} \quad & x_{k+1} = A_k x_k + B_k u_k + \xi_k + \epsilon_k C u_k \\
\textbf{Delayed Measurement} \quad & y_k = H x_{k-\delta_k} + \sigma_k \\
\textbf{State Estimate} \quad & \hat{x}_{k+1} = A_k \hat{x}_k + B_k u_k + K_k (\hat{x}_k^y - \hat{x}_k) + \eta_k \\
\textbf{Control Input} \quad & u_k = -L_k \hat{x}_k
\end{aligned} \tag{5.1}$$

which depend on the state  $x_k$ , delayed measurement  $y_k$ , control input  $u_k$ , and pseudomeasurement  $\hat{x}_k^y$ . The system includes linear process noise  $\xi_k \sim \mathcal{N}(0, \Omega^\xi)$ , multiplicative process noise  $\epsilon_k \sim \mathcal{N}(0, I)$ , measurement noise  $\sigma_k \sim \mathcal{N}(0, \Omega^\sigma)$ , and estimator noise  $\eta \sim \mathcal{N}(0, \Omega^\eta)$ . The matrix  $C = \alpha B_k$  ensures the multiplicative noise adds to the control input with scaling factor  $\alpha$ ; this process is consistent with control input noise in real motor control. The controller provides feedback using a state estimate produced by a Kalman filter, which uses the pseudomeasurement in place of an actual measurement. The optimization problem identifies the set of fixed estimator gains  $K_k$  and

controller gains  $L_k$  that minimize the cost

$$\text{Cost} = \sum_{k=1}^N (x_k^\top Q_k x_k + u_k^\top R_k u_k) \quad (5.2)$$

given initial estimate mean  $\hat{x}_1$  and covariance  $P_1$ . Unlike the linear case, multiplicative noise couples the optimal estimator and controller gains [36].

### 5.1.1.2 Delay Compensation

The system compensates for measurement delay by predicting the present-time full state from a delayed partial-state measurement [41]. This delay compensation includes three intermediate steps:

1. Acquire delayed partial-state measurement  $y_k$ .
2. Estimate delayed full state  $\tilde{x}_k$  via Kalman filter.
3. Extrapolate delayed full state over delay interval to obtain the pseudomeasurement  $\hat{x}_k^y$ .

The optimal estimator treats the pseudomeasurement as a noisy full-state measurement with known covariance. A linear Kalman filter produces the delayed full state from the delayed partial-state

measurement:

$$\begin{aligned}
K_k^y &= A_k P_k^y H^\top (H P_k^y H^\top + \Omega^\sigma)^{-1} \\
\tilde{x}_{k+1} &= A_k \tilde{x}_k + B_k u_{k-\delta k} + K_k^y (y_k - H \tilde{x}_k) \\
P_{k+1}^y &= \tilde{\Omega}^\xi + (A_k - K_k^y H) P_k^y A_k^\top
\end{aligned} \tag{5.3}$$

initialized with known  $\tilde{x}_1$  and  $P_1^y$ . The selected process noise covariance  $\tilde{\Omega}^\xi$  replaces the true process noise covariance  $\Omega^\xi$  to enable tracking of unmodeled dynamics. Extrapolation of the delayed full-state estimate over the interval  $\check{k} = 1$  to  $\check{k} = \delta \hat{k} - 1$  produces the pseudomeasurement:

$$\check{x}_{\check{k}+1} = A_k \check{x}_{\check{k}} + B_k u_{k-\delta k+\check{k}}. \tag{5.4}$$

where  $\delta \hat{k}$  is the estimated delay,  $\check{x}_{\check{k}}$  is the intermediate extrapolation state initialized with  $\check{x}_1 = \tilde{x}_k$ , and  $\hat{x}_k^y \equiv \check{x}_{\delta \hat{k}}$  defines the pseudomeasurement. Propagation of the assumed delayed full-state estimate covariance  $\check{\Omega}^\sigma$  over the delay interval produces the pseudomeasurement covariance  $\Omega^\delta$ :

$$\check{P}_{\check{k}+1} = A_k \check{P}_{\check{k}} A_k^\top + \Omega^\xi \tag{5.5}$$

where  $\check{P}_1 = \check{\Omega}^\sigma$  and  $\Omega^\delta \equiv \check{P}_{\delta k}$ . The ensuing optimization treats the pseudomeasurement  $\hat{x}_k^y$  as a noisy measurement with covariance  $\Omega^\delta$ .

### 5.1.1.3 Controller Gains

Todorov [36] derives an optimal controller for linear systems with multiplicative noise [36]. To start, assume the estimator includes a fixed set of known gains  $K_k$ . The optimal controller gains  $L_k$  may be calculated backward in time from known initial values  $S_N^x = Q_N$ ,  $S_N^e = 0$ , and  $s_N = 0$ :

$$\begin{aligned}
L_k &= \left( R_k + B_k^\top S_{k+1}^x B_k + C^\top (S_{k+1}^x + S_{k+1}^e) C \right)^{-1} B_k^\top S_{k+1}^x A_k \\
S_k^x &= Q_k + A_k^\top S_{k+1}^x (A_k - B_k L_k) \\
S_k^e &= A_k^\top S_{k+1}^x B_k L_k + (A_k - K_k)^\top S_{k+1}^e (A_k - K_k) \\
s_k &= \text{tr}(S_{k+1}^x \bar{\Omega}^\xi + S_{k+1}^e (\bar{\Omega}^\xi + \Omega^\eta + K_k \Omega^\delta K_k^\top)) + s_{k+1} \\
\text{Expected cost} &= \hat{x}_1^\top S_1^x \hat{x}_1 + \text{tr}((S_1^x + S_1^e) P_1) + s_1.
\end{aligned} \tag{5.6}$$

Using  $\bar{\Omega}^\xi$  instead of  $\Omega^\xi$  can add robustness to unmodeled dynamics.

### 5.1.1.4 Estimator Gains

Optimizing estimator gains given a fixed set of controller gains also reduces the expected cost [36].

A forward pass in time produces the optimal estimator gains given initial conditions  $P_1^e = P_1$ ,

$P_1^{\hat{x}} = \hat{x}_1 \hat{x}_1^\top$ , and  $P_1^{\hat{x}e} = 0$  (note,  $P_1^{\hat{x}e} = (P_1^{\hat{x}e})^\top$ ):

$$\begin{aligned}
K_k &= A_k P_k^e (P_k^e + \Omega^\delta)^{-1} \\
P_{k+1}^e &= \bar{\Omega}^\xi + \Omega^\eta + (A_k - K_k) P_k^e A_k^\top + C L_k P_k^{\hat{x}} L_k^\top C^\top \\
P_{k+1}^{\hat{x}} &= \Omega^\eta + K_k P_k^e A_k^\top + (A_k - B_k L_k) P_k^{\hat{x}} (A_k - B_k L_k)^\top \\
&\quad + (A_k - B_k L_k) P_k^{\hat{x}e} K_k^\top + K_k P_k^{e\hat{x}} (A_k - B_k L_k)^\top \\
P_{k+1}^{\hat{x}e} &= (A_k - B_k L_k) P_k^{\hat{x}e} (A_k - K_k)^\top - \Omega^\eta.
\end{aligned} \tag{5.7}$$

Repeating controller gain optimization given these improved estimator gains produces an even lower expected cost. Cycling through gain optimization until convergence produces the set of controller and estimator gains with the lowest expected cost.

#### 5.1.1.5 Algorithm Implementation

Now, implementation and simulation of the optimal control algorithm includes

1. Calculate the Kalman gains for the delayed full-state estimator via Eq. (5.3).
2. Calculate the pseudomeasurement covariance via Eq. (5.5).
3. Calculate the optimal open-loop controller gains via Eq. (5.6).
4. Iterate between optimal estimator gain calculation Eq. (5.7) and controller gain calculation Eq. (5.6) until convergence.



5. Simulate the system with Eqs. (5.1), (5.3), and (5.4).

### 5.1.2 Tremor Model Simulations

This research simulates two wrist biomechanics models with the presented optimal controller. First, a single degree-of-freedom (SDOF) model demonstrates the fundamental characteristics of delay-induced tremor. Then, a higher-order model produces simulated tremor with similar characteristics as real tremor, including time-varying amplitude and frequency. The models assume the delay estimate  $\delta\hat{k}$  is equal to the true feedback delay  $\delta k$  in healthy control, with increased true delay representing Parkinson's disease pathology. Control input saturation produces stable limit cycles for cases with increased delays.

#### 5.1.2.1 SDOF Tremor Model

First, this study applies the tremor model to a SDOF joint with a single input to the muscles:

$$\begin{aligned}
 J\ddot{\theta} + G\dot{\theta} + K\theta &= f + f_e \\
 \tau_2\dot{f} + f &= g \\
 \tau_1\dot{g} + g &= u
 \end{aligned} \tag{5.8}$$

which includes muscular torque  $f$  and external torque  $f_e$ . The CNS control input  $u$  activates the muscles, which include second-order low-pass filter dynamics with intermediate state  $g$  and time constants  $\tau_1$  and  $\tau_2$ . Rewrite these dynamics in the standard linear form:

$$\begin{aligned} \dot{x} &= Ax + Bu \\ x &= \begin{bmatrix} \theta & \dot{\theta} & f & g & \theta^* & f_e \end{bmatrix}^\top \\ A &= \begin{bmatrix} 0 & 1 & 0 & 0 & 0 & 0 \\ -K/J & -G/J & -1/J & 0 & 0 & 1/J \\ 0 & 0 & -1/\tau_2 & 1/\tau_2 & 0 & 0 \\ 0 & 0 & 0 & -1/\tau_1 & 0 & 0 \\ 0 & 0 & 0 & 0 & 0 & 0 \\ 0 & 0 & 0 & 0 & 0 & 0 \end{bmatrix} \\ B &= \begin{bmatrix} 0 & 0 & 0 & -1/\tau_1 & 0 & 0 \end{bmatrix}^\top. \end{aligned} \tag{5.9}$$

where the state is augmented with the desired position  $\theta^*$ . Discretizing over the small sample interval  $\Delta t$  enables application of the discrete controller:

$$\begin{aligned} A_k &\approx I + A\Delta t \\ B_k &\approx \Delta t A_k B. \end{aligned} \tag{5.10}$$

The human motor system includes sensory information related to muscle stretch and changes in stretch via muscle spindles along with muscle force from Golgi tendon organs [141]. This study

assumes equally delayed measurements of these quantities due to the close proximity of these mechanoreceptors. Thus, the observation matrix provides equally delayed measurements of the joint position, joint velocity, and muscle force:

$$H = \begin{bmatrix} 1 & 0 & 0 & 0 & 0 & 0 \\ 0 & 1 & 0 & 0 & 0 & 0 \\ 0 & 0 & 1 & 0 & 0 & 0 \end{bmatrix}. \quad (5.11)$$

The cost function depends on the task. For a posture task, the motor system attempts to maintain the desired position  $\theta^*$ . Thus, the controller should minimize  $(\theta - \theta^*)^2$ , producing

$$Q_k = \begin{bmatrix} 1 & 0 & 0 & -1 & 0 & 0 \end{bmatrix}^\top \begin{bmatrix} 1 & 0 & 0 & -1 & 0 & 0 \end{bmatrix} \quad (5.12)$$

for all  $k$ . When  $\theta^* = 0$ , the posture task is considered a resting task. For a reaching task, the motor system attempts to reach the desired position at the final time step  $N$  and maintain that position. Since the task only values final states,  $Q_k = 0$  for  $k < N$ . At final time  $k = N$ , the controller minimizes position error along with velocity and net force to ensure the joint remains at the desired position:

$$\begin{aligned} Q_N = & \begin{bmatrix} 1 & 0 & 0 & -1 & 0 & 0 \end{bmatrix}^\top \begin{bmatrix} 1 & 0 & 0 & -1 & 0 & 0 \end{bmatrix} \\ & + w_v \begin{bmatrix} 0 & 1 & 0 & 0 & 0 & 0 \end{bmatrix}^\top \begin{bmatrix} 0 & 1 & 0 & 0 & 0 & 0 \end{bmatrix} \\ & + w_f \begin{bmatrix} 0 & 0 & -1 & 0 & K & -1 \end{bmatrix}^\top \begin{bmatrix} 0 & 0 & -1 & 0 & K & -1 \end{bmatrix}. \end{aligned} \quad (5.13)$$

The weights  $w_v$  and  $w_f$  scale the influence of the final velocity and final net force compared to final position. Finally, both tasks include a scalar weight for control effort throughout the task:  $R_k = r$ .

Simulations use parameter values associated with wrist FE and controller values tuned to produce good performance for healthy movements [130]. Appendix B.1 presents the MATLAB code for these simulations, including parameter values. Figures 5.2 and 5.3 present a rest task and a reach-posture-reach-posture task, respectively. Both tasks demonstrate controller robustness for healthy motor control by including brief external impulses. The figures present performance given an increased feedback delay of 20 ms: the unaccounted delay leads to instability during rest and posture. However, reaching tasks are successful even with the increased delay. Figure 5.4 captures the fundamental characteristics for delay-induced tremor. A critical delay value produces instability (this value depends on the system parameters; in this case, 15 ms). As the the unaccounted delay increases, tremor amplitude increases and tremor frequency decreases. This property provides additional support for CNS delay as the source of parkinsonian tremor since disease progression produces larger amplitudes and decreased frequencies [33, 142]. In other words, this result suggests the CNS delay increases over time due to disease progression.

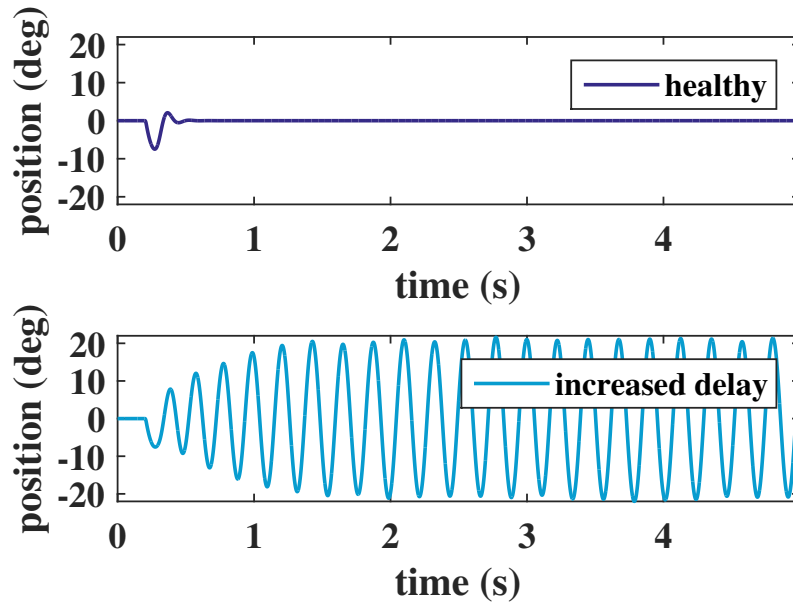


Figure 5.2: Simulation of a rest task with healthy control and increased feedback delay ( $\delta\hat{k} = \delta k + 20$ )

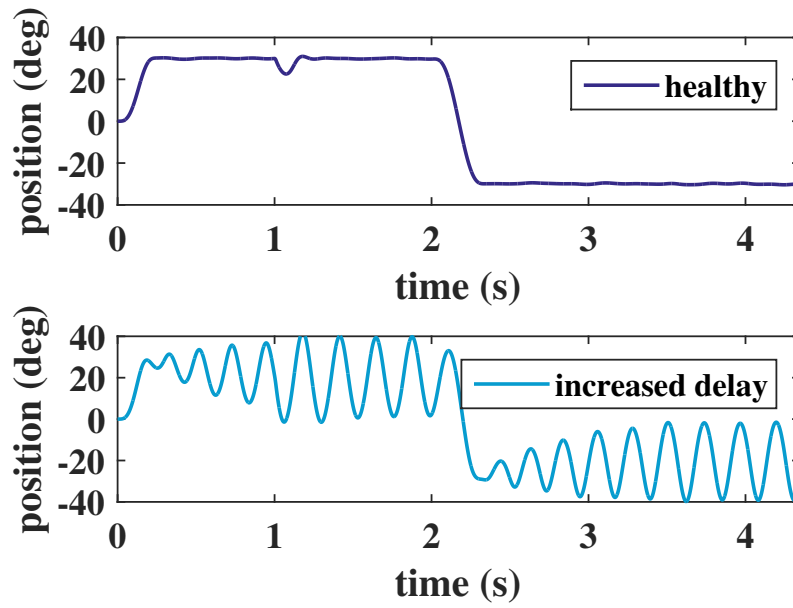


Figure 5.3: Simulation of a reach-posture-reach-posture task with healthy control and increased feedback delay ( $\delta\hat{k} = \delta k + 20$ )

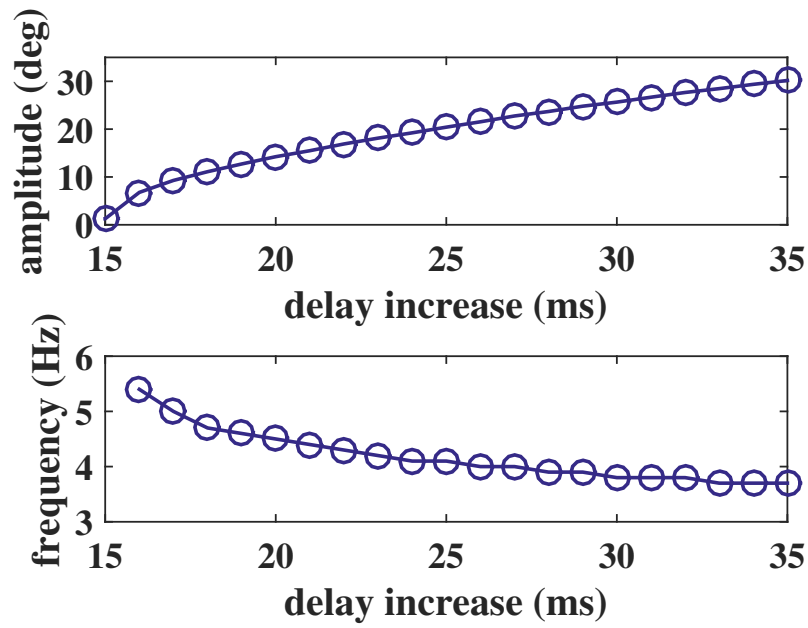


Figure 5.4: Rest tremor amplitude and frequency based on the increased CNS delay

#### 5.1.2.2 Higher-Order Tremor Model

The higher-order model demonstrates how added model complexities produce time-varying tremor amplitudes and frequencies. The model includes a 3DOF wrist with forearm pronation-supination

(PS), wrist FE, and wrist RUD:

$$\begin{aligned}
& \begin{bmatrix} I_{Hy} + I_{Ay} & 0 & 0 \\ 0 & I_{Hz} & 0 \\ 0 & 0 & I_{Hx} \end{bmatrix} \begin{bmatrix} \ddot{\alpha} \\ \ddot{\beta} \\ \ddot{\gamma} \end{bmatrix} + \begin{bmatrix} B_{\alpha\alpha} & B_{\alpha\beta} & B_{\alpha\gamma} \\ B_{\alpha\beta} & B_{\beta\beta} & B_{\beta\gamma} \\ B_{\alpha\gamma} & B_{\beta\gamma} & B_{\gamma\gamma} \end{bmatrix} \begin{bmatrix} \dot{\alpha} \\ \dot{\beta} \\ \dot{\gamma} \end{bmatrix} \\
& + \begin{bmatrix} K_{\alpha\alpha} & K_{\alpha\beta} & K_{\alpha\gamma} \\ K_{\alpha\beta} & K_{\beta\beta} & K_{\beta\gamma} \\ K_{\alpha\gamma} & K_{\beta\gamma} & K_{\gamma\gamma} \end{bmatrix} \begin{bmatrix} \alpha \\ \beta \\ \gamma \end{bmatrix} = \begin{bmatrix} f_{\alpha} \\ f_{\beta} \\ f_{\gamma} \end{bmatrix} + \begin{bmatrix} f_{e\alpha} \\ f_{e\beta} \\ f_{e\gamma} \end{bmatrix}.
\end{aligned} \tag{5.14}$$

where  $\alpha$ ,  $\beta$ , and  $\gamma$  refer to PS angle, FE angle, and RUD angle, respectively [130]. Appendix B.2 presents the MATLAB code for this simulation, including parameter values. The state matrices take a similar form as Eq. (5.9), scaled for the additional degrees-of-freedom.

The higher-order model includes additional CNS elements that contribute to tremor variation. First, noise exists in the human motor system at several levels [141]. This model adds noise to the control saturation. Second, as previously discussed, clinical evidence associates the basal ganglia with movement initiation [115]. Clinical evidence also points towards basal ganglia initiation of changes in tremor amplitude [51]. Initialization of the optimal controller represents basal ganglia initiation of a motor action in the proposed model. Thus, the higher-order model includes resetting of the motor program to reflect re-initiation of the task. In other words, the CNS senses the lack of task success and decides to redefine the controller and restart the task. The model includes random variation for the resetting time and cost function weights.

Figure 5.5 presents rest tremor for this 3DOF wrist model. The resulting tremor characteristics appear much more realistic compared to the SDOF model: tremor amplitude and frequency vary with time. Figure. 5.6 compares the simulated FE angle to the recorded wrist angles from [9] presented in Fig. 3.6. The simulated tremor (dark purple, thickest trace) exhibits similar amplitude and frequency variation as recorded tremor. Indeed, the simulated tremor produces amplitude and frequency standard deviations that are 16% and 4.7% of the mean values, respectively, compared to average values of 18% and 3.1% for recorded tremor. These results demonstrate that even though delay-induced tremor is produced by a clear phenomenon (increased CNS delay), the complexities of the human motor system can produce complex dynamic responses that obscure the tremor source. The fact that a delay-induced tremor model produces tremor with similar characteristics as real tremor provides additional evidence that Parkinson's disease may cause increased CNS delay and motivates clinical research exploring this hypothesis.



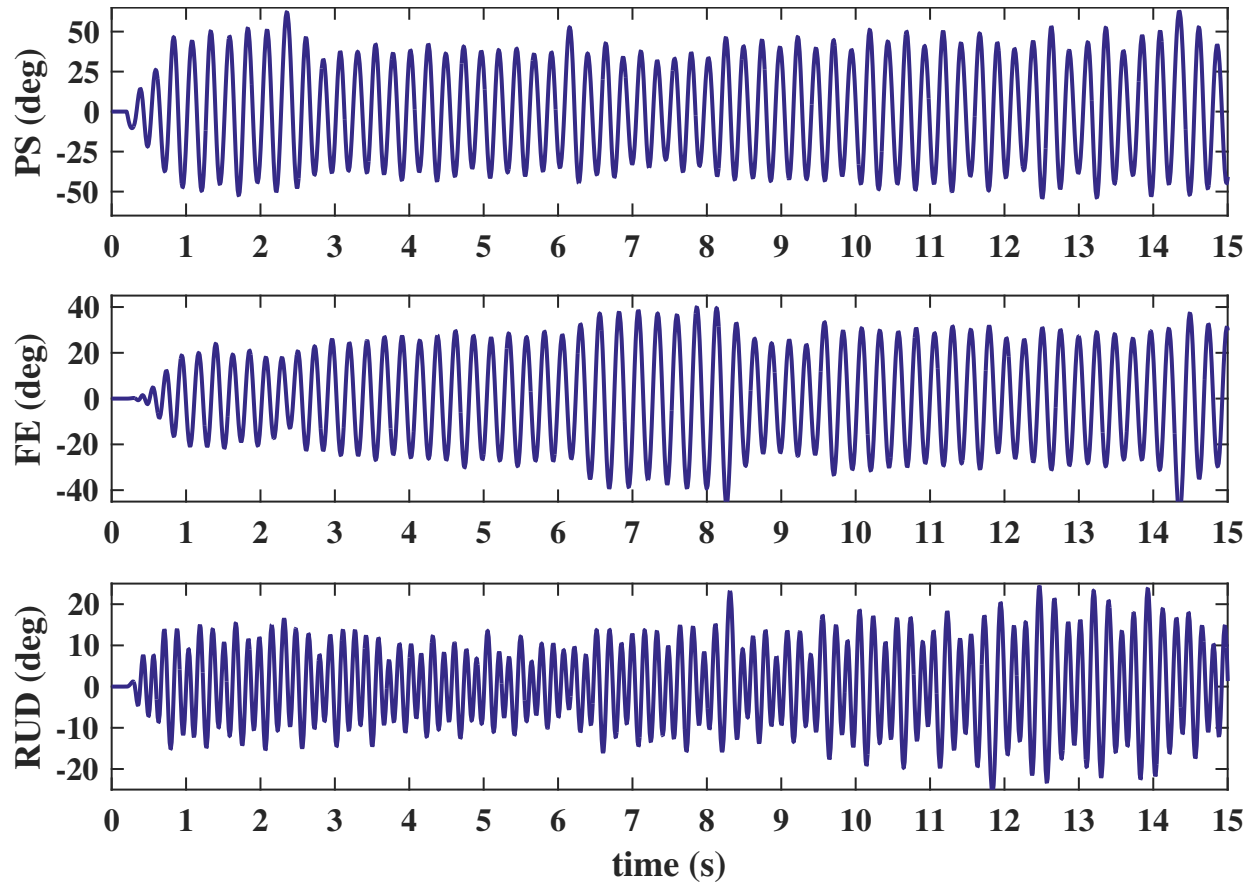


Figure 5.5: Adding complexities to the wrist model (three degrees-of-freedom, control saturation noise, controller resetting) produces tremor that more closely resembles real tremor recordings.

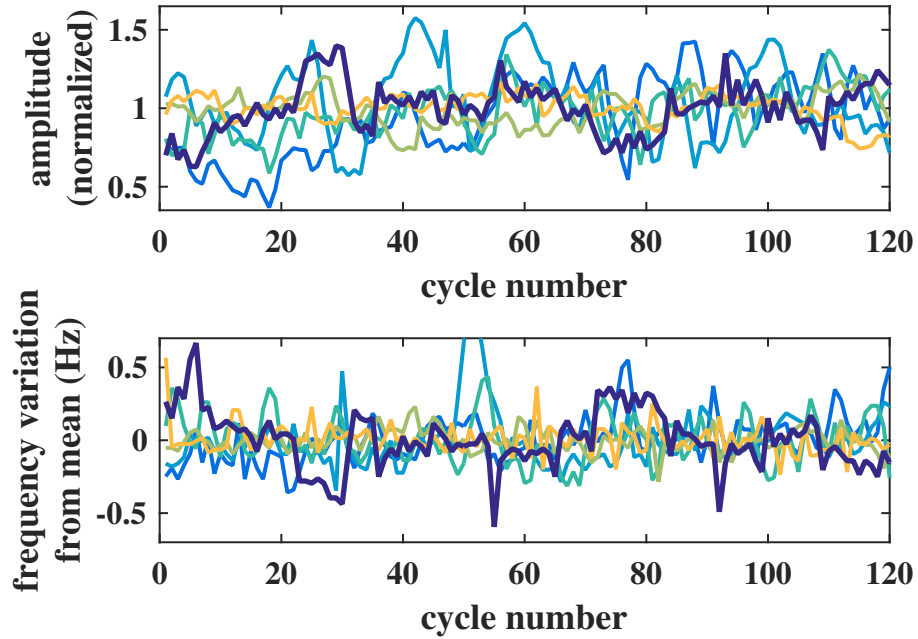


Figure 5.6: Simulated tremor has similar variation in amplitude and frequency as measured tremor (dark/thick trace = simulated, thin traces = 5 recorded tremor datasets from [9]).

## 5.2 Implications

The proposed delay-induced tremor model provides new interpretations of Parkinson's disease theories on pathophysiology and treatment effectiveness. Contextualizing the delay-induced tremor model with previous clinical observations also provides further support for this theory.

### 5.2.1 Physiological Models

*Basal Ganglia Gating Model:* The gating model suggests the basal ganglia acts as a gate for volitional movement, inhibiting the thalamus to prevent undesired motor action (gate closed) and disinhibiting the thalamus to allow desired motor action (gate open) [143]. The delay-induced tremor model suggests excessive inhibition may cause the gate to open only partially, allowing motor action but with delayed signal transfer through the thalamus. Thus, the basal ganglia gating model for volitional movement and the delay-induced tremor model mutually support each other.

*Dimmer-Switch Model:* The dimmer-switch model for parkinsonian tremor suggests the basal ganglia initiates tremor (onset/offset) while the CTC circuit drives tremor [51]. The delay-induced tremor model fits the clinical observations that support the dimmer-switch model, but provides different interpretations of neural characteristics. In the delay model, neural oscillations in the cerebellum and thalamus are the sensor, not the source, for the tremor. Similarly, oscillations in the motor cortex reflect the controller that produces tremor, but the oscillatory activity is the product of the feedback delay, not pathology in the motor cortex. Changes in tremor amplitude are the result of the basal ganglia re-initializing the motor program. Clinical studies indicate the neural networks in parkinsonian tremor are similar to those in healthy motor control, but include oscillatory thalamo-cortical activity. However, this fact does not require the oscillatory activity to be directly induced by abnormal neural bursting [144]. CTC circuit neural oscillation could be consistent with downstream effects of increased feedback delay.

### 5.2.2 Treatments

*Medications:* Dopaminergic medication decreases the inhibition from GPi to VL<sub>a</sub>. Removing or decreasing this excessive inhibition removes or decreases the additional delay.

*Deep Brain Stimulation:* Deep brain stimulation demonstrates tremor reduction when stimulating GPi, VL<sub>p</sub>, or the subthalamic nucleus (STN). Many Parkinson's disease models fail to address how stimulation of both the thalamus and basal ganglia produce tremor reduction (the dimmer-switch hypothesis is a leading model because both regions contribute to tremor) [50]. Like the dimmer-switch hypothesis, the delay-induced tremor model can explain DBS effectiveness for all targeted regions. The diagram in Fig. 5.1 provides insight into how DBS affects delay-induced tremor when considering the three DBS hypotheses: inhibition, excitation, and disruption [145]. Inhibition and disruption hypotheses suggest DBS inhibits neuronal activity or disrupts information flow, respectively. These two hypotheses have similar effect on the delay-induced tremor model (one reduces activity and one stops activity, so the difference is the extent of DBS effectiveness). Disruption of GPi reduces the excessive inhibition projected to the thalamus, reducing or eliminating the pathological delay in a similar manner as dopaminergic medication. Since STN input to GPi produces more GPi inhibitory output to the thalamus, disruption of STN also reduces inhibition and thalamic delay. Finally, disruption of VL<sub>p</sub> disrupts the feedback circuit, initially requiring the motor system to operate without feedback. The aftereffects of thalamotomy (lesion to VL<sub>p</sub>) support this concept: patients initially exhibit decreased perception of body position [52]. Neuroplasticity restores feedback through new neural pathways. Thus, DBS applied to VL<sub>p</sub> may also cause the

CNS to develop new feedback pathways that avoid the pathological delay in the thalamus. The excitation hypothesis for DBS provides another possibility: VLp excitation overcomes the pathological inhibition to decrease or remove the thalamic delay. However, the excitation hypothesis is counterintuitive for stimulation of basal ganglia regions: STN or GPi excitation increases thalamic inhibition. Thus, the delay-induced tremor model supports inhibition and disruption hypotheses for DBS.

*Functional Electrical Stimulation:* Functional electrical stimulation is a non-invasive approach that can offer moderate tremor reduction through electrical stimulation of muscles [62]. Stimulation above the motor threshold provides a clear tremor reduction mechanism: activating the muscles in the opposite direction of tremor reduces tremor. However, stimulation below the motor threshold also reduces tremor. Following the disruption theory of electrical stimulation, FES may disrupt afferent signals, thereby breaking the feedback loop in a similar manner as VLp stimulation. Another possibility is that FES increases noise in the proprioceptive feedback; the CNS detects this increase in sensor noise and adjusts optimal feedback accordingly.

### **5.2.3 Mechanical Tremor Suppression**

Chapters 3 and 4 evaluate tremor suppression for state-independent tremor. A delay-induced tremor may react differently to tremor suppression. Figure 5.7 illustrates the effect of tremor suppression on delay-induced tremor. Each datapoint corresponds to simulated suppression of rest tremor via velocity feedback. Tremor suppression reduces the amplitude and increases the

tremor frequency, mirroring the effect of decreased CNS delay. These simulations demonstrate two facts. First, mechanical tremor suppression is still effective for delay-induced tremor. Second, unlike fixed tremor, mechanical suppression of delay-induced tremor increases the tremor frequency. Thus, clinical evaluation of tremor frequency during tremor suppression may provide additional support for CNS delay as the cause of parkinsonian tremor.

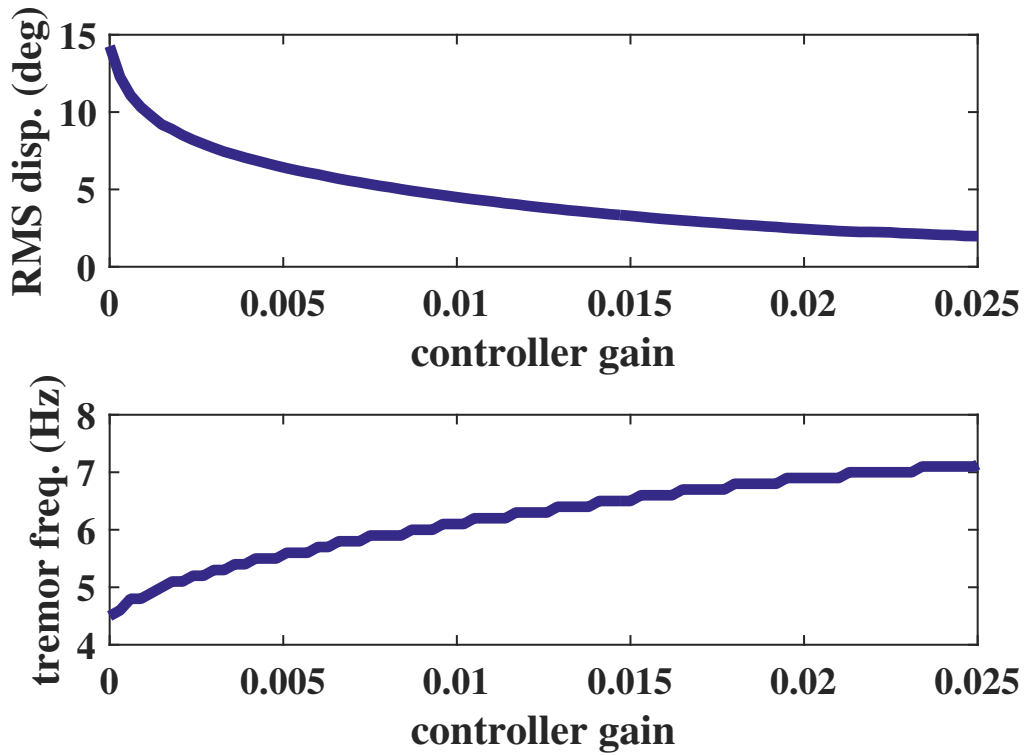


Figure 5.7: Mechanical suppression of delay-induced tremor reduces tremor amplitude and increases tremor frequency.

## **CHAPTER 6**

### **CONCLUSIONS & REMAINING QUESTIONS**

This dissertation applies a mechanical systems perspective to pathological tremor, evaluating mechanical tremor suppression with soft actuators and tremor generation in the human motor feedback loop. Typical tremor treatments are based on empirical findings and have varying effectiveness across patient populations. Selecting medication doses and DBS parameters involves significant guesswork since the mechanisms of tremor reduction are not well understood. Mechanical tremor suppression offers a potential alternative treatment with a well-defined mechanism for tremor reduction. In theory, mechanical tremor suppression reduces tremor irrespective of tremor pathophysiology. However, the bulkiness of typical actuators limits mechanical tremor suppression to laboratory settings. One of the primary objectives of this research is to establish a pathway towards soft, low-profile tremor suppression by exploring dielectric elastomers as tremor suppression actuators. Dielectric elastomer stack actuators actuate linearly and can conform to the human limb in the transverse direction to enable low-profile implementations. However, electrical safety limits restrict the DESA voltage and current, reducing actuation capabilities of actuators that already have relatively low actuation levels. As demonstrated in simulations, these limits can produce poor performance for DESA-based systems that must actuate to track voluntary motion. This research solves this problem by applying a tremor-active approach: DESAs actuate only to suppress tremor.

The human motor system must overcome the passive DESA dynamics. Simulations show excellent and robust tremor suppression, demonstrating the potential for DESA-based devices that suppress tremor at the cost of slight-to-moderate increases in patient effort for voluntary movements.

The promising DESA-based tremor suppression simulations in this research use relatively optimistic DESA parameters. Therefore, this dissertation also investigates the potential for achieving physical systems with acceptable performance. Since DESAs constitute a relatively young class of actuators (only proposed two decades ago!), DESAs currently lack commercial availability, and manufacturing processes require specialized equipment and techniques. Therefore, this research evaluates a scaled system to experimentally validate the fundamental characteristics found in simulations. Folded DESAs enable low-cost implementation, but with large layer thicknesses that produce very low actuation forces. A piezoelectrically actuated cantilever beam represents scaled-down human motion, including voluntary motion and tremor. Experiments demonstrate the ability of DESAs to reduce tremor in a physical system using a tremor-active approach. To work towards real applications, this research quantifies the necessary DESA parameters for clinical implementations by applying limits on the passive DESA dynamics, tracking error, and actuator size. Simulations indicate tremor-active control may achieve satisfactory performance even with moderate levels of current and voltage saturation. Evaluation of literature DESAs indicates two promising pathways for achieving DESAs that meet the necessary parameters for tremor suppression: scaling-up the number of layers of thin-layer silicone DESAs and decreasing crosslinker or adding plasticizer to UV-cured acrylic DESAs.



In addition to tremor suppression, this dissertation explores CNS delay as a potential mechanism for tremor generation in Parkinson's disease. Stochastic optimal control captures the fundamental characteristics of human motor control, with previous clinical evidence mapping control model components to physiological structures. This mapping and known pathological characteristics of Parkinson's disease motivate model structure. Parkinson's disease includes excessive inhibitory projection from the basal ganglia to the thalamus. The thalamus relays signals from the cerebellum to the primary motor cortex. Since the optimal control model represents the cerebellum and primary motor cortex as the state estimator and controller, respectively, increased thalamic inhibition represents an unaccounted CNS delay between estimator and controller. Simulations show that delays above a critical value produce instability, with higher delays producing higher amplitudes and lower tremor frequencies. Adding additional complexities of the human motor system produces simulated tremor with similar time-varying amplitude and frequency characteristics as recorded tremor, providing further evidence of CNS delay as a potential mechanism for tremor generation. A significant advantage of the delay-induced tremor hypothesis is its ability to capture a wide range of known Parkinson's disease characteristics. For example, delay-induced tremor explains the effectiveness of DBS targeting the basal ganglia and the thalamus: DBS disruption of signal flow either reduces excessive inhibition from the basal ganglia or breaks the unstable feedback loop. Finally, this research demonstrates two important properties for mechanical suppression of delay-induced tremor: mechanical suppression can still effectively reduce delay-induced tremor and suppression increases tremor frequency. The latter property may provide a pathway towards obtaining clinical evidence of delay-induced tremor.

## 6.1 Key Contributions

### 6.1.1 DESA-Based Tremor Suppression

While mechanical tremor suppression offers the potential for effective and robust tremor reduction, bulky actuators prohibit clinical implementations. This research is the first to propose dielectric elastomers as actuators for tremor suppression to improve clinical implementation potential. Key advantages of dielectric elastomers are their small size, low weight, low number of mechanical connections, stiffnesses on the same scale or lower than human muscle, electrical actuation, contractile actuation, and high energy density. These advantages can significantly improve patient acceptance of mechanical tremor suppression by enabling low-profile devices. However, such a system must overcome several disadvantages of dielectric elastomers, including their viscoelastic properties, relatively low actuation levels, need for high-voltage power electronics, and lack of commercial availability.

A primary contribution of this research is the development of a control approach that addresses the low actuation levels of dielectric elastomers. Since typical actuators are rigid in their passive state, they must actuate to suppress tremor and follow voluntary motion—this is a fully active approach since the actuators are active for tremor suppression and voluntary motion tracking. In contrast, this research proposes a tremor-active approach for DESA-based tremor suppression: the actuators are only active for tremor suppression while the human motor system overcomes the passive actuator dynamics to complete voluntary tasks. This approach is only possible with com-

pliant actuators like dielectric elastomers: tremor-active control leverages low actuator mechanical impedance to reduce actuation requirements. This approach assumes patients will accept increased effort for voluntary movements to gain low-profile tremor suppression. Simulations demonstrate tremor reduction ranging from typical medication performance to typical DBS performance depending on the voluntary motion and tremor characteristics. Achieving this level of performance in physical systems will make DESA-based tremor suppression a viable clinical treatment option at the very least, with the possibility for developing high-impact, ubiquitous devices.

A second contribution of this research is the evaluation of the outlook for achieving suitable physical implementations of DESA-based tremor suppression. This research provides the first experimental evidence that a DESA-based system can reduce motion in the tremor frequency range to a greater extent than the consequential reduction of motion in the voluntary range, thereby demonstrating an improvement over passive systems. Since the actuation capabilities of the DESAs in these experiments only enable suppression of a scaled-down system, this research identifies DESA parameters to enable implementation in clinical devices. Significantly, this study quantifies performance limits in terms of normalized parameters, generalizing the results for a class of similar joints. One key finding from this investigation is that tremor-active control can produce satisfactory performance even with moderate levels of controller saturation. These results further demonstrate the ability of tremor-active control to improve DESA implementation potential by significantly reducing actuation requirements. Overall, this analysis provides a map of DESA characteristics that meet clinical implementation requirements to motivate the development of commercially available DESAs that meet these requirements. This research identifies the recently developed manufac-

turing method for UV-cured acrylic DESAs as a promising approach for developing DESAs for tremor suppression. These DESAs include thousands of very thin layers to produce relatively large actuators with relatively large actuation abilities. While reported stiffness values are likely too large for tremor-active control, reducing crosslinker or adding plasticizer can decrease stiffness to achieve DESAs that meet the necessary parameters.

### **6.1.2 Tremor Produced via CNS Delay**

Uncovering tremor pathophysiology is an ongoing challenge as researchers work towards improved treatments, cure development, and fundamental understanding of human motor control. A major drawback for many pathophysiology theories is their inability to capture all disease characteristics. In particular, many theories fail to capture how DBS reduces tremor when stimulating the basal ganglia or the thalamus. Furthermore, many theories suggest separate pathologies for parkinsonian tremor and other Parkinson's disease symptoms. This research explores the idea that increased feedback delay in the human motor control loop produces parkinsonian tremor. This mechanism unifies the pathological element for tremor generation and other Parkinson's disease symptoms: excessive CNS inhibition slows movements and causes instability that produces tremor. The primary contribution of this research is the development of an evidence-based human motor control model with CNS delay. Simulations of this model demonstrate increased tremor amplitudes and decreased tremor frequencies as the unaccounted CNS delay increases. These characteristics mirror tremor characteristics as the disease progresses. This research also demonstrates simulated

tremor with time-varying amplitude and frequency that is similar to the variations observed in recorded tremor. This result provides further support for the delay-induced tremor hypothesis. Initially, delay-induced tremor may seem overly simplistic since it produces constant amplitude and frequency for baseline systems. However, adding more complexities of the human motor system produces time-varying amplitudes and frequencies consistent with recorded tremor. Thus, complex tremor characteristics may reflect the many complexities of human motor control while the fundamental cause of tremor is CNS delay.

Another key contribution of this study is the ability to relate the delay-induced tremor model to physiological structures. Previous clinical studies motivate model structure: increased thalamic delay from excessive basal ganglia inhibitory projections produces a delay between the cerebellum (estimator) and primary motor cortex (controller). This delay location provides insight into treatment effectiveness and current theories on tremor pathophysiology. Deep brain stimulation works by inhibiting or disrupting signal flow. Thus, DBS of the STN or GPi reduces tremor by decreasing the excessive inhibition that produces the delay. In addition, DBS of the VLp reduces tremor by breaking the feedback loop; neuroplasticity creates new feedback pathways for motor control. Clinical evidence that supports the dimmer-switch hypothesis of parkinsonian tremor also supports the delay-induced tremor model. Basal ganglia activity produces tremor onset by initializing motor action similar to healthy motor control. The CTC circuit drives tremor amplitude just as it executes healthy motor control, with thalamic delay causing instability. Finally, this research demonstrates the effect of tremor suppression on delay-induced tremor: suppression increases tremor frequency. This fact may present a pathway towards obtaining clinical evidence of

delay-induced tremor. Altogether, this research provides support for CNS delay as the source of parkinsonian tremor, motivating future work towards clinical investigation of this hypothesis.

## **6.2 Remaining Questions**

### **6.2.1 DESA Implementation**

This dissertation establishes the potential benefits of DESA-based tremor suppression, but clinical implementations require advances in DESA manufacturing and high-voltage power electronics. While the literature does not reveal any DESAs that meet the derived necessary parameters for tremor suppression, a recent process using UV-cured acrylic only requires minor adjustments to decrease the Young's modulus of the elastomer. These adjustments (decrease crosslinker concentration or add plasticizer) may be easily implemented in the existing manufacturing process. Even with the existence of manufacturing that produces satisfactory DESAs, the process must be scaled for mass manufacturing to enable widespread implementation of DESA-based tremor suppression.

Dielectric elastomer-based devices also require high-voltage power electronics—ideally in a compact and lightweight form. Despite requiring high voltages, dielectric elastomers operate at relatively low power, enabling operation with relatively small power electronics. Project Peta-pico-Voltron is one example of a relatively small power supply for DEA applications, while an extension for use with HASEL actuators further demonstrates the small profile of even prototype high-voltage power electronics. Furthermore, flyback converters improve energy efficiency by

enabling bidirectional energy flow. Ultimately, continued advances in compact high-voltage, low-current power electronics will facilitate future development of DESA-based tremor suppression devices. In addition, any device requires thorough evaluation of electrical safety for close interaction with the human body. Significantly, the results of this dissertation suggest DESA-based tremor suppression devices can be effective while meeting electrical safety limits.

A final consideration for clinical tremor suppression is general device design. This dissertation focuses on control design and establishing the feasibility of DESA-based tremor suppression. Actual implementations require detailed design considerations to ensure effective transfer of forces from DESAs to joints. The design must also consider ergonomics, user comfort, minimization of device profile, and application to multiple degrees of freedom.

### **6.2.2 Clinical Evaluation of Delay-Induced Tremor**

This dissertation provides theoretical evidence for delay-induced tremor. Future clinical investigation will help to evaluate the validity of this hypothesis. Mechanical tremor suppression is one promising approach to investigate delay-induced tremor clinically: tremor suppression will increase tremor frequency. Brain imaging studies also may help evaluate this hypothesis. This research used clinical evidence to identify the thalamus as a potential location of increased CNS delay (nominally between estimator and controller). However, other delay locations (or multiple delay locations) are conceivable with similar effect. One unclear element of the proposed model is exactly how excessive inhibition of VLa transfers to VLp. Another possibility is that VLa projects

this inhibition to M1: thus, the delay occurs in the primary motor cortex (in optimal control terminology, either just before or after the controller). Altogether, future clinical work should evaluate the validity of CNS delay as the source of tremor along with the exact locations of pathological delay. If future research establishes CNS delay as the source of tremor, this knowledge can inform improved treatments and even facilitate cure development.



**APPENDIX A**  
**MATLAB CODE FOR TREMOR SUPPRESSION SIMULATIONS**

## A.1 Fully Active Simulation

### A.1.1 Execution Script

```
%% Simulate adaptive notch filter controller
% Requires 'park01.mat' file: t=time, x=acceleration data
% Requires 'JarTaskBoth.mat' file: tjar=time, FEjar=FE angle (deg)
clear all; close all;
kdat = 1;
tremorfile = strcat('park0',num2str(kdat),'.mat');

%% System parameters
% DESA parameters
% Material parameters
Y = 0.5e6; eps = 6.9*8.854e-12; density = 1600;
k1 = 1.5*Y; n1 = 0.03*Y;
% Geometrical parameters
n = 2000; do = 50e-6; wo = 1e-2; Ao = wo^2; lo = n*do;
% Inertia
ma = density*Ao*n*do/3;
% Wrist parameters
mw = 0.00276; cw = 0.03; kw = 0.992;
ro = 3e-2; % moment arm of DEA about wrist joint
% DESA parameter vector
pdeap = [k1 n1 Y eps density n do wo]';
% Wrist parameter vector
pwrist = [mw cw kw ro]';

%% Controller parameters
% Notch filter
b1 = -3;
wT = 2*pi*5;
zeta = 0.01;
zeta2 = 0.1;
b2 = -8;
fs = 1000;
Ts = 1/fs;

% Electrical limits
Cap0 = n*eps*Ao/do;
currentlimit = 20e-3;
csat = 4445; % Voltage limit calculated from capacitance
usat = csat^2;
```

```

% High-pass filter
alpha0 = 27979; alpha1 = 631.5; alpha2 = 68.69; alpha3 = 1;
beta0 = 279.3; beta1 = 65.18; beta2 = 9.03; beta3 = 1;

%Band-pass filter
zetaf = 0.025;

% WFLC
muo = 0.00005; % Gain
mu = 0.005;
rho = 1;
xrk = [];
wok = 2*pi*5*Ts;
wo = wok;
M = 1;
for r = 1:M
    xrk(r,1) = sin(r*wo);
end
for r = M+1:2*M
    xrk(r,1) = cos((r-M)*wo);
end
wk = zeros(2*M,1);
wk(1,1) = 1;
xh = wk'*xrk;
xhv = xh;
wkv = wk';
fdom(1,1) = wok/Ts/(2*pi);

% DEA controller
c1 = 4/Ts^2; c2 = 2*k1/(Ts*n1); c3 = -16*ro^2*ma/Ts^3;
c4 = -8*ro^2*ma*k1/(Ts^2*n1); c5 = -4*ro^2*Ao*(Y+k1)/(Ts*lo);
c6 = -2*ro^2*Ao*Y*k1/(lo*n1); c7 = 4*ro*Ao*eps/(Ts^2*do^2);
c8 = 2*ro*Ao*eps*k1/(Ts*do^2*n1);
c78 = -c7-c8;
w1 = (c3+c4+c5+c6)/c78; w2 = (-3*c3-c4+c5+3*c6)/c78;
w3 = (3*c3-c4-c5+3*c6)/c78; w4 = (-c3+c4-c5+c6)/c78;
w5 = (-c1-c2)/c78; w6 = (c1-c2)/c78; w7 = (c1+c2)/c78; w8 = (-c1+c2)/c78;
w9 = (-c7+c8)/c78; w10 = (-c7-c8)/c78; w11 = (c7-c8)/c78;
wvec = [w1 w2 w3 w4 w5 w6 w7 w8 w9 w10 w11]';
yvec = [0 0 0 0]'; Mvec = [0 0 0 0]'; uvec = [0 0 0]';
xvec = [yvec; Mvec; uvec];

zetac = 1;
wc = 600;
Hue = ro*Ao*eps/do^2;
uv = [0; 0];
errv = [0 0 0]';
Mkh = 0;
Mkhv = 0;

%% Voluntary and tremor motion

```

```

% Tremor
load(tremorfile);
time = t;
tauT = 0.1*x;
tautremor = tauT;
Adata = max(x);
% Voluntary
load('JarTaskBoth.mat')
ttask = tjar;
xtask = FEjar;
t = t(1:find(t>ttask(end),1)-1);
time = t;
tautremor = tautremor(1:length(t));
tauT = tautremor;
tvol = t;
xvol = interp1(ttask,xtask,tvol);
xvolrad = pi/180*xvol;
xdvolrad = fDiff(xvolrad,t(2)-t(1),1);
xddvolrad = fDiff(xvolrad,t(2)-t(1),2);
tauvolaa = mw*xddvolrad+cw*xdvolrad+kw*xvolrad;
tauvol = tauvolaa;
tauV = tauvol;
TimmerV = [tvol tauvol];

% Combined wrist torque
tauw = tauV+tauT;
Timmer = [time tauw];

% Simulations with and without tremor
[tuncs,xuncs] = ode45(@ANFsmdDis,time,[0 0]',[],mw,cw,kw,0,Timmer);
xunc = xuncs(:,1);
[tvols,xvols] = ode45(@ANFsmdDis,time,[0 0]',[],mw,cw,kw,0,TimmerV);
xvol = xvols(:,1);

%% Integration parameters
options = [];
x0 = [0 0 0 0];
t0 = 0;
tf = 10;
Nsim = round(fs*tf);
t1 = t0;
t2 = t1+Ts;
t = t0;
x = x0;
taud = 0; tau dv = tau dv;
taudkv1 = [0 0]'; tau dv2 = tau dv1;
ykv = [0 0 0 0]';
xTk v = [0 0 0]';
xTv = 0;
xTfv = 0;
xTfk v = [0 0];

```

```

uk = 0; ukv = uk;

%% Numerical integration
% Integrate over single sampling interval; loop over entire time interval
for k=1:Nsim
    [tk,xk] = ode45(@ANFdea,[t1 t2],x0,options,pdeap,pwrist,Timmer,uk);
    t = [t; tk(end)];
    x = [x; xk(end,:)];
    t1 = t(end); t2 = t1+Ts;
    x0 = x(end,:);

    %% Calculate desired output torque of actuator
    yk = x(end,2); % Measurement and input to notch filter
    ykv = [yk; ykv(1:3)];
    taud1 = 1/(4/Ts^2+4*zeta*wT/Ts+wT^2)*(2*b1/Ts*ykv(1)-2*b1/Ts*ykv(3)+...
        (8/Ts^2-2*wT^2)*taudkv1(1)+(-4/Ts^2+4*zeta*wT/Ts-wT^2)*taudkv1(2));
    taud2 = 1/(4/Ts^2+8*zeta*wT/Ts+4*wT^2)*(2*b2/Ts*ykv(1)...
        -2*b2/Ts*ykv(3)+(8/Ts^2-8*wT^2)*taudkv2(1)+...
        (-4/Ts^2+8*zeta*wT/Ts-4*wT^2)*taudkv2(2));
    taudkv1 = [taud1; taudkv1(1)];
    taudkv2 = [taud2; taudkv2(1)];
    taud = taud1+taud2;
    taudv = [taudv; taud];

    %% Extract Mdea
    ukv = [ukv; uk];
    % Calculate acceleration from EOM
    xdd = 1/(mw+2*ro^2*ma)*(tauw(1:length(t))-cw*x(:,2)-kw*x(:,1)-...
        2*ro^2*Ao*Y/(3*lo)*(1+2./(1+ro^2/lo^2*x(:,1).^2).^2).*x(:,1)+...
        ro*Ao*eps/do^2*(ukv./(1-ro/lo*x(:,1)).*sign(ukv)).^3)+...
        ro*Ao*(x(:,3)./(1-ro/lo*x(:,1))-x(:,4)./(1+ro/lo*x(:,1))));
    Mdea = -2*ro^2*ma*xdd-...
        2*ro^2*Ao*Y/(3*lo)*(1+2./(1+ro^2/lo^2*x(:,1).^2).^2).*x(:,1)+...
        ro*Ao*eps/do^2*(ukv./(1-ro/lo*x(:,1)).*sign(ukv)).^3)+...
        ro*Ao*(x(:,3)./(1-ro/lo*x(:,1))-x(:,4)./(1+ro/lo*x(:,1)));

    % Calculate estimated actuator torque
    Mkh = Mdea(end);
    Mkhv = [Mkhv; Mkh];

    %% Calculate controller input that outputs desired torque
    err = taud-Mkh;
    errv = [err; errv(1:2)];
    uk = 1/(4/Ts^2+4/Ts*zetac*wc)*(wc^2/Hue*errv(1)+2*wc^2/Hue*errv(2)+...
        wc^2/Hue*errv(3)+8/Ts^2*uv(1)+(-4/Ts^2+4/Ts*zetac*wc)*uv(2));

    % Enforce electrical limits
    uc = uk;
    if abs(uc) > usat
        uc = usat*sign(uc);
    end
end

```

```

Vchecknew = sqrt(abs(uc)).*sign(uc);
Vcheckold = sqrt(abs(uv(1))).*sign(uv(1));
dVcheck = Vchecknew-Vcheckold;
dVmax = currentlimit/fs/Cap0;
if abs(dVcheck) > dVmax
    Vnew = Vcheckold+dVmax*sign(dVcheck);
    uc = Vnew^2*sign(Vnew);
end
uk = uc;
uv = [uk; uv(1)];

%% Estimate dominant tremor frequency
% High-pass filter
xTk = 1/(alpha3*8/Ts^3+alpha2*4/Ts^2+alpha1*2/Ts+alpha0)*...
    ((beta3*8/Ts^3+beta2*4/Ts^2+beta1*2/Ts+beta0)*ykv(1)+...
    (-beta3*24/Ts^3-beta2*4/Ts^2+beta1*2/Ts+3*beta0)*ykv(2)+...
    (beta3*24/Ts^3-beta2*4/Ts^2-beta1*2/Ts+3*beta0)*ykv(3)+...
    (-beta3*8/Ts^3+beta2*4/Ts^2-beta1*2/Ts+beta0)*ykv(4)+...
    (alpha3*24/Ts^3+alpha2*4/Ts^2-alpha1*2/Ts-3*alpha0)*xTk(1)+...
    (-alpha3*24/Ts^3+alpha2*4/Ts^2+alpha1*2/Ts-3*alpha0)*xTk(2)+...
    (alpha3*8/Ts^3-alpha2*4/Ts^2+alpha1*2/Ts-alpha0)*xTk(3));
xTk = [xTk; xTk(1:2)];
xTv = [xTv; xTk];

% Band-pass filter
xTf = 1/(4/Ts^2+4*zeta*wT/Ts+wT^2)*(4*zeta*f*wT/Ts*xTk(1)-...
    4*zeta*f*wT/Ts*xTk(3)+(8/Ts^2-2*wT^2)*xTfkv(1)+...
    (-4/Ts^2+4*zeta*wT/Ts-wT^2)*xTfkv(2));
xTfkv = [xTf; xTfkv(1)];
xTfv = [xTfv; xTf];

% WFLC
ek = xTf-wk'*xrk;
sumwx = 0;
for r = 1:M
    sumwx = sumwx+(wk(r)*xrk(M+r)-wk(M+r)*xrk(r));
end
wok = wok+2*muo*ek*sumwx;
wk = wk+2*mu*xrk*ek;
wo = rhow*wo+wok;
for r = 1:M
    xrk(r,1) = sin(r*wo);
end
for r = M+1:2*M
    xrk(r,1) = cos((r-M)*wo);
end
xh = wk'*xrk;
xhv(k+1,1) = xh;
wdom = wok;
fdom(k+1,1) = wdom/Ts/(2*pi);

```

```

wT = 2*pi*fdom(end);

end

%% Calculate actual actuator torque
xdd = 1/(mw+2*ro^2*ma)*(tauw(1:length(t))-cw*x(:,2)-kw*x(:,1)-...
    2*ro^2*Ao*Y/(3*lo)*(1+2./(1+ro^2/lo^2*x(:,1).^2).^2).*x(:,1)+...
    ro*Ao*eps/do^2*(ukv./(1-ro/lo*x(:,1)).*sign(ukv)).^3)+...
    ro*Ao*(x(:,3)./(1-ro/lo*x(:,1))-x(:,4)./(1+ro/lo*x(:,1))));
Mdea = -2*ro^2*ma*xdd-...
    2*ro^2*Ao*Y/(3*lo)*(1+2./(1+ro^2/lo^2*x(:,1).^2).^2).*x(:,1)+...
    ro*Ao*eps/do^2*(ukv./(1-ro/lo*x(:,1)).*sign(ukv)).^3)+...
    ro*Ao*(x(:,3)./(1-ro/lo*x(:,1))-x(:,4)./(1+ro/lo*x(:,1))));

%% Generate plots
% Convert to degrees
xcon = 180/pi*x(:,1);
xunc2 = 180/pi*xunc(1:length(t));
xvol2 = 180/pi*xvol(1:length(t));
trackerr = xcon-xvol2;

set(0,'DefaultAxesFontSize',12,'DefaultTextFontSize',12,...
    'DefaultAxesFontName','Times','DefaultTextFontName','Times',...
    'DefaultAxesFontWeight','bold','DefaultTextFontWeight','bold',...
    'DefaultLineLineWidth',2,'DefaultLineMarkerSize',10,...
    'DefaultFigureColor','w','DefaultFigurePosition',...
    [100 100 0.4*[1600 1600]]);
Colm = colormap(parula(7));
Col = {Colm(1,:),Colm(2,:),Colm(3,:),Colm(4,:),...
    Colm(5,:),Colm(5,:),Colm(6,:),Colm(7,:)};
V = sqrt(abs(ukv)).*sign(ukv);
dVplot = diff(V); dVplot = [0; dVplot];
figure; subplot(3,1,1); plot(t,xunc2,'Color',Col{7})
hold on; plot(t,xcon,'Color',Col{3})
hold on; plot(t,xvol2,'Color',Col{1})
xlim([t0 10])
ylim([-25 10])
legend({'uncontrolled','controlled','desired'},'Position',...
    [0.28 0.842 0.72 0.2],...
    'Units','normalized','Orientation','horizontal');
ylabel('\boldmath$\theta$ \textbf{(deg)}','interpreter','latex')
ax = gca;
ax.YTick = [-25:5:10];
subplot(3,1,2); plot(t,V/1000/4.445,'Color',Col{1})
xlim([t0 10])
ylabel('\boldmath$V/V_{\mathrm{lim}}$','interpreter','latex')
ylim([-1 1])
ax = gca;
ax.YTick = [-1:0.5:1];
subplot(3,1,3); plot(t,dVplot/dVmax,'Color',Col{1})
xlim([t0 10])

```

```
ylim([-1.1 1.1])
xlabel('time (s)')
ylabel('\boldmath$\Delta V/\Delta V_{\mathrm{lim}}$', 'interpreter', 'latex')
```

## A.1.2 Associated Functions

### A.1.2.1 ANFdea

```
function dx = ANFdea(t,x,pdeap,pwrist,Timmer,u)

% Unwrap parameters
% DEAP parameter vector
k1 = pdeap(1); n1 = pdeap(2); Y = pdeap(3); eps = pdeap(4); rho = pdeap(5);
n = pdeap(6); do = pdeap(7); wo = pdeap(8);
Ao = wo^2; lo = n*do; ma = rho*Ao*n*do/3;
% Wrist parameter vector
mw = pwrist(1); cw = pwrist(2); kw = pwrist(3); ro = pwrist(4);

% Wrist torque
tautime = Timmer(:,1); torque = Timmer(:,2);
tw = interp1(tautime,torque,t);

% Differential equations of motion
% x = [theta thetadot sigmamwl sigmamwr]
dx1 = x(2);
dx2 = 1/(mw+2*ro^2*ma)*(tw-cw*x(2)-kw*x(1)-...
    2*ro^2*Ao*Y/(3*lo)*(1+2/(1-ro^2/lo^2*x(1)^2)^2)*x(1)+...
    ro*Ao*eps/do^2*(u/(1-ro/lo*x(1)*sign(u))^3)+...
    ro*Ao*(x(3)/(1-ro/lo*x(1))-x(4)/(1+ro/lo*x(1))));
dx3 = -ro*k1/lo*x(2)-k1/n1*x(3);
dx4 = ro*k1/lo*x(2)-k1/n1*x(4);
dx = [dx1 dx2 dx3 dx4]';
```

### A.1.2.2 ANFsmdDis

```
function dx = ANFsmdDis(t,x,mw,cw,kw,taud,Timmer)

% Wrist torque
```



```

tautime = Timmer(:,1); torque = Timmer(:,2);
tw = interp1(tautime,torque,t);

% Differential equations of motion
% Wrist
dx1 = x(2);
dx2 = 1/mw*(tw+taud-cw*x(2)-kw*x(1));
dx = [dx1 dx2]';

```

### A.1.2.3 fDiff

```

function yd = fDiff(y,dx,nOrder)

ind = 2:length(y)-1;
yd = zeros(size(y));

if nOrder == 1,
    yd(ind) = 1/(2*dx)*(y(ind+1)-y(ind-1));
    yd(1) = 1/(2*dx)*(-y(3)+4*y(2)-3*y(1));
    yd(end) = 1/(2*dx)*(3*y(end)-4*y(end-1)+y(end-2));
elseif nOrder == 2,
    yd(ind) = 1/dx^2*(y(ind+1)-2*y(ind)+y(ind-1));
    yd(1) = 1/dx^2*(-y(4)+4*y(3)-5*y(2)+2*y(1));
    yd(end) = 1/dx^2*(2*y(end)-5*y(end-1)+4*y(end-2)-y(end-3));
end

```

## A.2 Tremor-Active Simulation

### A.2.1 Execution Script

```

%% Simulate tremor-active suppression
% Requires 'et02.mat' file: t=time, x=acceleration data
% Requires 'JarTaskBoth.mat' file: tjar=time, FEjar=FE angle (deg)
close all; clear all;
options = [];
kdat = 2;
tremorfile = strcat('et0',num2str(kdat),'.mat');

```

```

%% Define parameters
% DESA parameters
% Material parameters
Y = 0.5e6; eps = 6.9*8.854e-12; density = 1600;
k1 = 1.5*Y; n1 = 0.03*Y;
% Geometrical parameters
n = 2000; do = 50e-6; wo = 1e-2; Ao = wo^2; lo = n*do;
% Inertia
m = density*Ao*n*do/3;
% Capacitance
Cap0 = n*eps*Ao/do;
% Wrist parameters
mw = 0.00276; cw = 0.03; kw = 0.992;
ro = 3e-2; % moment arm of DEA about wrist joint
% Controller parameters
gainfA = 3e7;
currentlimit = 20e-3;
csat = 4445; % Voltage limit calculated from capacitance
usat = csat^2;
fs = 1000; T = 1/fs;
% DESA parameter vector
pdeap = [k1 n1 Y eps density n do wo]';
% Wrist parameter vector
pwrist = [mw cw kw ro]';

%% Calculate muscular torque
% Specify tremor torque
load(tremorfile);
Adata = max(x);
tautremor = 0.1*x;
TimmerT = [t tautremor];

% Specify voluntary motion
load('JarTaskBoth.mat')
ttask = tjar;
xtask = FEjar;
t = t(1:find(t>ttask(end),1)-1);
time = t;
tautremor = tautremor(1:length(t));
tauT = tautremor;
tvol = t;
xvol = interp1(ttask,xtask,tvol);
xvolrad = pi/180*xvol;
xdvolrad = fDiff(xvolrad,t(2)-t(1),1);
xddvolrad = fDiff(xvolrad,t(2)-t(1),2);
tauvolaa = mw*xddvolrad+cw*xdvolrad+kw*xvolrad;
[tsigf,sigmwf] = ode45(@sigfeom,tvol,0,[],k1,n1,ro,lo,tvol,xdvolrad);
[tsige,sigmwe] = ode45(@sigeeom,tvol,0,[],k1,n1,ro,lo,tvol,xdvolrad);
tauvol = tauvolaa+2*ro^2*m*xddvolrad+...
    2*ro^2*Ao*Y/(3*lo)*(1+2./(1-ro^2/lo^2*xvolrad.^2).^2).*xvolrad+...
    ro*Ao*(sigmwe./(1+ro/lo*xvolrad)-sigmwf./(1-ro/lo*xvolrad));

```

```

TimmerV = [tvol tauvol];

% Simulated voluntary motion
[tvol,xvols] = ode45(@DEAfull,t,[0 0 0 0]',options,...
    pdeap,pwrist,TimmerV,[0; 0],0,30);
xvol = xvols(:,1);

torque = tautremor+tauvol;
tautime = t;

Timmer = [tautime torque];
% Simulated uncontrolled system
[tuncs,xuncs] = ode45(@DEAfull,t,[0 0 0 0]',options,...
    pdeap,pwrist,Timmer,[0; 0],0,30);
xunc = xuncs(:,1);

%% Initialization of filter parameters
% BMFLC for residual estimate
flow = 4; fhigh = 7;
wa = round(2*pi*flow); wb = round(2*pi*fhigh); % frequency range
beta = 50; % number of frequencies
eta = 0.00001; % gain
wvec = [wa:1/beta:wb]';
Tp = 0.5; dT = 1/fs; delta = Tp/dT; alpha1 = 0.05; rho = alpha1^(1/delta);
phi = [];
t0 = 0;
N = beta*(wb-wa);
for k = 0:N-1
    phi(k+1,1) = sin(wa*t0+(k/beta)*t0);
end
for k = N:2*N-1
    phi(k+1,1) = cos(wa*t0+(k/beta)*t0);
end
theta = zeros(length(phi),1);
xh = theta'*phi;
xhv = xh;

%% Integration parameters
x0 = [0 0 0 0];
t0 = 0;
tf = t(end);
fss = fs; % Sampling frequency of controller in Hz
Ts = 1/fss;
Nsim = round(fss*tf)-1;
t1 = t0;
t2 = t1+Ts;
t = t0;
x = x0;
uin = 0; uv = [0; 0];
gainfv = 0;
gainfv2 = 0;

```

```

%% Numerical integration
% Integrate over single sampling interval; loop over entire time interval
for k=1:Nsim
    [tk,xk] = ode45(@DEAfull,[t1 t2],x0,options,...
        pdeap,pwrist,Timmer,uv(end-1:end),t1,Ts);
    t = [t; tk(end)];
    x = [x; xk(end,:)];
    t1 = t(end); t2 = t1+Ts;
    x0 = x(end,:);

    % BMFLC
    E = x(end,2)-xh;
    theta = rho*theta+2*eta*phi*E;
    for kn = 0:N-1
        phi(kn+1,1) = sin(wa*t1+(kn/beta)*t1);
    end
    for kn = N:2*N-1
        phi(kn+1,1) = cos(wa*t1+(kn/beta)*t1);
    end
    xh = theta'*phi;
    xhv(k+1,1) = xh;

    % Ratio of low to high frequency power of tremor estimate
    Nwin = fs*3;
    if k == 1
        Xrwinv = 0;
    end
    if length(xhv) >= Nwin
        xhwin = xhv(end-Nwin+1:end);
    else
        xhwin = [zeros(Nwin-length(xhv),1); xhv];
    end
    Nf = length(xhwin);
    delf = fs/Nf;
    f = [0:Nf-1]*delf;
    f = f';
    Xwin = abs(fft(xhwin,Nf))*2/Nf;
    fvolw = find(f>=2,1);
    fh1 = find(f>=flow,1)-1;
    fh2 = find(f>=fhigh,1);
    Xvolw = sum(Xwin(1:fvolw));
    Xhw = sum(Xwin(fh1:fh2));
    Xrwin = Xvolw/(Xhw+1e-11);
    Xrwinv(k+1,1) = Xrwin;

    % Calculate next controller input
    % Feedback controller with adaptive gain
    gainf = gainfA*exp(-9*Xrwin);
    gainfv(k+1,1) = gainf;
    if length(gainfv) > 1000

```

```

    gainf = mean(gainfv(end-1000:end));
end
gainfv2(k+1,1) = gainf;
% Check voltage saturation
uc = -gainf*xhv(end);
if abs(uc) > usat
    uc = usat*sign(uc);
end
% Check current saturation
uin = uc;
uvun(k+1,1) = uc;
Vchecknew = sqrt(abs(uc)).*sign(uc);
Vcheckold = sqrt(abs(uv(end))).*sign(uv(end));
dVcheck = Vchecknew-Vcheckold;
dVmax = currentlimit/fs/Cap0;
if abs(dVcheck) > dVmax
    Vnew = Vcheckold+dVmax*sign(dVcheck);
    uin = Vnew^2*sign(Vnew);
end
uv(k+1,1) = uin;
end

%% Plot results
set(0,'DefaultAxesFontSize',12,'DefaultTextFontSize',12,...
    'DefaultAxesFontName','Times','DefaultTextFontName','Times',...
    'DefaultAxesFontWeight','bold','DefaultTextFontWeight','bold',...
    'DefaultLineLineWidth',2,'DefaultLineMarkerSize',10,...
    'DefaultFigureColor','w','DefaultFigurePosition',...
    [100 100 0.4*[1600 1600]]);
Colm = colormap(parula(7));
Col = {Colm(1,:),Colm(2,:),Colm(3,:),Colm(4,:),...
    Colm(5,:),Colm(5,:),Colm(6,:),Colm(7,:)};
u = sqrt(abs(uv)).*sign(uv);
dVplot = diff(u); dVplot = [0; dVplot];
figure; subplot(3,1,1); plot(tautime,xunc*180/pi,'Color',Col{7})
hold on; plot(t,x(:,1)*180/pi,'Color',Col{3})
hold on; plot(tautime,xvol*180/pi,'Color',Col{1})
xlim([t0 10])
ylim([-25 10])
legend({'uncontrolled','controlled','desired'},'Position',...
    [0.28 0.842 0.72 0.2],'Units','normalized','Orientation','horizontal');
ylabel('\boldmath$\theta$ \textbf{(deg)}','interpreter','latex')
ax = gca;
ax.YTick = [-25:5:10];
subplot(3,1,2); plot(t,u/1000/4.445,'Color',Col{1})
xlim([t0 10])
ylabel('\boldmath$V/V_{\mathrm{lim}}$','interpreter','latex')
ylim([-1 1])
ax = gca;
ax.YTick = [-1:0.5:1];
subplot(3,1,3); plot(t,dVplot/dVmax,'Color',Col{1})

```

```

xlim([t0 10])
ylim([-1.1 1.1])
xlabel('time (s)')
ylabel('\boldmath$\Delta V/\Delta V_{\mathrm{lim}}$', 'interpreter', 'latex')

```

## A.2.2 Associated Functions

### A.2.2.1 DEAfull

```

function dx = DEAfull(t,x,pdeap,pwrist,Timmer,uin,tu0,Ts)

% Unwrap parameters
% DEAP parameter vector
k1 = pdeap(1); n1 = pdeap(2); Y = pdeap(3); eps = pdeap(4); rho = pdeap(5);
n = pdeap(6); do = pdeap(7); wo = pdeap(8);
Ao = wo^2; lo = n*do; m = rho*Ao*n*do/3;
% Wrist parameter vector
mw = pwrist(1); cw = pwrist(2); kw = pwrist(3); ro = pwrist(4);

% Controller input
u = interp1([tu0; tu0+Ts],uin,t);

% Wrist torque
tautime = Timmer(:,1); torque = Timmer(:,2);
tw = interp1(tautime,torque,t);

% Differential equations of motion
% x1=theta, x2=theta_dot, x3=sigma_maxwell_r, x4=sigma_maxwell_l
dx1 = x(2);
dx3 = k1*ro/lo*x(2)-(k1/n1)*x(3);
dx4 = -k1*ro/lo*x(2)-(k1/n1)*x(4);
dx2 = (1/(mw+2*ro^2*m))*(tw-cw*x(2)-kw*x(1)-...
    2*Y*ro^2*Ao/(3*lo)*(1+2/(1-ro^2/lo^2*x(1)^2)^2)*x(1)+...
    eps*ro*Ao/do^2*u/(1-ro/lo*x(1)*sign(u))^3+...
    ro*Ao*x(4)/(1-ro/lo*x(1))-ro*Ao*x(3)/(1+ro/lo*x(1)));
dx = [dx1 dx2 dx3 dx4]';

```

### A.2.2.2 fDiff

```

function yd = fDiff(y,dx,nOrder)

ind = 2:length(y)-1;
yd = zeros(size(y));

if nOrder == 1,
    yd(ind) = 1/(2*dx)*(y(ind+1)-y(ind-1));
    yd(1) = 1/(2*dx)*(-y(3)+4*y(2)-3*y(1));
    yd(end) = 1/(2*dx)*(3*y(end)-4*y(end-1)+y(end-2));
elseif nOrder == 2,
    yd(ind) = 1/dx^2*(y(ind+1)-2*y(ind)+y(ind-1));
    yd(1) = 1/dx^2*(-y(4)+4*y(3)-5*y(2)+2*y(1));
    yd(end) = 1/dx^2*(2*y(end)-5*y(end-1)+4*y(end-2)-y(end-3));
end

```

### A.2.2.3 sigfeom

```

function dsigf = sigfeom(t,x,k1,n1,ro,lo,tvol,xovolrad)

kin = find(tvol>t,1);
if isempty(kin)
    thetadot = xovolrad(end);
else
    thetadot = (xovolrad(kin)-xovolrad(kin-1))/...
        (tvol(kin)-tvol(kin-1))*(t-tvol(kin-1))+xovolrad(kin-1);
end
dsigf = -ro*k1/lo*thetadot-k1/n1*x(1);

```

### A.2.2.4 sigfeom

```

function dsige = sigfeom(t,x,k1,n1,ro,lo,tvol,xovolrad)

kin = find(tvol>t,1);
if isempty(kin)
    thetadot = xovolrad(end);
else
    thetadot = (xovolrad(kin)-xovolrad(kin-1))/...
        (tvol(kin)-tvol(kin-1))*(t-tvol(kin-1))+xovolrad(kin-1);
end
dsige = ro*k1/lo*thetadot-k1/n1*x(1);

```

**APPENDIX B**  
**MATLAB CODE FOR DELAY-INDUCED TREMOR SIMULATIONS**



## B.1 SDOF Reach-Posture-Reach-Posture Task

### B.1.1 Execution Script

```
% Run reach-posture-reach-posture task with and without CNS delay
close all; clear all;
set(0,'DefaultAxesFontSize',12,'DefaultTextFontSize',12,...
    'DefaultAxesFontName','Times','DefaultTextFontName','Times',...
    'DefaultAxesFontWeight','bold','DefaultTextFontWeight','bold',...
    'DefaultLineLineWidth',1.5,'DefaultLineMarkerSize',10,...
    'DefaultFigureColor','w','DefaultFigurePosition',...
    [100 100 0.35*[1400 1000]]);
Colm = colormap(parula(7));
Col = {Colm(1,:),Colm(2,:),Colm(3,:),Colm(4,:),Colm(5,:),Colm(6,:)};

%% Healthy case
tdeltdiff = 0e-3; % Zero CNS delay
MrprpTask;
subplot(2,1,1); plot(t,x1,'Color',Col{1});
xlabel('time (s)')
ylabel('position (deg)')
legend('healthy')
xlim([0 t(end)])
ylim([-40 40])
ax = gca;
ax.YTick = [-40 -20 0 20 40];

%% CNS delay case
tdeltdiff = 20e-3; % 20 ms CNS delay
MrprpTask;
subplot(2,1,2); plot(t,x1,'Color',Col{3});
xlabel('time (s)')
ylabel('position (deg)')
legend('increased delay')
xlim([0 t(end)])
ylim([-40 40])
ax = gca;
ax.YTick = [-40 -20 0 20 40];
```

## B.1.2 Associated Scripts and Functions

### B.1.2.1 MrprpTask

```
%% Reach-posture-reach-posture task
% Define CNS delay 'tdeldiff' before running script

%% Define parameters
nst = 6;
thetastar = 30*pi/180;
xh1 = zeros(nst,1); % initial state estimate
xh1(5,1) = thetastar;
P1 = zeros(nst,nst); % initial state estimate error covariance
Py1 = eye(nst,nst);
Py1(5,5) = 1e-9;
xhydel0 = xh1;
% State and control history (must be at least as long as delay)
xHist0 = zeros(nst,1,1000);
xHist0(:, :, end) = xh1;
uHist0 = zeros(1000,1);

%% Reaching task
treach = 0.25;
pulse = [1; 0.1; 0];
[tr,xr,ur,xhr,xhydelr,Pr,Pry] = MreachingFun(xh1,P1,Py1,...
    treach,thetastar,uHist0,xHist0,xhydel0,tdeldiff,pulse);

%% Posture task
tpost = 1.75;
pulse = [1-0.25; 0.01; -1];
uHist0 = ur;
xHist0 = xr;
xhydel0 = xhydelr(:, :, end);
xh1 = xhr(:, :, end);
P1 = Pr(:, :, end);
Ply = Pry(:, :, end);
[tp,xp,up,xhp,xhydelp,Pp,Ppy] = MpostureFun(xh1,P1,Py1,...
    tpost,thetastar,uHist0,xHist0,xhydel0,tdeldiff,pulse);

%% Another reaching task
treach2 = 0.35;
pulse = [0.1; 0.1; 0];
thetastar = -30*pi/180;
uHist0 = up;
```

```

xHist0 = xp;
xHist0(5,1,end) = thetastar;
xhydel0 = xhydelp(:, :, end);
xhydel0(5,1) = thetastar;
xh1 = xhp(:, :, end);
xh1(5,1) = thetastar;
P1 = Pp(:, :, end);
Ply = Ppy(:, :, end);
[tr2, xr2, ur2, xhr2, xhydelr2, Pr2, Pry2] = MreachingFun(xh1, P1, Py1, ...
    treach2, thetastar, uHist0, xHist0, xhydel0, tdeldiff, pulse);

%% Another posture task
tpost2 = 2;
pulse = [1; 0.1; 0];
uHist0 = ur2;
xHist0 = xr2;
xhydel0 = xhydelr2(:, :, end);
xh1 = xhr2(:, :, end);
P1 = Pr2(:, :, end);
Ply = Pry2(:, :, end);
[tp2, xp2, up2, xhp2, xhydelp2, Pp2, Ppy2] = MpostureFun(xh1, P1, Py1, ...
    tpost2, thetastar, uHist0, xHist0, xhydel0, tdeldiff, pulse);

%% Assemble results
t = [tr(1:end-1); tp+tr(end)];
t = [t; tr2(2:end)+t(end)];
t = [t; tp2(2:end)+t(end)];
x1r(:,1) = xr(1,1,1:end-1);
x1p(:,1) = xp(1,1,:);
x1r2(:,1) = xr2(1,1,2:end);
x1p2(:,1) = xp2(1,1,2:end);
x1 = 180/pi*[x1r; x1p; x1r2; x1p2];
xh1r(:,1) = xhr(1,1,1:end-1);
xh1p(:,1) = xhp(1,1,:);
xh1r2(:,1) = xhr2(1,1,2:end);
xh1p2(:,1) = xhp2(1,1,2:end);
xh1 = 180/pi*[xh1r; xh1p; xh1r2; xh1p2];
u = [ur(1:end-1); up; ur2(1:end-1); up2(1:end-1)];

```

### B.1.2.2 MreachingFun

```

function [t,x,u,xh,xhydel,P,Py] = MreachingFun(xh1,P1,Py1,tf,...
    thetastar,uHist0,xHist0,xhydel0,tdeldiff,pulse)

```

```

Mparameters;
Mreaching;
Mcontrolgains;
Msimulation;

```

### B.1.2.3 MpostureFun

```

function [t,x,u,xh,xhydel,P,Py] = MpostureFun(xh1,P1,Py1,tf,...
    thetastar,uHist0,xHist0,xhydel0,tdeldiff,pulse)

```

```

Mparameters;
Mposture;
Mcontrolgains;
Msimulation;

```

### B.1.2.4 Mparameters

```

%% Define parameters
G = 0.03;
I = 0.00276;
Kj = 0.992;
usat = 0.9;
tau1 = 40e-3;
tau2 = 40e-3;
delh = 50e-3;
delt = delh+tdeldiff;

dt = 1e-3;
delk = round(delt/dt);
delkh = round(delh/dt);

A = [0 1 0 0 0 0; -Kj/I -G/I 1/I 0 0 1/I; 0 0 -1/tau2 1/tau2 0 0;...
    0 0 0 -1/tau1 0 0; 0 0 0 0 0 0; 0 0 0 0 0 0];
B = [0 0 0 1/tau1 0 0]';
Ak = eye(length(A))+A*dt;
Bk = dt*Ak*B;
nst = length(Ak);
H = [1 0 0 0 0 0; 0 1 0 0 0 0; 0 0 1 0 0 0];

uHist = zeros(delk,1);

```

```

uHist = uHist0(end-delk:end-1);
xHist = zeros(nst,1,delk);
xHist(:,:,1:delk) = xHist0(:,:,end-delk:end-1);

```

### B.1.2.5 Mreaching

```

%% Reaching task for optimal control model

%% Cost function weights
wv = 0.25; % final velocity weight
wf = 1.5; % final muscle force weight
r = 1e-5; % control weight
pvec = [1 0 0 0 -1 0]'; % positional accuracy
vvec = [0 wv 0 0 0 0]'; % zero velocity at final time
fvec = wf*[0 0 -1 0 Kj -1]'; % zero net static force at final time
QN = pvec*pvec'+vvec*vvec'+fvec*fvec';
Qk = 0;
Rk = r;

%% Noise parameters
N = round(tf/dt);
% States over a nominal reaching trajectory help to select noise parameters
out = RelReach(30*pi/180,0.25,dt,I,G,Kj,taul,tau2);
% Multiplicative noise
alpha = 0.1;
C = alpha*Bk;
% Controller Process noise
Omxim = eye(nst);
Omxim(1,1) = 0.1*pi/180;
Omxim(2,2) = Omxim(1,1)*out(2);
Omxim(3,3) = Omxim(1,1)*out(3);
Omxim(4,4) = Omxim(1,1)*out(4);
Omxim(5,5) = Omxim(1,1)*1e-3;
Omxim(6,6) = Omxim(3,3);
Omxim = 1e-3*Omxim;
Omxib = 1e2*Omxim;
% Estimator noise
Ometa = 0*Omxim;
Ometa(6,6) = 1*Ometa(6,6);
% Process noise
Omxl = 0*Omxim;
% Measurement noise
Omsig = 1e-1*Omxim(1:3,1:3);
% Estimator measurement noise
Omsigb = 1e-2*Omxim;

```

### B.1.2.6 Mposture

```
%% Posture task for optimal control model

%% Cost function weights
r = 3e-3; % control weight
pvec = [1 0 0 0 -1 0]'; % positional accuracy
QN = pvec*pvec';
Qk = QN;
Rk = r;

%% Noise parameters
N = round(tf/dt);
% States over a nominal reaching trajectory help to select noise parameters
out = RelReach(30*pi/180,0.25,dt,I,G,Kj,taul,tau2);
% Multiplicative noise
alpha = 0.1;
C = alpha*Bk;
% Controller Process noise
Omxim = eye(nst);
Omxim(1,1) = 0.1*pi/180;
Omxim(2,2) = Omxim(1,1)*out(2);
Omxim(3,3) = Omxim(1,1)*out(3);
Omxim(4,4) = Omxim(1,1)*out(4);
Omxim(5,5) = Omxim(1,1)*1e-3;
Omxim(6,6) = Omxim(3,3);
Omxim = 1e-3*Omxim;
Omxib = 1e2*Omxim;
% Estimator noise
Ometa = 0*Omxim;
Ometa(6,6) = 1*Ometa(6,6);
% Process noise
Omxib = 0*Omxim;
% Measurement noise
Omsig = 1e-1*Omxim(1:3,1:3);
% Estimator measurement noise
Omsigb = 1e-2*Omxim;
```

### B.1.2.7 Mcontrolgains

```
%% Calculate optimal controller
```

```

%% Calculate gains for measurement estimator and pseudomeasurement cov.
% Measurement estimator gains
Kyk = zeros(nst,size(H,1),N-1);
Pykv = zeros(nst,nst,N);
Pykv(:, :, 1) = Py1;
for k = 1:N-1
    Pyk = Pykv(:, :, k);
    Kyk = Ak*Pyk*H'*inv(H*Pyk*H'+Omsig);
    Pykv(:, :, k+1) = Omxib+(Ak-Kyk*H)*Pyk*Ak';
    Kykv(:, :, k) = Kyk;
end
% Pseudomeasurement covariance (ignoring multiplicative noise)
Vkv = zeros(nst,nst,N);
for k = 1
    Vold = Omsigb;
    for kex = 1:delkh
        Vnew = Ak*Vold*Ak'+Omxi;
        Vold = Vnew;
    end
    Vk = Vold;
    Vkv(:, :, k) = Vk;
end

%% Calculate optimal open-loop controller gains
Kkv = zeros(nst,nst,N-1);
kbv = linspace(N-1,1,N-1)';
Lkv = zeros(1,nst,N);
S = zeros(nst,nst,N);
Sx = S;
Se = S;
s = zeros(N,1);
Sx(:, :, N) = QN;
% Calculate control gains backward in time
for kb = 1:N-1
    k = kbv(kb);
    Sxp = Sx(:, :, k+1);
    Sep = Se(:, :, k+1);
    Kk = Kkv(:, :, k);
    Lk = inv(Rk+Bk'*Sxp*Bk+C'*(Sxp+Sep)*C)*Bk'*Sxp*Ak;
    Lkv(:, :, k) = Lk;
    Sx(:, :, k) = Qk+Ak'*Sxp*(Ak-Bk*Lk);
    Se(:, :, k) = Ak'*Sxp*Bk*Lk+(Ak-Kk)'*Sep*(Ak-Kk);
    s(k,1) = trace(Sxp*Omxim+Sep*(Omxim+Ometa+Kk*Vk*Kk'))+s(k+1,1);
end
costv = xh1'*Sx(:, :, 1)*xh1+trace((Sx(:, :, 1)+Se(:, :, 1))*P1)+s(1);

%% Update Kalman gains and control gains until convergence
nitcon = 15;
for kitcon = 2:nitcon
    %% Update Kalman gains given controller gains

```

```

Pe = zeros(nst,nst,N);
Px = Pe; Pxe = Pe;
Pe(:, :, 1) = P1;
Px(:, :, 1) = xh1*xh1';
for k = 1:N-1
    Lk = Lkv(:, :, k);
    Pek = Pe(:, :, k);
    Pvk = Px(:, :, k);
    Pvek = Pxe(:, :, k);
    Pexk = Pvek';
    Kk = Ak*Pek*inv(Pek+Vk);
    Kkv(:, :, k) = Kk;
    Pe(:, :, k+1) = Omxim+Ometa+(Ak-Kk)*Pek*Ak'+C*Lk*Pvk*Lk'*C';
    Px(:, :, k+1) = Ometa+Kk*Pek*Ak'+(Ak-Bk*Lk)*Pvk*(Ak-Bk*Lk)'+...
        (Ak-Bk*Lk)*Pvek*Kk'+Kk*Pexk*(Ak-Bk*Lk)';
    Pxe(:, :, k+1) = (Ak-Bk*Lk)*Pvek*(Ak-Kk)'-Ometa;
end

%% Update controller gains given Kalman gains
kbv = linspace(N-1,1,N-1)';
Lkv = zeros(1,nst,N);
S = zeros(nst,nst,N);
Sx = S;
Se = S;
s = zeros(N,1);
Sx(:, :, N) = QN;
for kb = 1:N-1
    k = kbv(kb);
    Sxp = Sx(:, :, k+1);
    Sep = Se(:, :, k+1);
    Kk = Kkv(:, :, k);
    Lkv(:, :, k) = inv(Rk+Bk'*Sxp*Bk+C'*(Sxp+Sep)*C)*Bk'*Sxp*Ak;
    Sx(:, :, k) = Qk+Ak'*Sxp*(Ak-Bk*Lkv(:, :, k));
    Se(:, :, k) = Ak'*Sxp*Bk*Lkv(:, :, k)+(Ak-Kk)'*Sep*(Ak-Kk);
    s(k,1) = trace(Sxp*Omxim+Sep*(Omxim+Ometa+Kk*Vk*Kk'))+s(k+1);
end
costv(kitcon,1) = xh1'*Sx(:, :, 1)*xh1+trace((Sx(:, :, 1)+...
    Se(:, :, 1))*P1)+s(1);
end

```

### B.1.2.8 Msimulation

```

%% Simulate optimal control human motor system model

%% Initialize system

```



```

x = zeros(nst,1,N);
x(:, :, 1) = xHist0(:, :, end);
xh = x;
xh(:, :, 1) = xh1;
xhydel = xh;
xhydel(:, :, 1) = xhydel0;
y = zeros(size(H,1),1,N-1);
xhy = xh;
u = zeros(N,1);
costkv = zeros(N,1);
P = zeros(nst,nst,N);
P(:, :, 1) = P1;
Py = zeros(nst,nst,N);
Py(:, :, 1) = Py1;

%% Simulate over each time step
for k = 1:N-1
    % Unwrap values at k
    xk = x(:, :, k);
    xhk = xh(:, :, k);
    Lk = Lkv(:, :, k);
    if Qk == QN
        Lk = Lkv(:, :, round(N/2));
    end
    Pk = P(:, :, k);
    Pyk = Py(:, :, k);
    % Control input
    uk = -Lk*xhk;
    if abs(uk) > usat
        uk = usat*sign(uk);
    end
    % Noise terms
    xik = Omxi*randn(nst,1);
    sigk = Omsig*randn(3,1);
    etak = Ometa*randn(nst,1);
    epsk = randn;
    % State update
    xkp = Ak*xk+Bk*uk+xik+epsk*C*uk;
    if k == round(pulse(1)/dt)
        xkp(6,1) = pulse(3);
    elseif k == round((pulse(1)+pulse(2))/dt)
        xkp(6,1) = 0;
    end
    % Measurement
    xdelkv = MatrixHist(x,xHist,k);
    xdelk = xdelkv(:, :, 1);
    yk = H*xdelk+sigk;
    % Delayed state estimate from measurement
    uEx = VectorHist(u,uHist,k);
    Kyk = Kykv(:, :, k);
    xhydelk = xhydel(:, :, k);

```

```

xhydelp = Ak*xhydelk+Bk*uEx(1)+Kyk*(yk-H*xhydelk);
Pyp = Omxi+(Ak-Kyk*H)*Pyk*Ak';
% Extrapolate state estimate from measurement
xold = xhydelk;
for kex = 1:delkh
    uold = uEx(kex);
    xnew = Ak*xold+Bk*uold;
    xold = xnew;
end
xhyk = xold;
% Estimate
Kk = Kkv(:, :, k); % Non-adaptive
xhp = Ak*xhk+Bk*uk+Kk*(xhyk-xhk)+etak;
Pp = Omxi+Ometa+(Ak-Kk)*Pk*Ak'+C*uk*uk'*C';
% Store new values
x(:, :, k+1) = xkp;
y(:, :, k) = yk;
xhy(:, :, k) = xhyk;
u(k, 1) = uk;
xhydel(:, :, k+1) = xhydelp;
xh(:, :, k+1) = xhp;
costkv(k, 1) = xk'*Qk*xk+uk'*Rk*uk;
P(:, :, k+1) = Pp;
Py(:, :, k+1) = Pyp;
end
costkv(N, 1) = xkp'*QN*xkp;
cost = sum(costkv);

t = [0:dt:tf-dt]';
x1(:, 1) = 180/pi*x(1, 1, :);
x2(:, 1) = x(2, 1, :);
x3(:, 1) = x(3, 1, :);
x1h(:, 1) = 180/pi*xh(1, 1, :);
y1(:, 1) = 180/pi*y(1, 1, :); y1(end+1) = y1(end);
y1h(:, 1) = 180/pi*xhy(1, 1, :);
Fe(:, 1) = x(6, 1, :);
Feh(:, 1) = xh(6, 1, :);

```

### B.1.2.9 RelReach

```

function out = RelReach(thetastar,tf,T,J,G,Kj,taul,tau2)

% Calculate state values over reaching interval
t = [0:T:tf]';
theta = thetastar*(t/tf-1/(2*pi)*sin(2*pi*t/tf));

```

```

thetad = thetastar/tf*(1-cos(2*pi*t/tf));
thetadd = 2*pi*thetastar/tf^2*sin(2*pi*t/tf);
thetaddd = 4*pi^2*thetastar/tf^3*cos(2*pi*t/tf);
thetadddd = -8*pi^3*thetastar/tf^4*sin(2*pi*t/tf);
f = J*thetadd+G*thetad+Kj*theta;
fd = J*thetaddd+G*thetadd+Kj*thetad;
fdd = J*thetadddd+G*thetaddd+Kj*thetadd;
g = tau2*fd+f;
gd = tau2*fdd+fd;
u = tau1*gd+g;

% Normalize rms values by final position
out1 = rms(theta)/thetastar;
out2 = rms(thetad)/thetastar;
out3 = rms(f)/thetastar;
out4 = rms(g)/thetastar;

% Output rms of u to help calculate multiplicative noise
out5 = rms(u);

% Normalize sum of squared control by squared final position
out6 = sum(u.^2)/thetastar^2;

% Generate output vector
out = [out1 out2 out3 out4 out5 out6]';

```

### B.1.2.10 VectorHist

```

function Xv = VectorHist(X,Xhist,k)

% Given a one-dimensional variable X in which X(k,1) is value
% of the scalar at time k, output the variable Xv which is the portion
% of X and Xhist needed to integrate from k-delk to k, where
% Xhist is the previous time history of the scalar with length kdel

% Xv is Matrix(k-delk:k-1)

delk = length(Xhist);
if k > delk
    Xv(1:delk) = X(k-delk:k-1);
elseif k == 1
    Xv = Xhist;
else
    Xv(1:delk-k+1) = Xhist(end-(delk-k):end);
    Xv(delk-k+2:delk) = X(1:k-1);

```

```
end
```

### B.1.2.11 MatrixHist

```
function Xv = MatrixHist(X,Xhist,k)

% Given a three-dimensional variable X in which X(:, :, k) is value
% of the matrix at time k, output the variable Xv which is the portion
% of X and Xhist needed to integrate from k-delk to k, where
% Xhist is the previous time history of the matrix with length kdel

% Xv is Matrix(:, :, k-delk:k-1)

delk = length(Xhist(1,1,:));
if k > delk
    Xv(:, :, 1:delk) = X(:, :, k-delk:k-1);
elseif k == 1
    Xv = Xhist;
else
    Xv(:, :, 1:delk-k+1) = Xhist(:, :, end-(delk-k):end);
    Xv(:, :, delk-k+2:delk) = X(:, :, 1:k-1);
end
```

## B.2 3DOF Rest Tremor

### B.2.1 Execution Script

```
%% Simulate 3DOF wrist with delay, tremor resetting, and saturation noise
close all; clear all;

%% Define parameters
tdeltdiff = 20e-3; % CNS delay
nst = 18; ninp = 3; % number of states, number of DOF
thetastar = 0*pi/180; % desired position
xh0 = zeros(nst,1); % initial state estimate
xh0(5,1) = thetastar;
P1 = zeros(nst,nst); % initial state estimate error covariance
Py1 = 1e-5*eye(nst,nst);
```

```

xhydel0 = xh0;
% State and control history (must be at least as long as delay)
xHist0 = zeros(nst,1,1000);
xHist0(:, :, end) = xh0;
uHist0 = zeros(ninp,1,1000);
% Tremor resetting parameters
tmean = 2;
Omtmean = 0.8;

%% Initial execution of rest task
trest = tmean+Omtmean*randn;
while trest <= 0.01
    trest = tmean+Omtmean*randn;
end
pulse = [0.2; 0.01; -1];
[tr,xr,ur,xhr,xhydelr,Pr,Pry] = M3postureFun(xh0,P1,Py1,...
    trest,thetastar,uHist0,xHist0,xhydel0,tdeldiff,pulse);

t = tr;
x1(:,1) = xr(1,1,:);
xh1(:,1) = xhr(1,1,:);
x2(:,1) = xr(7,1,:);
xh2(:,1) = xhr(7,1,:);
x3(:,1) = xr(13,1,:);
xh3(:,1) = xhr(13,1,:);
u1(:,1) = ur(1,1,:);
u2(:,1) = ur(2,1,:);
u3(:,1) = ur(3,1,:);

%% Rest task with tremor resetting
for kreset = 1:15
    tpost = tmean+Omtmean*randn;
    while tpost <= 0.01
        tpost = tmean+Omtmean*randn;
    end
    pulse = [0.2; 0.01; 0];
    uHist0 = ur;
    xHist0 = xr;
    xhydel0 = xhydelr(:, :, end);
    xh0 = xhr(:, :, end);
    P1 = Pr(:, :, end);
    Ply = Pry(:, :, end);
    [tp,xp,up,xhp,xhydelp,Pp,Ppy] = M3postureFun(xh0,P1,Py1,...
        tpost,thetastar,uHist0,xHist0,xhydel0,tdeldiff,pulse);
    ur = up; xr = xp; xhydelr = xhydelp; xhr = xhp; Pr = Pp; Pry = Ppy;

    t = [t; tp(2:end)+t(end)];
    x1p = []; x1p(:,1) = xp(1,1,2:end);
    x1 = [x1; x1p];
    xh1p = []; xh1p(:,1) = xhp(1,1,2:end);
    xh1 = [xh1; xh1p];

```

```

x2p = []; x2p(:,1) = xp(7,1,2:end);
x2 = [x2; x2p];
xh2p = []; xh2p(:,1) = xhp(7,1,2:end);
xh2 = [xh2; xh2p];

x3p = []; x3p(:,1) = xp(13,1,2:end);
x3 = [x3; x3p];
xh3p = []; xh3p(:,1) = xhp(13,1,2:end);
xh3 = [xh3; xh3p];

u1p = []; u1p(:,1) = up(1,1,2:end);
u1 = [u1; u1p];
u2p = []; u2p(:,1) = up(2,1,2:end);
u2 = [u2; u2p];
u3p = []; u3p(:,1) = up(3,1,2:end);
u3 = [u3; u3p];
end
x1 = 180/pi*x1;
x2 = 180/pi*x2;
x3 = 180/pi*x3;

%% Plot tremor time series
set(0, 'DefaultAxesFontSize',12, 'DefaultTextFontSize',12,...
    'DefaultAxesFontName', 'Times', 'DefaultTextFontName', 'Times',...
    'DefaultAxesFontWeight', 'bold', 'DefaultTextFontWeight', 'bold',...
    'DefaultLineLineWidth',1.5, 'DefaultLineMarkerSize',10,...
    'DefaultFigureColor', 'w', 'DefaultFigurePosition',...
    [100 100 0.4*[1800 1200]]);
Colm = colormap(parula(7));
Col = {Colm(1,:), Colm(2,:), Colm(3,:), Colm(4,:), Colm(5,:), Colm(6,:)};

figure;
subplot(3,1,1); plot(t,x1, 'Color',Col{1});
ylabel('PS (deg)')
xlim([0 15])
ylim([-65 65])
ax = gca;
ax.XTick = [0:1:15];
ax.YTick = [-50:25:50];
subplot(3,1,2); plot(t,x2, 'Color',Col{1});
ylabel('FE (deg)')
xlim([0 15])
ylim([-45 45])
ax = gca;
ax.XTick = [0:1:15];
ax.YTick = [-40:20:40];
subplot(3,1,3); plot(t,x3, 'Color',Col{1});
xlabel('time (s)')
ylabel('RUD (deg)')
xlim([0 15])

```

```
ylim([-25 25])
ax = gca;
ax.XTick = [0:1:15];
ax.YTick = [-20:10:20];
```

## B.2.2 Associated Scripts and Functions

### B.2.2.1 M3postureFun

```
function [t,x,u,xh,xhydel,P,Py] = M3postureFun(xh1,P1,Py1,tf,...
    thetastar,uHist0,xHist0,xhydel0,tdeldiff,pulse)

%% Define parameters
Kaa = 0.756; Baa = 0.0236;
Kbb = 0.992; Bbb = 0.03;
Kgg = 2.92; Bgg = 0.0882;
Kab = 0.0175; Kag = 0.291; Kbg = -0.0991;
Bab = 0.000791; Bag = 0.00831; Bbg = -0.00316;
Igg = 0.00317; Ibb = 0.00276; Iaa = 0.000501+0.00137;
taua1 = 40e-3; taua2 = 40e-3;
taub1 = 40e-3; taub2 = 40e-3;
taug1 = 40e-3; taug2 = 40e-3;
delh = 50e-3;
delt = delh+tdeldiff;

usat = [0.8 0.9 2.5]';
Omusat = [0.2 0.3 1]';

%% Discretization parameters
dt = 1e-3;
delk = round(delt/dt);
delkh = round(delh/dt);

%% Calculate matrices
Arz = zeros(1,18);

Ar1 = Arz; Ar1(2) = 1;
Ar2 = 1/Iaa*[-Kaa -Baa 1 0 0 1 -Kab -Bab 0 0 0 0 -Kag -Bag 0 0 0 0];
Ar3 = Arz; Ar3(3) = -1/taua2; Ar3(4) = 1/taua2;
Ar4 = Arz; Ar4(4) = -1/taua1;
Ar5 = Arz; Ar6 = Arz;

Ar7 = Arz; Ar7(8) = 1;
```

```

Ar8 = 1/Ibb*[-Kab -Bab 0 0 0 0 -Kbb -Bbb 1 0 0 1 -Kbg -Bbg 0 0 0 0];
Ar9 = Arz; Ar9(9) = -1/taub2; Ar9(10) = 1/taub2;
Ar10 = Arz; Ar10(10) = -1/taub1;
Ar11 = Arz; Ar12 = Arz;

Ar13 = Arz; Ar13(14) = 1;
Ar14 = 1/Igg*[-Kag -Bag 0 0 0 0 -Kbg -Bbg 0 0 0 0 -Kgg -Bgg 1 0 0 1];
Ar15 = Arz; Ar15(15) = -1/taug2; Ar15(16) = 1/taug2;
Ar16 = Arz; Ar16(16) = -1/taug1;
Ar17 = Arz; Ar18 = Arz;

A = [Ar1; Ar2; Ar3; Ar4; Ar5; Ar6; Ar7; Ar8; Ar9;...
      Ar10; Ar11; Ar12; Ar13; Ar14; Ar15; Ar16; Ar17; Ar18];

B = zeros(18,3);
B(4,1) = 1/taua1; B(10,2) = 1/taub1; B(16,3) = 1/taug1;

Ak = eye(length(A))+A*dt;
Bk = dt*Ak*B;
nst = length(Ak);

H = zeros(9,18);
H(1,1) = 1; H(2,2) = 1; H(3,3) = 1;
H(4,7) = 1; H(5,8) = 1; H(6,9) = 1;
H(7,13) = 1; H(8,14) = 1; H(9,15) = 1;

nmea = size(H,1);
ninp = size(B,2);

%% History matrices
uHist = zeros(ninp,1,delk);
uHist(:, :, 1:delk) = uHist0(:, :, end-delk:end-1);
xHist = zeros(nst,1,delk);
xHist(:, :, 1:delk) = xHist0(:, :, end-delk:end-1);

%% Posture task
rb = 2e-3+0.8e-3*randn; % control weight
rg = 0.5e-3+0.2e-3*randn; % control weight
ra = 2e-3+0.8e-3*randn;

wpb = 1;
wpg = 1;
wpa = 1;

pvz = zeros(nst,1);
pveca = pvz; pvecb = pvz; pvecg = pvz;
pveca(1) = 1; pveca(5) = -1; pveca = pveca*wpa;
pvecb(7) = 1; pvecb(11) = -1; pvecb = pvecb*wpb;
pvecg(13) = 1; pvecg(17) = -1; pvecg = pvecg*wpg;
QN = pveca*pveca'+pvecb*pvecb'+pvecg*pvecg';
QN = QN;

```



```

Qk = QN;
Rk = [ra 0 0; 0 rb 0; 0 0 rg];

%% Noise parameters
N = round(tf/dt);
outb = RelReach(30*pi/180,0.25,dt,Ibb,Bbb,Kbb,taub1,taub2);
outg = RelReach(30*pi/180,0.25,dt,Igg,Bgg,Kgg,taug1,taug2);
outa = RelReach(30*pi/180,0.25,dt,Iaa,Baa,Kaa,taua1,taua2);
% Multiplicative noise
alpha = 0.1;
C = alpha*Bk;
% Controller process noise
Omxim = eye(nst);
Omxim(1,1) = 0.1*pi/180;
Omxim(2,2) = Omxim(1,1)*outa(2);
Omxim(3,3) = Omxim(1,1)*outa(3);
Omxim(4,4) = Omxim(1,1)*outa(4);
Omxim(5,5) = Omxim(1,1)*1e-3;
Omxim(6,6) = 1e0*Omxim(3,3);
Omxim(7,7) = 0.1*pi/180;
Omxim(8,8) = Omxim(1,1)*outb(2);
Omxim(9,9) = Omxim(1,1)*outb(3);
Omxim(10,10) = Omxim(1,1)*outb(4);
Omxim(11,11) = Omxim(1,1)*1e-3;
Omxim(12,12) = 1e0*Omxim(9,9);
Omxim(13,13) = 0.1*pi/180;
Omxim(14,14) = Omxim(1,1)*outg(2);
Omxim(15,15) = Omxim(1,1)*outg(3);
Omxim(16,16) = Omxim(1,1)*outg(4);
Omxim(17,17) = Omxim(1,1)*1e-3;
Omxim(18,18) = 1e0*Omxim(15,15);
Omxim = 1e-3*Omxim;
Omxib = 1e2*Omxim;
% Estimator noise
Ometa = 0*Omxim;
% Process noise
Omxib = 0*Omxim;
% Measurement noise
Omsig = zeros(round(nmea),round(nmea));
for koms = 1:nmea
    Omsig(koms,koms) = 1e-1*Omxim(koms,koms);
end
% Estimator measurement noise
Omsigb = 1e-2*Omxim;

%% Calculate gains for measurement estimator and pseudomeasurement cov.
% Measurement estimator gains
Kykv = zeros(nst,size(H,1),N-1);
Pykv = zeros(nst,nst,N);
Pykv(:, :, 1) = Py1;
for k = 1:N-1

```

```

    Pyk = Pykv(:, :, k);
    Kyk = Ak*Pyk*H'*inv(H*Pyk*H'+Omsig);
    Pykv(:, :, k+1) = Omxib+(Ak-Kyk*H)*Pyk*Ak';
    Kykv(:, :, k) = Kyk;
end
% Pseudomeasurement covariance (ignoring multiplicative noise)
Vkv = zeros(nst,nst,N);
for k = 1
    Vold = Omsigb;
    for kex = 1:delkh
        Vnew = Ak*Vold*Ak'+Omxi;
        Vold = Vnew;
    end
    Vk = Vold;
    Vkv(:, :, k) = Vk;
end

%% Calculate optimal open-loop controller gains
Kkv = zeros(nst,nst,N-1);
kbv = linspace(N-1,1,N-1)';
Lkv = zeros(ninp,nst,N);
S = zeros(nst,nst,N);
Sx = S;
Se = S;
s = zeros(N,1);
Sx(:, :, N) = QN;
% Calculate control gains backward in time
for kb = 1:N-1
    k = kbv(kb);
    Sxp = Sx(:, :, k+1);
    Sep = Se(:, :, k+1);
    Kk = Kkv(:, :, k);
    Lk = inv(Rk+Bk'*Sxp*Bk+C'*(Sxp+Sep)*C)*Bk'*Sxp*Ak;
    Lkv(:, :, k) = Lk;
    Sx(:, :, k) = Qk+Ak'*Sxp*(Ak-Bk*Lk);
    Se(:, :, k) = Ak'*Sxp*Bk*Lk+(Ak-Kk)'\*Sep*(Ak-Kk);
    s(k,1) = trace(Sxp*Omxim+Sep*(Omxim+Ometa+Kk*Vk*Kk'))+s(k+1,1);
end
costv = xh1'*Sx(:, :, 1)*xh1+trace((Sx(:, :, 1)+Se(:, :, 1))*P1)+s(1);

%% Update Kalman gains and control gains until convergence
nitcon = 15;
for kitcon = 2:nitcon
    %% Update Kalman gains given controller gains
    Pe = zeros(nst,nst,N);
    Px = Pe; Pxe = Pe;
    Pe(:, :, 1) = P1;
    Px(:, :, 1) = xh1*xh1';
    for k = 1:N-1
        Lk = Lkv(:, :, k);
        Pek = Pe(:, :, k);

```

```

    Pvk = Px(:, :, k);
    Pvek = Pxe(:, :, k);
    Pexk = Pvek';
    Kk = Ak*Pek*inv(Pek+Vk);
    Kkv(:, :, k) = Kk;
    Pe(:, :, k+1) = Omxim+Ometa+(Ak-Kk)*Pek*Ak'+C*Lk*Pvk*Lk'*C';
    Px(:, :, k+1) = Ometa+Kk*Pek*Ak'+(Ak-Bk*Lk)*Pvk*(Ak-Bk*Lk)'+...
        (Ak-Bk*Lk)*Pvek*Kk'+Kk*Pexk*(Ak-Bk*Lk)';
    Pxe(:, :, k+1) = (Ak-Bk*Lk)*Pvek*(Ak-Kk)'-Ometa;
end

%% Update controller gains given Kalman gains
kbv = linspace(N-1,1,N-1)';
Lkv = zeros(ninp,nst,N);
S = zeros(nst,nst,N);
Sx = S;
Se = S;
s = zeros(N,1);
Sx(:, :, N) = QN;
for kb = 1:N-1
    k = kbv(kb);
    Sxp = Sx(:, :, k+1);
    Sep = Se(:, :, k+1);
    Kk = Kkv(:, :, k);
    Lkv(:, :, k) = inv(Rk+Bk'*Sxp*Bk+C'*(Sxp+Sep)*C)*Bk'*Sxp*Ak;
    Sx(:, :, k) = Qk+Ak'*Sxp*(Ak-Bk*Lkv(:, :, k));
    Se(:, :, k) = Ak'*Sxp*Bk*Lkv(:, :, k)+(Ak-Kk)'*Sep*(Ak-Kk);
    s(k,1) = trace(Sxp*Omxim+Sep*(Omxim+Ometa+Kk*Vk*Kk'))+s(k+1);
end
costv(kitcon,1) = xh1'*Sx(:, :, 1)*xh1+trace((Sx(:, :, 1)+...
    Se(:, :, 1))*P1)+s(1);
end

%% Initialize system for simulation
x = zeros(nst,1,N);
x(:, :, 1) = xHist0(:, :, end);
xh = x;
xh(:, :, 1) = xh1;
xhydel = xh;
xhydel(:, :, 1) = xhydel0;
y = zeros(nmea,1,N-1);
xhy = xh;
u = zeros(ninp,1,N);
costkv = zeros(N,1);
P = zeros(nst,nst,N);
P(:, :, 1) = P1;
Py = zeros(nst,nst,N);
Py(:, :, 1) = Py1;

%% Simulate over each time step
for k = 1:N-1

```

```

% Unwrap values at k
xk = x(:, :, k);
xhk = xh(:, :, k);
Lk = Lkv(:, :, k);
Pk = P(:, :, k);
Pyk = Py(:, :, k);
% Control input
uk = -Lk*xhk;
for kinp = 1:ninp
    usatk = usat(kinp)+Omusat(kinp)*randn;
    if abs(uk(kinp)) > usatk
        ukkinp = usatk*sign(uk(kinp));
        if sign(ukkinp) ~= sign(uk(kinp))
            ukkinp = -ukkinp;
        end
        uk(kinp) = ukkinp;
    end
end
% Noise terms
xik = Omxi*randn(nst,1);
sigk = Omsig*randn(nmea,1);
etak = Ometa*randn(nst,1);
epsk = randn(ninp,1);
epskm = zeros(ninp);
for kinp = 1:ninp
    epskm(kinp,kinp) = epsk(kinp);
end
% State update
xkp = Ak*xk+Bk*uk+xik+C*epskm*uk;
if k == round(pulse(1)/dt)
    xkp(6,1) = pulse(3);
elseif k == round((pulse(1)+pulse(2))/dt)
    xkp(6,1) = 0;
end
% Measurement
xdelkv = MatrixHist(x,xHist,k);
xdelk = xdelkv(:, :, 1);
yk = H*xdelk+sigk;
% Delayed state estimate from measurement
uEx = MatrixHist(u,uHist,k);
Kyk = Kykv(:, :, k);
xhydelk = xhydel(:, :, k);
xhydelp = Ak*xhydelk+Bk*uEx(:, :, 1)+Kyk*(yk-H*xhydelk);
Pyp = Omxi+(Ak-Kyk*H)*Pyk*Ak';
% Extrapolate state estimate from measurement
xold = xhydelk;
for kex = 1:delkh
    uold = uEx(:, :, kex);
    xnew = Ak*xold+Bk*uold;
    xold = xnew;
end

```

```

xhyk = xold;
% Estimate
Kk = Kkv(:, :, k); % Non-adaptive
xhp = Ak*xhk+Bk*uk+Kk*(xhyk-xhk)+etak;
Pp = Omxi+Ometa+(Ak-Kk)*Pk*Ak'+C*uk*uk'*C';
% Store new values
x(:, :, k+1) = xkp;
y(:, :, k) = yk;
xhy(:, :, k) = xhyk;
u(:, :, k) = uk;
xhydel(:, :, k+1) = xhydelp;
xh(:, :, k+1) = xhp;
costkv(k, 1) = xk'*Qk*xk+uk'*Rk*uk;
P(:, :, k+1) = Pp;
Py(:, :, k+1) = Pyp;
end
costkv(N, 1) = xkp'*QN*xkp;
cost = sum(costkv);

t = [0:dt:(N-1)*dt]';
x1(:, 1) = 180/pi*x(7, 1, :);
x2(:, 1) = x(2, 1, :);
x3(:, 1) = x(3, 1, :);
x1h(:, 1) = 180/pi*xh(7, 1, :);
y1(:, 1) = 180/pi*y(4, 1, :); y1(end+1) = y1(end);
y1h(:, 1) = 180/pi*xhy(7, 1, :);
Fe(:, 1) = x(6, 1, :);
Feh(:, 1) = xh(6, 1, :);
u1(:, 1) = u(1, 1, :);

```

### B.2.2.2 RelReach

```

function out = RelReach(thetastar,tf,T,J,G,Kj,tau1,tau2)

% Calculate state values over reaching interval
t = [0:T:tf]';
theta = thetastar*(t/tf-1/(2*pi)*sin(2*pi*t/tf));
thetad = thetastar/tf*(1-cos(2*pi*t/tf));
thetadd = 2*pi*thetastar/tf^2*sin(2*pi*t/tf);
thetaddd = 4*pi^2*thetastar/tf^3*cos(2*pi*t/tf);
thetadddd = -8*pi^3*thetastar/tf^4*sin(2*pi*t/tf);
f = J*thetadd+G*thetad+Kj*theta;
fd = J*thetaddd+G*thetadd+Kj*thetad;
fdd = J*thetadddd+G*thetaddd+Kj*thetadd;
g = tau2*fdd+f;

```

```

gd = tau2*fdd+fd;
u = tau1*gd+g;

% Normalize rms values by final position
out1 = rms(theta)/thetastar;
out2 = rms(thetad)/thetastar;
out3 = rms(f)/thetastar;
out4 = rms(g)/thetastar;

% Output rms of u to help calculate multiplicative noise.
out5 = rms(u);

% Normalize sum of squared control by squared final position
out6 = sum(u.^2)/thetastar^2;

% Generate output vector
out = [out1 out2 out3 out4 out5 out6]';

```

### B.2.2.3 MatrixHist

```

function Xv = MatrixHist(X,Xhist,k)

% Given a three-dimensional variable X in which X(:, :, k) is value
% of the matrix at time k, output the variable Xv which is the portion
% of X and Xhist needed to integrate from k-delk to k, where
% Xhist is the previous time history of the matrix with length kdel

% Xv is Matrix(:, :, k-delk:k-1)

delk = length(Xhist(1,1,:));
if k > delk
    Xv(:, :, 1:delk) = X(:, :, k-delk:k-1);
elseif k == 1
    Xv = Xhist;
else
    Xv(:, :, 1:delk-k+1) = Xhist(:, :, end-(delk-k):end);
    Xv(:, :, delk-k+2:delk) = X(:, :, 1:k-1);
end

```

## LIST OF REFERENCES

- [1] National Institute of Neurological Disorders and Stroke, “Tremor fact sheet,” NINDS, Bethesda, MD, NIH Publication No. 12-4734, 2012.
- [2] J. B. Gao, “Analysis of amplitude and frequency variations of essential and parkinsonian tremors,” *Medical and Biological Engineering and Computing*, vol. 42, no. 3, pp. 345–349, 2004.
- [3] G. Deuschl, J. Raethjen, M. Lindermann, and P. Krack, “The pathophysiology of tremor,” *Muscle & Nerve*, vol. 24, no. 6, pp. 716–735, 2001.
- [4] D. Lorenz, D. Schwieger, H. Moises, and G. Deuschl, “Quality of life and personality in essential tremor patients,” *Movement Disorders*, vol. 21, no. 8, pp. 1114–1118, 2006.
- [5] C. Jenkinson, V. Peto, R. Fitzpatrick, R. Greenhall, and N. Hyman, “Self-reported functioning and well-being in patients with parkinson’s disease: Comparison of the short-form health survey (sf-36) and the parkinson’s disease questionnaire (pdq-39),” *Age and Aging*, vol. 24, no. 6, pp. 505–509, 1995.
- [6] E. D. Louis and J. J. Ferreira, “How common is the most common adult movement disorder? update on the worldwide prevalence of essential tremor,” *Movement Disorders*, vol. 25, no. 5, pp. 534–541, 2010.
- [7] E. D. Louis and R. Ottman, “How many people in the USA have essential tremor? deriving a population estimate based on epidemiological data,” *Tremor Other Hyperkinet. Mov.*, vol. 4, no. 259, pp. 1–4, 2014.
- [8] G. Deuschl, J. Raethjen, H. Hellriegel, and R. Elble, “Treatments of patients with essential tremor,” *Lancet Neurol.*, vol. 10, no. 2, pp. 148–161, 2011.
- [9] J. Timmer, S. Häußler, M. Lauk, and C. H. Lücking, “Pathological tremors: Deterministic chaos or nonlinear stochastic oscillators?” *Chaos*, vol. 10, no. 1, pp. 278–288, 2000.
- [10] J. Kotovsky and M. J. Rosen, “A wearable tremor-suppression orthosis,” *Journal of Rehabilitation Research & Development*, vol. 35, no. 4, pp. 373–387, 1998.
- [11] D. Case, B. Taheri, and E. Richer, “Design and characterization of a small-scale magnetorheological damper for tremor suppression,” *IEEE/ASME Transactions on Mechatronics*, vol. 18, no. 1, pp. 96–103, 2013.

- [12] —, “Dynamical modeling and experimental study of a small-scale magnetorheological damper,” *IEEE/ASME Transactions on Mechatronics*, vol. 19, no. 3, pp. 1015–1024, 2014.
- [13] —, “A lumped-parameter model for adaptive dynamic mr damper control,” *IEEE/ASME Transactions on Mechatronics*, vol. 20, no. 4, pp. 1689–1696, 2015.
- [14] B. Taheri, D. Case, and E. Richer, “Robust controller for tremor suppression at musculoskeletal level in human wrist,” *IEEE Transactions on Neural Systems and Rehabilitation Engineering*, vol. 22, no. 2, pp. 379–388, 2014.
- [15] —, “Adaptive suppression of severe pathological tremor by torque estimation,” *IEEE/ASME Transactions on Mechatronics*, vol. 20, no. 2, pp. 717–727, 2015.
- [16] E. Rocon, J. M. Belda-Lois, A. F. Ruiz, M. Manto, J. C. Moreno, and J. L. Pons, “Design and validation of a rehabilitation robotic exoskeleton for tremor assessment and suppression,” *IEEE Trans. Neural Syst. Rehabil. Eng.*, vol. 15, no. 3, pp. 367–378, 2007.
- [17] E. Rocon, M. Manto, J. Pons, S. Camut, and J. M. Belda, “Mechanical suppression of essential tremor,” *The Cerebellum*, vol. 6, no. 1, pp. 73–78, 2007.
- [18] E. Rocon and J. L. Pons, *Exoskeletons in Rehabilitation Robotics*. Heidelberg, Germany: Springer, 2011.
- [19] G. Herrnstadt and C. Menon, “Admittance-based voluntary-driven motion with speed-controlled tremor rejection,” *IEEE/ASME Transactions on Mechatronics*, vol. 21, no. 4, pp. 2108–2119, 2016.
- [20] —, “Voluntary-driven elbow orthosis with speed-controlled tremor suppression,” *Frontiers in Bioengineering and Biotechnology*, vol. 4, no. 29, pp. 1–10, 2016.
- [21] Y. Zhou, M. D. Naish, M. E. Jenkins, and A. L. Trejos, “Design and validation of a novel mechatronic transmission system for a wearable tremor suppression device,” *Robotics and autonomous systems*, vol. 91, no. 1, pp. 38–48, 2017.
- [22] E. Rocon, J. M. Belda-Lois, J. J. Sanchez-Lacuesta, and J. L. Pons, “Pathological tremor management: Modelling, compensatory technology and evaluation,” *Technology & Disability*, vol. 16, no. 1, pp. 3–18, 2004.
- [23] Y. Zhou, M. E. Jenkins, M. D. Naish, and A. L. Trejos, “Development of a wearable tremor suppression glove,” in *Proceedings of IEEE International Conference on Biomedical Robotics and Biomechatronics*. Enschede, The Netherlands: IEEE, Aug. 2018, pp. 26–29.
- [24] A. H. Zamanian and E. Richer, “Adaptive notch filter for pathological tremor suppression using permanent magnet linear motor,” *Mechatronics*, vol. 63, p. 102273, 2019.



- [25] P. Brochu and Q. Pei, “Advances in dielectric elastomers for actuators and artificial muscles,” *Macromolecular Rapid Communications*, vol. 31, no. 1, pp. 10–36, 2010.
- [26] I. A. Anderson, T. A. Gisby, T. G. McKay, B. M. O’Brien, and E. Calius, “Multi-functional dielectric elastomer artificial muscles for soft and smart machines,” *Journal of Applied Physics*, vol. 112, no. 4, p. 041101, 2012.
- [27] T. A. Gisby, B. M. O’Brien, and I. A. Anderson, “Self sensing feedback for dielectric elastomer actuators,” *Applied Physics Letters*, vol. 102, no. 19, p. 193703, 2013.
- [28] G. Rizzello, D. Naso, A. York, and S. Seelecke, “Closed loop control of dielectric elastomer actuators based on self-sensing displacement feedback,” *Smart Materials and Structures*, vol. 25, no. 3, p. 035034, 2016.
- [29] —, “A self-sensing approach for dielectric elastomer actuators based on online estimation algorithms,” *IEEE/ASME Transactions on Mechatronics*, vol. 22, no. 2, pp. 728–738, 2017.
- [30] Z. Hu, M. Hao, S. Xu, Q. Xiao, and N. Lan, “Evaluation of tremor interference with control of voluntary reaching movements in patients with parkinson’s disease,” *J. Neuroeng. Rehabil.*, vol. 16, p. 38, 2019.
- [31] A. J. Dinnerstein, T. Frigyesi, and M. Lowenthal, “Delayed feedback as a possible mechanism in parkinsonism,” *Percept. Mot. Ski.*, vol. 15, no. 3, pp. 667–680, 1962.
- [32] H. J. Palanthandalam-Madapusi, “Is parkinsonian tremor a limit cycle?” *J. Mech. Med. Biol.*, vol. 11, no. 5, pp. 1017–1023, 2011.
- [33] V. V. Shah, S. Goyal, and H. J. Palanthandalam-Madapusi, “Clinical facts along with a feedback control perspective suggest that increased response time might be the cause of parkinsonian rest tremor,” *J. Comput. Nonlinear Dyn.*, vol. 12, no. 1, p. 011007, 2017.
- [34] E. Todorov and M. I. Jordan, “Optimal feedback control as a theory of motor coordination,” *Nat. Neurosci.*, vol. 5, no. 11, pp. 1226–1235, 2002.
- [35] S. H. Scott, “Optimal feedback control and the neural basis of volitional motor control,” *Nature Reviews Neuroscience*, vol. 5, pp. 532–545, 2004.
- [36] E. Todorov, “Stochastic optimal control and estimation methods adapted to the noise characteristics of the sensorimotor system,” *Neural Comput.*, vol. 17, no. 5, pp. 1084–1108, 2005.
- [37] D. W. Franklin and D. M. Wolpert, “Computational mechanisms of sensorimotor control,” *Neuron*, vol. 72, no. 3, pp. 425–442, 2011.
- [38] —, “The computational and neural basis of voluntary motor control and planning,” *Trends Cogn. Sci.*, vol. 16, no. 11, pp. 541–549, 2012.

- [39] S. H. Scott, T. Cluff, C. R. Lowrey, and T. Takei, “Feedback control during voluntary motor actions,” *Current Opinion in Neurobiology*, vol. 33, pp. 85–94, 2015.
- [40] F. Crevecoeur and S. H. Scott, “Priors engaged in long-latency responses to mechanical perturbations suggest a rapid update in state estimation,” *PLoS Comput. Biol.*, vol. 9, no. 8, p. e1003177, 2013.
- [41] F. Crevecoeur and M. Gevers, “Filtering compensation for delays and prediction errors during sensorimotor control,” *Neural Comput.*, vol. 31, no. 4, pp. 738–764, 2019.
- [42] C. N. Riviere and N. V. Thakor, “Modeling and canceling tremor in human-machine interfaces,” *IEEE Engineering in Medicine and Biology*, vol. 15, no. 3, pp. 29–36, 1996.
- [43] C. N. Riviere, S. Rader, and N. V. Thakor, “Adaptive canceling of physiological tremor for improved precision in microsurgery,” *IEEE Trans. Biomed. Eng.*, vol. 45, no. 7, pp. 839–846, 1998.
- [44] G. Deuschl, P. Bain, and M. Brin, “Consensus statement of the movement disorder society on tremor,” *Movement Disorders*, vol. 13, no. S3, pp. 2–23, 1998.
- [45] D. J. Wile, R. Ranaway, and Z. H. T. Kiss, “Smart watch accelerometry for analysis and diagnosis of tremor,” *Journal of Neuroscience Methods*, vol. 230, pp. 1–4, 2014.
- [46] A. M. Woods, M. Nowostawski, E. A. Franz, and M. Purvis, “Parkinson’s disease and essential tremor classification on mobile device,” *Pervasive and Mobile Computing*, vol. 13, pp. 1–12, 2014.
- [47] C. W. Hess and S. L. Pullman, “Tremor: Clinical phenomenology and assessment techniques,” *Tremor Other Hyperkinet. Mov.*, vol. 2, pp. tre-02-65-365-1, 2012.
- [48] G. Deuschl, J. Raethjen, R. Baron, M. Lindemann, H. Wilms, and P. Krack, “The pathophysiology of parkinsonian tremor: a review,” *J. Neurol.*, vol. 247, no. S5, pp. V33–V48, 2000.
- [49] M. F. Dirkx, H. Zach, B. R. Bloem, M. Hallett, and R. C. Helmich, “The nature of postural tremor in Parkinson’s disease,” *Neurology*, vol. 90, no. 13, pp. e1095–e1103, 2018.
- [50] R. C. Helmich, I. Toni, G. Deuschl, and B. R. Bloem, “The pathophysiology of essential tremor and parkinson’s tremor,” *Curr. Neurol. Neurosci. Rep.*, vol. 13, no. 9, p. 378, 2013.
- [51] R. C. Helmich, M. Hallett, G. Deuschl, I. Toni, and B. R. Bloem, “Cerebral causes and consequences of parkinsonian resting tremor: a tale of two circuits?” *Brain*, vol. 135, no. 11, pp. 3206–3226, 2012.
- [52] C. Duval, J.-F. Danealut, W. D. Hutchinson, and A. F. Sadikot, “A brain network model explaining tremor in Parkinson’s disease,” *Neurobiol Dis*, vol. 85, pp. 49–59, 2016.

- [53] B. S. Connolly and A. E. Lang, "Pharmacological treatment of parkinson disease," *JAMA*, vol. 311, no. 16, pp. 1670–1683, 2014.
- [54] J. S. Perlmuter and J. W. Mink, "Deep brain stimulation," *Annu. Rev. Neurosci.*, vol. 29, pp. 229–257, 2006.
- [55] A. L. Benabid, S. Chabardes, J. Mitrofanis, and P. Pollak, "Deep brain stimulation of the subthalamic nucleus for the treatment of Parkinson's disease," *Lancet Neurol*, vol. 8, no. 1, pp. 67–81, 2009.
- [56] A. Umemura, J. L. Jaggi, H. I. Hurtig, A. D. Siderowf, A. Colcher, M. B. Stern, and G. H. Baltuch, "Deep brain stimulation for movement disorders: morbidity and mortality in 109 patients," *Journal of Neurosurgery*, vol. 98, no. 4, pp. 779–784, 2003.
- [57] J. Pepper, L. Zrinzo, B. Mirza, T. Foltynie, P. Limousin, and M. Hariz, "The risk of hardware infection in deep brain stimulation surgery is greater at impulse generator replacement than at the primary procedure," *Sterotactic and Functional Neurosurgery*, vol. 91, no. 1, pp. 56–65, 2013.
- [58] L. C. Shih, K. LaFaver, C. Lim, E. Papavassiliou, and D. Tarsy, "Loss of benefit in VIM thalamic deep brain stimulation (DBS) for essential tremor (ET): How prevalent is it?" *Parkinsonism Relat. Disord.*, vol. 19, no. 7, pp. 676–679, 2013.
- [59] G. Mandybur and M. Gartner, "Deep brain stimulation for movement disorders," Mayfield Clinic, Cincinnati, OH, Tech. Rep., 2016.
- [60] J. Álvaro Gallego, E. Rocon, J. M. Belda-Lois, and J. L. Pons, "Neuroprosthesis for tremor management through the control of muscle co-contraction," *Journal of Neuroengineering and Rehabilitation*, vol. 10, no. 36, pp. 1–12, 2013.
- [61] A. Prochazka, J. Elek, and M. Javidan, "Attenuation of pathological tremors by functional electrical stimulation I: Method," *Annals of Biomedical Engineering*, vol. 20, no. 2, pp. 205–224, 1992.
- [62] S. Dosen, S. Muceli, J. L. Dideriksen, J. P. Romero, E. Rocon, J. Pons, and D. Farina, "Online tremor suppression using electromyography and low-level electrical stimulation," *IEEE Trans. Neural Syst. Rehabil. Eng.*, vol. 23, no. 16, 2015.
- [63] J. L. Dideriksen, C. M. Laine, S. Dosen, S. Muceli, E. Rocon, J. L. Pons, J. Benito-Leon, and D. Farina, "Electrical stimulation of afferent pathways for the suppression of pathological tremor," *Frontiers in Neuroscience*, vol. 11, p. 178, 2017.
- [64] J. Hendricks, "A second-generation joystick for people disabled by tremor," in *Proc. 14th Annual RESNA Conf.* Elmsford, NY: RESNA, 2002, pp. 248–251.
- [65] Liftware. (2017) Liftware steady. [Online]. Available: <https://www.liftware.com/steady/>

- [66] K. C. Veluvolu, U. X. Tan, W. T. Latt, C. Y. Shee, and W. T. Ang, “Bandlimited multiple fourier linear combiner for real-time tremor compensation,” in *Proceedings of the Conference of the IEEE EMBS*. Lyon, France: IEEE, Aug. 2007, pp. 2847–2850.
- [67] K. C. Veluvolu, W. T. Latt, and W. T. Ang, “Double adaptive bandlimited multiple Fourier linear combiner for real-time estimation/filtering of physiological tremor,” *Biomedical Signal Processing and Control*, vol. 5, no. 1, pp. 37–44, 2010.
- [68] G. Herrnstadt, M. J. McKeown, and C. Menon, “Controlling a motorized orthosis to follow elbow volitional movement: tests with individuals with pathological tremor,” *Journal of NeuroEngineering and Rehabilitation*, vol. 16, p. 23, 2019.
- [69] Y. Matsumoto, M. Seki, Y. Nakashima, T. Ando, Y. Kobayahsi, H. Iijima, M. Nagaoka, and M. G. Fujie, “Algorithm to demodulate an electromyogram signal modulated by essential tremor,” *Robomech Journal*, vol. 4, p. 15, 2017.
- [70] Y. Bar-Cohen, “Electroactive polymers as artificial muscles – reality and challenges,” in *Proceedings of the AIAA Structures, Structural Dynamics, & Materials Conference*. Seattle, WA: AIAA, Apr. 2001, pp. 2001–1492.
- [71] R. E. Pelrine, R. D. Kornbluh, and J. P. Joseph, “Electrostriction of polymer dielectrics with compliant electrodes as a means of actuation,” *Sensors and Actuators A*, vol. 64, no. 1, pp. 77–85, 1998.
- [72] R. Pelrine, R. Kornbluh, J. Joseph, R. Heydt, Q. Pei, and S. Chiba, “High-field deformation of elastomeric dielectrics for actuators,” *Materials Science and Engineering C*, vol. 11, no. 2, pp. 89–100, 2000.
- [73] G. Kovacs, L. Düring, S. Michel, and G. Terrasi, “Stacked dielectric elastomer actuator for tensile force transmission,” *Sensors and Actuators A*, vol. 155, no. 2, pp. 299–307, 2009.
- [74] P. Lotz, M. Matysek, and H. F. Schlaak, “Fabrication and application of miniaturized dielectric elastomer stack actuators,” *IEEE/ASME Transactions on Mechatronics*, vol. 16, no. 1, pp. 58–66, 2011.
- [75] T. A. Gisby, S. Xie, E. P. Calius, and I. A. Anderson, “Integrated sensing and actuation of muscle-like actuators,” in *Proceedings of the SPIE Smart Structures & Materials & NDE Conference*. San Diego, CA: SPIE, Apr. 2009, p. 728707.
- [76] J.-S. Plante and S. Dubowsky, “On the performance mechanisms of dielectric elastomer actuators,” *Sensors and Actuators A*, vol. 137, no. 1, pp. 96–109, 2007.
- [77] G. Kovacs, P. Lochmatter, and M. Wissler, “An arm wrestling robot driven by dielectric elastomer actuators,” *Smart Materials and Structures*, vol. 16, no. 2, pp. S306–S317, 2007.

- [78] Q. Pei, M. Rosenthal, S. Stanford, H. Prahlaad, and R. Pelrine, "Multiple-degrees-of-freedom electroelastomer roll actuators," *Smart Materials and Structures*, vol. 13, no. 5, pp. N86–N92, 2004.
- [79] C. Jordi, S. Michel, G. Kovacs, and P. Ermanni, "Scaling of planar dielectric elastomer actuators in an agonist-antagonist configuration," *Sensors and Actuators A: Physical*, vol. 161, no. 1–2, pp. 182–190, 2010.
- [80] G. Kofod, W. Wirges, M. Pajanen, and S. Bauer, "Energy minimization for self-organized structure formation and actuation," *Applied Physics Letters*, vol. 90, no. 8, p. 081916, 2007.
- [81] U. Gupta, Y. Wang, H. Ren, and J. Zhu, "Dynamic modeling and feedforward control of jaw movements driven by viscoelastic artificial muscles," *IEEE/ASME Transactions on Mechatronics*, vol. 24, no. 1, pp. 25–35, 2019.
- [82] G. Rizzello, P. Serafino, D. Naso, and S. Seelecke, "Towards sensorless soft robotics: self-sensing stiffness control of dielectric elastomer actuators," *IEEE Transactions on Robotics*, vol. 36, no. 1, pp. 174–188, 2020.
- [83] T. Hoffstadt and J. Maas, "Analytical modeling and optimization of deap-based multilayer stack-transducers," *Smart Materials and Structures*, vol. 24, no. 9, p. 094001, 2015.
- [84] H. Haus, M. Matysek, H. MöBinger, and H. F. Schlaak, "Modelling and characterization of dielectric elastomer stack actuators," *Smart Materials and Structures*, vol. 22, no. 10, p. 104009, 2013.
- [85] F. Klug, S. Solano-Arana, H. Mößinger, F. Förster-Zügel, and H. F. Schlaak, "Fabrication of dielectric elastomer stack transducers (dest) by liquid deposition modeling," in *Proceedings of the SPIE Smart Structures & Materials & NDE Conference*. Portland, OR: SPIE, Mar. 2017, p. 101632Q.
- [86] F. Carpi and D. D. Rossi, "Contractile folded dielectric elastomer actuators," in *Proceedings of the SPIE Smart Structures & Materials & NDE Conference*. San Diego, CA: SPIE, Mar. 2007, p. 65240D.
- [87] F. Carpi, C. Salaris, and D. De Rossi, "Folded dielectric elastomer actuators," *Smart Materials and Structures*, vol. 16, no. 2, pp. S300–S305, 2007.
- [88] H. F. Schlaak, M. Jungmann, M. Matysek, and P. Lotz, "Novel multilayer electrostatic solid state actuators with elastic dielectric," in *Proceedings of the SPIE Smart Structures & Materials & NDE Conference*. San Diego, CA: SPIE, Apr. 2005, pp. 121–133.
- [89] M. Duduta, R. J. Wood, and D. R. Clarke, "Multilayer dielectric elastomers for fast, programmable actuation without prestretch," *Advanced Materials*, vol. 28, no. 36, pp. 8058–8063, 2016.

- [90] G. Kovacs and L. Düring, “Contractive tension force stack actuator based on soft dielectric EAP,” in *Proceedings of the SPIE Smart Structures & Materials & NDE Conference*. San Diego, CA: SPIE, Apr. 2009, p. 72870A.
- [91] J. Maas, D. Tepel, and T. Hoffstadt, “Actuator design and automated manufacturing process for deap-based multilayer stack-actuators,” *Meccanica*, vol. 50, no. 11, pp. 2839–2854, 2015.
- [92] O. A. Araromi, A. T. Conn, C. S. Ling, J. M. Rossiter, R. Vaidyanathan, and S. C. Burgess, “Spray deposited multilayered dielectric elastomer actuators,” *Sensors and Actuators A: Physical*, vol. 167, no. 2, pp. 459–467, 2011.
- [93] N. H. Chuc, N. H. L. Vuong, D. S. Kim, H. P. Moon, J. C. Koo, Y. K. Lee, J.-D. Nam, and H. R. Choi, “Fabrication and control of rectilinear artificial muscle actuator,” *IEEE/ASME Transactions on Mechatronics*, vol. 16, no. 1, pp. 167–176, 2011.
- [94] H. Jung, S. Yang, K. Cho, M. Song, C. Nguyen, H. Phung, U. Kim, H. Moon, J. Koo, J. Nam, and H. Choi, “Design and fabrication of twisted monolithic dielectric elastomer actuator,” *International Journal of Control, Automation, and Systems*, vol. 15, no. 1, pp. 25–35, 2017.
- [95] Z. Li, M. Sheng, M. Wang, P. Dong, B. Li, and H. Chen, “Stacked dielectric elastomer actuator (sdea): casting process, modeling and active vibration isolation,” *Smart Materials and Structures*, vol. 27, no. 7, p. 075023, 2018.
- [96] M. Landgraf, S. Reitelshöfer, J. Franke, and M. Hedges, “Aerosol jet printing and lightweight power electronics for dielectric elastomer actuators,” in *Proceedings of International Electric Drives Production Conference 2013*. Nuremberg, Germany: IEEE, Oct. 2013, pp. 29–30.
- [97] M. Duduta, E. Hajiesmaili, H. Zhao, R. J. Wood, and D. R. Clarke, “Realizing the potential of dielectric elastomer artificial muscles,” *Proceedings of the National Academy of Sciences*, vol. 116, no. 7, pp. 2476–2481, 2019.
- [98] G.-Y. Gu, U. Gupta, J. Zhu, L.-M. Zhu, and X. Zhu, “Modeling of viscoelastic electromechanical behavior in a soft dielectric elastomer actuator,” *IEEE Transactions on Robotics*, vol. 33, no. 5, pp. 1263–1271, 2017.
- [99] B. Nolte, S. Kempfle, and I. Schäfer, “Does a real material behave fractionally? applications of fractional differential operators to the damped structure borne sound in viscoelastic solids,” *Journal of Computational Acoustics*, vol. 11, no. 3, pp. 451–489, 2003.
- [100] K. Jung, K. J. Kim, and H. R. Choi, “A self-sensing dielectric elastomer actuator,” *Sensors and Actuators A: Physical*, vol. 143, no. 2, pp. 343–351, 2008.
- [101] S. Schlatter, P. Illenberger, and S. Rosset, “Peta-pico-Voltron: An open-source high voltage power supply,” *HardwareX*, vol. 4, p. e00039, 2018.

- [102] S. K. Mitchell, X. Wang, E. Acome, T. Martin, K. Ly, N. Kellaris, V. G. Venkata, and C. Keplinger, “An easy-to-implement toolkit to create versatile and high-performance HASEL actuators for untethered soft robots,” *Advanced Science*, vol. 6, no. 14, p. 1900178, 2019.
- [103] T. Hoffstadt and J. Maas, “Optimized control of a flyback-converter for bidirectional feeding of DEAP transducers,” in *Proc. SPIE Smart Struc.* San Diego, CA: SPIE, Mar. 2014, p. 905613.
- [104] S. Pourazadi, A. Shagerdmootaab, H. Chan, M. Moallem, and C. Menon, “On the electrical safety of dielectric elastomer actuators in proximity to the human body,” *Smart Materials and Structures*, vol. 26, no. 11, p. 115007, 2017.
- [105] M. Desmurget and S. Grafton, “Forward modeling allows feedback control for fast reaching movements,” *Trends in Cognitive Neuroscience*, vol. 4, no. 11, pp. 423–431, 2000.
- [106] I. L. Kurtzer, J. A. Pruszynski, and S. H. Scott, “Long-latency reflexes of the human arm reflect an internal model of limb dynamics,” *Curr. Biol.*, vol. 18, no. 6, pp. 449–453, 2008.
- [107] R. S. Maeda, T. Cluff, P. L. Gribble, and J. A. Pruszynski, “Feedforward and feedback control share an internal model of the arm’s dynamics,” *J. Neurosci.*, vol. 38, no. 49, pp. 10 505–10 514, 2018.
- [108] R. Shadmehr and F. A. Mussa-Ivaldi, “Adaptive representation of dynamics during learning of a motor task,” *Journal of Neuroscience*, vol. 14, no. 5, pp. 3208–3224, 1994.
- [109] M. A. Smith, A. Ghazizadeh, and R. Shadmehr, “Interacting adaptive processes with different timescales underlie short-term motor learning,” *PLoS Biology*, vol. 4, no. 6, p. e179, 2006.
- [110] S. H. Scott, “Optimal feedback control and the neural basis of volitional motor control,” *Nature Reviews Neuroscience*, vol. 5, pp. 532–545, 2004.
- [111] F. Crevecoeur and I. Kurtzer, “Long-latency reflexes for inter-effector coordination reflect a continuous state feedback controller,” *J Neurophysiol.*, vol. 120, no. 5, pp. 2466–2483, 2018.
- [112] J. Y. Nashed, F. Crevecoeur, and S. H. Scott, “Influence of the behavioral goal and environmental obstacles on rapid feedback responses,” *Journal of Neurophysiology*, vol. 108, no. 4, pp. 999–1009, 2012.
- [113] D. A. Nowak, D. Timmann, and J. Hermsdörfer, “Dexterity in cerebellar agenesis,” *Neuropsychologia*, vol. 45, no. 4, pp. 696–703, 2007.
- [114] R. C. Miall, L. O. D. Christensen, O. Cain, and J. Stanley, “Disruption of state estimation in the human lateral cerebellum,” *PLoS Biology*, vol. 5, no. 11, p. e316, 2007.

- [115] R. Shadmehr and J. W. Krakauer, “A computational neuroanatomy for motor control,” *Exp Brain Res.*, vol. 185, no. 3, pp. 359–381, 2008.
- [116] D. M. Wolpert, R. C. Miall, and M. Kawato, “Internal models in the cerebellum,” *Current Opinion in Neurobiology*, vol. 2, no. 9, pp. 338–347, 1998.
- [117] M. Manto, J. M. Bower, A. B. Conforto, J. M. Delgado-García, S. N. F. da Guarda, M. Gerwig, C. Habas, N. Hagura, R. B. Ivry, P. Mariën, M. Molinari, E. Naito, D. A. Nowak, N. O. B. Taib, D. Pelisson, C. D. Tesche, C. Tilikete, and D. Timmann, “Consensus paper: Roles of the cerebellum in motor control—the diversity of ideas on cerebellar involvement in movement,” *Cerebellum*, vol. 11, pp. 457–487, 2012.
- [118] P. Mazzoni, A. Hristova, and J. W. Krakauer, “Why don’t we move faster? Parkinson’s disease, movement vigor, and implicit motivation,” *Journal of Neuroscience*, vol. 27, no. 27, pp. 7105–7116, 2007.
- [119] R. S. Turner and M. Desmurget, “Basal ganglia contributions to motor control: a vigorous tutor,” *Current Opinion in Neurobiology*, vol. 20, no. 6, pp. 704–716, 2010.
- [120] S. H. Scott, “The role of primary motor cortex in goal-directed movements: insights from neurophysiological studies on non-human primates,” *Current Opinion in Neurobiology*, vol. 13, no. 6, pp. 671–677, 2003.
- [121] J. A. Pruszynski, I. Kurtzer, J. Y. Nashed, M. Omrani, B. Brouwer, and S. H. Scott, “Primary motor cortex underlies multi-joint integration for fast feedback control,” *Nature*, vol. 478, pp. 387–390, 2011.
- [122] M. A. Sommer, “The role of the thalamus in motor control,” *Current Opinion in Neurobiology*, vol. 13, no. 6, pp. 663–670, 2003.
- [123] M. K. Horne and E. G. Butler, “The role of the cerebello-thalamo-cortical pathway in skilled movement,” *Progress in Neurobiology*, vol. 46, no. 2–3, pp. 199–213, 1995.
- [124] C. R. Kelley and J. L. Kauffman, “Exploring dielectric elastomers as actuators for hand tremor suppression,” in *Proc. SPIE Smart Struc.* Portland, OR: SPIE, Mar. 2017, p. 1016322.
- [125] —, “Tremor suppression controller for dielectric elastomer orthosis,” in *Proc. SPIE Smart Struc.* Denver, CO: SPIE, Mar. 2018, p. 1059427.
- [126] —, “Tremor-active controller for dielectric elastomer-based pathological tremor suppression,” *IEEE/ASME Transactions on Mechatronics*, p. to appear, 2020.
- [127] Z. Suo, “Theory of dielectric elastomers,” *Acta Mechanica Solida Sinica*, vol. 23, no. 6, pp. 549–578, 2010.



- [128] G. T. Yamaguchi, *Dynamic modeling of musculoskeletal motion: a vectorized approach for biomechanical analysis in three dimensions*. Boston: Kluwer Academic Publishers, 2001.
- [129] S. K. Charles and N. Hogan, “Dynamics of wrist rotations,” *J. Biomech.*, vol. 44, no. 4, pp. 614–621, 2011.
- [130] A. W. Peaden and S. K. Charles, “Dynamics of wrist and forearm rotations,” *J. Biomech.*, vol. 47, no. 11, pp. 2779–2785, 2014.
- [131] A. Murgia, P. J. Kyberd, P. H. Chappell, and C. M. Light, “Marker placement to describe the wrist movements during activities of daily living in cyclical tasks,” *Clinical Biomechanics*, vol. 19, no. 3, pp. 248–254, 2004.
- [132] S. F. Atashzar, M. Shahbazi, O. Samotus, M. Tavakoli, M. S. Jog, and R. V. Patel, “Characterization of upper-limb pathological tremors: application to design of an augmented haptic rehabilitation system,” *IEEE Journal of Selected Topics in Signal Processing*, vol. 10, no. 5, pp. 888–903, 2016.
- [133] C. R. Kelley and J. L. Kauffman, “Necessary dielectric elastomer parameters for wearable tremor suppression,” in *Proc. SPIE Smart Struc.* Denver, CO: SPIE, Mar. 2019, p. 109661T.
- [134] —, “Scaled tremor suppression with folded dielectric elastomer stack actuators,” in *Proc. SPIE Smart Struc.* Anaheim, CA: SPIE, Apr. 2020, p. 1137568.
- [135] H. Jung, K. Cho, J. Park, S. Yang, Y. Kim, K. Kim, C. Nguyen, H. Phung, P. Hoang, H. Moon, J. Koo, and H. Choi, “Musclelike joint mechanism driven by dielectric elastomer actuator for robotic applications,” *Smart Materials and Structures*, vol. 27, no. 7, p. 075011, 2018.
- [136] CTSsystems, “Polymer actuator ct25.2,” <http://www.ct-systems.ch/index.php/products/polymer-actuator-ct25-2>, 2019, accessed: 2019-03-03.
- [137] X. Niu, H. Stoyanov, W. Hu, R. Leo, P. Brochu, and Q. Pei, “Synthesizing a new dielectric elastomer exhibiting large actuation strain and suppressed electromechanical instability without prestretching,” *Journal of Polymer Science, Part B: Polymer Physics*, vol. 51, no. 3, pp. 197–206, 2013.
- [138] C. R. Kelley and J. L. Kauffman, “Optimal control perspective on Parkinson’s disease: Increased delay between state estimator and controller produces tremor,” p. in review, 2020.
- [139] T. Honda, S. Nagao, Y. Hashimoto, K. Ishikawa, T. Yokota, H. Mizusawa, and M. Ito, “Tandem internal models execute motor learning in the cerebellum,” *PNAS*, vol. 115, no. 28, pp. 7428–7433, 2018.
- [140] V. V. Shah, S. Goyal, and H. J. Palanthandalam-Madapusi, “A possible explanation of how high-frequency deep brain stimulation suppresses low-frequency tremors in parkinson’s disease,” *IEEE Trans. Neural Syst. Rehabil. Eng.*, vol. 25, no. 12, pp. 2498–2508, 2017.

- [141] E. Burdet, D. W. Franklin, and T. E. Milner, *Human Robotics: Neuromechanics and Motor Control*. Cambridge, Massachusetts: The MIT Press, 2013.
- [142] B. Hellwig, P. Mund, B. Schelter, B. Guschlbauer, J. Timmer, and C. H. Lücking, “A longitudinal study of tremor frequencies in Parkinson’s disease and essential tremor,” *Clinical Neurophysiology*, vol. 120, no. 2, pp. 431–435, 2009.
- [143] C. Bosch-Bouju, B. I. Hyland, and L. C. Parr-Brownlie, “Motor thalamus integration of cortical, cerebellar and basal ganglia information: implications for normal and parkinsonian conditions,” *Front. Comput. Neurosci.*, vol. 7, p. 163, 2013.
- [144] M. Hallett, “Tremor: Pathophysiology,” *Parkinsonism and Related Disorders*, vol. 20, no. S1, pp. S118–S122, 2014.
- [145] S. Chiken and A. Nambu, “Mechanism of deep brain stimulation: Inhibition, excitation, or disruption?” *The Neuroscientist*, vol. 22, no. 3, pp. 313–322, 2016.